Using molecular approaches to understand Complex I deficiency in mouse models

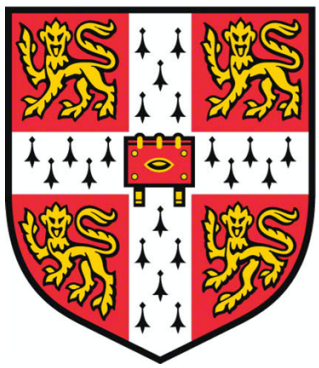

Zhan Yin

MRC Mitochondrial Biology Unit

Clare Hall
University of Cambridge

This thesis is submitted for the degree of Doctor of Philosophy

January 2021

Declaration

This thesis is the result of my own work, carried out at Medical Research Council Mitochondrial Biology Unit between October 2016 and January 2021. It includes nothing which is the outcome of work done in collaboration except as declared in the acknowledgement and specified in the text.

The content is not substantially the same as any work that has already been submitted before for any degree or other qualification at the University of Cambridge or any other University or similar institution except as declared in the preface and specified in the text.

It does not exceed the prescribed 60,000-word limit for the Degree Committee.

Zhan Yin

January 2021

Contributions

Dr Carlo Viscomi (University of Padova, Italy) has helped with the mouse colony management in Chapter 3 and Chapter 4.

In Chapter 3.3, the cryo-EM data analysing and model building were helped by Dr Hannah Bridges (MRC MBU, University of Cambridge). The structure interpretation was helped by Dr Hannah Bridges and Mr Daniel N. Grba. The experiments in Chapter 3.6 were carried out by Mr Nils Burger, Dr Andrew M. James, Dr Amin Mottahedin and Dr Hiran A. Prag and supervised by Professor Michael P. Murphy's group (MRC MBU, university of Cambridge). Mr Nils Burger carried out the CoQ and peptide mass spectrometry analyses, and the mitochondrial O_2 consumption and ROS analyses with the assistance of Dr Andrew M. James. Dr Amin Mottahedin and Dr Hiran A. Prag analysed tissue succinate levels. The *in vivo* cardiac IR injury experiments were carried out by Dr Duvaraka Kula-Alwar and supervised by Dr Thomas Krieg's group (Department of Medicine, University of Cambridge). The isolated Langendorff-perfused hearts after ischemia was performed by Dr Dunja Aksentijevic (Queen Mary University of London). The work from this chapter have been accepted and published in Nature Communications (Yin et al., 2021).

In Chapter 4.2, the tissue collection was aided by Dr Ahmed-Noor Adam Agip and Mr Daniel N. Grba (MRC MBU, university of Cambridge). In Chapter 4.3, the data collection sessions were carried out with the help of Dr Alistair Siebert, Dr Yuriy Chaban (UK National Electron Bio-Imaging Centre), and Dr James Blaza (Department of Chemistry, University of York).

In Chapter 5, the data collection for optimised grids conditions were helped by Dr James Blaza and Dr Dima Chirgadze (Department of Biochemistry, University of Cambridge).

Acknowledgements

First, and foremost, my thanks go to Professor Judy Hirst for her excellent supervision over the last four years. Her guidance and advice have been invaluable. This project would not be possible without her constant support and encouragement.

I would like to thank Dr Hannah Bridges and Dr John Wright for their generous help throughout my PhD from demonstrating experiments, giving critical comments on experimental results to providing suggestions on my thesis. I would also like to thank Dr Jamie Blaza for investing time and efforts to teach me cryo-EM techniques and give me suggestions about my projects and career. My appreciation also goes to Dr Carlo Viscomi who helped me a lot with mice work and Dr Dima Chirgadze for helping me with all my cryo-EM training and data collection in the Department of Biochemistry. And my thanks always go to Mr Andrew Raine and Mr Merlin Hartley for their constant IT support throughout my data analysis period and also Dr Tristan Croll for helping me with ISOLDE.

I would like to thank all the members in Hirst group who always helped me out during my difficult time. Special thanks to Dr Justin Fedor, Dr John Wright, Dr Andrew Jones, and Dr Riccardo Serreli for teaching me the biochemical assays and generous providing reagents when I run out of my stocks. I also want to thank Dr Olivier Biner for providing me the opportunity for collaborating with his project and eventually we published the excellent work together. I would also thank my colleague and also my friend Mr Daniel Grba who is always willing to help and support me in many aspects.

I would like to say thank you to all my collaborators who have supported the ND6 project and made contributions to this work. I would like to thank Professor Micheal Murphy's lab and Dr Thomas Krieg's lab with whom we together have done excellent works.

Last but not least, my greatest appreciation goes to my loving family. I don't think I could make this far without your enormous support and love.

I would like to dedicate this thesis to my husband and my parents.

Abstract

Complex I (NADH:ubiquinone oxidoreductase), a major electron entry point to the mitochondrial respiratory chain, couples electron transfer from NADH to ubiquinone to proton pumping across the mitochondrial inner membrane, and generates the proton motive force that drives ATP synthesis and transport processes. The ~1 MDa mammalian complex contains 45 subunits, and pathological mutations in both its mitochondrial and nuclear encoded subunits result in diverse neuro-muscular disorders. Recent high-resolution mammalian complex I structures have been solved by single-particle cryo-electron microscopy (cryo-EM) in characterised biological states and provide mechanistic insights. However, the molecular bases of genetically-determined complex I dysfunctions remain unclear. Here, two mouse models of complex I-linked mitochondrial disease were analysed structurally by cryo-EM to understand the mechanisms of their pathogenesis.

The first part of this thesis explores complex I from the ND6-P25 mouse model, which contains a mitochondrial-DNA point mutation leading to a proline to leucine substitution at position 25 in the ND6 subunit of complex I. The cryo-EM structure of ND6-P25L complex I showed a subtle local structural change resulting in rapid global conversion to a deactive state of the enzyme. Furthermore, the mutant enzyme was unable to catalyse reactive oxygen species production by reverse electron transfer, and the mutant mouse heart is protected against ischemia-reperfusion injury, substantiating a direct link between the two effects.

The second part of this thesis describes a structural study of complex I from the *ndufs4* knockout mouse model. Although the variant complex I is highly unstable, following sample optimisation its structure was obtained at 2.9 Å resolution by cryo-EM. The variant complex I lacking the NDUFS4 subunit is in the active state and, unusually, contains a density resembling ubiquinone in its active site. Absence of NDUFS4 allows motion of the NADH dehydrogenase domain and loss of the NDUFA12 subunit, explaining the instability of the variant complex.

Finally, investigations aimed at improving cryo-EM grid preparations for complex I and tackling the problems of limited sample concentration and preferred orientation are described. Grids were modified with graphene, graphene-oxide, polylysine and thiol-PEG; improved numbers of particles could be observed using very low protein concentrations, although with preferred orientation and partial loss of enzyme integrity.

Abbreviations

A/D	Active/ deactive
A6L	ATP synthase Fo subunit 8
AAV	Adeno-associated virus
AFIS	Aberration-free image shift
ANT1	Adenine nucleotide translocator1
$APAD^+$	3-acetylpyridine-adenine dinucleotide
ATP	Adenosine triphosphate
BCA	Bicinchoninic acid assay
BN-PAGE	Blue native PAGE
BS^3	Bis- (sulfosuccinimidyl)suberate
CHAPS	Asolectin and 3-[(3-Cholamidopropyl)dimethylammonio]-1-propanesulfonate hydrate
CPU	Central processing unit
Cryo-EM	Cryo-electron microscopy
CTF	Contrast transfer function
Cyt *c*	Cytochrome *c*
DTNB	5,5′-Dithio-bis-(2-nitrobenzoic acid)
DTT	Dithiothreitol
E.coli	*Escherichia coli*
EDTA	Ethylenediaminetetraacetic acid
EGTA	Ethylene glycol-bis(β-aminoethyl ether)-N,N,N′,N′-tetraacetic acid
EPR	Electron paramagnetic resonance
ETC	Electron transport chain
FAD	Flavin adenine dinucleotide
FeCN	Potassium hexacyanoferrate (III)
FeS	Iron-sulfur
FET	Forward electron transfer
FMN	Flavin mononucleotide
FSC	Fourier shell correlation
FumC	Fumarate hydratase
GO	Graphene oxide
GPU	Graphical processing unit
H_2O_2	Hydrogen peroxide
HAR	Hexammineruthenium
HET	Heterozygous
HPC	High-performance computing
HRP	Horseradish peroxidase
IL-6	Interleukin
IMM	Inner mitochondrial membrane
IMS	Intermembrane space
IR	Ischemia/Reperfusion

KO	Knockout
LHON	Leber hereditary optic neuropathy
LS	Leigh syndrome
MaeB	Malic dehydrogenase
MnSOD	Manganese superoxide dismutase
MPI	Message passing interface
MRI	Magnetic resonance imaging
mtDNA	Mitochondrial DNA
NAD^+	Nicotinamide adenine dinucleotide
NADH	Nicotinamide adenine dinucleotide (Reduced)
NADPH	Nicotinamide adenine dinucleotide phosphate
nDNA	Nuclear DNA
NEM	N-ethylmaleimide
NHS	N-Hydroxysuccinimide
$O_2^{\bullet-}$	Superoxide ion
$OH^{\cdot}$	Hydroxyl radical
OMM	Outer mitochondrial membrane
OXA1	Cytochrome oxidase assembly translocase
OXPHOS	Oxidative phosphorylation
PCR	Polymerase chain reaction
PD	Distal module
PEG	Polyethylene glycol
PINK1	PTEN-induced putative kinase 1
PKA	cAMP-dependent protein kinase
PP	Proximal module
Q-site	Ubiquinone binding site
RAM	Random access memory
RET	Reverse electron transport
RGC	Retinal ganglion cells
RMSD	Root-mean-square deviation
ROS	Reactive oxygen species
SD	Standard deviation
SMPs	Submitochondrial particles
SOD	Superoxide dismutase
T. thermophiluds	*Thermus thermophilus*
TCA cycle	Ricarboxylic acid cycle
TEM	Transmission electron microscopy
Tiff	Tagged image file format
TMH	Transmembrane helixes
VDAC	Voltage-dependent anion channel proteins
WT	Wild type
Y. lipolytica	*Yarrowia lipolytica*

Table of Contents

Chapter 1. Introduction

1.1 The Mitochondrion

Biological systems require energy to perform daily activities. Adenosine triphosphate (ATP) is the major source of energy at the cellular level. The free energy released through hydrolysis of the phosphodiester bond to form ADP is used to drive energetically unfavorable processes in the cell. The major site of ATP generation is the plasma membrane of prokaryotes or a specific cellular organelle, the mitochondrion, in eukaryotes. The endosymbiotic theory describes the origin of this organelle as a bacterial cell being engulfed by an archaeal host cell, in order for it to adapt to the transition from an anaerobic to an oxygen-rich environment on earth (Saga, 1967; Lane & Martin, 2010). However, there is still an open question at which stage of eukaryotic evolution mitochondrial endosymbiosis occurred (Ettema, 2016; Martin, 2017).

1.1.1 The structure of the mitochondrion

Mitochondria, as the main energy-transducing organelle in eukaryotes, can be observed under the light microscope, but their internal structure was only revealed by electron microscopy (Palade, 1952). As shown in Fig 1.1, the mitochondria from different tissues and species usually share a common structure containing double-layered membranes, the outer mitochondrial membrane (OMM) and the inner mitochondrial membrane (IMM), separating the organelle into two compartments, which are the intermembrane space (IMS) and the matrix (Horvath & Daum, 2013).

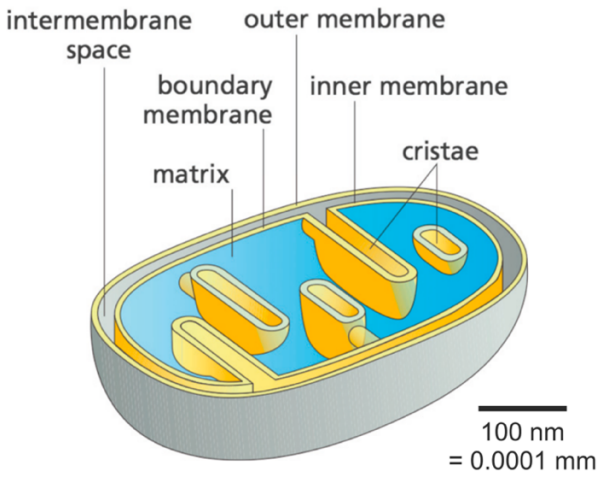

Fig 1.1 Illustration of membrane compartments in the mitochondrion. This image was adapted from Kühlbrandt (2015).

The highly permeable OMM contains special pores formed by voltage-dependent anion channel proteins (VDAC) and it is recognized as a platform for apoptosis execution (Bayrhuber et al., 2008). The IMM, with its distinct cristae structure, is known to be the location of the oxidative phosphorylation (OXPHOS) enzymes for ATP synthesis (Kühlbrandt, 2015). In contrast to the OMM, the IMM is a highly selective diffusion barrier with a membrane potential generated and only allows specific molecules to be transported through the membrane. A study also showed that the yeast complex V (ATP synthase) forms dimers at ~90° located at the curved cristae tip, while the rest of the complexes are located at the inner boundary membrane (Davies et al., 2011). The IMS is formed by a ~20 nm gap between IMM and OMM. The proteins and small molecules trafficking in and out of the mitochondria must pass through the IMS. The TIM/TOM complex (translocase of the inner membrane/ translocase of the outer membrane) spanning the IMS plays a role in translocating protein produced from nuclear DNA through the mitochondrial membrane (MacPherson & Tokatlidis, 2017). The matrix has an alkali pH (7.9-8) and is the compartment for many metabolic reactions such as the tricarboxylic acid cycle (TCA cycle) as well as the place for the mitochondrial-specific protein synthesis (Llopis, McCaffery, Miyawaki, Farquhar & Tsien, 1998). The matrix of mitochondria also contain a unique circular mitochondrial DNA (mtDNA), which is different from the nuclear DNA (nDNA). In humans, the mtDNA encodes 13 proteins (7 subunits of complex I, 1 subunit of complex III, 3 subunits of complex IV and 2 subunits of complex V), 22 tRNAs, and 2 mitochondrial ribosomal RNA (Anderson et al., 1981).

1.1.2 The functions of mitochondria

Apart from playing their role as the cellular powerhouse, mitochondria are also associated with many other physiological activities such as biosynthesis and signaling (Fig 1.2).

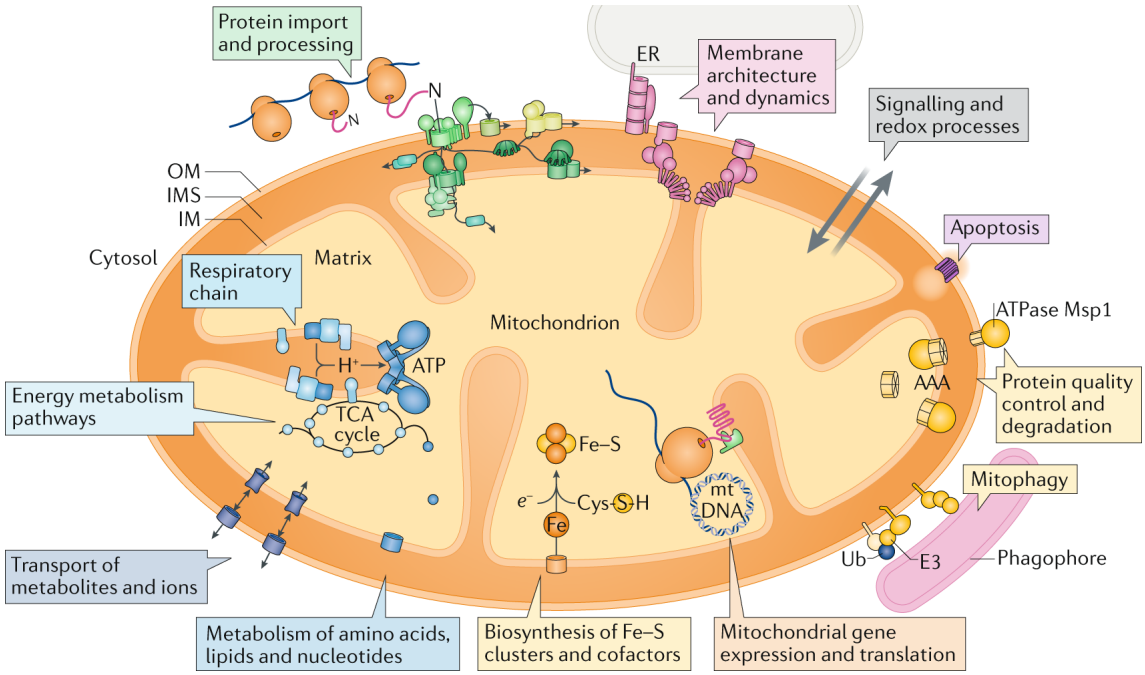

Fig 1.2 Overview of mitochondrial functions. Mitochondria have multiple functions assigned to different protein and complexes. The image was adapted from Pfanner, Warscheid & Wiedemann (2019).

One of the key roles of the mitochondria is as a biosynthetic hub. Mitochondria participate in the synthesis pathways of nucleotides, fatty acids, and amino acids (Ahn & Metallo, 2015). These pathways can be mis-regulated by stress signals, resulting in tumorigenesis (Vyas, Zaganjor & Haigis, 2016). Mitochondria also participate in heme synthesis and iron–sulfur cluster-containing protein assembly (Stehling & Lill, 2013). Mitochondria help the biogenesis of iron–sulfur cluster-containing proteins required for the mitochondrial respiratory chain as well as cytosolic amino acid biosynthesis and nuclear DNA synthesis (Kispal, Csere, Prohl & Lill, 1999). In brief, ferrous ion is imported into the mitochondrial matrix by IMM and assembled into iron–sulfur clusters requiring electrons from NAD(P)H (Froschauer, Schweyen & Wiesenberger, 2009). More than 30 components are involved in this iron–sulfur cluster assembly machinery (Stehling & Lill, 2013). Heme synthesis is also a complex process which requires eight reactions in both the mitochondria and cytosol. The biosynthesis of heme is also

considered as a way to store iron to maintain iron homeostasis and prevent oxidative damage (Richardson et al., 2010).

Apart from their biosynthesis roles, Ca^{2+} is actively transported in and out of mitochondria (Slater & Cleland, 1953). The influx–efflux machinery of mitochondrial Ca^{2+} maintains the Ca^{2+} homeostasis in the cell (Giorgi, Marchi & Pinton, 2018). Ca^{2+} is a signaling molecule in cells that is involved in many physiological processes including muscle contraction and neuronal excitation (Cannell, Cheng & Lederer, 1995; Billups & Forsythe, 2002). Furthermore, mitochondrial Ca^{2+} signaling is also implicated in aging and innate immunity (Bratic & Larsson 2013; Rongvaux, 2017). The Ca^{2+} in the cytosol is imported to the mitochondrial matrix through VDAC on the OMM and the mitochondrial Ca^{2+} uniporter (MCU) complex on IMM (Shoshan-Barmatz, Krelin & Shteinfer-Kuzmine, 2018). The apoptosis regulator Bcl-2 family proteins can regulate the Ca^{2+} influx by interacting with VDAC (Rostovtseva & Bezrukov, 2008; Martinou & Youle, 2011). The release of Ca^{2+} into the cytosol can initiate cell apoptosis and autophagy (Nunnari & Suomalainen, 2012). In addition, PTEN-induced putative kinase 1 (PINK1) can also stimulate Ca^{2+} efflux, which regulates mitochondrial fission and fusion (Twig et al., 2008; Youle & Narendra, 2011).

1.2 The respiratory chain and bioenergetics

In eukaryotic cells, glycolysis generates ATP by converting glucose into pyruvate in the cytosol with an overall gain of two ATP and nicotinamide adenine dinucleotide (NADH), but the majority of cellular ATP is generated through the respiratory chain in mitochondria. The respiratory chain, also known as the electron transport chain (ETC), is made of four membrane-bound protein complexes (complex I-IV) located in the IMM. Together with complex V they also called the oxidative phosphorylation enzymes. As shown in Fig 1.3, during oxidative phosphorylation the electrons from NADH are accepted by complex I and passed to membrane-bound ubiquinone to form ubiquinol; complex III accepts electrons from ubiquinol generated from complex I and II and transfers them to cytochrome *c* (Cyt *c)* which passes its electrons to complex IV to reduce O_2 into H_2O. This process is coupled to the formation of a proton gradient across the membrane by the translocation of protons out of the matrix and into the IMS by complexes I, III, and IV. This proton motive force drives the synthesis of ATP by complex V.

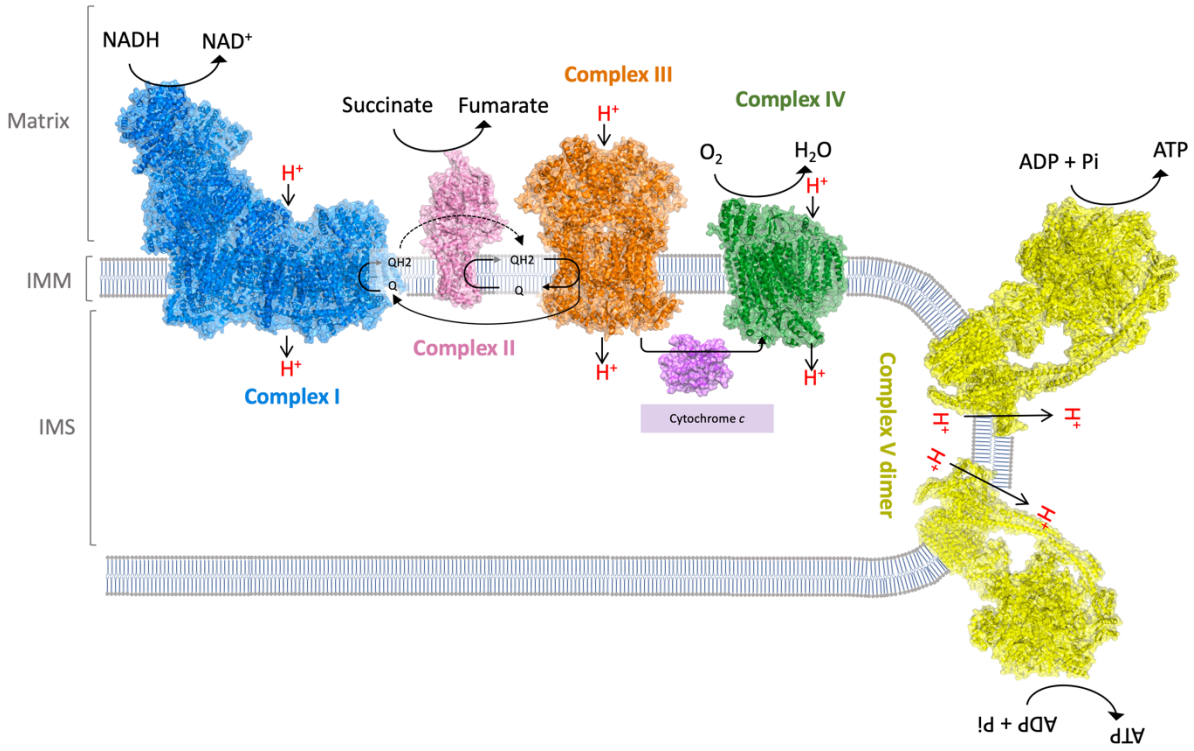

Fig 1.3 The oxidative phosphorylation enzymes in inner mitochondrial membrane proteins. Complex I (blue), complex III (orange), and complex IV (green) pump protons from the matrix towards IMM coupled with the electron transfer. Complex II (pink) oxidases succinate to fumarate and reduces ubiquinone (UQ). Cyt *c* is shown in purple. Complex V (yellow) generates ATP into the matrix driven by the proton gradient. The cartoon representation is based on the mammalian cryo-EM and crystal structures from the Protein Data Bank (complex I, PDB: 6ZR2; complex II, PDB: 1ZOY; complex III: 1BGY; complex IV, PDB:5Z62; complex V: 6ZQN, Cyt *c:* 2N9J).

1.2.1 Substrates and cofactors

NADH is the primary electron donor to the ETC. It is accumulated in the mitochondrial matrix mainly in two ways (Stein & Imai, 2012). First, the NADH is generated through the TCA cycle and fatty acid oxidation in the matrix from pyruvate from glycolysis and fatty acids from lipid degradation (Wallace, 2009). The second resource is malate transported by the malate-aspartate shuttle. Malate in the matrix is oxidised to oxaloacetate by malate dehydrogenase and produces NADH (Kane, 2014). Apart from its role in the ETC, NADH is also required in many essential metabolic pathways such as amino acid synthesis and ethanol metabolism (Grant, 2012; Louvet & Mathurin, 2015).

There are two electron carriers that play roles in electron transport between the ETC complexes: ubiquinone and Cyt *c*. Ubiquinone (Coenzyme Q or UQ) is a lipid-soluble mobile electron and proton carrier with a redox-active benzoquinone ring and an isoprenoid chain. The biothsynthesis of ubiquinone includes several steps which involves several Coq protein: the polymerisation of isopernyl tail (Coq1), the 4-hydroxybenzoate attachement (Coq2) as well as the head modification (Coq3-10) (Subramanian et al., 2019). The Coenzyme Q is capable of carrying two electrons, which gives it three redox states during electron transfer: reduced, semi-reduced, and fully oxidized (Hirst, 2010; Xia et al., 2013, Wikström, Sharma, Kaila, Hosler & Hummer, 2015). It is involved in electron transfer from complex I and II to complex III. The number of isoprenoid units varies among species: UQ10 is the most common ubiquinone observed in humans, but UQ9 is more common in mice (Wang, Oxer & Hekimi, 2015). UQ8 is observed in bacteria and UQ6 is found in yeast (Onur, 2014). The UQ is known as an antioxidant, preventing oxidative stress in aging, and UQ deficiency is associated with mitochondrial disorders such as myopathies, encephalopathy, hypertonia and seizures (Wang & Hekimi, 2013).

Cyt *c*, as the other electron carrier, is a water-soluble hemeprotein generated in the cytosol as an apoprotein, interacting with heme lyase and translocated into IMS by TOM (Nicholson, Hergersberg & Neupert, 1988). In mitochondira, the majority of Cyt *c* are bound to the IMM, while a minimum of 15% mitochodrial Cyt *c aretightly membrane bound* thorugh electrostatic interations (Garrido et al., 2006). Cyt *c* is a single-electron carrier and transfers electrons between complex III and IV in respiratory chain. In cytosol, the release of Cyt *c* from mitochondria is also associated with the apoptosis pathway (Ott, Robertson, Gogvadze, Zhivotovsky & Orrenius, 2002).

1.2.2 Complex I

NADH ubiquinone oxidoreductase (also known as complex I) is one of the electron acceptor of the ETC. Two electrons from NADH are transferred to ubiquinone, generating ubiquinol as a reduced product. Each NADH oxidisation is associated with four protons pumping across the membrane (Jones, Blaza, Varghese & Hirst, 2017). The catalysis reaction is shown below

(Brandt, 2006; Sazanov, 2015). The in-detail function and structure of complex I will be discussed in Chapter 1.3.

$$NADH + H^+ + Q + 4H^+(matrix) \rightarrow NAD^+ + QH_2 + 4H^+ (inter\ membrane\ space)$$

1.2.3 Complex II

Succinate ubiquinone dehydrogenase (also known as complex II) is a complex which does not pump protons in the ETC. Complex II is also involved in the TCA cycle to oxidise succinate to fumarate. During this process, two electrons are introduced into the ETC and two electrons are delivered from succinate to form reduced ubiquinol and sent to complex III. The overall reaction is shown below (Sun, Zhou, Pang, Xu & Rao, 2013).

$$Succinate + Q \rightarrow Fumarate + QH_2$$

Complex II is made of four nuclear-encoded subunits (Fig 1.4). The hydrophilic subunit A and B in the matrix contain the flavin adenine dinucleotide (FAD) cofactor and three iron-sulfur clusters (Hägerhäll, 1997). FAD facilitates the oxidation of succinate to fumarate and two electrons oxidise by FAD and then passed down through the iron-sulfur clusters to reduce one ubiquinone. The membrane region containing two transmembrane subunits with a heme group in the middle forms an integral part of the complex (Sun et al., 2005).

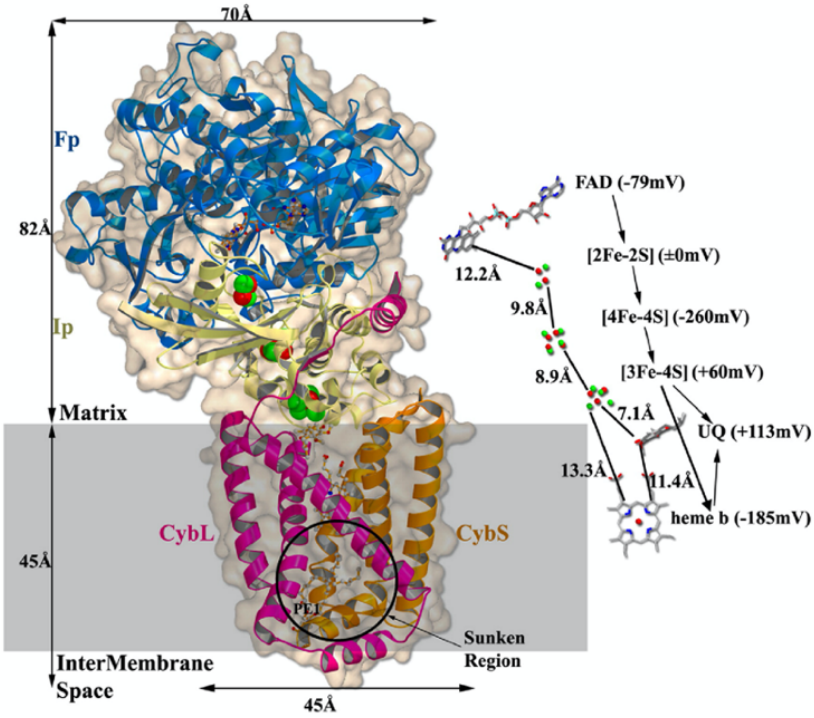

Fig 1.4 Structure of the mitochondrial respiratory Complex II. Hydrophilic subunit A (Fp in blue) contains FAD. Hydrophilic subunit B (Ip in cream) contains iron-sulfur clusters. Both subunit A and B form the hydrophilic domain. The two transmembrane peptides CybL (pink) and CybS (gold) anchored in the IMM. They form the hydrophobic domain of complex II. The image was adapted from Sun et al., 2005.

1.2.4 Complex III

Q-cytochrome *c* oxidoreductase (also known as complex III, cytochrome *c* reductase) in mammalian species is a dimer with 11 protein subunits, within which the cytochrome *b* subunit is encoded by mtDNA. In the bovine complex III, the cytochrome *b* subunit contains two hemes (b_L and b_H), the cytochrome *c* subunit has one heme (c_1) and the Rieske iron-sulfur proteins has a iron-sulfur cluster (2Fe-2S) (Iwata et al., 1998). Complex III transfers electrons from ubiquinol to Cyt *c* coupled with the generation of the proton gradient across the mitochondrial membrane. The reaction catalysed by complex III is given below (Millett, Havens, Rajagukguk & Durham, 2013).

$$QH_2 + 2\text{Cyt } c_{ox} + 2H^+ \text{ (matrix)} \rightarrow Q + 2\text{Cyt } c_{red} + 4H^+ \text{ (inter membrane space)}$$

Complex III pumps protons via a Q-cycle mechanism, which involves two steps of electron transfer by one-electron carriers. As shown in Fig 1.5, ubiquinol is firstly bound at the Q_p site (near the P-side) and oxidised to release two protons into the IMM. During oxidation of

ubiquinol, one electron passes through the Rieske iron-sulfur protein to reduce the cytochrome c_1 subunit; another electron takes the path through the cytochrome *b* hemes (b_L and b_H) to reduce ubiquinone at the Q_N site (on the negative (N) side) to ubisemiquione. The second step begins after the release of first oxidised ubiquinone and binding of a second ubiquinol at the Q_p site. Again, the electrons undergo the same pathway but the ubisemiquinone is reduced to quinol with two protons gained from the matrix (Xia et al., 1997, 2013). Thus, a net transfer of two protons through the membrane into IMS occurs.

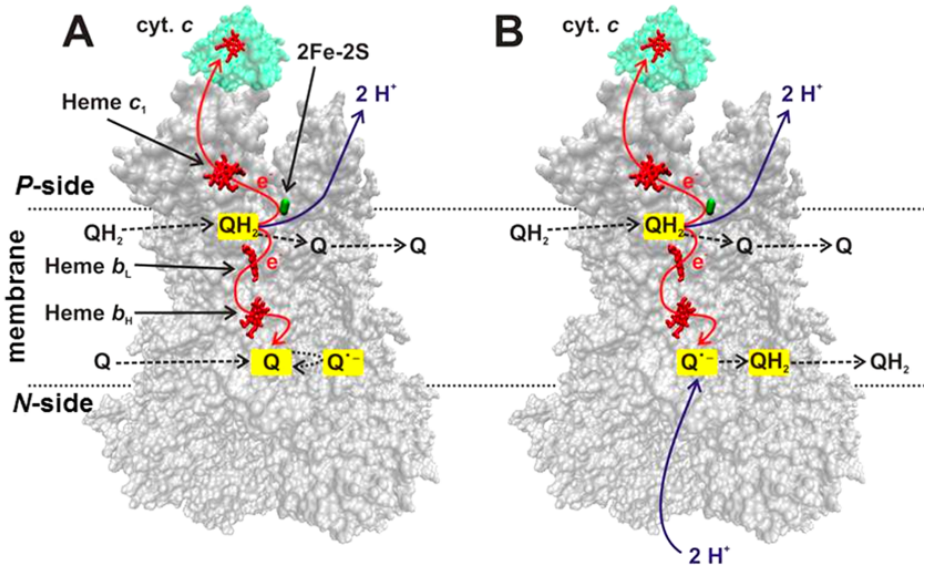

Fig 1.5 Q -cycles mechanism in complex III. The figure shows the Q-cycles in the two steps of electron transfer (A and B). Both start with the oxidation of ubiquinol at the Q_P site (near P-side). Heme b_L is low potential heme b, heme b_H is high potential hemes b. The electron transfer pathways are marked as red arrows, the proton transfer pathways are marked in blue. The image was adapted from Wikström et al., 2015.

1.2.5 Complex IV

Cytochrome c oxidase (also called complex IV), as the final complex in the ETC, pumps protons across the IMM with electrons transferred from O2 to H2O. Complex IV is an integral membrane protein with 13 subunits in mammalian and within which 3 subunits (COX1, COX2 and COX3) are encoded by mtDNA (Kadenbach & Hüttemann, 2015; Zong et al., 2018). The reaction catalysed by complex IV is shown below (Konstantinov, 2012). The reaction requires four Cyt c to be oxidised to donate four electrons to reduce O2.

$$4\text{Cyt } c_{red} + O_2 + 8H^+ \text{(matrix)} \rightarrow 4\text{Cyt } c_{ox} + 2H_2O + 4H^+ \text{(inter membrane space)}$$

The complex, as shown in Fig 1.6, also contains two copper centres (dinuclear CuA centre and heme a3/CuB binuclear centre) and a heme group (heme a). Cyt c in the intermembrane space is oxidised with the donation of one electron moving from dinuclear CuA centre towards heme a3/CuB. Then the oxygen binding at the heme a3/CuB center is reduced: the oxygen atom is first reduced to OH– by the protons transported from the matrix via K- and D-proton conducting channels, then followed with the further reduction of the other oxygen atom to OH–. And then the two OH– are protonated and released as H2O (Yoshikawa, Muramoto & Shinzawa-Itoh, 2011). In this process, four Cyt c are oxidised to reduce one O2 with a total number of eight protons gained from the matrix, and four protons are pumped into IMS (Muramoto et al., 2010).

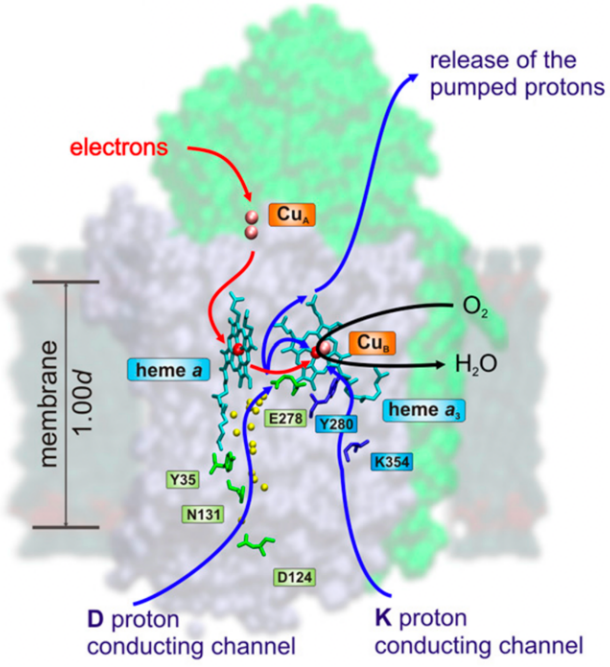

Fig 1.6 Enzyme catalytic scheme of complex IV. The path of electron transfer is in red, the proton transfer pathway is in blue. The image was adapted from Belevich et al., 2010.

1.2.6 Complex V

ATP synthase (complex IV) is a 580 kDa complex with 15 different subunits in humans, within which the subunits a and A6L (also called ATP synthase 6 and ATP synthase 8) are mitochondrial encoded. The ATP synthase forms dimers in cristae and contributes to the membrane curvature (Blum, Hahn, Meier, Davies & Kühlbrandt, 2019; Paumard et al. 2002).

It uses the proton motive force generated by complex I, III, and IV to generate ATP. The reaction is shown below (Igamberdiev & Kleczkowski, 2015).

$$ADP^{3-} + Pi^{2-} + Mg^{2+} + H^{+} \rightarrow MgATP^{2-} + H_2O$$

As shown in Fig 1.7, ATP synthase consists of two functional domains: a hydrophobic F_o domain bound in the IMM and a hydrophilic F_1 domain extending into the matrix. The F_1 domain is composed of five different subunits: three α and β subunits form the binding site for ATP, ADP, and Pi; one γ, δ and ε together build the central stalk. F_o contains a ring of c subunits. In mammalian species, the ring shape structure is made of 8 c subunits (Watt, Montgomery, Runswick, Leslie & Walker, 2010). The peripheral stalk, made of subunits OSCP, b, d, F6 together with subunit a and the supernumerary subunits constitute the enzyme stator connecting F_1 to F_o (Devenish, Prescott, Boyle & Nagley, 2000). The c-ring rotation starts with the protons bound to aspartate/glutamate at the proton entrance channel of each c subunits in IMM. The c-ring rotation drives the movement of subunit γ which introduces the conformation change on subunit β at the catalytic sites. The conformational change in subunit β facilities the release of ATP (Walker, 2013). For each 360° rotation of the c-ring, 3 ATP are produced.

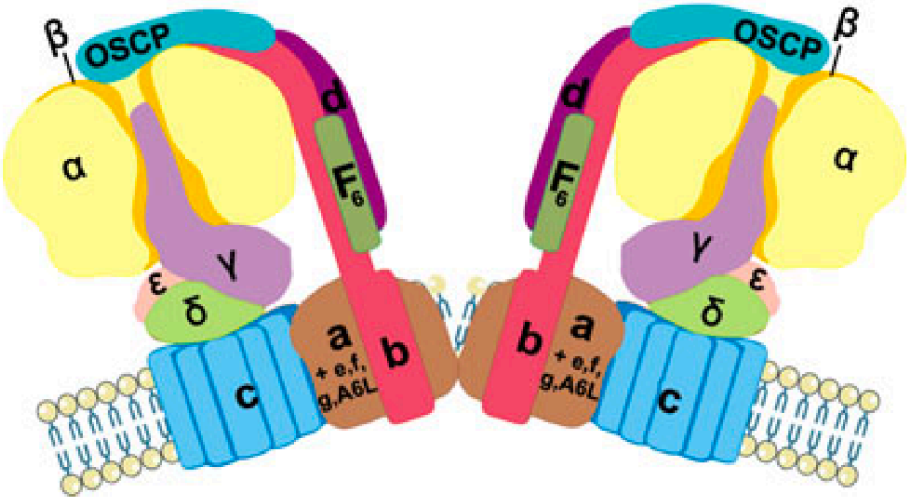

Fig 1.7 Dimerised mammalian complex V. The major subunits are presented in different colours. Image was adapted from Jonckheere, Smeitink, & Rodenburg, 2012.

1.2.7 Supercomplexes

The supercomplexes are a super-assemble of respiratory chain complexes firstly identified from the comigration of the complex I, III, and IV on blue native gel electrophoresis (BN-PAGE) of digitonin-solubilised mitochondrial membrane (Schägger & Pfeiffer, 2000). The later studies of *in situ* arrangement of supercomplex in mammals, yeast, and plants through cryo-electron tomography has validated the supercomplexes are a true phenomenon *in vivo* rather than solublisation artefacts (Davies, Blum & Kühlbrandt, 2018). In the mammalian tissues, the supercomplexes have various combinations and stoichiometry including CI-$CIII_2$-CIV_{1-4}, CI-$CIII_2$, and $CIII_2$-CIV_{1-2} (Enríquez, 2016; Greggio et al., 2017). In specific, the supercomplex containing CI, CIII, and CIV which can perform NADH:O_2 oxidoreduction are named respirasomes (Gu et al., 2016; Milenkovic, Blaza, Larsson & Hirst, 2017).

Although the phenomenon of supercomplexes was observed, the function of these large membrane protein complexes remains debatable. The proposed major roles for supercomplexes include stablising of individual complexes (Hirst, 2018) and channeling of substrates (Wheeldon et al., 2016). The study of supercomplex assembly by knocking out the genes relevant to the complexes component has shown that the supercomplex provides the scaffold for complex I assembly (Calvaruso et al., 2012). Recent biochemical studies have shown that the supercomplex cannot enhance catalysis by quinone channeling (Fedor & Hirst, 2018). The alternative possibilities of the function of supercomplex include decreasing ROS production (Murphy, 2009), preventing protein aggregation in the protein-rich IMM (Greggio et al., 2017; Blaza, Serreli, Jones, Mohammed & Hirst, 2014), and regulating respiratory chain activity (Guerrero-Castillo et al., 2017).

1.3 The structure of complex I

1.3.1 The development of the complex I structure study

NADH:ubiquinone oxidoreductase (complex I) is one of the largest membrane protein complexes (about 1MDa in eukaryotes, 550 kDa in prokaryotes) and one of the entry points for electrons into the respiratory chain in mitochondria (Berg, Tymoczko & Stryer, 2002). The structure of complex I is crucial for understanding the enzyme function and mechanism and has been progressively determined through various species (Baradaran, Berrisford, Minhas & Sazanov, 2013; Zickermann et al., 2015; Zhu et al., 2016). The first complex I structure information was determined in *Neurospora crassa* by electron microscopy in 1991 (Hofhaus et al., 1991). For the very first time, the complex I was characterised as an L-shape with two arms: one hydrophilic arm and one hydrophobic arm (Hofhaus et al., 1991).

The first high resolution complex I structure was acquired by crystallography of the *Thermus thermophilus* (*T. thermophilus*) hydrophilic arm solved in two different resolutions (4.0 and 3.3 Å) (Hinchliffe and Sazanov, 2005; Sazanov and Hinchliffe, 2006). The hydrophilic arm structures from *T. thermophilus* complex I illustrated the arrangements of multiple iron-sulfur clusters in redox centers which showed evidence that electron transfer and proton translocation occur in separate compartments of complex I. A membrane domain structure from *Escherichia coli* (*E.coli*) was resolved at 3.0 Å which contained six transmembrane subunits with an antiporter-like arrangement (Efremov & Sazanov, 2011). After which, a complete complex I structure from *T. thermophilus* was observed at 3.3 Å with crystallography, in which 7 subunits in the hydrophilic domain and 7 subunits in the hydrophilic domain were observed (Baradaran et al., 2013). The x-ray structures of mitochondrial complex I from *Yarrowia lipolytica* (*Y. lipolytica*) with the resolution of 3.6 to 3.9 Å suggested an active-deactive transition in the structure during catalysis in eukaryotes (Zickermann et al., 2015). With the development of cryo-electron microscopy (cryo-EM), the mammalian complex I was determined from bovine (4.2 Å) and ovine (3.9 Å) heart mitochondria (Zhu et al., 2016; Fiedorczuk et al., 2016). As well as the 14 core domains which are conserved in bacterial complex I, 31 accessory subunits

were also identified (Vinothkumar, Zhu & Hirst, 2014; Zhu, Vinothkumar & Hirst, 2016). The supercomplex I_1III_2 structures from ovine heart mitochondria and megacomplex $I_1III_2IV_1$ from the porcine-heart mitochondria and human cell culture have also been resolved by cryo-EM (Wu, Gu, Guo, Huang & Yang, 2016, Guo, Zong, Wu, Gu & Yang, 2017; Letts, Fiedorczuk, Degliesposti, Skehel & Sazanov, 2019). Then, a high-resolution cryo-EM complex I structure from mouse heart mitochondria showed two biochemically defined states: active (3.3 Å) and de-active states (3.9 Å) (Agip et al., 2018). Recently, the complex I structure with an atomic resolution (2.7 Å) from *Y. lipolytica* has shown much more details of the residues and the ordered arrangement of water molecules around proposed proton-pumping subunits (Grba & Hirst, 2020). The latest complex I structure from ovine (2.6Å) and inhibitor-bound structure from mouse (3.0 Å) have also provided the rationale to implicate the quinone-binding site and possible proton-pumping mechanisms (Bridges et al., 2020; Kampjut, & Sazanov, 2020). As the subunits of complex I were identified in different species, there is no standard nomenclature for complex I subunits (as shown in Table 1.1 below for reference).

Table 1.1 Nomenclature of Complex I subunits across different species. *

	Eukaryote			*Prokaryote*			
Domain	***Bos tarus***	***Homo sapiens/Mus musculus***	***Yarrowia lipolytica***	***Thermus thermophilus***	***Paracoccus denitirifican***	***Escherichia coli***	**Module**
Hydrophobic arm	ND1	ND1	NU1M	Nqo8	Nqo8	NuoH	PP
	ND2	ND2	NU2M	Nqo14	Nqo14	NuoN	PP
	ND3	ND3	NU3M	Nqo7	Nqo7	NuoA	PP
	ND4	ND4	NU4M	Nqo13	Nqo13	NuoM	PD
	ND4L	ND4L	NULM	Nqo11	Nqo11	NuoK	PP
	ND5	ND5	NU5M	Nqo12	Nqo12	NuoL	PD
	ND6	ND6	NU6M	Nqo10	Nqo10	NuoJ	PP
Hydrophilic arm	24 kDa	NDUFV2	NUHM	Nqo2	Nqo2	NuoE	N
	49 kDa	NDUFS2	NUCM	Nqo4	Nqo4	NuoD	Q
	30 kDa	NDUFS3	NUGM	Nqo5	Nqo5	NuoC	Q
	51 kDa	NDUFV1	NUBM	Nqo1	Nqo1	NuoF	N
	75 kDa	NDUFS1	NUAM	Nqo3	Nqo3	NuoG	N
	PSST	NDUFS7	NUKM	Nqo9	Nqo9	NuoB	Q
	TYKY	NDUFS8	NUIM	Nqo6	Nqo6	NuoI	Q
Supernumerary subunits	10 kDa	NDUFV3					N
	13 kDa	NDUFS6	NUMM		pdNUMM		N/Q
	15 kDa	NDUFS5	NIPM				PP
	18 kDa	NDUFS4	NUYM		pdNUYM		N
	39 kDa	NDUFA9	NUEM				Q
	42 kDa	NDUFA10					PP
	SDAPα	NDUFAB1α	ACPM				Q
	SDAPβ	NDUFAB1β					PD
	AGGG	NDUFB2					PD
	ASHI	NDUFB8	NIAM				PD
	B8	NDUFA2	NI8M				N
	B9	NDUFA3	NI9M				PP
	B12	NDUFB3	NB2M				PD
	B13	NDUFA5	NUFM				Q
	B14	NDUFA6	NB4M				Q
	B14.5a	NDUFA7	NUZM				Q
	B14.5b	NDUFC2	NEBM				PP
	B14.7	NDUFA11	NUJM				PP
	B15	NDUFB4	NB5M				PD
	B16.6	NDUFA13	NB6M				PP
	B17	NDUFB6					PD
	B17.2	NDUFA12	N7BM		pdN7BM		N/Q
	B18	NDUFB7	NB8M				PD
	B22	NDUFB9	NI2M				PD
	ESSS	NDUFB11	NESM				PD
	KFYI	NDUFC1					PP
	MNLL	NDUFB1					PD
	MWFE	NDUFA1	NIMM				PP
	PGIV	NDUFA8	NUPM				PP
	PDSW	NDUFB10	NIDM				PD
	SGDH	NDUFB5	NUNM				PD
Species specific subunits			ST1				Q
			NUXM				PP
			NUUM	nqo15			N
				nqo16			Q

*The last column on the right shows the subunits in function modules: N-module (NADH oxidation module); Q-module (ubiquinone reduction module), P-module (proton pump module, PP-proximal, PD-distal). The table was adapted from Marino (2019) and Wirth, Brandt, Hunte & Zickermann (2016).

1.3.2 Core subunits

Complex I is made of 14 core subunits that are conserved from bacterial to eukaryotic species. From the genetic and structural prospects, the core subunits of complex I can be divided into a hydrophilic domain/arm and a hydrophobic domain/arm. The hydrophilic domain contains subunits 75 kDa, 51 kDa, 49 kDa, 30 kDa, 24 kDa, PSST and TYKY (also called NDUFS1, NDUFV1, NDUFS2, NDUFS3, NDUFV2, NDUFS7 and NDUFS8 in mouse), which are all encoded by nDNA; the hydrophobic domain contains ND1, ND2, ND3, ND4, ND4L, ND5 and ND6, which are all encoded by mtDNA. From the functional point of view, the complex I can be separated into three sections: N-, P-, and Q-modules (Fig 1.8A). The N-module is made of three subunits: 75 kDa, 51 kDa, and 24 kDa (also called NDUFS1, NDUFV1, and NDUFV2 in mouse) in the head part of the hydrophilic domain containing the flavin mononucleotide (FMN). The Q-module, followed the N-module on the peripheral domain, is made of 4 subunits 49 kDa, 30 kDa, PSST and TYKY (NDUFS2, NDUFS3, NDUFS7, and NDUFS8 in mouse). The N-module together with the Q-module contain 8 iron-sulfur clusters which transfer the electrons from NADH towards the ubiquinone. The P-module, same as the hydrophobic arm, is considered as the proton-pumping module on the IMM. The P-module can be further divided into a proximal (PP) module containing ND1, ND2, ND3, ND4L, and ND6 and a distal (PD) module containing subunits ND4 and ND5 (Wirth et al., 2016). As well as the core subunits, mammalian complex I has extra supernumerary subunits wrapping around the core subunits (Fig 1.8B).

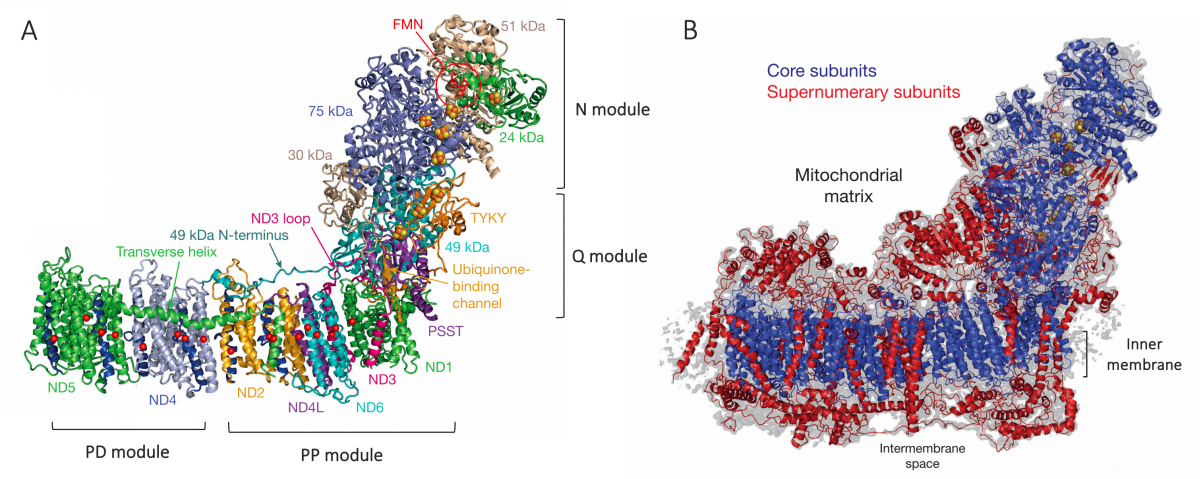

Fig 1.8 Structure of complex I from bovine. (A) Core subunits of complex I from mouse heart mitochondria. (B) Complex I structure of core and supernumerary subunits from bovine heart mitochondria. Subunits coloured in blue represent the homologous (core) subunits. The supernumerary subunits are highlighted in red. The image was adapted from Zhu et al. (2016) with modifications.

1.3.3 Supernumerary subunits

Eukaryotic complex I contains extra accessory (supernumerary) subunits. Different species may have a different number of accessory subunits and some are species-specific (Wirth et al., 2016). For example, *Y. lipolytica* contains 28 supernumerary subunits with three fungi-specific accessory subunits (Parey et al., 2018). Bovine and mouse have 31 supernumerary subunits in which 8 are mammalian specific (Zhu et al., 2016; Agip et al., 2018). From the perspective of evolution, the recruitment of supernumerary subunits likely followed an opportunistic pathway of evolution that could have started even before the original endosymbiotic event (Yip, Harbour, Jayawardena, Fearnley & Sazanov, 2011).

Considering the overall structure of supernumerary subunits, the proposed overall functions of facilitating assembly and maintaining the stability of the complex are widely recognised (Stroud et al., 2016; Hirst, 2011; Angerer et al., 2011). The absence of NDUFS4 (18 kDa in bovine) or NDUFS6 (13 kDa in bovine) in patient cells has been reported with the formation of an immature 830-kDa subcomplex (Scacco et al., 2003; Kirby et al., 2004). The NDUFA9 (39 kDa in bovine) subunit has also been suggested to help the attachment of the peripheral domain (Stroud, Formosa, Wijeyeratne, Nguyen & Ryan, 2013). Interestingly, the homologous protein

to the 39 kDa is associated with dehydrogenase reductases, but no remaining enzymatic activity of this subunit is reported in complex I (Elurbe & Huynen, 2016); the NDUFS6 subunit harbors a Zn-binding site, it is reported to facilitate the complex I assembly, but the original function is still unknown (Kmita et al., 2015). A recent summary report of mutations in 20 of the supernumerary subunits has shown that the assembly of complex I is interrupted due to the mutation-caused weak binding with other subunits or the absence of the mutated supernumerary subunits (Dang et al., 2020).

Apart from helping the assembly and maintaining the stability of complex I, there are also other proposed functions of several specific supernumerary subunits (Kmita & Zickermann, 2013). For example, the phosphorylation of NDUFB11 (ESSS) and NDUFA1 (MWFE) were identified to be cAMP/PKA-dependent (Palmisano, Sardanelli, Signorile, Papa & Larsen, 2007), and NDUFB10 (PDSW) was phosphorylated by Src kinase in cancer cells (Hebert-Chatelain et al., 2012). These experiments all suggest the possible regulation role of complex I by supernumerary-subunits phosphorylation. Besides, there are also supernumerary subunits maintaining their function while being recruited to form complex I, such as the mitochondrial acyl carrier proteins SDAP (NDUFAB1 in human), which can synthesis fatty acids (Runswick, Fearnley, Skehel& Walker, 1991; Cronan, Fearnley & Walker, 2005).

1.3.4 Assembly of complex I

Mammalian complex I contains 44 different subunits of which 37 are nDNA encoded and 7 are mtDNA encoded. The assembly of the enzyme requires at least 13 assembly factors, encoded by the nucleus, which play a role in the assembly subunits or associated with the biogenesis of cofactors (Sánchez-Caballero, Guerrero-Castillo & Nijtmans, 2016). The assembly of complex I invovles in multiple mitochondrial pathways. The complex I proteins encoded by nDNA are synthesized in the cytosol and transported onto the IMM by TOM complex and TIM23 (Glick, Beasley & Schatz, 1992). The seven mtDNA encoded hydrophobic subunits are generated by mitochondrial ribosomes in the matrix and inserted into IMM by the cytochrome oxidase assembly (OXA1) translocase (Pfeffer, Woellhaf, Herrmann & Förster, 2015; Hell, Neupert & Stuart 2001; Stiller et al., 2016). The study of complex I assembly by using TALEN and

CRISPR/Cas9 gene-editing tools to edit genes in HEK293T cells has shown that some assembly factors are strictly required for building up a functional complex I (Stroud et al., 2016). Together with the study of patients with complex I mutations and complexome profiling, an assembly pathway has been proposed as shown in Fig 1.9. In brief, the assembly starts with the early building blocks on Q-, N- and PD-module. Then the central modules including P- and Q-modules are associated together, becoming intermediate subassemblies. The final stage includes the attachment of intermediate with N- and Q-module and the formation of supercomplex (Guerrero-Castillo et al., 2017).

In the early stage of the assembly pathway, five subassemblies are formed discretely. The NDUFV1, NDUFV2, NDUFS1 and NDUFA2 assembled into an early stage N-module with the association of assembly factor NUBPL which is proposed to incorporate iron-sulfur clusters of complex I (Sheftel et ali., 2009). The remaining subunits located between N- and Q- modules (NDUFV3, NDUFS4) are loaded in the late stage of the pathway (Kmita et al., 2015). The Q-module is assembled with nine subunits in which NDUFS2, NDUFS3, NDUFS7 and NDUFS8 are core subunits, NDUFA5, NDUFA6, NDUFA7, NDUFA9 and NDUFAB1 are accessory subunits. Two assembly factors, NDUFAF3 and NDUFAF4, are associated to stabilise the PP-module attachment in the next step. As NDUFS7 and NFUFS8 contain iron-sulfur clusters, the assembly factor NUBPL is also involved in this process (Sánchez-Caballero et al., 2016). The PP-module assembly is separated into PP-a and PP-b. The PP-a consists of ND1, NDUFA1, NDUFA3, NDUFA8 and NDUFA13. The NDUFAF3 and NDUFAF4- bound Q-module is then docked onto the PP-a aided by binding of TIMMDC1 (Andrews et al., 2013, Guarani et al., 2014). The PP-b module is assembled independent from the PP-a module and consisting of four core subunits (ND2, ND3, ND4L and ND6) and two accessory subunits (NDUFC1 and NDUFC2). The assembly pathway of PP-b required mitochondrial complex I assembly complex which is made of four assembly factors: ECSIT, NDUFAF1, ACAD9 and TMEM126B (Heide et al., 2012). The PD-module is generated as PD-a and PD-B in the early stage of assembly. PD-a module contains one core subunit (ND4) with 5 accessory subunits (NDUFB5, NDUFB6, NDUFB10 and NDUFB11) (Guarani et al., 2014). The PP-b module also

contains one core subunit (ND5) with 5 accessory subunits (NDUFB3, NDUFB7, NDUFB8, NDUFB9 and NDUFAB1) (Angerer, 2015).

The next step of the assembly pathway is to join the discrete modules. Specifically, the PP-b firstly interacts with PD-a to form PP-b/PD-a subassembly at a mass of ~680 kDa (Heide et al., 2012). Then accessory subunits NDUFS5, NDUFB10 is associated with the subassembly with the help of FOXRED1 (Formosa et al., 2015). The Q/PP-a module and PD-modules are docked on to form an 830 kDa intermediate (Vogel et al., 2007). The final stage is the attachment of N-module at the peripheral arm. The assembly factor NDUFAF2 was proposed to be important but not essential for the N-module loading process (Kmita et al., 2015).

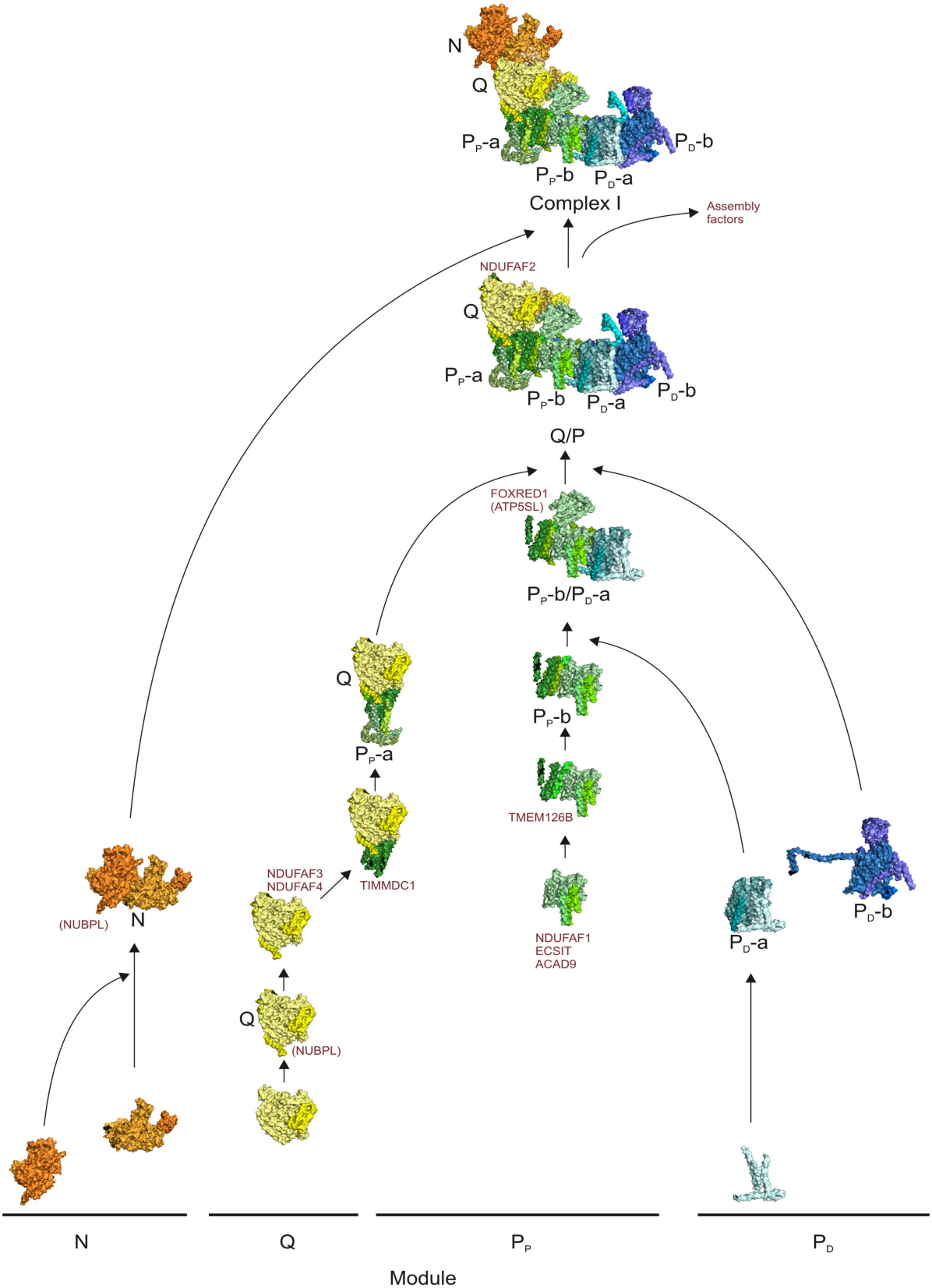

Fig 1.9 The mammalian complex I assembly pathway. The cartoon representation is based on the bovine heart cryo-EM structure (PDB: 4UQ8). Subunits from different domains are coloured differently. The names of the assembly factors are in red. The names of the subassemblies are marked in black. The figure was adapted from Sánchez-Caballero et al. (2016) with modifications.

1.4 general mechanism of complex I

1.4.1 NADH oxidation and FMN reduction

Electrons entering the respiratory chain start with the NADH binding with its nicotinamide ring over the isoalloxazine moiety of FMN in the NDUFV1 subunit, from which hydride is transferred to FMN and NAD^+ is released from the flavin site (Berrisford & Sazanov, 2009; Birrell, Yakovlev & Hirst, 2009). The NADH oxidation reaction at the flavin site is known to be reversible as the NAD^+ has slightly higher than redox potential than the flavin. *In vitro*, flavin oxidation can occur with hydrophilic electron acceptors such as 3-acetylpyridine-adenine dinucleotide ($APAD^+$) and potassium hexacyanoferrate (III) (ferricyanide or FeCN) in a "ping-pong" mechanism which means that the reaction can be inhibited by high NADH concentrations (Yakovlev & Hirst, 2017). The NADH:$APAD^+$ reaction is also used to quantify the relative content of functional complex I (Pryde & Hirst, 2011; Fedor, Jones, Di Luca, Kaila & Hirst, 2017).

1.4.2 Electron transfer and ubiquinone reduction

The electrons from the reduced FMN have to pass down seven iron-sulphur clusters (Fig 1.10A). The clusters chain is formed of [2Fe–2S] (N1b) and [4Fe–4S] (the other six clusters) in complex I. The electrons are transferred following the reduction potential stepping-stones in the sequence from N3 to N2 (Fig 1.10B) until they reach the quinone binding site. In studies carried out by electron paramagnetic resonance (EPR) on bovine complex I, the electron transfer between active sites appears to be an alternating potential energy profile and this was defined as supporting efficient energy transfer (Roessler et al., 2010; Bridges, Bill & Hirst, 2012).

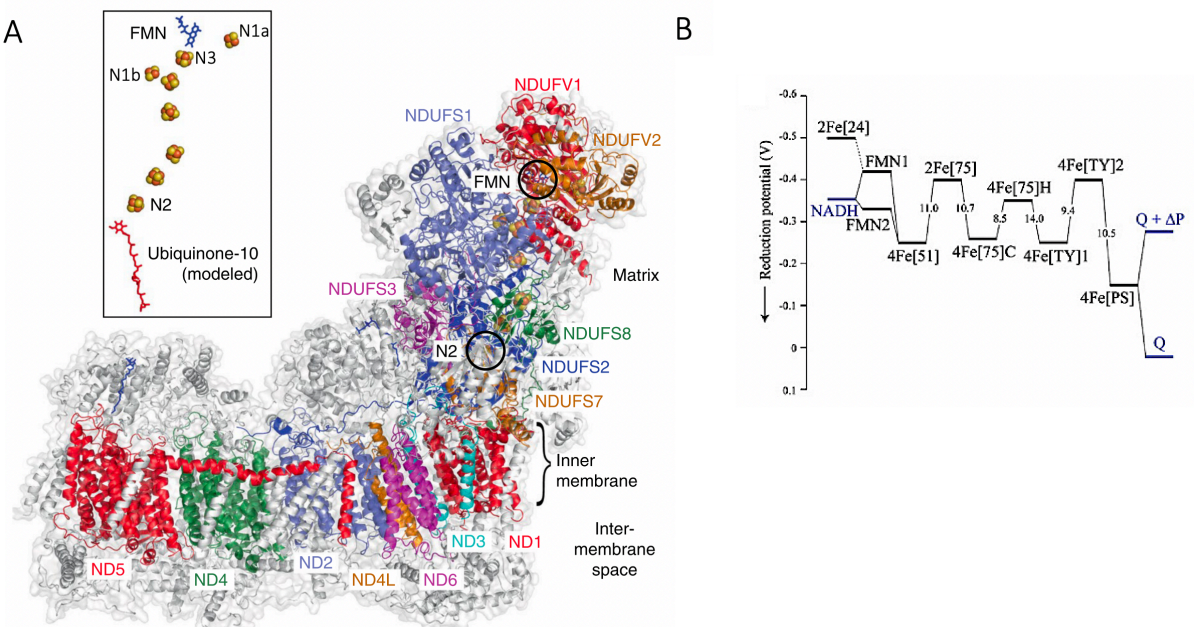

Fig 1.10 Illustrations of iron-sulfur clusters in complex I (A) Arrangement of iron-sulphur clusters in complex I from the mouse. Image adapted from Agip et al. (2018). (B) Energy potential profile of cofactors in complex I. Figure adapted from Hirst (2010).

An isolated binuclear cluster N1a is not involved in this process in mammals, but it is might play a role in oxidative damage prevention (Hinchliffe et al., 2005). It has also shown that the reduction of N1a in *E.coli* could alter the local structure to stabilise the binding of NAD^+ (Gnandt, Schimpf, Harter, Hoeser & Friedrich, 2017).

The electrons passing down the iron-sulfur clusters are taken by ubiquinone at the ubiquinone binding site (also known as Q-site). The Q-site was identified in structural studies as a narrow tunnel starting near the N2 cluster and with a length of about 20 Å, extending towards the exit/entrance in the inner mitochondrial membrane (Baradaran et al. 2013). However, how exactly quinone binding and disassociation from its binding position, especially the changes of head group location inside the Q-tunnel, are still controversial. It was also proposed that there are two alternating ubiquinone-binding positions which have the role of ubiquinone reduction and protonation separately (Zickermann et al., 2015, Parey et al., 2018). The recent high-resolution cryo-EM structure of complex I with quinone-like inhibitor-bound has shown the inhibitor headgroup located adjacent to NDUFS2 His59 and Tyr108, indicating the likely binding position of the quinone head group (Bridges et al., 2020).

1.4.3 Proton pumping

The process of complex I oxidoreduction not only includes electron transfer and ubiquinone reduction, but it is also coupled with proton translocation possibly powered by long-range conformational changes in membrane domain (Ohnishi and Salerno, 2005; Efremov, Baradaran & Sazanov, 2010; Hunte, Zickermann & Brandt, 2010). Proton channels in the P-module were proposed to facilitate proton translocation across the IMM (Wikström, 1984; Galkin, Dröse & Brandt, 2006). Three channels in the antiporter-like subunits ND2, ND4, and ND5 are considered to be the proton pumping channels (Efremov & Sazanov, 2011). These channels share a similar overall folding pattern and they all contain highly conserved charged residues, which could contribute to the formation of proton channels (Efremov & Sazanov, 2011). The recent structure study from yeast complex I has shown a series of ordered water molecules associated with the charged residues and indicating potential water influx points in ND2, ND4 and ND5 for protonation (Grba & Hirst, 2020). A fourth proton translocation channel, the E-channel, located at the interface of ND1, ND4L, and ND6 and shown to have conserved residues and a high abundance of glutamates was also proposed as a potential proton pumping channel (Baradaran et al., 2013). Apart from the structural studies, it was biochemically reported that complex I pumps four protons stoichiometrically during proton translocation (Jones et al., 2017), which also supports the four-channel mechanism.

1.4.4 ROS production and reverse electron transfer in complex I

Reactive oxygen species (ROS) are aerobic metabolism byproducts that are formed in different organelles within the cell. There are two major types of ROS: radicals like superoxide ion ($O_2^{\bullet-}$) and hydroxyl radical ($OH^{\cdot}$); and the non-radicals such as H_2O_2 (Bachi, Dalle-Donne & Scaloni, 2013). Superoxide within mitochondria can be rapidly converted to H_2O_2 by manganese superoxide dismutase (MnSOD) (Murphy, 2009; Wong, Dighe, Mezera, Monternier & Brand, 2017). Mitochondria are considered as an important resource and sink of cellular ROS (Starkov, 2008). Complex I, complex II and complex III are all reported as the possible sites of ROS production (Zorov, Juhaszova, & Sollott, 2014), and $O_2^{\bullet-}$ production is predominantly from complex I (Murphy, 2009). Complex I generates ROS mainly in two ways. Firstly, the complex

I can produce superoxide ion in forward electron transfer (FET) with NADH present. It reacts with O_2 at the reduced FMN site to generate $O_2^{\bullet-}$ (Kussmaul & Hirst, 2006). The other mechanism which can also generate $O_2^{\bullet-}$ through the reduced FMN is called reverse electron transport (RET) (Adam-Vizi & Chinopoulos, 2006). It was found that for complex I in the presence of a reduced of CoQ pool and increased proton-motive force, this can trigger the reduction of NAD^+ to NADH at the FMN site (Hinkle, Butow, Racker & Chance, 1967). During the process, the electron leakage through FMN can occur to produce superoxide (Hirst, King & Pryde, 2008). Another hypothesis of an alternative site of ROS production at the quinone-binding site was also proposed (Brand et al., 2013; Hu et al., 2017).

Mitochondrial ROS (mtROS) play an important role in many physiological events including cell proliferation, hypoxia adaptation, and cell fate determination (Sies & Jones, 2020), but excessive ROS can cause irreversible cell damage leading to the occurrence of numerous diseases including Parkinson's disease, cancer, diabetes and cardiomyopathy (Morais et al., 2014; Idelchik, Begley, Begley & Melendez, 2017; Sabharwal and Schumacker, 2014; Peoples, Saraf, Ghazal, Pham & Kwong, 2019). It is known that complex I can cause a burst of ROS during the ischemia-reperfusion process, which is a phenomenon when the blood supply is blocked (ischemia) and then restored (reperfusion) (Eltzschig and Eckle, 2011; Hausenloy & Yellon, 2013). During such a process, the complex I generated ROS could cause serious damage to the tissue (Chouchani et al., 2016).

1.4.5 Active/deactive transition of mammalian complex I

Mammalian complex I is known to have two discrete states, which are the active (A-form) and deactive status (D-form). The A-form enzyme can undergo deactivation with depleted oxygen, and the reactivation of deactivated complex I can be achieved by adding a small amount of NADH aerobically (Babot et al., 2014). The A/D transition is first reported from horse heart complex I. It was found that the complex I exhibited a distinct lag phase in NADH oxidation rate, suggesting a possible "inactive complex" (Minakami et al., 1964). In vitro experiments showed that the active to deactive (A/D) transition can be achieved by removal of substrate, changing of pH, and physiological temperatures (incubation at 30°C) (Kotlyar and Vinogradov,

1990). The latter studies also showed that the lag phase in deactivated complex I can be prolonged by increasing pH and introducing divalent cations or fatty acids (Kotlyar et al., 1992; Loskovich et al., 2005; Babot et al., 2014).

Interestingly, the A/D transition in complex I varies between organisms. There was no A/D transition phenomenon identified in P. denitrificans or T. thermophilus (Maklashina et al., 2003; Kotlyar, Albracht & Spanning, 1998), but a resting/active (R/A) transition has been reported in E.coli (Belevich et al., 2017). However, the A/D transition was identified in vertebrates such as frog, rat, chicken and cow and also in fungi such as *Y. lipolytica* (Maklashina et al., 2003).

The A- and D-form complex I were reported to have different sensitivity to rotenone, which indicated a possible conformation change around the ubiquinone-iron-sulfur cluster N2 junction region, perturbating the binding of the inhibitor (Grivennikova, Maklashina, Gavrikova, Vinogradov, 1997). It was also found that the D-form complex I can be blocked from NADH:ubiquinone oxidoreduction irreversibly by treating with a sulfhydryl reagent such as N-ethylmaleimide (NEM) (Fig 1.11A), while the A-form complex I is completely insensitive to sulfhydryl reagents (Kotlyar, et al.,1992; Blaza, Vinothkumar & Hirst, 2018). The NEM was able to bind the critical cysteine residue Cys39 in ND3 subunit during deactive state as it was non-accessible in A-form (Galkin & Moncada, 2008; Chouchani et al., 2014). The structure study of D-form bovine complex I has shown that several loops in ND1 and 39 KDa subunits around ubiquinone-binding site is disordered to prevent ubiquinone binding (Fig 1.11B), indicating a unique characteristic of the D-form complex I (Blaza, Vinothkumar & Hirst, 2018). Specifically, the TMHs 1 and 2, containing Cys39, were not observed in the structure in the ND3, which shows that the Cys39 in the ND3 subunit can be solvent accessible to bind NEM in the D-form (Blaza, Vinothkumar & Hirst, 2018).

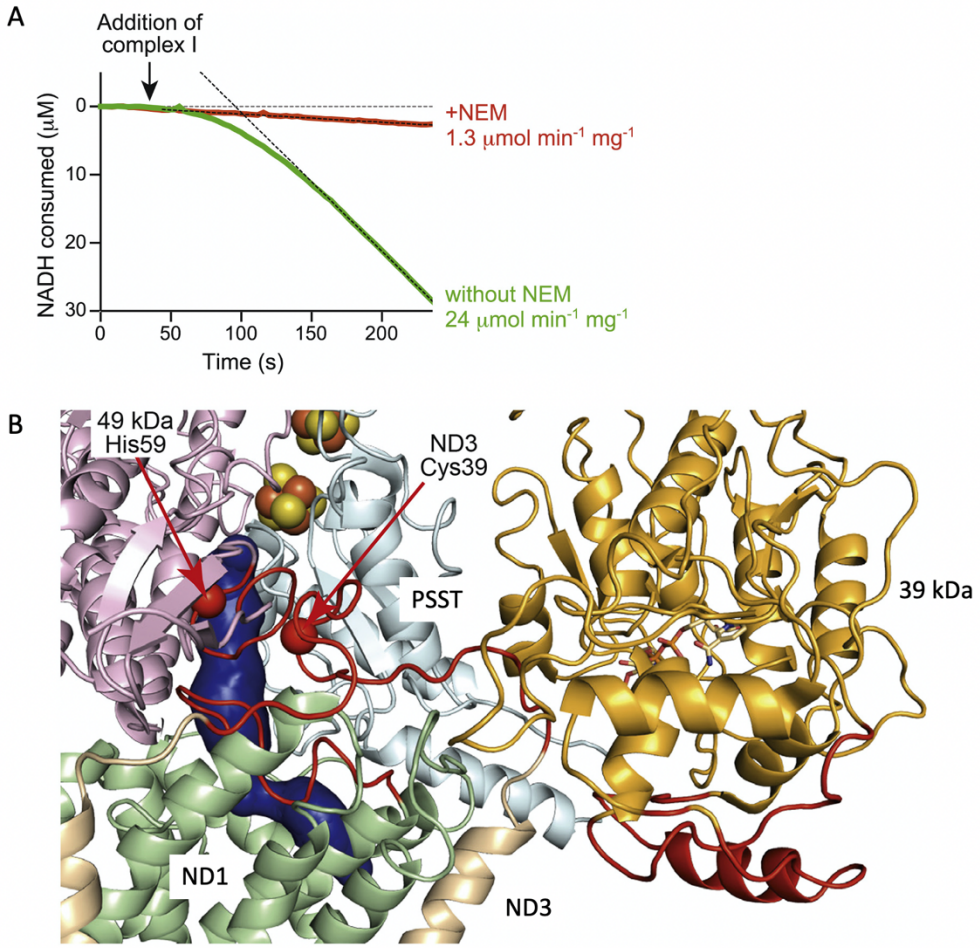

Fig 1.11 Characteristics of the D-form complex I. The images were adapted from Blaza et al., 2018. (A) NADH:decylubiquinone oxidoreduction assays on the deactivated complex I with/without NEM treatment. NEM prevents the reactivation of deactivated protein. (B) The figure was created by combining the structure of the A-form (PDB: 5LC5) with information about the D-form. The coloured structures are the disordered subunits in the D-form. The proposed ubiquinone-binding site is marked in blue.

A later cryo-EM structure study of mouse complex I characterised the differences of the structures from the two biochemical states (Agip et al., 2018): (1) The angle between the peripheral arm and membrane domain is different, the D-form has a larger angle than the active state. This is illustrated by the relative movement and interaction change between two subunits, NDUFA5 and NDUFA10. (2) In the D-form, the disordered ND3 loops show poor density indicating a disordered structure, while in A-form the ND3 loop presents a clear order with cys39 in the non-solvent accessible position. (3) Other differences include the presence of a π-bulge in TMH3 of the ND6 subunit, as identified in the mouse complex I deactivate state.

1.5 Mitochondrial diseases and complex I deficiencies

1.5.1 Mitochondrial disease associated with OXPHOS deficiencies

A deficiency in the OXPHOS system is commonly known as the "mitochondrial disease" (Gorman et al., 2016). It is known that the OXPHOS system is composed of five membrane-embedded enzymes (complex I-V) and two electron carriers (ubiquinone and cytochrome *c*). All of the five protein complexes except complex II, have subunits that are encoded by both nDNA and mtDNA. Biosynthesis of the enzymes in the OXPHOS system requires assembly factors, and damage to the protein complex or the disruption of protein assembly can result in the dysfunction of the enzyme which leads to a group of metabolic syndromes (Gorman et al., 2016). The damage to the complex is usually from chronic oxidative stress (Guo, Sun, Chen & Zhang, 2013). The disruption of the assembly process could be due to the mutations on nDNA and mtDNA (Gorman et al., 2015; Taylor & Turnbull, 2005).

The phenotypes of mitochondrial disease show high heterogeneity. Genetic mutations may have different clinical symptoms in patients (Tucker, Compton, Calvo & Thorburn, 2011; Ghiselli & Milani, 2019). The most affected organs include heart, muscle, and brain with high energy demands. Besides, the severeness and onset time of the disease are different. For example, Leigh syndrome (LS) has a very early clinical onset in children with a severe encephalopathy (Darin, Oldfors, Moslemi, Holme & Tulinius, 2001), while Leber hereditary optic neuropathy (also known as LHON syndrome) is an acute vision loss mainly occurring in young male adult (Kirches, 2011). To date, hundreds of mutations found in mtDNA and more than one thousand mutations found in nDNA have been associated with mitochondria diseases (Torraco, Peralta, Iommarini & Diaz, 2015). To understand the pathogenesis, 125 identified disease-causing point mutations on both nDNA and mtDNA of complex I were analysed on the complex I cryo-EM structure (Fiedorczuk & Sazanov, 2018). However, the low genotype-phenotype correlation, the dual genetic control, and variable clinical onset make the diagnose and prevention of mitochondrial disease challenging.

1.5.2 Complex I related diseases: Leigh syndrome, Leber's hereditary optic neuropathy

Complex I deficiency occupies about 30% of the cause of mitochondrial defects in paediatric patients (Skladal, Halliday & Thorburn, 2003; Alston, Rocha, Lax, Turnbull & Taylor, 2017). And more than 50% of patients with complex I deficiency died by the age of two (Koene et al., 2012). Genetically, the diseases caused by complex I deficiency usually are caused by mutations of structural subunits or assembly factors of the enzyme. Complex I deficiency is known to be associated with a wide variety of clinical presentations, the most common phenotypes include LS, LHON, fatal infantile lactic acidosis and encephalomyopathy lactic acidosis and stroke-like episodes (MELAS) (Fassone & Rahman, 2012; Rodenburg, 2016).

LHON was first reported with a characteristic pattern of visual loss in 1871 by Theodore Leber (Leber, 1871), and the non-Mendelian inheritance of the disease was explained in 1988 as the first human disease caused by mitochondrial DNA point mutation (*m.11778G>A MT-ND4*) (Wallace et al., 1988). The hallmark of the disease is the inherited vision loss in one eye, followed by a similar loss in the second eye within weeks. It begins in a person's adolescence with a strong gender bias of onset on male vs female (Poincenot, Pearson & Karanjia, 2019). To date, three primary mutations (*m.11778G>A MT-ND4, m.3460G>A MT-ND1, m.14484T>C MT-ND6*) as well as more than 18 rare mutations were reportedly associated with LHON. It was believed that, apart from the primary mtDNA mutation, there are secondary factors that cause the vision loss, such as environmental factors, heteroplasmy of mtDNA, and the nDNA background (Yu-Wai-Man, Griffiths, Hudson & Chinnery, 2009). The only approved drug for LHON is idebenone working as an analog of ubiquinone (Klopstock et al., 2013; Shemesh, Sood & Margolin, 2020).

Leigh syndrome (LS), a life-threatening neurodegenerative disease, was firstly described by Denis Archibald Leigh in 1951 (Leigh, 1951). The LS has a wide spectrum of presentations include hypotonia, epilepsy, respiratory stress, neurodevelopmental delay, ataxia, and lactic acidosis (Fassone & Rahman, 2012). The diagnostic hallmarks include symmetrical lesions in the basal ganglia or brain stem on MRI and OXPHOS dysfunction in biochemical analysis of

muscle biopsies (Baertling et al., 2014). It has been reported that OXPHOS system dysfunction is the major cause of LS, in which many cases are associated with complex I deficiency (Fiedorczuk & Sazanov, 2018). More than 75 disease-associated genes were identified, within which 23 gene mutations causing Leigh or Leigh-like syndrome are associated with complex I including a series of nDNA gene-encoded subunits and assembly factors (Lake, Compton, Rahman & Thorburn, 2016; Schubert Baldo & Vilarinho, 2020). Although non-specific therapeutic strategies are applied, there is no causative treatment for LS as the clinical trials are limited by high variable phenotypes and early death of the patients (Chen et al., 2018). The knowledge and experience gained from LS animal models are required for developing more effective treatments.

1.5.3 Current therapies

The currently approved clinical treatments of mitochondrial disorders are limited to vitamins and cofactors (such as Q10) as antioxidants for symptom-based treatment, but many pre-clinical works and a few clinical trials have shown promising results as effective treatments tailored for specific mitochondrial disorders (Garone & Viscomi, 2018; Russell, Gorman, Lightowlers & Turnbull, 2020).

There are several pre-clinical therapies, targeting the common metabolic pathways relevant to the mitochondrial disease. This includes the boost of mitochondrial biogenesis, reducing chronic-oxygen related damage, bypassing the OXPHOS defects, and mitochondrial replacement therapy (Hirano, Emmanuele & Quinzii, 2018). Other more disease-tailored treatments include gene therapies to replace the defective DNA and shift the mutation heteroplasmy (Garone & Viscomi, 2018; Zhang et al., 2020).

The potential therapeutic approaches have been developing rapidly, however, the translating of the pre-clinical studies to effective and safe treatment to patients remains challenging. The knowledge of the pathogenic mechanisms underlying these diseases is still in urgent need for further development of the treatment and drug design.

1.5.4 Mouse models for mitochondrial complex I dysfunction

Complex I dysfunction is one of the most frequently observed OXPHOS disorders as complex I plays an important role as an entry point of ETC (Kirby et al., 1999). It is known that 7 out of 13 mtDNA encoded protein subunits belong to complex I, which is statistically more likely to be affected by mtDNA mutations. Recent studies also showed that a series of genes encoding for assembly factors are also associated with complex I defect resulting in neurological diseases (Mckenzie and Ryan, 2010; Pagniez-Mammeri et al., 2012). To understand the pathogenic mechanisms behind mutations, mouse models mimicking clinical phenotypes were generated (Table 1.2). The mouse models associated with complex I deficiency have mutations in nDNA encoded subunits, mtDNA encoded subunits or in the assembly factors. Specifically, *ndufs4* is widely mutated in various mouse models. Two whole-body *ndufs4* knockout mouse models with different genetic manipulations have shown common features of neurological disorder to some extent (Kruse et al., 2008; Leong et al., 2012). The other tissue specific *ndufs4* knockout in mouse heart or brain have shown various phenotypes such as cardiomyopathy or encephalopathy (Sterky et al., 2012; Karamanlidis et al., 2013; Quintana et al., 2010). The *Ndufs6* and *Ndufa5* knockouts were also reported with defects of complex I and negative effects on the high energy demand organs, such as heart and kidney (Ke et al., 2012; Forbes et al., 2013; Peralta et al., 2013). Mutagenesis in mtDNA is challenging due to the lack of mtDNA editing tools and dificulties of transporting RNAs into mitochondria. However, there are a few point mutations generated on ND4 and ND6 subunits. Interestingly, the phenotypes from these mouse models are all associated with LHON syndrome (Lin et al., 2012; Qi, Sun, Lewin, Hauswirth & Guy, 2007). In addition, the *m.13997G>A MT-ND6* mutation was also claimed to increase the rate of tumorigenesis in low metastatic potential cells due to overproduction of reactive oxygen species (Ishikawa, Imanishi, Takenaga & Hayashi, 2012). Furthermore, the Harlequin mouse with a decreased content of AIF (an assembly factor of complex I) was reported (Klein et al., 2002). The decreasing of AIF in Harlequin mouse was shown increased ROS production and neuron damage (Klein et al., 2002).

The mouse models with complex I dysfunction shown evidence of how complex I defects result in clinical phenotypes of several diseases on multiple organs and tissues. The mutations in those genes also provide valuable information for investigating the molecular characteristics of complex I in terms of loss of function. Furthermore, the mouse models provide the possibility to investigate and reveal the mechanism behind the mutant complex I at the molecular level.

Table 1.2 Mouse models of complex I deficiency*

	Gene	Genetic manipulation	Phenotype	References
nDNA-encoded subunits	*Ndufs4*	Whole body knock-out (Mox2-Cre)	Leigh-like, blindness, ataxia, retarded growth rate, lethargy	Kruse et al. (2008)
		Whole body knock-out (fky/fky)	Neurological impairment	Leong et al. (2012)
		Neurons and glia knock-out (Nestin-Cre)	Fatal progressive encephalopathy, ataxia, glial reactivity and neuronal loss; breathing dysfunction	Quintana et al. (2010, 2012)
		Dopaminergic neurons knock-out (Dat-Cre)	No overt neurodegeneration	Sterky et al. (2012)
		Heart/skeletal-muscle knock-out (Mck-Cre)	Cardiomyopathy	Sterky et al. (2012)
		Heart knock-out (αMhc-Cre)	Cardiomyopathy induced after stress condition	Karamanlidis et al. (2013)
		Truncated knock-in (Stop codon)	Embryonic lethality	Ingraham et al. (2009)
	Ndufs6	whole body knock-down (gene trap)	Cardiomyopathy, systolic dysfunction, renal disease, with altered ultrastructure and release of kidney damage biomarkers in urine	Ke et al. (2012) Forbes et al. (2013)
	Ndufa5	Whole body (gene trap)	Embryonic lethality	Peralta et al. (2013)
		Neurons knock-out (CaMKIIα-Cre)	Partial defect of CI in neurons that leads to lethargy and loss of motor skills at 10 months	Peralta et al. (2013)
mtDNA-encoded subunits	*Nd6*	*m.13997G>A MT-ND6* mutation cell fused with ρo ES cells	Lymphoma formation and metastasis	Hashizume et al. (2012)
		Enucleated LMTK$^-$ cell lines carrying *m.13997G>A MT-ND6* mutation fused with female mouse ES cells deprived of mitochondria.	Clinical features of LHON: decreased retinal response and swollen axons in the optic tract; CI deficiency in liver and brain; high levels of ROS in the brain	Lin et al. (2012)
	Nd4	*m.11778G>A MT-ND4 mutation* (AAV-ND4/ R340H construct)	Features of LHON: abnormal mitochondrial morphonology, high ROS level, swelling optic nerve head, progressive demise of ganglion cells	Qi et al. (2007)
Assembly factor	*Aif1*	Harlequin mouse	Late-onset neurodegenerative disorders, high ROS level, low complex I activity	Klein et al. (2002)

*The table was adapted from Torraco et al. (2015) and Irwin, Parameshwaran & Pinkert (2013) with some changes.

1.6 Cryo-electron microscopy by single particle analysis

1.6.1 The development of cryo-electron microscopy

Cryo-EM of single-particle specimens (also known as single particle analysis or SPA) is a technique to determine the structure of proteins without crystallization. Different from conventional transmission electron microscopy (TEM), single particle cryo-EM uses frozen-hydrated biological samples with mathematical and computational approaches to reconstruct protein structures from projections (Frank, 2016). Shortly after the development of the electron microscope by Ernst Ruska, Ladislaus Marton published his opinions of studying biological material with the electron microscope (Marton, 1934). In his report, the major destruction of putting organic materials under an intense electron beam was discussed, and two potential solutions suggested: cooling biological material temperatures and use of negative stain for sample preparation (Marton, 1934). Negative stain is a method of applying electron-dense metal compounds (such as uranium) to the surrounding of the biological specimen to provide an electron-density contrast between the biological material and metallic background (Brenner, S., & Horne, 1959). Negative stain has been used to enhance the contrast of sampled under EM, which has been established since 1940 and commonly used and modified during the following years (Hall, Jakus & Schmitt, 1945; Brenner & Horne, 1959; Huxley & Zubay, 1961). It was Aaron Klug and his colleagues who noted that in order to generate the three-dimensional (3D) structure of a protein complex, the observations of two-dimensional (2D) objections from different directions are required (Klug & Finch, 1965). The first 3D structure of bacteriorhodopsin solved by EM was published by Richard Henderson and Nigel Unwin with a resolution of 7 Å (Henderson & Unwin, 1975). In 1981, the method of preserving proteins in a non-crystalline form of frozen-hydrated samples at low temperature (about –190 ºC) was discovered by Dubochet and Alasdair McDowall (Dubochet & McDowall, 1981). It was also found that the vitreous ice was stable with the temperature kept below –160 ºC (Dubochet et al., 1988). The method of vitrifying water (also called “plunge freezing”) is universally recognized and applied in the field of single particle analysis. The first high-resolution structure determined by cryo-EM was published in 1990 (Henderson et al., 1990). Since then, the studies

with cryo-EM have grown as an accelerated number of high-resolution structures determined by cryo-EM were deposited in the protein data bank in the last 30 years (Fig 1.12).

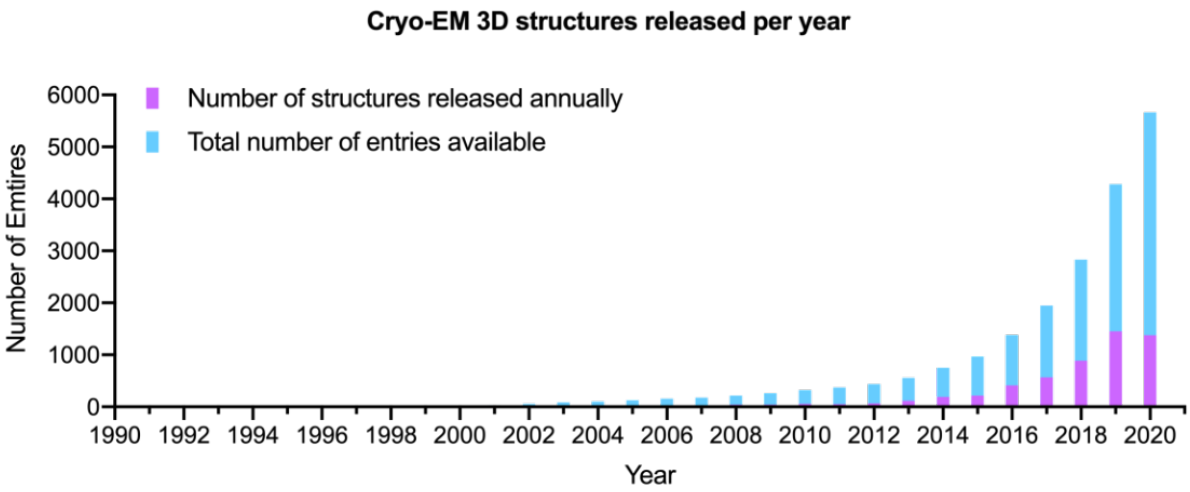

Fig 1.12 Growth of structures from cryo-EM experiments released every year. The data was adapted from Protein Data Bank (Berman, 2000).

In 2017, the Nobel prize in chemistry was awarded to Jacques Dubochet, Joachim Frank, and Richard Henderson for “developing cryo-electron microscopy for the high-resolution structure determination of biomolecules in solution". Nowadays, the cryo-EM field has been rapidly developed with a common workflow (Fig 1.13) from sample preparation to data analysis (Doerr, 2016; Sgro & Costa, 2018; Kim et al., 2018).

In brief, this process is divided into seven steps (Fig1.13). The experiment begins with a purified protein sample. Then the sample is applied on a cryo-grid which is a small metal disc with meshes. The protein sample applied on the surface of the grid is gently blotted away the excess until a thin layer of sample solution remains on the grid surface. Then the grid is rapidly plunge-frozen in a cryogen (such as liquid ethane) to form vitrified ice. As the protein samples are different in size and shape, various ways have been explored to optimise the sample purification and grids optimisation protocols for purifying fragile proteins and eliminate protein orientational biases on the grids (Doerr, 2016).

The third step is to screen the sample on grids under a TEM. The grids showing good particle distribution and minimum ice containment are considered as a candidate for data collection. Then the 2D electron micrographs with low electron dose are captured to avoid radiation

damage on single particles. The 2D projections of protein particles are reconstructed to an initial 3D structure by a series of imaging processing methods. CryoSPARC and RELION are two of the most commonly used data processing software packages (Zivanov, et al., 2018; Punjani, Rubinstein, Fleet & Brubaker, 2017). The final density map with high resolution is generated by iterative refinements and validations. Then the protein sequence is fitted into the map to build the 3D model of the protein.

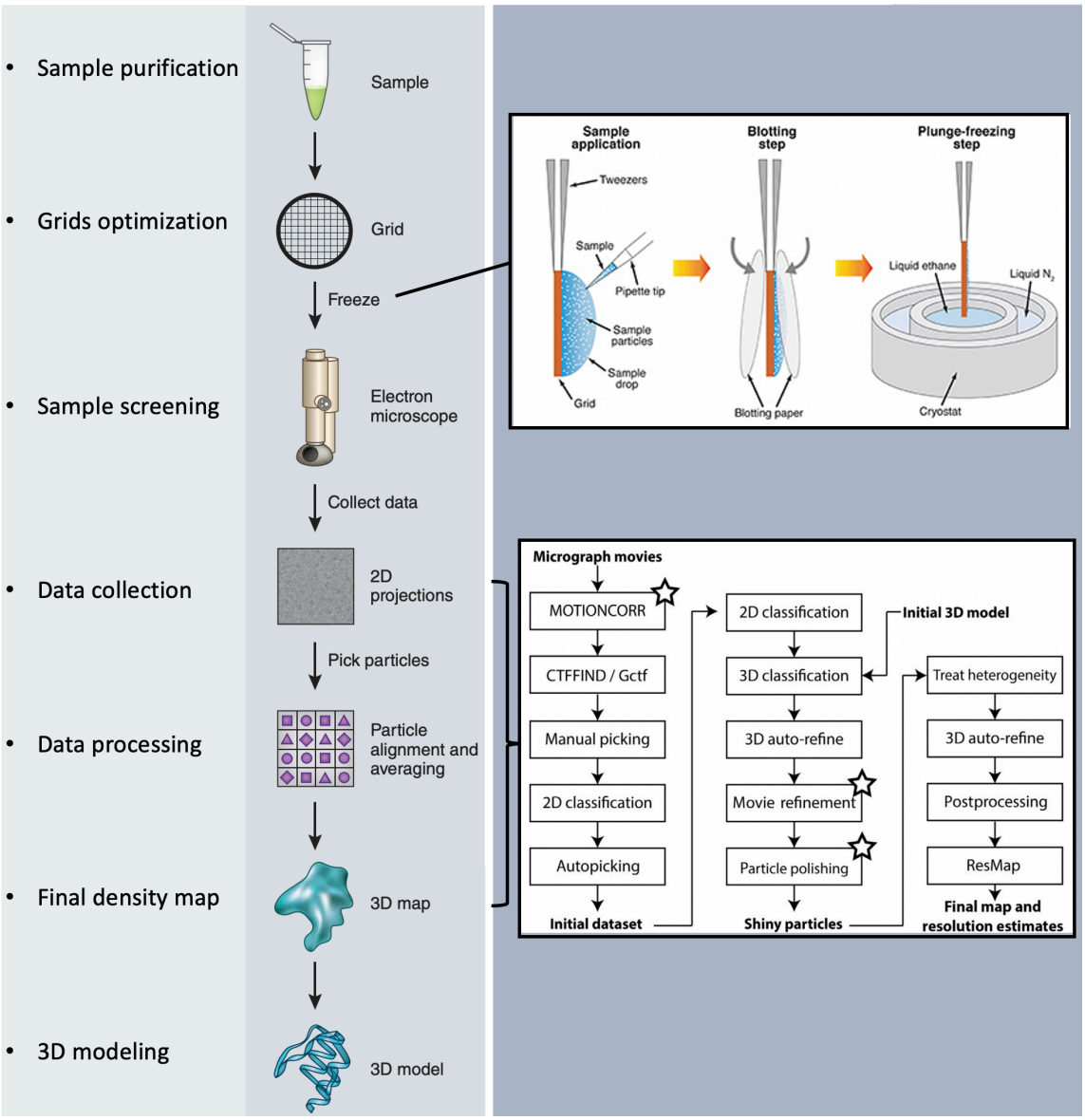

Fig 1.13 The workflow of a protein structure determination by single particle cryo-EM. The image was adapted from Doerr (2016), Sgro & Costa (2018) and Scheres (2016) with some modifications.

1.6.2 Grids selection and modification

EM grids are a round shaped metal disks (~3 mm in diameter) with meshes used to support the specimen during electron beam exposure. The conventional TEM grid is made of copper or nickel (Sgro & Costa, 2018). The number of the meshes on the grid are various and they control the size of the grid pitch. Commonly used copper grids are between 200 to 300 mesh.

Cryo-EM grids require an additional step of forming a uniform layer of vitrified ice with protein samples in random orientations on the surface of metal grids. The conventional processes include applying a sample solution droplet on the grid surface, blotting the exceed solution to generate the thin water layer, and then fast-frozen by plunge freezing (Sgro & Costa, 2018). These processes can be performed in commercially designed vitrification robots, for example, the Vitrobot and the Leica EM GP plunge freezer. The Vitrobot is a semi-automatic plunge-freezing machine with a temperature and moisture control chamber and a liquid-ethane containing pot. In addition, the blotting time and force can also be controlled. The application of the conventional tissue-blotting method can lose 99.9% of the sample during the process (Arnold et al., 2017). A recently developed device, the “Spotition” robot with an inkjet dispenser, is able to minimize the deposition waste and achieve time-resolved sample freezing (Jain, Sheehan, Crum, Carragher & Potter, 2012; Dandey et al., 2020).

Preparing good, monodispersed particles on frozen-hydrated grids is still challenging as it was suggested that the fragile proteins and complexes exposed to the air-water interface could introduce damage to the structure during the freezing process (Dubochet et al., 1988; Glaeser, 2018). However, the grids coated with amorphous carbon membrane can provide extra support to hold the samples away from the air-water interface and is considered as a common approach for cryo-EM studies (Williams and Glaeser, 1972; Russo & Passmore, 2014a; Han et al., 2016). It is known that a thin carbon layer (ideally less than 10 nm) can improve particle distribution (Thompson, Walker, Siebert, Muench, & Ranson, 2016).

Although the amorphous carbon film is wildly used, the problems of inconsistent thickness between batches and deterioration of quality over time should be considered (Thompson et al.,

2016). Besides, amorphous carbon film and the ice layer it supports have could introduce image blurring and loss of information content due to the radiation-induced changes (Russo & Passmore, 2014a). Novel materials, such as graphene coating layer and gold made grids, are reported to reduce beam-induced motion with a consistent thickness (Yoshioka, Carragher & Potter, 2010; Russo & Passmore, 2014b, 2016). Graphene is made of flat-monolayered carbon crystalline lattice (Geim & Novoselov, 2007). The graphene-coated grids have a higher electron conductivity with less background noise than the amorphous carbon- coated grids during imaging (Geim & Novoselov, 2007). A recent modification of the graphene surface with hydrogen gas plasma cleaning was able to increase the hydrophilicity of the grid surface for better particle partitions (Russo & Passmore, 2014b). Another alternative, graphene oxide (GO), has similar characteristics as graphene and better hydrophilicity without modifications (Pantelic, Meyer, Kaiserm, Baumeister & Plitzko, 2010). Recent studies showed the stability of gold grids under TEM is much higher than copper giving higher quality images with less blurring (Passmore & Russo, 2016; Russo & Passmore, 2016).

To achieve better sample partitioning and random particle orientation on the grids, the surface properties can be modified by several processes. For example, the most common approach of glow-discharging/plasma-cleaning treatment was used to enhance the particle affinity on the grid surface (Grassucci, Taylor & Frank, 2007). Less common methods such as poly-L-lysine or detergent treatment are also able to achieve homogeneous dispersion on grids (Cheung et al., 2013). Some of the methods are highly sample dependent, for example, polyethylene glycol coated (PEGylated) gold grids could improve the particle partition inside the grid holes for complex I (Meyerson et al., 2014; Blaza et al., 2018). The improvements of support films that mentioned above have shown the potential to improve the quality of the cryo-EM data.

1.6.3 Sample purification strategy with crosslinkers

Crosslinking helps to stabilize the structure of protein complexes and it is a popular technique applied in mass spectrometry to conserve the protein's native global structure (Schmidt & Robinson, 2014). Recently, crosslinkers have been widely used in the cryo-EM field to stabilize macromolecules or large complexes with minimal effects on protein structure and function

(Rozbeský, et al., 2018; Kasinath, et al., 2018; Irwin, et al., 2019). To strengthen the stability of large complexes, a series of sample purification methods with gradient-based in-tube crosslinking are proposed, including GraFix, GraDeR and ArgaFix (Kastner et al., 2008; Hauer et al., 2015; Adamus et al., 2019). These sample preparation protocols without chromatography can provide more gentle purification procedures and environments to the protein. GraFix and GraDeR used glycerol gradient to concentrate the sample, remove the excess detergent and other undesired proteins after solubilization (Hauer et al., 2015). However, the concentrated sample with the treatment of crosslinker often causes a problem with aggregation. ArgaFix embedded protein in agarose before crosslinking to avoid aggregation (Adamus et al., 2019). Although these methods are able to preserve the fragile protein complex structure, the structures produced from single-particle cryo-EM is at an intermediate resolution (>4 Å). This is because removing the glycol from the particles is challenging, which could result in poor image contrast for data collection (Kastner et al., 2008; Hauer et al., 2015; Adamus et al., 2019).

The most commonly used crosslinkers in cryo-EM are bis- (sulfosuccinimidyl)suberate (BS^3) (Fig 1.14A) and glutaraldehyde (Fig 1.14B). Glutaraldehyde, a linear 5-carbon dialdehyde, is soluble in water as well as in organic solvents (Migneault, Dartiguenave, Bertrand & Waldron, 2004). It was first used as the fixation chemical for tissues in the 1960s and later on widely applied as a mild crosslinking agent for the immobilization of enzymes in aqueous buffer (Sabatini, Bensch & Barrnett, 1963). Glutaraldehyde can react with functional groups such as amine, thiol, and phenol in a natural pH (Habeeb & Hiramoto, 1968). However, it is worth noting that a protein with high lysine content showed an effect of solublisation by glutaraldehyde treatment (Broun, 1976), and enzyme solubility during the reaction with glutaraldehyde was highly pH dependent (Habeeb & Hiramoto, 1968). Thus, glutaraldehyde crosslinking is not applicable to a protein with high lysine content on the surface. It was also reported that the enzyme activity was decreased proportionally to the concentration of glutaraldehyde as it distorts the enzyme accessibility to the substrates (Chui & Wan, 1997). To apply glutaraldehyde crosslinking for cryo-EM sample preparation, the choice of pH and testing of biological activity of the protein should be taken into account. In recent studies, glutaraldehyde-fixation was used to stabilise protein structure and inactive virus at the same

time in the cryo-EM studies (Kastner et al. 2008; Huiskonen, Overby, Weber & Grünewald, 2009; Zhang, et al., 2011). However, the resolutions of the structure are in the intermediate range, which makes it difficult to determine the effects of the fixation process (Parvate et al., 2020).

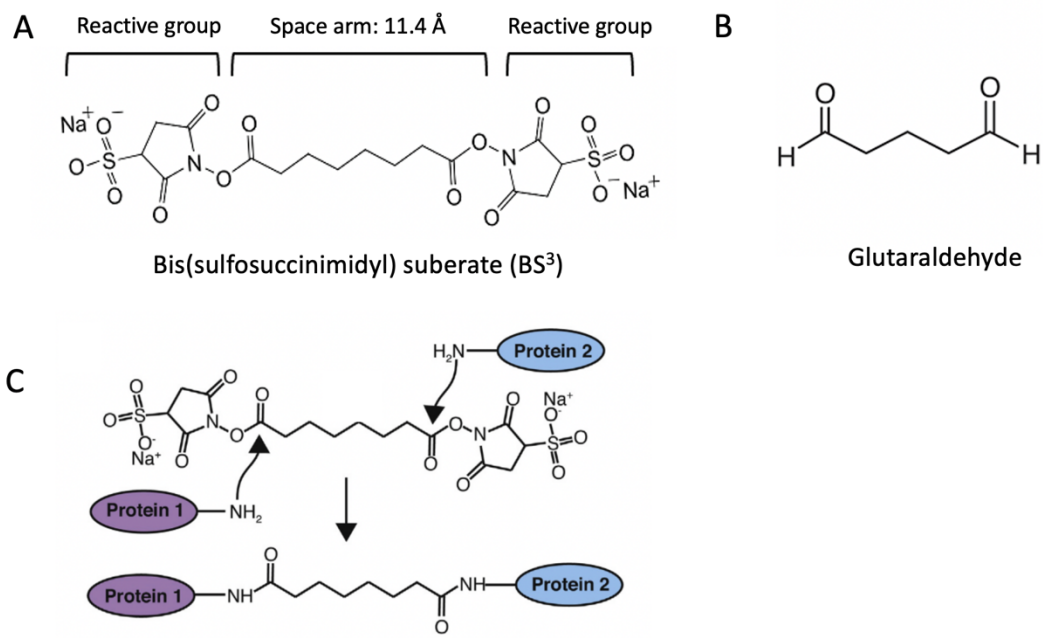

Fig 1.14 Structure of crosslinkers. (A) structure of BS^3 with two reaction group and a space arm of 11.4 Å. The figure was adapted from Schmidt &Urlaub (2017). (B) structure of glutaraldehyde. (C) The NHS ester reaction between proteins and BS^3.

Bis(sulfosuccinimidyl) suberate (BS3) is a water-soluble crosslinker that forms stable amide bonds with the primary amino group by NHS ester reaction (Fig 1.14C). In proteins, BS3 specifically targets lysine and N-terminus of each polypeptide within the distance of its spacer arm (11.4 Å) (Shi, Pei, Liu & Zhang, 2017). The long space arm of BS3 allows the intramolecular crosslinking as well as intermolecular crosslinking among proteins. The irreversible formation of amide bonds occurs rapidly with primary amino groups in pH 7 to 9. It has been reported that only high BS3 concentration (100 to 500-fold molar excess of BS3, 0.69 mM to 3.45mM BS3 with 0.2 mg/mL protein in this case) affects human carbonic anhydrase I protein structure locally, but the protein fold remains unchanged, (Rozbeský et al., 2018). The BS3 crosslinker has been used in the cryo-EM field for tackling macromolecules and protein complexes. A human postcatalytic spliceosome, a nearly 2 MDa complex, was determined at 3.3 Å in resolution with 0.5 mM BS3 crosslinking with 1mg/mL purified protein

solution (Fica, Oubridge, Wilkinson, Newman & Nagai, 2019). Polycomb repressive complex 2 was crosslinked at 1.5-2.0 mg/mL with 0.5 mM BS3 which gives a resolution of 3.5 Å after 3D reconstruction (Kasinath et al., 2018). A mammalian RNA polymerase II complex, 550 kDa complex of 12 subunits, was determined at the resolution of 3.4 Å by cryo-EM with 3 mM BS3 (Liu, Farnung, Wigge & Cramer, 2018). Incubation with BS3 is able to reinforce complex interaction and stability, however, it also raises the concern of introduce intermolecular aggregation and loss of biological activities. Thus, the crosslinking conditions (concentration, time, temperature, and pH) should all be optimised for every sample (Shi et al., 2017).

1.7 Aims of this thesis

Studies of complex I in multiple model systems during the past few decades have solved complex I structures and explained parts of the enzyme's catalytic mechanism. However, the pathogenesis of complex I mutations has not been explained on a molecular basis.

This study aims to explain mutation-caused enzyme dysfunctions at a molecular level. The focus is put on two complex I-deficient relevant mouse models: the ND6-P25L and *ndufs4*$^{-/-}$ mouse models. The structural determination of the mutant enzymes by cryo-EM will be combined with biochemical assays and *in vivo* studies. Besides, challenges of cryo-EM grid preparation and protein purification will be overcome to solve the bottle-neck problems arising from limited protein concentration and fragile complexes.

Chapter 2. Material and Methods

2.1 Materials and reagents

Solutions and buffers were prepared from Milli-Q water supplied by the Millipore academic water purification system (Millipore Ltd.) or nuclease-free H_2O (Thermo Fisher Scientific). N-Dodecyl β-D-maltoside (DDM) was purchased from Glycon Biochemicals. Thiol-PEG reagents were purchased from SensoPath Technologies (USA). All other reagents and chemicals used in this work are supplied by Sigma-Aldrich unless otherwise stated.

2.2 Mouse work

All procedures were approved by the local ethics committees of the MRC Laboratory of Molecular Biology and the University of Cambridge and by the UK Home Office (project license: P6C97520A). The ND6-P25L mouse strain (Lin et al., 2012) was generously provided by Professor Douglas Wallace (University of Pennsylvania). The *ndufs4*$^{-/-}$ mutant mice were provided by Carlo Viscomi (MBU, University of Cambridge). The mutant mice (ND6-P25L and *ndufs4*$^{-/-}$ strain) have a C57BL/6J genetic background. The wild type (WT) mice, with the same genetic background of C57BL/6J, were purchased from Charles river UK, Ltd. (Kent, UK). To produce constitutive *ndufs4* knockout (KO) mice, mice heterozygous for *ndufs4* knockout (*ndufs4*$^{+/-}$) were inbred. To maintain the ND6-P25L strain, an ND6-P25L female mouse was crossed with a WT male mouse. The welfare of the mice was monitored to avoid pain, suffering and distress according to the principle of 3Rs (Replacement, Reduction and Refinement). Euthanasia was performed on *ndufs4*$^{-/-}$ mice at 4 to 5 weeks old before the further onset of sever symptoms such as loss of body weight, loss of motor skill, blindness (Kruse et al., 2008). ND6 mice did not display any obvious phenotype up to 78 weeks.

2.2.1 Genotyping

To maintain mouse colonies, ear notches were used for genotyping. The automated genomic DNA extractions were performed by using Promega Maxwell® 16 purification system and kits

(Promega). In brief, ear notches were collected and transferred into the Maxwell® 16 DNA purification cartridges and the tissue in the lysis buffer was rapidly broken down by the plunger. The DNA was captured by the Magnesill™ Paramagnetic particles and purified by series of washes. The extracted DNA was transferred into 300 µL of nuclease-free H_2O.

Polymerase chain reaction (PCR) was performed using primers as in Table 2.1. The primers were diluted in nuclease-free H_2O to a stock of 100 µmol/L. A master mix was prepared with 0.15 µL GoTaq® G2 polymerase and 2 µL DNA to make a total volume of 25 µL for each sample (Table 2.2). A positive and a negative control were run in the same PCR program (Table 2.3).

To visualize the PCR products, 2% (w/v) low molecular weight agarose gel was poured with 0.5 µg/ml ethidium bromide. A volume of 5 µL the amplified DNA products were loaded on the gel with a 1 kb DNA ladder (New England Biolabs). The electrophoresis was performed at 100 V for 17 min. The fluorescence of ethidium bromide (which intercalates to DNA) was then imaged on a ChemiDoc™ imaging system (Bio-Rad).

The PCR product of wide type allele with wild type forward and reverse primers would show a 150 bp band after electrophoresis. While the PCR product of *ndufs4*$^{\Delta}$ allele with wild type forward and *ndufs4* reverse primers would show a 250bp band. For ND6-P25L, the PCR product of 700bp in size was sent for sequence to confirm the point mutation.

Table 2.1 Genotyping primer

	Forward	**Reverse**
Wild type	5'- AGCCTGTTCTCATACCTCGG-3'	5'- GCTCTCTATGAGGGTACAGAG-3'
Ndufs4	(same as above) 5'- AGCCTGTTCTCATACCTCGG-3'	5'- GGTGCATACTTATACTACTAGTAG-3'
ND6-P25L	5'- TACCCGCAAACAAAGATCACCCAG-3'	5'- TTAGGCAGACTCCTAGAAGG-3'

Table 2.2 Master PCR mix

Master mix buffer	5.00 µL
2.5mM dNTP	2.00 µL
DMSO	1.25 µL
Forward primer	0.60 µL
Reverse primer	0.60 µL

GoTaq® G2 polymerase	0.15 μL
DNA extraction	2.00 μL

Table 2.3 Genotyping PCR program

Temp	**Purpose**	**Duration**	**Cycles**
95°C	Initial denaturation	3 min	1
95°C	Denaturation	30 sec	
53°C (56°C *)	Annealing	30 sec	34 (25*)
72°C	Extension	45 sec	
72°C	Final extension	5 min	1
4°C	Storage		

2.2.2 Tissue harvesting

All mice were sacrificed by cervical dislocation in accord with the UK Animals (Scientific Procedures) Act, 1986 (PPL: P6C97520A, approved by the local ethics committees of the MRC Laboratory of Molecular Biology and the University of Cambridge and by the UK Home Office). Heart, brain, liver and kidney tissue were excised from both wild type (WT) and mutant mice. The tissue collection process was aided by Dr Ahmed-Noor Adam Agip and Mr Daniel N. Grba. Heart and brain tissues were immersed immediately in ice-cold homogenization medium AT containing 10 mM Tris-HCl (pH 7.4 at 4°C), 75 mM sucrose, 225 mM sorbitol, 1 mM ethylene glycol-bis(β-aminoethyl ether)-N,N,N′,N′-tetraacetic acid (EGTA) and 0.1% (w/v) fatty acid-free bovine serum albumin. Liver and kidney tissues were stored in ice-cold homogenization medium A, which contains 0.32 M sucrose, 1 mM Ethylenediaminetetraacetic acid (EDTA), and 10 mM Tris–HCl (pH 7.4 at 4°C). All tissues in ice-cold solution were transferred to lab within one hour of animal sacrifice for mitochondrial isolation.

2.3 Mitochondrial membrane preparation

2.3.1 Mitochondrial extraction

Mitochondria were prepared as described previously (Fernández-Vizarra et al., 2010) with a few alterations.

For heart or brain tissue, a volume of 10 mL homogenization medium AT was added per gram of tissue. Then, the tissue was cut into small pieces with scissors then homogenized by seven to ten strokes of a Potter–Elvehjem homogenizer (Thomas Scientific) fitted with a Teflon pestle at 1,000 rpm at 4°C on a stirrer (IKA® RW20 Digital overhead stirrer). The homogenate was centrifuged (1,000 xg, 5 min), and the pellet was removed. Then the supernatant was centrifuged (9,000 xg, 10 min) to collect the crude mitochondrial pellet.

For liver or kidney tissue, homogenization medium A was added to give 4 mL/g of liver or 5 mL/g of kidney tissue. Then the tissue was cut into small pieces with scissors then homogenized by five to eight strokes of at 600 rpm at 4°C. The homogenate was centrifuged (1,000 xg, 5 min), then the supernatant was centrifuged (15,000 xg, 10 min) to collect the crude mitochondrial pellet.

The pelleted mitochondria were suspended in resuspension buffer (20 mM Tris-HCl or 20 mM 4-(2-hydroxyethyl)-1-piperazineethanesulfonic acid (HEPES), 1 mM EDTA, 10% glycerol, pH 7.4 at 4°C) to a protein concentration of ~10 mg/mL and stored as aliquots at –80°C. The protein concentration was measured by bicinchoninic acid (BCA) protein assay with Pierce™ BCA Protein Assay Kit (ThermoFisher Scientific).

2.3.2 Mitochondrial membrane isolation

Mitochondrial membranes were prepared as described previously (Agip, et al. 2018). Mitochondrial suspensions were thawed on ice and diluted into 5mg/mL with resuspension buffer. Then the suspension was sonicated using a Q700 Sonicator (Qsonica) at 65% amplitude and three 5-s bursts of sonication (with 30-s intervals on ice). After that, the suspension was

centrifuged at 75,000 xg for 1 hour at 4°C. The pellets containing mitochondrial membranes were homogenized in resuspension buffer to a final protein concentration of ~5 mg/mL measured by BCA. Pierce protease inhibitor tablets were added to the suspensions at a proportion of 1 tablet to 50mL suspension and the suspension aliquots were frozen and stored at –80°C.

2.4 Complex I purification

Complex I was purified as described previously (Agip, et al. 2018) with a few alterations for different mouse mutant strains. The detailed methods are shown below.

2.4.1 Mitochondrial membrane solubilisation

An amount of 20 to 30 mg membranes was thawed on ice and 0.005% PMSF (w/v) was added. This was then transferred into an Eppendorf Thermomixer 5355 Comfort 2.0 ML Block Shaker (Eppendorf) at 4°C and shaken at 400 rpm for 30 min. Once the shaker started, a fresh 10% DDM stock was added dropwise into the membrane suspension up to a final concentration of 1% DDM (v/v). After 30 minutes solubilizing, the suspension was transferred to Optima™ MAX Benchtop Ultracentrifuge (Beckman Coulter™) and centrifuged at 48,000 xg at 4°C in an MLA80 rotor (Beckman Coulter™) for 30 min. The supernatant was collected and kept on ice.

2.4.2 Anion-exchange chromatography

Buffers and anion-exchange column were prepared the day before membrane solubilization and complex I purification. Buffer A contained 20 mM Tris-HCl, 1 mM EDTA, 0.1% DDM, 10% ethylene glycol (v/v, VWR), 0.005% soybean asolectin (Avanti) and 0.005% CHAPS (Calbiochem) pH corrected to 7.14 at 23°C. Buffer B was the same as buffer A with 1 M NaCl added. Both buffers were filtered with 500 mL Vacuum Filter with 0.1 µm pore (Corning) and stored at 4°C. The Hi-Trap Q HP anion exchange column (GE Healthcare) (1 mL or 5 mL depending on the supernatant volume) was prepared by washing with 10 mL buffer A followed with buffer B and repeated 2 to 3 times. On the day of membrane solubilization, the column was pre-equilibrated with buffer A in the 4°C cold room by using a MINIPULS 3 peristaltic pump (Gilson) at a flow rate about 1 mL/ min.

The membrane supernatant was loaded onto the anion exchange column. Before attaching the column onto the Äkta micro system (GE Healthcare), the pumps and system pressure were

checked. The pressure should be in the range of 1 MPa to 6 MPa at the flow rate of 0.5 mL/min. Then the system was washed with buffer A twice. Protein elution was monitored at 280 nm and 420 nm and the column pressure alarm was set to 2.2 MPa, and flow rate was set at 0.3 mL/min. After attaching the loaded anion exchange column onto the Äkta micro system it was washed with 20% buffer B to wash out unwanted proteins from the mixture. Then the concentration of buffer B was raised to 35% at which complex I starts to elute. The complex-I containing fractions eluted around 3 mL as a second peak and these fractions were concentrated together to a volume of about 100 µL with a 100 kDa MWCO Vivaspin 500 concentrator (Sartorius) with a Techne Genofuge 16M Microcentrifuge (Jencons) at 4°C.

2.4.3 Size-exclusion chromatography

Complex I from anion-exchange chromatography was further purified and desalted by size-exclusion chromatography. Buffer C (20 mM Tris-HCl pH 7.14 at 23°C, 10% ethylene glycol, 150 mM NaCl and 0.05% DDM) was used as the elution buffer. Complex I was eluted with a Superose 6 Increase 5/150 column (GE Healthcare) with buffer C.

The Hi-Trap Q HP anion exchange column was removed, and the system was washed with buffer C before attaching the pre-equilibrated Superose 6TM Increase 5/150 column. The flow rate was set at 0.03 mL/minute and the pressure limit was set at 2.5 MPa. Protein was injected into a 100 µl size loop and load onto the column by a 100 µL Hamilton syringe (Cole-parmer). The fractions at the first peak (around 1.5mL) were collected. The concentration of each fraction was checked by BCA assay kit (ThermoFisher Scientific). In order to store the purified complex I, the fractions were further mixed with 30% glycerol and fast-frozen in liquid nitrogen. The frozen fractions were stored at –80°C. To further use the purified complex I making cryo-EM grids, the glycerol was not added and the fresh fractions need to be used. In addition, the fractions need to reach the concentration above 3 mg/mL before applying on cryo-EM grids. A gentle centrifuge with a 100 kDa MWCO Vivaspin 500 concentrator at 4°C was applied if necessary.

2.4.4 BS^3 crosslinking

The BS^3 crosslinker was prepared immediately before use. For protein concentration smaller than 5 mg/mL, the final BS^3 concentration should be around 0.25 to 5 mM. BS^3 was first dissolved in water to 100 mM and then further diluted in HEPES resuspension buffer (20 mM HPEPS, 1mM EDTA, 10% Glycerol, pH 7.4 at 4°C) based upon the needs. The reaction takes 30 min at room temperature. The quenching buffer (1 M Tris-HCl, pH 7.5 at 4°C) was added to a final concentration of 50 mM Tris. To finish the quenching reaction, incubation was needed for 15 min at room temperature after adding the quenching buffer.

2.5 Protein visualization

2.5.1 Blue native-PAGE

Blue-native PAGE (BN-PAGE) was used to separate membrane protein complexes. Before loading the sample onto the BN-PAGE, mitochondrial membranes were solubilized with 1% DDM at 4°C for 30 min and centrifuged at 14,000 rpm for 30 min by using a Techne Genofuge 16M Microcentrifuge at 4°C. For each sample, 30 µL solubilized membrane was mixed with 10 µL blue strain mixture which contained 8.5 µL NativePAGE™ sample buffer (Invitrogen) and 1.5 µL 5% Coomassie G-250 (Amnesco). Then 30 mg of each sample was loaded onto Native PAGE™ Novex 3–12% Bis-Tris Gels (ThermoFisher Scientific). 200 mL 1X NativePAGE™ Anode Buffer was prepared with 10mL NativePAGE Running Buffer (20X) and 190 mL deionized water. The 1X NativePAGE™ Anode Buffer was filled into the outer buffer chamber. Two kinds of cathode buffer were prepared. 200 mL dark blue Cathode Buffer contained 10 mL NativePAGE Running Buffer (20X), 10 mL NativePAGE™ Cathode Additive (20X) and 180 mL deionized water. The light blue Cathode Buffer was made of 10 mL NativePAGE Running Buffer (20X), 1 mL NativePAGE™ Cathode Additive (20X) and 180 mL deionized water. The dark blue Cathode Buffer was filled into the inner buffer chamber. The electrophoresis started with 100 V for 30 min. Once the samples migrated into the gel, the dark blue Cathode Buffer was replaced by the light blue Cathode Buffer. The electrophoresis continued at 180V for 1.5 h until the dye front reached the end.

In-gel activity assays of NADH dehydrogenase was performed by adding nitro blue tetrazolium (NBT) and NADH to the enzyme to form blue or purple precipitate formazan upon reduction. The gel was removed from the chamber and washed with water. Before starting the reaction, the gel was incubated in buffer A (20 mM Tris-HCl, NADH 100 µM, pH at 7.5 in room temperature) for 10 min. It was then incubated in the Buffer B (20 mM Tris-HCl, 1 mg/mL NBT) 5 to 10 min.

The BN-PAGE was alternatively Coomassie stained if in-gel activity assays were nor required. The washed gel was immersed in Coomassie blue strain (40% methanol, 10% acetic acid and

0.05% Coomassie R250) for 15 minutes in room temperature, and washed in de-stain solution (20% methanol, 7.5% acetic acid) for overnight.

2.5.2 Two dimensional BN/SDS-PAGE

To identify protein complex integrity and interactions, a second dimension SDS-PAGE was performed after BN-PAGE. The protein complex bands detected in BN-PAGE were cut from the gel. Each slice was equilibrated in a separate Eppendorf tube with equilibration buffer A (75 mM Tris-HCl, 6 M urea, 20% glycerol, 2% SDS, 10 mg/mL threo-1,4-Dimercapto-2,3-butanediol (DTT), pH 7.4 at room temperature) for 15 minutes. Then the slices were transferred to equilibration buffer B (75 mM Tris-HCl, 6 M urea, 20% glycerol, 2% SDS, 25 mg/mL iodoacetamide, pH 7.4 at room temperature) for 15 min. Slices were then rinsed in SDS sample loading buffer (10% SDS, 20% glycerol, 0.2M Tris-HCl, 0.05% bromophenolblue, pH 6.8 at room temperature) before the gel slices were loaded into each well of a NuPAGE 4-12% Bis/Tris SDS-PAGE gel (ThermoFisher Scientific). 1X NuPAGE MES SDS Running Buffer was filled in both inner and outer chambers. The electrophoresis was run at 10 mA for 1 hour and increased to 40 mA until the dye front reached the end.

2.6 Kinetic activity measurements

All assays were carried out in assay buffer K (10 mM Tris-SO_4, 250 mM sucrose, pH 7.4) at 32°C with a SPECTRAmax PLUS384 spectrophotometer (Molecular Devices, UK) in 96-well plates (Cole-Parmer) unless otherwise stated. Detailed descriptions of kinetic assays are presented in Table 2.4 and Table 2.5 below.

2.6.1 NAD(P)H oxidation on mitochondrial membrane and purified complex I

Measurements were modified from the methods described previously (Birrell, Yakovlev & Hirst, 2009, Kussmaul & Hirst, 2006). NADH:O_2 assays were carried out with 200 µM NADH, 1.5 µM horse heart cytochrome *c* and typically 10 ug/mL membranes. The reaction was monitored at 380-340 nm (ε = 4.81 mM^{-1} cm^{-1}). Various alterations were made on this assay to investigate complex I kinetic activity under different conditions. The channel-forming peptide alamethicin was dissolved in DMSO and added to permeabilize the membrane before the reaction. Complex I inhibitors, Piericidin A or Rotenone were added to the membrane as a control. Flavin-site NADH oxidation assay, NADH:3-Acetylpyridine adenine dinucleotide ($APAD^+$) transhydrogenation, was carried using 200 µM NADH, 500 µM $APAD^+$ and 1 µM of Piericidin A and monitored at 400-450 nm (ε =3.16 mM^{-1} cm^{-1}).

Similarly to NADH:O_2 assays, NADPH:O_2 was carried with 1 mM nicotinamide adenine dinucleotide phosphate (NADPH), 11.5 µM cytochrome *c* and 2 mg/mL mitochondrial membrane. Potassium hexacyanoferrate (III) (FeCN) was added to oxidase NADPH when required. The reaction was monitored at 380-340 nm (ε = 4.81 mM^{-1} cm^{-1}).

Purified complex I catalytic activity was measured at 380-340 nm (ε = 4.81 mM^{-1} cm^{-1}) with the NADH: decylubiquinone assay. In brief, 0.5 µg/mL complex I was added to 0.075% (w/v) asolectin and 3-[(3-Cholamidopropyl)dimethylammonio]-1-propanesulfonate hydrate (CHAPS) and 100 µM decylubiquinone in 20 mM Tris-HCl (pH 7.5 at 32°C).The reaction was initialized by adding 100 µM NADH.

2.6.2 Succinate dehydrogenase by complex II on mitochondrial membrane

The measurement for succinate dehydrogenase activity was modified from the methods described previously by Jones and Hirst (2013). In brief, succinate oxidation was measured by a stoichiometric coupled enzyme assay. Succinate was oxidized to fumarate by succinate dehydrogenase, then fumarate hydratase (FumC) converted fumarate into malate. Malate was then converted to pyruvate to reduce NADP+ to NADPH by oxaloacetate decarboxylating malic dehydrogenase (MaeB). Succinate:O2 oxidoreduction assay was monitored at 340-380 nm (ε = 4.81 mM-1cm-1). Membrane (10 mg/mL) was permeabilized by 15 μM alamethicin and incubated with 1.5 μM cytochrome c in Tris-HCl buffer which contained 2 mM MgSO4, 2 mM K2SO4 and 5 mM succinate. 90 μg/mL FumC and 500 μg/mL MaeB were added for the specific and stoichiometric coupled assays. Atpenin A5, a complex II inhibitor, was used in control experiments. Then 2 mM NADP+ was added to initiate the reaction.

Table 2.4 Kinetic Assays

Reaction	Reagent	Working Concentration	Notes
NADH:O_2 ε 340nm-380nm = 4.8 mM^{-1} cm^{-1}	NADH	200μM	
	cytochrome *c*	1.5 μM	
	Membrane	10 ug/mL	
	Alamethicin	10, 15 ug/mL	Membrane permeabilization
	Rotenone	1 μM	Complex I inhibition
	PiericidinA	1 μM	Complex I inhibition
NADH:$APAD^+$ ε 400nm -450nm =3.16mM^{-1} cm^{-1}	NADH	200 μM	
	Membrane	10 ug/mL	
	$APAD^+$	500 μM	
	PiericidinA	1 μM	Complex I inhibitor
NADPH:O_2 ε 340nm-380nm = 4.8 $mM^{-1}cm^{-1}$	NADPH	1 mM	
	cytochrome *c*	1.5 μM	
	Membrane	2 mg/mL	
	FeCN	2 mM	
NADH:decylubiquinone ε 340nm-380nm = 4.8 $mM^{-1}cm^{-1}$	NADH	100μ	
	Complex I	0.5 μg/mL	
	Asolection/CHAPS	0.075%	
	Decylubiquinone	100 μM	
Succinate:O_2 ε 340nm-380nm = 4.8 $mM^{-1}cm^{-1}$	$NADP^+$	2mM	
	cytochrome *c*	1.5 μM	
	Membrane	10 μg /mL	
	$MgSO_4$	2 mM	
	K_2SO_4	2 mM	
	Succinate	5 mM	
	FumC	90 μg/mL	
	MaeB	500 μg/mL	
	Atpenin A5	2 μM	

2.6.3 Hydrogen peroxide production

Amplex Red oxidation was used to measure hydrogen peroxide (H_2O_2) production. In brief, 40 ug/mL mitochondrial membrane was mixed with 2 unit/mL horseradish peroxidase (HRP), 10 μM Amplex Red and 10 unit/mL superoxide dismutase from bovine erythrocytes (SOD). Then the reaction was initiated with 30 μM NADH and monitored at 557-620 nm (ε = 51.60 $mM^{-1}cm^{-1}$). In addition, three background condition assays (see Table 2.5) were used in order to calculate complex I specific H_2O_2 production which are shown in the Table 2.5 as follows:

Catalytic rate (nmol min^{-1} mg^{-1}) = Catalytic rate $_{condition\ A}$ – (Catalytic rate $_{condition\ B}$+ Catalytic rate $_{condition\ C}$ - Catalytic rate $_{condition\ D}$)

Table 2.5 H_2O_2 production Assay

Reagent		**Condition**			
Name	**Concentration**	**A**	**B**	**C**	**D**
NADH	30 µM	✓	✓	✓	✓
Cytochrome *c*	1.5 µM	✓	✓	✓	✓
Membrane	40 ug/mL	✓	✓		
Piericidin A	5 µM	✓	✓	✓	✓
Amplex Red	10 µM	✓	✓	✓	✓
HRP	2 unit/mL	✓	✓	✓	✓
SOD	10 unit/mL	✓	✓	✓	✓
Catalase	5000 unit/mL		✓		✓

2.7 Determine the ratio of active/de-active state complex I by NEM

Complex I was deactivated in the membranes by incubating at 37°C for 30 minutes. N-ethylmaleimide (NEM) could modify cysteine-39 on ND3 subunit in de-actived status of complex I irreversibly. The reaction inhibited A/D transitions and catalysis of complex I (Galkin et al. 2008). The deactive complex I proportion can be measured by NADH oxidation with and without the NME treatment as described previously (Blaza et al., 2018). 200 mM NEM was prepared by dissolving in DMSO immediately before use. 50 µL of 2 mg/mL membrane was incubated with 0.5 µL 200 mM NEM on ice for 30 min. Then 10 µg/mL membrane was used to measure NADH oxidation. The active/deactive ratio was calculated by the catalytic rate of NADH oxidation without/with NEM treatment.

2.8 Election microscopy grids preparation

Election microscopy grids were prepared with different grids types and conditions. The grids types including continuous carbon coated copper grids, gold grids and graphene coated gold grids were used in the experiments. Plunge-freezing or negative staining was carried out after applying the sample on grids depends on different imaging requirements. For plunge-freezing, an FEI Vitrobot IV (Thermo Fisher scientific) was used with a humidity of 100% at 4°C. 2.5 µL solution was applied on one side of the grid. The other blotting parameters including blotting force, blotting time and waiting time varied according to the types of grids.

2.8.1 Thiol-PEG Ultrafoil Au grids

Gold grids are known to improve stabililty and image quality due to its preservation of tension during colling process and the high conductivity at cryogenic temperatures (Russo and Passmore, 2014). Thiol-PEG reagent coated UltrAuFoil® gold grids were prepared as described previously (Blaza et al., 2018). For cryo-EM imaging of complex I, the UltrAuFoil® gold grids with a hole size of 0.6 µm and space of 1 µm were selected (R0.6/1). The grids were washed with acetone a few times and air dried. Then the grids were plasma cleaned by glow discharging the surface at 20 mA for 60 sec under a low pressure (0.1 – 1 mbar) with a glow discharge

system (EMITECH). Within the 30 min of glow discharge, grids were transferred into an anaerobic glovebox (Belle technologies and incubated with 5 mM 11-mercaptoundecyl hexaethyleneglycol (SPT-0011P6, SensoPath Technologies) in ethanol for 48 hours. On the day of plunge-freezing, the grids were taken out immediately before use from the anaerobic glove box and washed with ethanol 3 times and air dried.

2.8.2 Graphene oxide grids

Graphene oxide (GO) grids were prepared as descried previously (Bokori-Brown et al., 2016) with a few alterations. In general, GO was diluted to 0.4 mg/mL with distilled water and used immediately. The GO suspension was then spun for 15 seconds at 300 rcf to remove aggregates. The suspension was sonicated for 10 sec to further avoid any aggregations. Quantifoil Cu 300 R1.2/1.3 grids were washed with acetone and air dried. Then the grids were glow discharged (with carbon side facing up) at 20 mA for 90 sec under a low pressure (0.1 – 1 mbar) with the EMITECH glow-discharger before applying GO. 2.5 to 3 µL of GO was applied on the carbon side of the grid and incubated for 1 minute before blotting with a Whatman No. 1 filter paper (Whatman). Then the grid was washed with a drop of 20 µL distilled water on the carbon side and blotted by the filter paper. This process was repeated three times with two washes on the carbon side and one on the other side. The grid was air dried for 5 min before applying the sample.

2.8.3 Polylysine treated grids

It is known that polylysine- treated girds are able to attach macromolecules for imaging under TEM (Williams, 1977). The preparation of polylysine coated grids was described previously (Guo & Jiang, 2015). The grid's hydrophilic surface was treated with a drop of 0.1% (w/v) polylysine solution (Sigma P8920) and this remained on the grid surface for 30 seconds before blotting off with a filter paper. The grids were air dried for 5 minutes before use.

2.9 Cryo-EM imaging

2.9.1 T12 cryo-imaging

An FEI Tecnai T12 (FEI Company) was operated at an accelerating voltage of 120 kV with a LaB6 filament. For negative stained grid samples, the room temperature sample holder was used; for cryo-grids, the cryo-sample holder was inserted. The cryo-sample holder needed to undergo a "zeolite cycle" on a dry pumping station at least for 2 hours before use. Images were acquired with the objective aperture size at 3 (150 µm) and a condenser aperture size at 3 (100 µm). A Gatan UltraScan 1000XP Model 994 CCD detector which has 2k x 2k sensor with 14 µm physical pixels was used to capture the images. The defocus range was at –2 to –5 µm. The images were acquired with an exposure of 8 to 10 seconds and a total dose of less than 100 electrons/Å^2. The grids were imaged at different nominal magnifications from 11,500 x to 42,000 x, depending on the requirements of the resolution. The images were saved in a tagged image file format (Tiff).

2.9.2 Talos Arctica cryo-EM screening and data collecting

A Talos Arctica 200kV cryo-electron microscope (Thermo Scientific) in department of biochemistry, University of Cambridge, was used mainly for an efficient screening of grid conditions as it has an automated loading cassette that can handle 12 samples in each loading. The falcon III detector in linear mode was used for this process. The nominal magnification was 73,000 x with a calibrated pixel size of 1.43 Å per pixel. A C2 aperture at the size of 70 µm and an objective aperture at the size of 100 µm were applied. The defocus was set to – 4 µm for screening and the total dose was about 50 electrons/Å^2. The grid conditions were evaluated based on the ice thickness, extent of contamination and particle distribution. Each grid was scored based on those conditions with a maximum score of 5 (good ice thickness gradient, no contaminations and 20 to 30 particles on each image) and minimum score of 0 (ice too thick or thin, heavy contaminations and too few or many particles on one image). The grids with the highest scores were selected for a further "deep screening" to check each promising grid squares to identify the best grid squares and holes for future data collection.

2.9.3 Titan Krios cryo-EM data collecting

Automated data collections on grids for the *ndufs4*$^{-/-}$ mouse complex I datasets were carried out with the help of Dr Alistair Siebert, Dr Yuriy Chaban at the electron Bio-Imaging Centre (eBIC), Diamond Light Source,Harwell Campus, Oxford, U.K. The data collections of ND6-P25L mouse complex I datasets were carried out with the help of Dr Dima Chirgadze at the department of Biochemistry, University of Cambridge, Cambridge, U.K. The datasets of wild type mouse complex I with optimized grids conditions was collected with the help of Dr James Blaza and Dr Dima Chirgadze in the Nanoscience centre and department of biochemistry, University of Cambridge, Cambridge, U.K.

The FEI Titan Krios cryo-electron microscope (Thermo scientific) was operated at an accelerating voltage of 300 kV. Datasets were collected with different detectors and modes. Both linear and counting-mode were used. Detectors including a Falcon III, Gatan K2 and Gatan K3 detector were chosen for different data sets. A GIF Quantum energy filter in zero-energy-loss mode with a slit width of 20 eV was used for specific modes. One exposure was made for each grid hole. The pixel size and dose varied depending on the sample conditions. The data collection parameters were set in the EPU software (Thermo Scientific) as shown in the Table 2.6 below. The micrographs were gain reference corrected and saved in MRC file format or Tiff format (for NDUFS4 heart data only).

Table 2.6 Data collection parameters

	ND6-P25L Heart 1st data set	**ND6-P25L Heart 2nd data set**	**NDUFS4 Kidney**	**NDUFS4 Heart**
Detector	K2 counting	K2 counting	Falcon III linear	K3 counting
Magnification	130,000	130,000	59,000	64,000
Pixel size (Å)	1.054	1.055	1.46	1.34
Electron exposure (e–/Å^2)	50.02	50.38	32.83	44.77
Exposure time (second)	10	10	1.5	5.4
Defocus range (μm)	-1.5 to -3.0	-1.8 to -3.0	-2.1 to -3.3	-1.5 to -2.9
Objective aperture (μm)	100	100	100	100
C2 aperture (μm)	50	50	50	50
Number of micrographs	1519	1749	4311	7310
Number of frames in each micrograph	40	25	59	25
Energy filter slit size (eV)	20	20	None	20

2.10 Cryo-EM data analysis

2.10.1 Computation and software

The software used for image processing including RELION (Scheres, 2012) and cryoSPARC (Punjani, Rubinstein, Fleet & Brubaker, 2017) required a high-performance computational environment on a Linux HPC (high-performance computing) cluster. The cluster was the compression of several 16-core Intel Xeon CPUs (central processing unit) with a 256 GB RAM (random access memory). For GPU (graphical processing unit) acceleration, an 8-core Intel Xeon CPUs, 256 Gb RAM and 4 NVIDIA GTX-1080 GPU co-processors were employed with an MPI (message passing interface) and CUDA (Compute Unified Device Architecture)-7.5 installed.

2.10.2 Image processing with RELION

The output of the raw data from EPU contained jpg format images of each micrograph. These images were firstly inspected manually and the micrographs with obvious contaminations or suspicious background were removed before any further processing. Then the micrographs were imported into RELION as a movie format. The workflow used is illustrated in Figure 2.1 below. To minimize beam-induced movement between frames in each micrograph, Motioncor2.0 (Zheng et al., 2017), a software to correct movement and align frames by cross-correlation, was used via RELION with 5 x 5 non-overlapping patches in both dose weighted mode and non-dose weighted mode. Then the defocus and aberration of each micrograph was estimated and corrected by the fitness to the contrast transfer function (CTF). A GPU-accelerated computer program, Gctf (Zhang, 2016), was used for CTF determination. After that, particles from each micrograph were picked with “autopicking” option in RELION and the selected particles were extracted with a box size of 450. A reference-free 2D classification job with 50 to 100 output classes was able to produce 2D classes with different orientations of complex I and non-complex I classes. The 2D classes with different orientations of complex I were selected for further 3D classification. Then a 3D classification job was set to produce 4 to 6 3D classes with a low pass filtered 3D reference. The 3D classes were evaluated and the

particles in each class were used for 3D-auto refinement. 3D auto refinement jobs were performed with a mask applied to remove the noise around the protein. Then a per-particle CTF refinement job was performed to further refine CTF parameters and correct bam tilt in for each particle. Then particle polishing was used to correct radiation damage and residual motion on each particle. The final 3D auto refinement was performed on polished particles with a soft mask generated by RELION "mask create" function. The post process step was performed with a tight mask and the two independent half datasets were compared to estimate the final resolution by the gold-standard Fourier shell correlation (FSC) curves (Henderson et al., 2012).

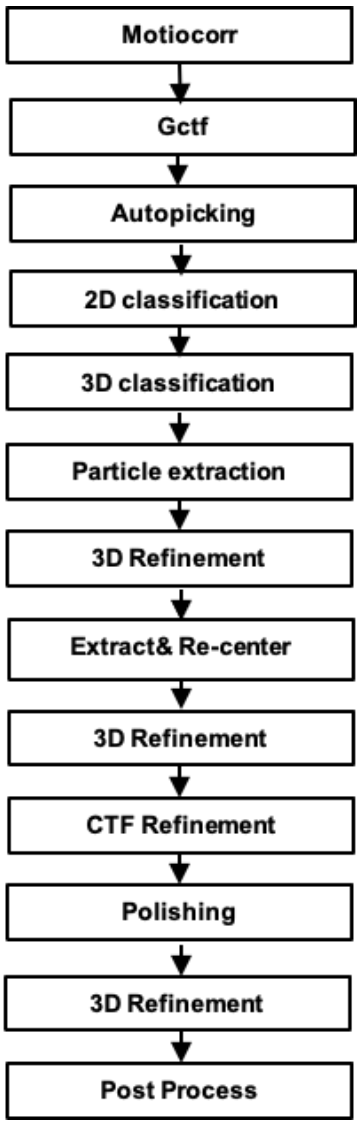

Figure 2.1 Cryo-EM data processing workflow. All the steps from motion correction by Motioncorr to Post process were carried out in RELION if not otherwise specified.

2.10.3 Model building

The ND6-P25L and deactive mouse complex I model building were performed in Coot version 0.8.9.2 and 0.9-pre (Emsley, Lohkamp, Scott & Cowtan, 2010), ISOLDE (Croll, 2017), PHENIX (Afonine et al., 2018) and Chimera 1.13 (Pettersen et al., 2004). An updated active mouse complex I model (PDB: 6ZR2) was initially used as a template to build deactive mouse complex I model. Each subunit of the active complex I model was fitted into the deactive complex I map separately in Chimera to give a coarse fitting. Then the coarse fitted model was manually refined in Coot by the real space refine function. To better fit the model into the map, ISOLDE was used to perform a real-time molecular-dynamics flexible fitting with given ligand and ion cluster restrains. Then the model was then further evaluated by real-spaced refinement in PHENIX to optimize geometry. The automatic evaluation results of the refinement were then used to guide the manually correction in Coot. A re-refinement in PHENIX was conducted with the manually corrected model in Coot. The final model was deposited into RCSB PDB (PDB: 7AK5).

The model building for ND6-P25L-CI was similar to deactive complex I. The newly built deactive complex I model was used as the template to generate ND6-P25L-CI model. Firstly, each subunit of the template model was fitted into the map separately in Chimera to give a coarse fitting. Then the model was manually refined in Coot. The model after manual refinement in Coot was then further evaluated by real-spaced refinement in PHENIX to optimize geometry with restrains. The final model was generated by a few rounds of manual and automatic refinement (PDB: 7AK6).

The NDUFS4 model building was carried out in Coot 0.9-pre. The active (PDB:6G2J) and deactive (PDB:6G72) complex I models were fitted into the density map of the NDUFS4 lacking complex I. Then the active complex I model (PDB:6G2J) was used to manually coarse fit the model to the density map in Coot by the real space refine function.

Chapter 3. Molecular characterization of complex I from ND6-P25L mouse model

3.1 Introduction

3.1.1 The structure and function of the ND6 subunit

The ND6 subunit of complex I is one of the mtDNA encoded transmembrane subunits (Fig 3.1A). This subunit is located close to the hydrophilic domain and the proposed quinone binding site (Efremov et al., 2010). ND6 is one of the 14 core subunits of complex I and contains 5 transmembrane helixes (TMH 1-5) which share common general features between bacteria, yeast, and mammals (Baradaran et al., 2013, Vinothkumar et al., 2014; Zickermann et al., 2015). There are notable structural differences between yeast and mammalian ND6. For example, the relative position of TMH4 (in Fig 3.1B) in ND6 is closer to the other TMHs in mouse complex I than in the yeast and bacterial homologues. Besides this, TMH3 in the ND6 subunit of mammalian complex I is identified in a full α-helical conformation in the active state, whereas the deactive state features a characteristic π-bulge. (Fig 3.1C). The function of ND6 has been discussed in many studies. ND6 has been proposed to play a role in the mechanism of inter-connection between proton pumping and electron transfer (Kao et al., 2005; Pätsi et al., 2008; Gonzalez-Halphen et al., 2011). Subsequent structural studies have suggested that the ND6, together with ND1 and ND4L, may form a fourth proton-pumping channel (Efremov& Sazanov, 2011; Berrisford, Baradaran, & Sazanov, 2016) in accordance with the current consensus stoichiometry of four protons pumped per NADH oxidised (Jones et al., 2017).

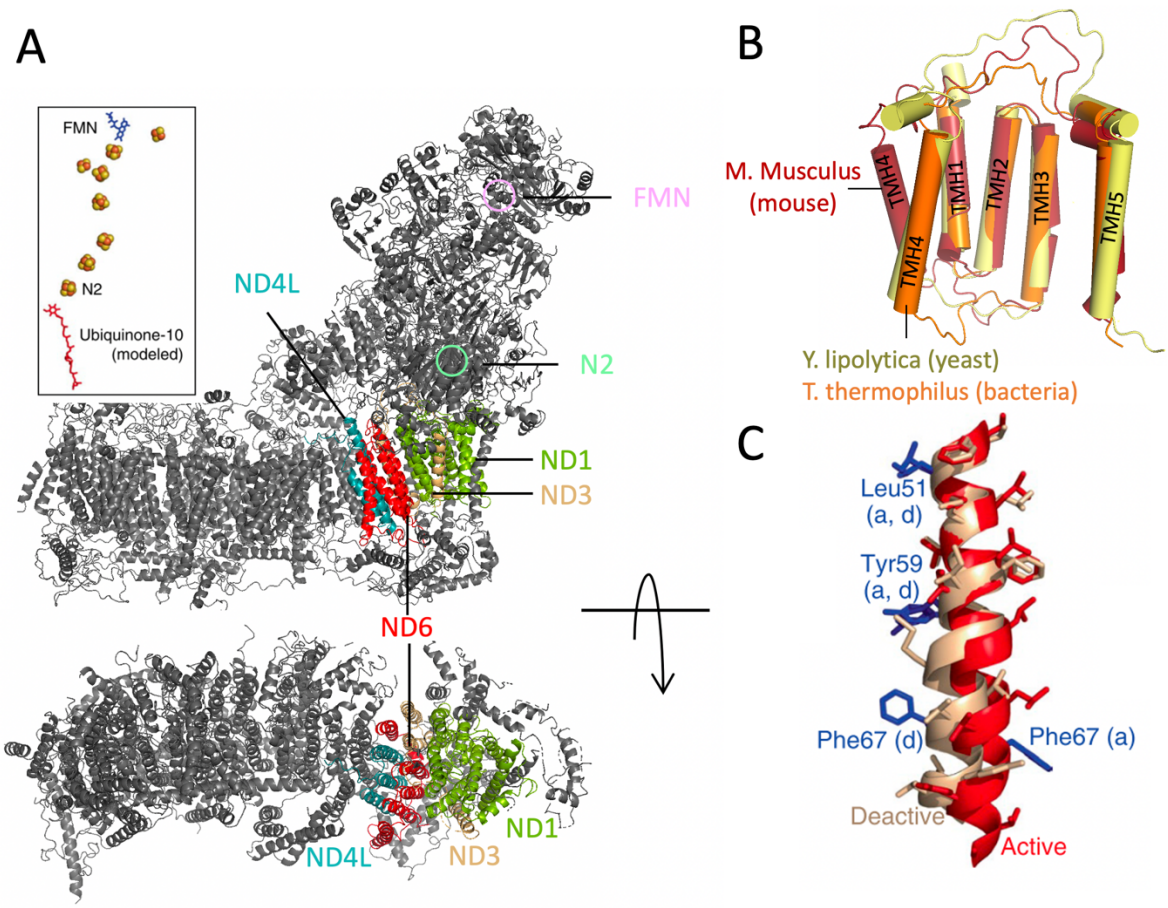

Fig 3.1 Structure and location of the ND6 subunit in complex I. (A) ND6 (in red) is in the transmembrane domain of complex I, surrounded by ND1 (green), ND3 (wheat) and ND4L (blue). The location of the adjacent iron-sulfur cluster (N2) is indicated in bright green. The flavin site is highlighted in pink. This image was modified from Agip et al. (2018). (B) The aligned structure of the ND6 subunit in different species. TMH4 is located in a different position in mouse compared to the yeast and bacteria. The alignment was generated using the mouse active model (red, PDB: 6G2J), yeast complex I model (yellow, PDB: 6YJ4) and bacterial complex I model (orange, PDB: 4HEA). (C) The π-bulge present in TMH3 of deactive mouse complex I (wheat) compared with active mouse complex I (red). The Phe67 (in dark blue) is shown in two distinct locations in active and deactive mammalian complex I. This image is adapted from Agip et al. (2018).

3.1.2 Disease associated with point mutations on ND6 subunit

ND6 has several highly conserved sequences among mammalian species (Fig 3.2A) and point mutations that occur in such areas of ND6 are always identified as pathological (Chinnery et al., 2001). There are currently 13 pathogenic variants identified within the ND6 subunit, the locations of which are highlighted in Fig 3.2B (Chinnery et al., 2001; Fiedorczuk & Sazanov, 2018; Du et al., 2020). The mutations in the ND6 subunit described have been reported to lead to severe neuromuscular diseases including LHON syndrome and Leigh syndrome (Jun, Brown & Wallace, 1994; Chinnery et al., 2001). LHON syndrome, which affects 1 in 25,000 of the

British population, is an acute central vision loss occurring mainly in young male adults initially with one eye onset followed by the second within a short period (Man, Turnbull & Chinnery, 2002). Leigh syndrome is a severe neurological degeneration disorder usually onset in the patient's early childhood with the progressive inability of movement and stunting of growth (Baertling et al., 2014).

It remains unclear why the optic nerve is prone to be affected by the pathogenic variants in ND6 in humans. In addition to ND6, ND1 and ND4 are also hot spots for LHON associated pathogenic variants (Howell et al., 1991; Wallace et al., 1988). The LHON with pathogenic variants on ND6, ND1 and ND4 has been suggested that a higher number of mitochondria are observed in the unmyelinated, intraocular part of the axon (Gueven, 2014). The energy deficiency caused by complex I dysfunction, chronic oxidative stress, and a susceptibility to apoptosis could potentially damage this part of the axon and result in retinal ganglion cells (RGC) apoptosis (Gueven, 2014). However, current observations do not explain the strong sex bias of the LHON (Man et al., 2002). This suggests that secondary factors which modulate the phenotypic expression could exist; however, such secondary effects are not yet understood. A better understanding of the relationship between mtDNA mutations and optic nerve dysfunctions is therefore required in future studies to establish the role of ND6 mutations in LHON.

The pathogenic variants in ND6 are mainly presented at positions in the second and third transmembrane helices (Fig 3.2B). The *m.13997G>A MT-ND6* pathogenic variant was first identified in a young patient with Leigh syndrome and severe sensory-neural deafness (Malfatti et al., 2007). This mutation is located in the connection loop between TMH1 and TMH2 (Fig 3.2B). Sequence analysis of the mtDNA showed that the patient has a homoplasmic mutation in muscle and fibroblasts (Malfatti et al., 2007). It was documented that the patient presented with developmental delay, muscle hypotonia, and ocular apraxia from the first month of life. At four months old, cerebral atrophy and symmetric signal changes in basal nuclei were observed by an MRI study. At seven months old, the patient had an acute episode of metabolic failure and the patient was deceased by eight months old (Malfatti et al., 2007). Muscle and

fibroblasts samples from the patient all showed low complex I activity with normal function of other OXPHOS complexes (Malfatti et al., 2007). The NBT-sensitive in-gel activity assay on BN-PAGE showed nearly no complex I activity from the patient's samples (Malfatti et al., 2007).

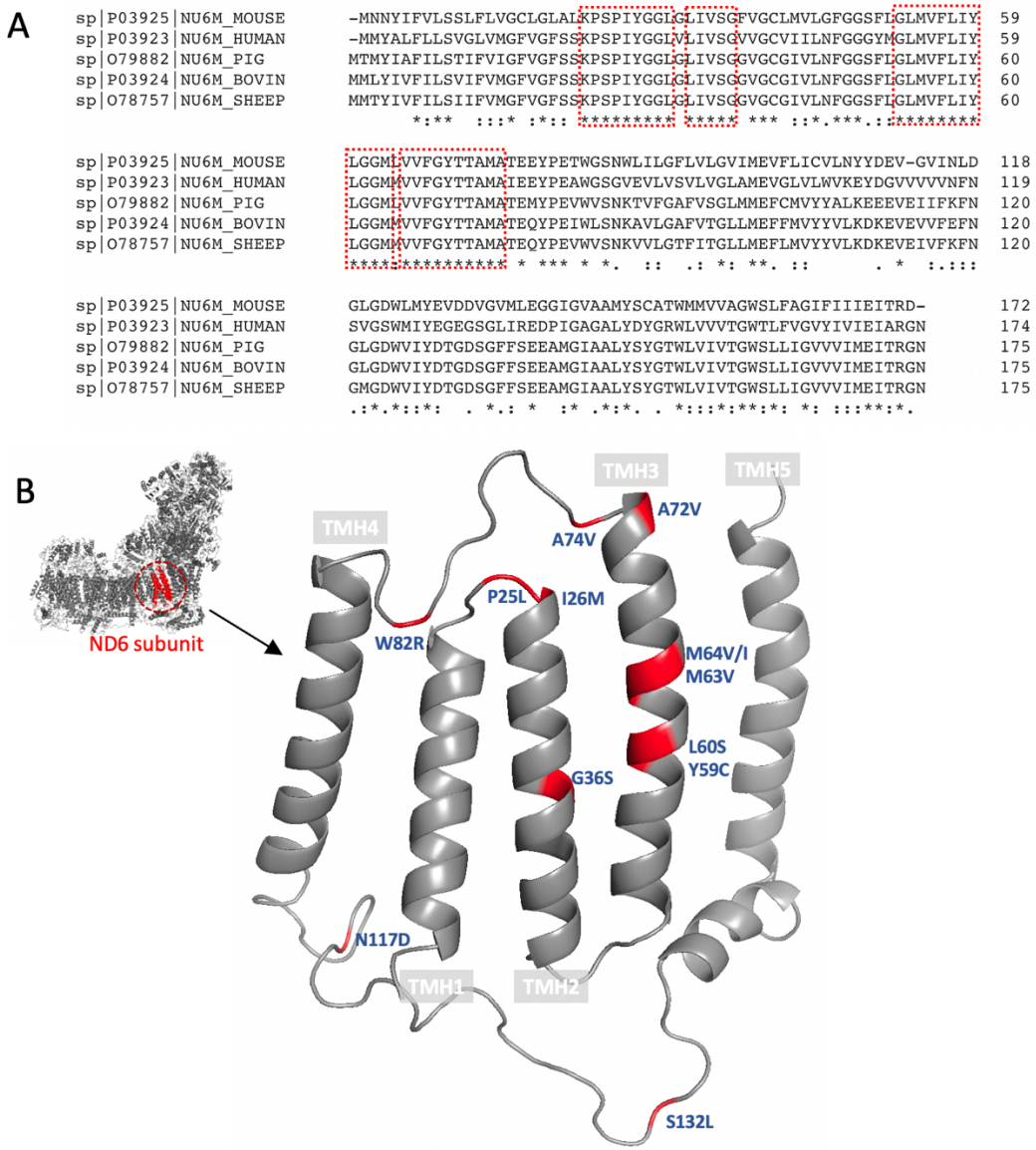

Fig 3.2 Point mutations in the ND6 subunit. (A) Multiple sequence alignment performed using Clustal-Omega (1.2.4) (Sievers, 2011). Red squares show sequences with more than three continuous conserved amino acids. Asterisks (*) indicate positions with fully conserved residue. Colons (:) indicate strongly similar properties between groups. Periods (.) indicate weakly similar properties between groups. (B) The 13 reported clinically relevant point mutations in ND6 (Fiedorczuk & Sazanov, 2018). The model was generated from the active mouse complex I model (PDB: 6G2J). Single amino acid substitution positions on the ND6 subunit are labelled in red.

3.1.3 The mouse model with the ND6-P25L point mutation

In order to investigate the pathogenesis associated with ND6 subunit point mutations, a mouse model of ND6-P25L was generated and reported with optic atrophy that could be used as a model phenotype of LHON syndrome in humans (Lin et al., 2012). The ND6-P25L mice showed an age-related loss of small caliber optic nerve fibers and axonal swelling in RGCs but no loss of visual response (Lin et al., 2012). At the cell level, abnormal mitochondrial morphology was identified in RGC axons (Lin et al., 2012). At the molecular level, the complex I from ND6-P25L mouse liver displayed a decrease in NADH:ubiquinone oxidoreductase activity in liver or synaptosomes concomitant with an increase in ROS production during forward electron transfer. Interestingly, an increase in reverse electron transfer associated ROS production was not detected (Lin et al., 2012). It was suggested that chronic oxidative damage could be the cause of LHON syndrome in this mouse model (Lin et al., 2012). A further study on ND6-P25L mouse showed that the ND6-P25L mouse has a unique stress-response signature: a 30-minute psychosocial stressor exposure could induce a global "diabetes-like" hyperglycemia. Additionally, an inflammatory response was identified in ND6-P25L mouse hippocampus with a high concentration of the inflammation marker Interleukin 6 (IL-6) present (Picard et al., 2015).

In a further study, the ND6-P25L mouse was combined with a nuclear DNA mutation (ANT1 KO) (McManus et al., 2019). ANT1 is an adenine nucleotide translocator that exports ATP across the IMM into the cytoplasm (Picard et al., 2015). ANT1 deficiency causes myopathy and cardiomyopathy, and the severity is considered to be relevant to the mtDNA lineage (Strauss et al., 2013). The ANT1 KO/ND6-P25L combined mouse showns an increased severity of cardiomyopathy and shorten lifespan compared to the ANT1 KO alone (McManus et al., 2019). Another interesting observation is that the ND6-P25L mouse was prone to develop lymphomas in C57BL/6 (B6) mice background while not in C57BL/6(A/J) gene background (Hashizume et al., 2015). These results suggest that nuclear DNA-mitochondrial DNA interactions could possibly modulate the severity and the onset of the phenotypes as well.

Collectively, the ND6-P25L mouse model has demonstrated several clinically relevant phenotypes. It was believed that the ND6-P25L mouse has shown chronic oxidative damage to organs (Lin et al., 2012). The severity and presentation of the phenotypes in ND6-P25L mouse could be dependent on environmental factors (such as stress) or nuclear DNA background (Picard et al., 2015; McManus et al., 2019).

3.1.4 Aims

The aim of this chapter was to investigate the structural and functional basis of complex I in the disease-presenting ND6-P25L mouse model by using cryo-EM single-particle analysis and various of biochemical assessments to assess the complex I activity, ROS production as well as active/deactive state transition.

3.2 Tissue collection and molecular characterisation of complex I

3.2.1 Mice breeding and colony managing

The ND6-P25L female mice (*m.13997G>A MT-ND6*) with a genetic background of C57BL/6J was kindly provided by Professor Douglas Wallace (University of Pennsylvania). The ND6-P25L mice were set up to breed following a standard procedure with a breeding lifespan of 30 to 40 weeks. One 8-week-old wild type (WT) male mouse with the same genetic background of C57BL/6J was accommodated with one or two female ND6-P25L mice at the age of 8 to 11 weeks old. As shown in Table 3.1, this strain has a weak breeding performance with a smaller litter size and fewer litters during the reproductive life span compared to WT mice. The average litter size of the ND6 strain is 3.4 ± 0.3 offspring compared to 4.9 in the WT. The average number of litters each ND6 female mouse can deliver during their reproductive life span is 2.7± 0.3, which is less than the WT mouse (5.4 litters).

Table 3.1 Breeding performance comparison between WT and ND6-P25L strain

Strain	Mean litter size	Mean number of litters
WT *	4.9	5.4
ND6-P25L **	3.4 ± 0.3	2.7 ± 0.3

* Data adapted from Lambert (2007) from 50 pair-mated females

**Data from 13 pair-mated females, data are mean values ± S.E.M (n= 13)

The mice body weight was recorded over time with the results shown in Fig 3.3. The female mice from 5 weeks old to 12 weeks old were monitored, and the male mice were monitored until 24 weeks old. No obvious difference in the body weight between the ND6-P25L and WT mice was observed. However, the reproductive capacity and litter size of the ND6-P25L mice are significantly smaller than the WT mice. This data suggests that the mutation is possibly influencing the breeding performance of this mouse strain.

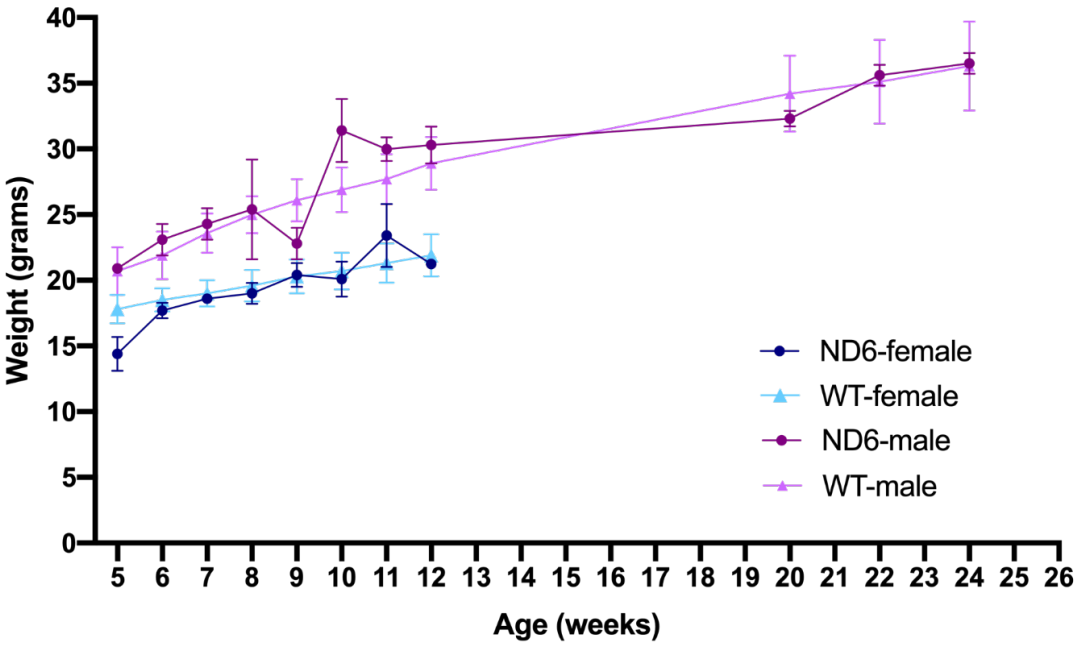

Fig 3.3 Growth rate of ND6-P25L mice compared with WT mice. The bodyweight of ND6-P25L female mice was recorded from week 5 to 12; the bodyweight of ND6-P25L male mice was recorded from week 5 to 24. The data of ND6-P25L mouse shows the mean values with standard deviation (SD), n = 3-7. The mean values and SD of WT mouse body weight were obtained from the Jackson laboratory (Bodyweight information for C57BL/6J (000664), 2020), n = 360.

3.2.2 Tissue collection and membrane preparation

The ND6-P25L and WT mice at ages between 8 to 22 weeks old were sacrificed by cervical dislocation. To ensure freshness of the sample, the tissue collected from the mice was immediately immersed in cold homogenization medium and transferred from the animal facility to the lab on ice within 30 min. A detailed sample preparation method is described in Chapter 2.2.2. Tissue weight was recorded before homogenisation for mitochondria isolation (Table 3.2). The mitochondria were extracted from the heart, brain, and kidney tissue according to the established protocol (Fernández-Vizarra et al., 2010). The tissue weight measured from the ND6-P25L and age-matched WT mice shows no significant difference. Furthermore, the mitochondrial weight per mouse from ND6-P25L mice was similar to WT. These results indicate that the mutation has a minor influence on organ growth and mitochondrial production.

Table 3.2 Tissue and protein yield efficiency of different organs

Tissue type		Tissue weight per mouse (g) *	Mitochondrial protein weight per mouse (mg)*
Heart	**WT**	0.17±0.01	1.05±0.05
	ND6-P25L	0.19±0.03	0.93±0.24
Brain	**WT**	0.54±0.03	4.25±1.45
	ND6-P25L	0.65±0.07	4.53±1.28
Kidney	**WT**	0.40±0.08	7.44±0.34
	ND6-P25L	0.55±0.05	6.10±0.68

*Data are mean ± SEM (n= 4-7, from 4 to 7 mitochondrial preparations, each preparation comprising four to five mice).

Mitochondria isolated from the heart, brain and kidney were broken down by sonication. The mitochondrial membrane and matrix were then separated by centrifugation (detailed methods are shown in Chapter 2.3.2). About 30 μg of isolated membrane from ND6-P25L and WT mice heart were solubilised and loaded onto the BN-PAGE, then stained with Coomassie blue as shown in Fig 3.4A. The staining intensity was measured by plot profiles in ImageJ and is shown in Fig 3.4B as an indication of protein abundance. The two plots showed a remarkable similarity in both pattern and intensity; therefore, no obvious difference in size and amount of complex I in heart mitochondria membranes was identified between the ND6-P25L and the WT mice. And the five protein complexes of OXPHOS system are all identifiable in both the ND6-P25L and the WT with no significant difference identified

The in-gel NBT staining performed on solubilised membrane from heart, brain, kidney and liver is shown in Fig 3.4C. To further investigate the integrity of the mutant complex I from ND6-P25L (ND6-P25L-CI), a 2D SDS-PAGE with the complex I band cut from previous BN-PAGE was obtained. As shown in Fig 3.4D, the bands in the 2D SDS-PAGE showa similar pattern observed between the ND6-P25L and the WT.

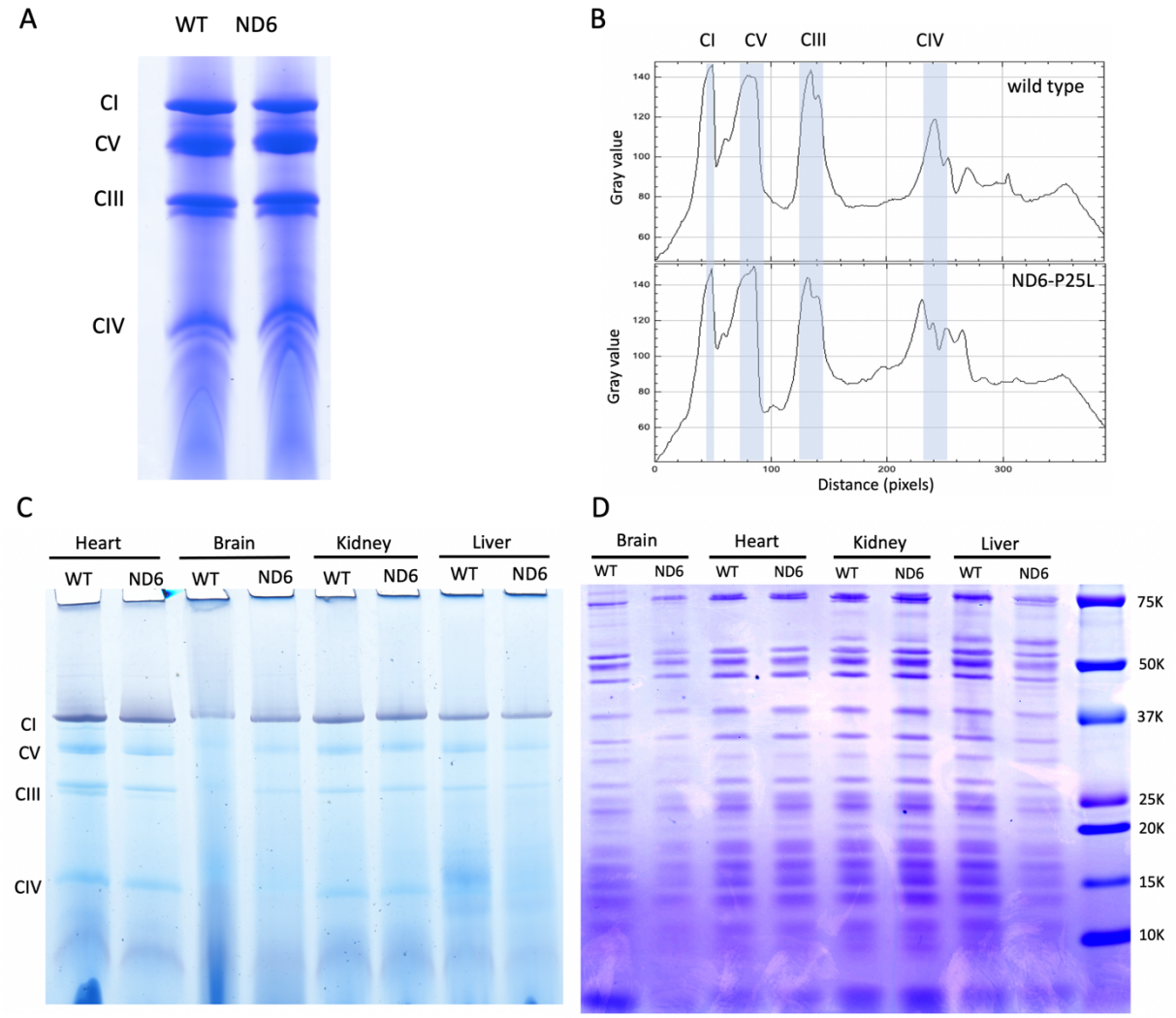

Fig 3.4 ND6-P25L and WT mitochondrial membrane protein analysis on BN-PAGE and 2D SDS-PAGE. (A) Coomassie blue stain of heart mitochondrial membrane protein on BN-PAGE. (B) The plot profile of the gel image from (A) obtained using ImageJ. Peaks in the plots correspond to the bands on the BN-PAGE, showing their relative intensities. (C) In-gel NADH oxidation activity assays with NBT on BN-PAGE (kidney, heart, liver, brain). (D) Coomassie blue staining on 2D SDS-PAGE of complex I band excised from the BN-PAGE.

3.2.3 Catalytic activity and protein integrity of ND6-P25L-CI

After the heart mitochondrial membranes were collected, the catalytic activity of complex I from WT and ND6-P25L was measured (detailed methods are given in chapter 2.6). Specifically, the rate of NADH oxidation through complex I, III, and IV has been measured by the NADH:O_2 assay on alamethicin pre-treated membranes (Fig 3.5A). Alamethicin is a channel-forming reagent used to permeabilise the mitochondrial membrane, allowing substrates to cross the membrane so that the measured complex I activity is not limited by the membrane permeability (Gostimskaya, Grivennikova, Zharova, Bakeeva & Vinogradov, 2002). The rate

of NADH oxidation in ND6-P25L mitochondrial membranes is 79.2 ± 2.5% of the WT, indicating a loss of complex I activity in the ND6-P25L mutant. To further investigate whether the loss of membrane activity is due to a decreased enzyme expression or an intrinsic effect from the mutation, the NADH:$APAD^+$ assay (Fig 3.5B), was performed as an indicator of the complex I content on the membranes. The NADH:$APAD^+$ transhydrogenation reaction, which measures the flavin site oxidation of complex I (Birrell, Yakovlev & Hirst, 2009), showed the reaction rate in ND6-P25L mutant was 82.3 ± 1.8% of that in the WT, indicating a lower complex I content in the ND6-P25L membranes. Thus, the normalised NADH oxidation activity of individual complex I between ND6-P25L and WT is similar, and the lower complex I activity in ND6-P25L is due to the lower content of complex I on the membranes. This is also reflected in the NADH-induced H_2O_2 production in the membranes (Fig 3.5C), which shows that the ND6-P25L-CI has a 21.0 ± 1.9% lower rate of H_2O_2 production to the WT complex I (WT-CI), which can also be attributed to the lower complex I content in the ND6-P25L membranes.

The rate of succinate oxidation (Fig 3.5D) through complex II, III, and IV was also measured on alamethicin treated mitochondrial membranes. There was no significant difference in succinate:O_2 activity between WT and ND6-P25L, which indicates that the mutation does not affect the succinate oxidation pathway through complex II, III, and IV, confirming that the decreased NADH:O_2 activity is a complex I-specific effect. As this ND6-P25L mutation was suggested to disturb ubiquinone binding capacity in *E. coli* (Kao et al., 2008), the quinone analogue piericidin A was used to identify if there are any alterations influencing Q-site binding capacity due to the mutation. Fig 3.5E and F show piericidin A binding to complex I was not affected in the ND6-P25L mutant with similar IC_{50} values observed in both the mutant and the WT membranes. Therefore, the binding capacity to piericidin A was not changed in ND6-P25L-CI and the Q-site in considered to be fully formed and active for ubiquinone reduction.

In summary, the individual ND6-P25L-CI has shown a normal catalytic capacity and no influence on the succinate oxidation pathway. The lower complex I activity and NADH-induced H_2O_2 production rate in ND6-P25L was due to a decrease in the complex I content in the heart

mitochondrial membranes rather than an intrinsic effect on the enzyme activity itself. The similar IC_{50} values of piericidin A between ND6-P25L and WT further suggested a similar Q-tunnel conformation when binding inhibitors.

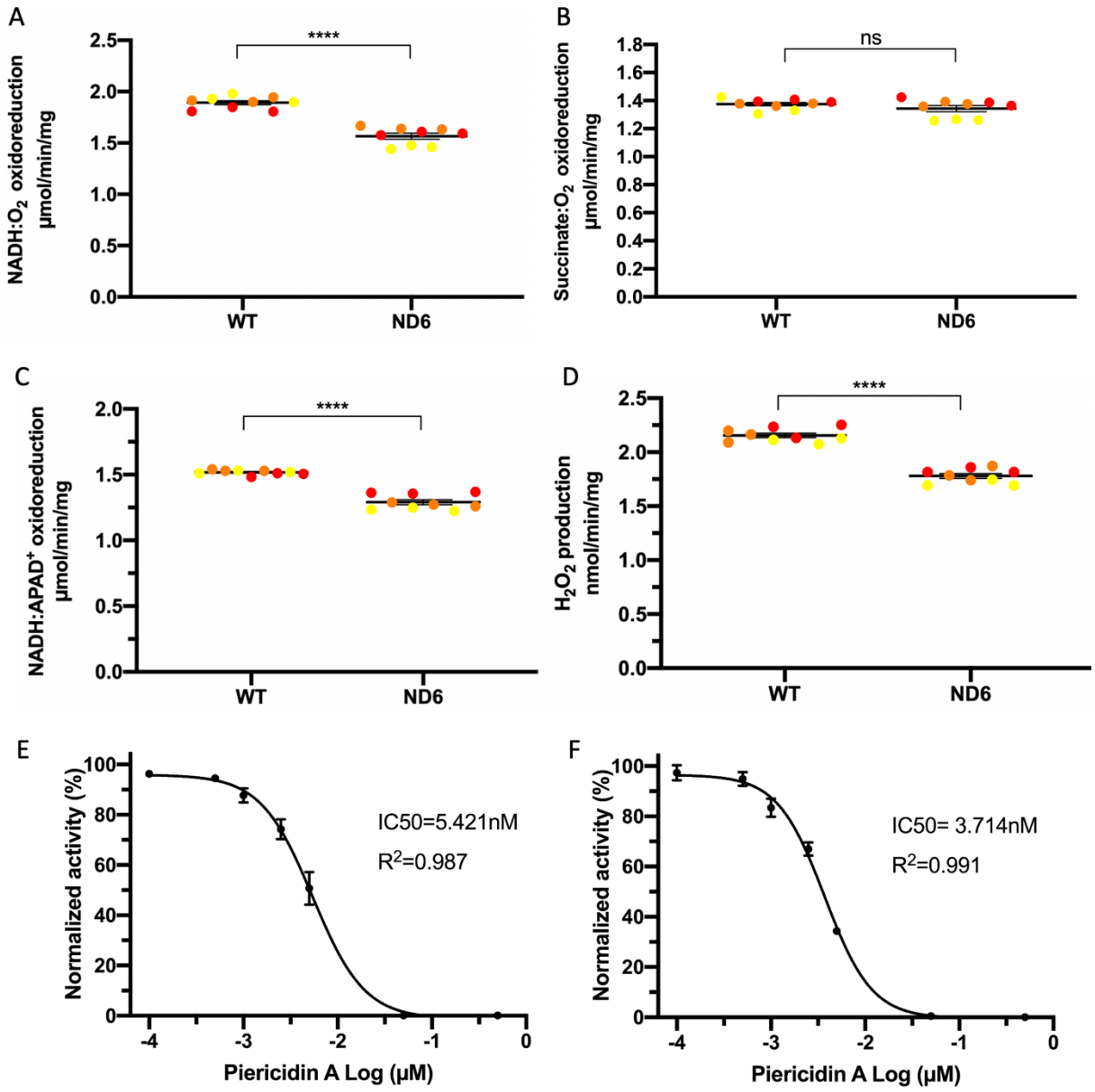

Fig 3.5 Catalytic activity of ND6-P25L-CI and WT-CI in mitochondrial membranes. (A) The rate of inhibitor-sensitive NADH oxidation through complex I, III and IV. (B) The rate of inhibitor-sensitive succinate oxidation through complex II, III and IV. (C) NADH induced H_2O_2 production rate. (D) The NADH:$APAD^+$ oxidoreduction rate. All data are mean ± SEM (n = 3, the three different colour dots represent three independent membrane preparations) with Student's-test (**** $p < 0.0001$). (E) & (F) NADH:O_2 IC_{50} of piericidin A on complex I in WT (E) and ND6-P25L (F) heart mitochondrial membranes. The data are mean ± SEM (n = 3, three technical replicates).

3.3 ND6-P25L-CI structure reconstruction by cryo-EM

3.3.1 Purification of Complex I

A two-step chromatographic purification strategy was performed to purify complex I from mouse heart mitochondrial membranes as described previously (Sharpley, Shannon, Draghi & Hirst, 2006; Agip et al., 2018). During this process, 17 to 20 mg of ND6-P25L heart mitochondrial membranes were used for purification. The complex I containing fractions were eluted at peak 2 in 350 mM NaCl (Fig 3.6A).

As shown in Fig 3.6B, complex I was eluted at a volume of around 1.6 mL (peak 1), and the separated complex IV peak appeared at 1.8 mL (peak 2) after the elution of complex I. The complex I peak fractions were collected at a concentration of 3.5 mg/mL. The activity of isolated complex I was assessed by NADH:decylubiquinone oxidoreduction assay. The catalytic activity of the ND6-P25L-CI was 7.83 ± 0.44 (n = 3) μmol min^{-1} mg^{-1}. Interestingly, the NADH:decylubiquinone oxidoreduction in ND6-P25L-CI is lower than the reported activity of purified WT-CI (10 to 12 μmol min^{-1} mg^{-1}) by Agip et al. (2018). The low activity of ND6-P25L-CI could possible due to its instability after removing the phospholipid environment during detergent solubilisation.

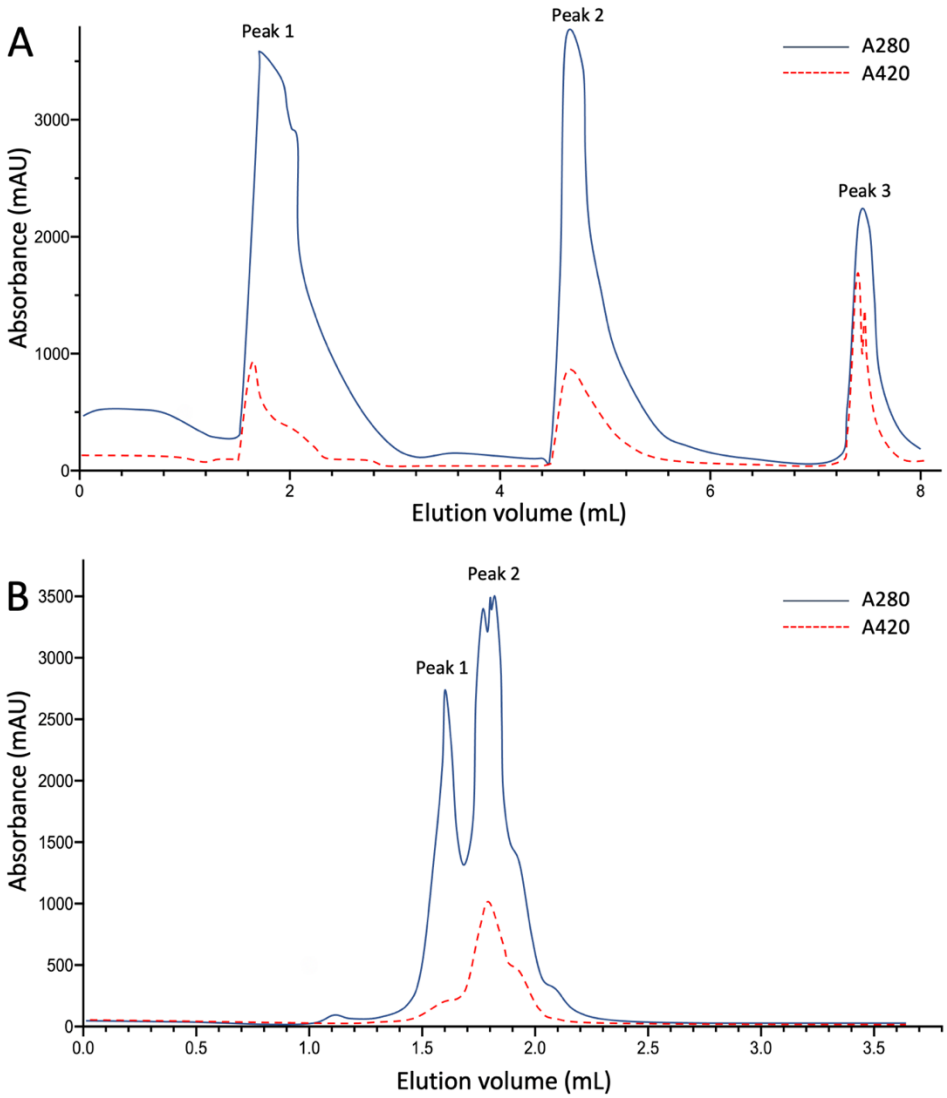

Fig 3.6 ND6-P25L heart mitochondrial membrane elution profiles. (A) The chromatography plot from the anion-exchange column. Solubilised membrane was separated and OXPHOS complexes were eluted into peaks. Peak 2 contains ND6-P25L-CI. The fractions around peak 2 were collected and concentrated for the following size-exclusion purification. The absorbance was measured at 280 nm (blue line) and 420 nm (red line). (B) The chromatography plot from the size exclusion column. The concentrated elution fraction was injected onto the size-exclusion column. The fractions at peak 1 were purified complex I which were collected for cryo-EM studies. The concentration of the fractions was measured by BCA assay and the catalytic activity of ND6-P25L complex I was measured by NADH:decylubiquinone oxidoreduction assay.

3.3.2 Cryo-EM grids freezing

The freshly purified complex I was applied onto the cryo-EM grids immediately. The procedure for this was described in Chapter 2.8.1. In brief, a volume of 2.5 µL ND6-P25L-CI (~3.5 mg/mL) was applied to PEGylated UltrauFoil R0.6/1 gold grids, with a total of 14 grids prepared. The ND6-P25L-CI droplet remained on the surface of the grid in the Vitrobot chamber for 10 sec before blotting away. During the 10 sec waiting time, a flattening of droplets on the surface of

the grids was observed, and in some grids, the suspension penetrated to the other side of the grid within the 10 second blotting time. This observation of flattening (shown in Fig 3.7B) indicated a successful PEGylation of the gold-grid surface as the PEGylation created a hydrophilic surface. In the preparation session, all 14 PEGylated grids showed the flattening of the droplet on the grid surface. The grids were then plunge-frozen by the Vitrobot, within which two grids were applied with the elution buffer without complex I as a control. The blotting time was set in the range of 9 to 10 sec, and the blotting force was controlled between -8 to -10. These different parameters were applied to screen out the best condition for this sample. After plunge freezing by the Vitrobot, the grids were manually mounted with clip rings for the autoloading cartridge in Talos Arctica electron microscopy for screening.

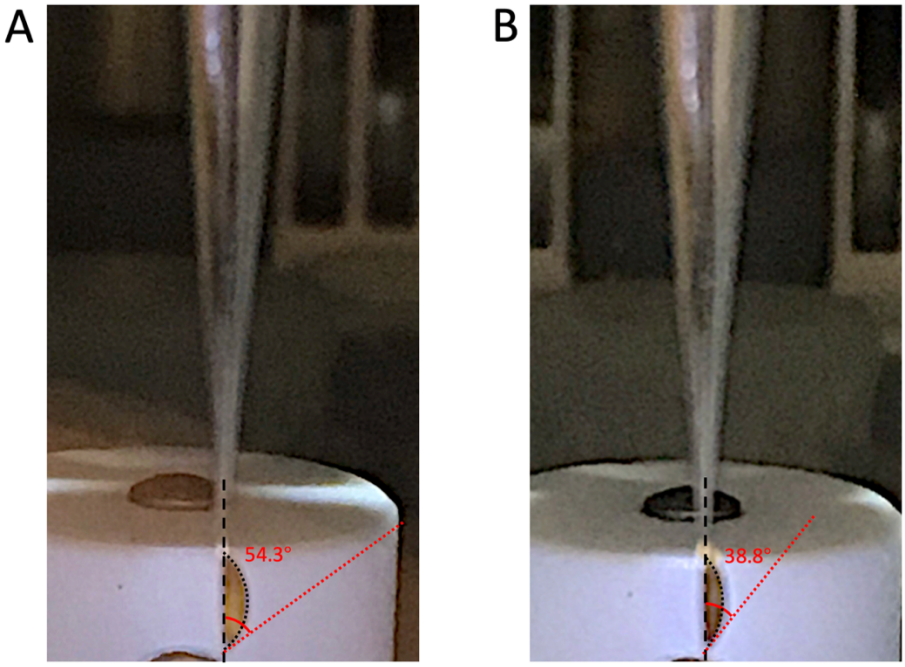

Fig 3.7 The flattening of the sample droplet on a PEGylated gold grid. (A) 2.5 µL of complex I elution sample was applied on PEGylated gold-grid in the control chamber of the Vitrobot. The contact angle was measured as shown in red. (B) 10 sec after applying the sample droplet onto the PEGylated gold-grid. The contact angle was smaller as the droplet became flattened.

3.3.3 Cryo-EM grids screening and automated data collection

The cryo-grids were loaded onto the Talos Arctica electron microscopy in the Department of Biochemistry, University of Cambridge to screen the grids with the best conditions for data collection. The ice thickness, ice contaminations and particle distribution were all evaluated.

Fig 3.8 represents some micrographs collected during the grid screening session. Fig 3.8A shows an atlas taken by EPU software at low magnification. This atlas image shows the different size of grid squares as an indication of ice thickness gradient (Rice et al., 2018). As shown in Fig 3.8A, the grid square size increased from left to right, illustrating the change in ice thickness from thick to thin.

Fig 3.8B represents a good quality micrograph with a sufficient number of complex I particles without obvious aggregation. The red circles mark out some of the different orientations of complex I particles captured in this micrograph. Fig 3.8C and D are all unfavourable grids observed during screening. Fig 3.8C shows very few particles in this grid, while Fig 3.8D shows that the grid has a crystalline ice background caused by unsuccessful vitrification. These grids were removed during the screening session.

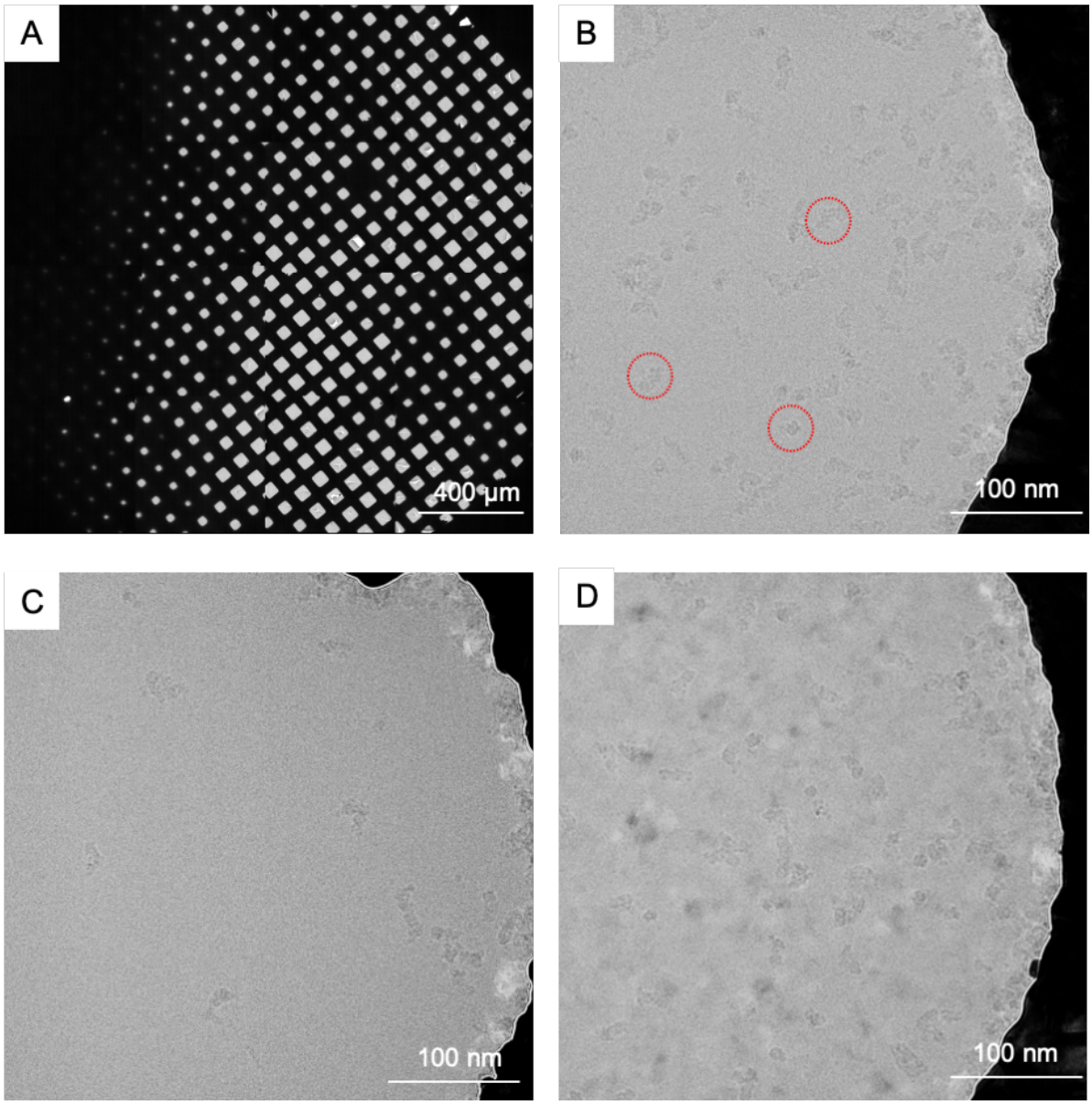

Fig 3.8 Representative cryo-EM images for grid screening. (A) An atlas of the grid taken at low magnification shows an ice gradient across the grid from left to right. (B) A micrograph showing optimal complex I distribution on the frozen grid. The red circles mark out different orientations of complex I on the grid. (C) A micrograph taken from a grid with thinner ice shows a decrease in particle number. (D) The micrograph of the crystalline ice indicates the bad vitrification of the grid.

Finally, the cryo-EM data was collected on the best grid selected using a FEI 300 kV Titan Krios microscope in the Department of Biochemistry, University of Cambridge. Two datasets were collected on the same microscope with similar setups. The repeated data set (2^{nd} data set) was collected for the purpose of increasing the particle numbers. As shown in Table 3.3, the micrographs were collected in electron counting mode with Gatan K2 summit direct detection camera and a GIF Quantum energy filter (slit width of 20 eV). The magnification for data collection was 130,000x with a calibrated pixel size of 1.054 Å/pixel (1.055 Å/pixel for the 2nd

dataset). The exposure time was set to 10 sec which gives an overall dose of around 50 e^- /Å^2. The electrons were captured into 40 (1st dataset) or 25 frames (2nd dataset). The C2 aperture and the objective aperture were set at 50 µm and 100 µm respectively. The defocus range was from -1.5 µm to -3.0 µm (-1.8 µm to -3.0 µm in the 2nd dataset). Throughout the data collection sessions, 1,519 micrographs (1st dataset) were collected within 45 hours and 1,749 micrographs (2nd dataset) were collected within 54.7 hours with a collection speed of ~34 micrographs/ hour and ~32 micrographs/ hour respectively.

Table 3.3 Electron microscope setups for cryo-EM data collection

	1st data collection	**2nd data collection**
Microscope	Titan Krios	
Detector	K2 counting	
Voltage (kV)	300	
Magnification	130,000	
Gun lens	6	
Spot size	4	
C2 aperture (µm)	50	
Objective aperture (µm)	100	
Energy filter slit size (eV)	20	
Pixel size (Å)	1.054	1.055
Exposure time (sec)	10	10
Electron exposure (e^-/Å^2)	50.015	50.376
Dose rate (e^-/Å^2/sec)	5.002	5.038
Defocus range (µm)	-1.5 to -3.0	-1.8 to -3.0
Number of fractions	40	25
Number of collected images	1,519	1,749
Data collection speed (micrographs/ hour)	34	32

3.3.4 Cryo-EM data processing and merging

The micrographs from both datasets were automatically collected in MRC format by EPU1.2. Following the inspection, 1,492 micrographs from the first dataset were retained for analysis and imported into RELION 3.0 for further data processing. As described in chapter 2.10.2, the imported images were corrected using whole-frame micrograph movie-alignment using MotionCor2 (Zheng et al., 2018), and the contrast transfer function (CTF) of the motion-corrected images were estimated using Gctf (Zhang, 2016). A small subset of particles (5,000

to 10,000) was firstly manually picked as a template and 2D classification was performed on this subset. Then automatic particle picking was performed on all micrographs. The result was manually checked to remove the obvious contaminants which were incorrectly identified as protein particles.

As shown in Fig 3.9A, 75,147 particles were picked after automatic particle picking. The first round of 2D classification for these particles was performed to clean out the bad particles. Following the results of the first 2D classification, 42,622 particles were selected from the good 2D classes with high signal to noise contrast, while the remaining particles were discarded due to poor 2D average class alignment. A further round of 2D classification and 3D classification gave a result of 37,665 good particles. With those particles, a 3D classification was performed to split particles into 4 classes on the basis of homogeneity. Fine angular sampling (0.9°) was applied to distinguish the difference between classes. The two major classes (class 3 contains 12,978 particles, class 4 contains 12,651 particles) showed a similarity of 99.86% by using the 'fit in map' function in UCSF Chimera (Pettersen et al., 2004). Thus, these two major classes were combined (total of 25,629 particles) and taken for a further 3D refinement. The two minor classes contain 3,327 particles in class 1 and 8,709 particles in class two respectively. Class 1 has shown the opposite chirality to the other classes. As the handedness of the structure cannot be determined from 2D images without a stage tilting (Bendory, Bartesaghi & Singer, 2020; He, 2018), this minor class was flipped and compared with the other two major classes by using the 'Fit in Map' function in Chimera. This minor class showed a similarity of 98.55% to the other two major classes. After the CTF refinement and a final 3D refinement, the final map has a global resolution of 3.8 Å based on the gold-standard criterion of FSC=0.143 (Fig 3.9A).

The second dataset was collected on the same microscope with a nearly identical setup. As shown in Fig 3.9B, 1,749 micrographs were collected and around 57,326 particles were automatically picked. The good classes from 2D classification were selected and 42,190 particles were taken for 3D classification. The major class (class 1) with 20,758 particles was selected as the good 3D class. Similar to the first dataset, the second dataset also contained a minor class (class 2 with 7,768 particles) with the opposite handedness. The density maps from

class 3 and 4 with 5,213 and 8,451 particles show an incomplete complex I structure. The final map has a global resolution of 3.9 Å based on the gold standard criterion of FSC=0.143 (Fig 3.9B).

To further improve the resolution, the two data sets were joined following the protocol from Wilkinson, Kumar & Casañal (2019) as shown in Fig 3.10A. The 25,629 polished particles from the first dataset were merged with about 20,758 particles from the second dataset giving a total particle number of 46,387. The merged data set was also processed in RELION 3.0. However, the resolution of the merged data resulted remains at 3.9 Å, which suggests that the resolution obtained was not limited by particle numbers. It was then considered whether the resolution was limited by particle orientations. To assess this, the 2D classes with particles for 3D classification from the two data sets were selected (shown in Fig 3.10B). There is no substantial difference between the selected good 2D classes and no strong orientational bias was identified. Secondly, the orientation distribution efficiency for 3D refinement particles from the two data sets was shown by the angle distribution (angdist.bild) files in Chimera along with the density map (Fig 3.10C). The high coverage of angles indicates a good particle orientation distribution efficiency. Therefore, both of the data sets show a high angle coverage, indicating the particle orientations is not limiting the resolution.As a result, other intrinsic limitation factors to the resolution should be considered: such as the heterogeneity of particles due to multiple catalytic states or the instability of the mutant structure.

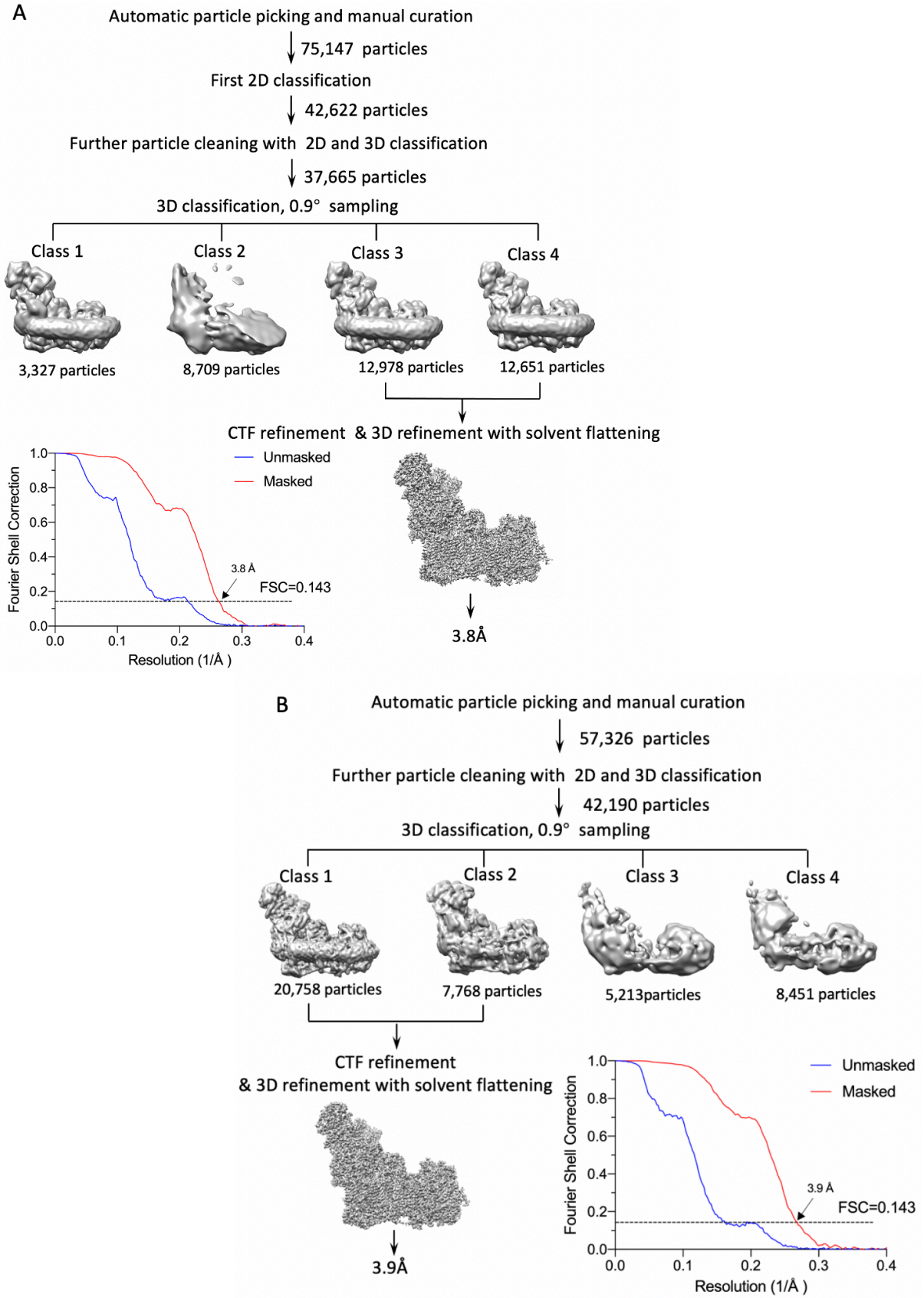

Fig 3.9 Classification and refinement scheme for ND6-P25L mouse complex I from 1st data sets (A) and 2nd data set (B). Auto-picked particles were manually curated and cleaned with 2D classification. The particles from selected 2D classes were used for 3D classification. FSC curves of two refined maps with (red) and without (blue) masks after post-processing are shown in the bottom of each figure.

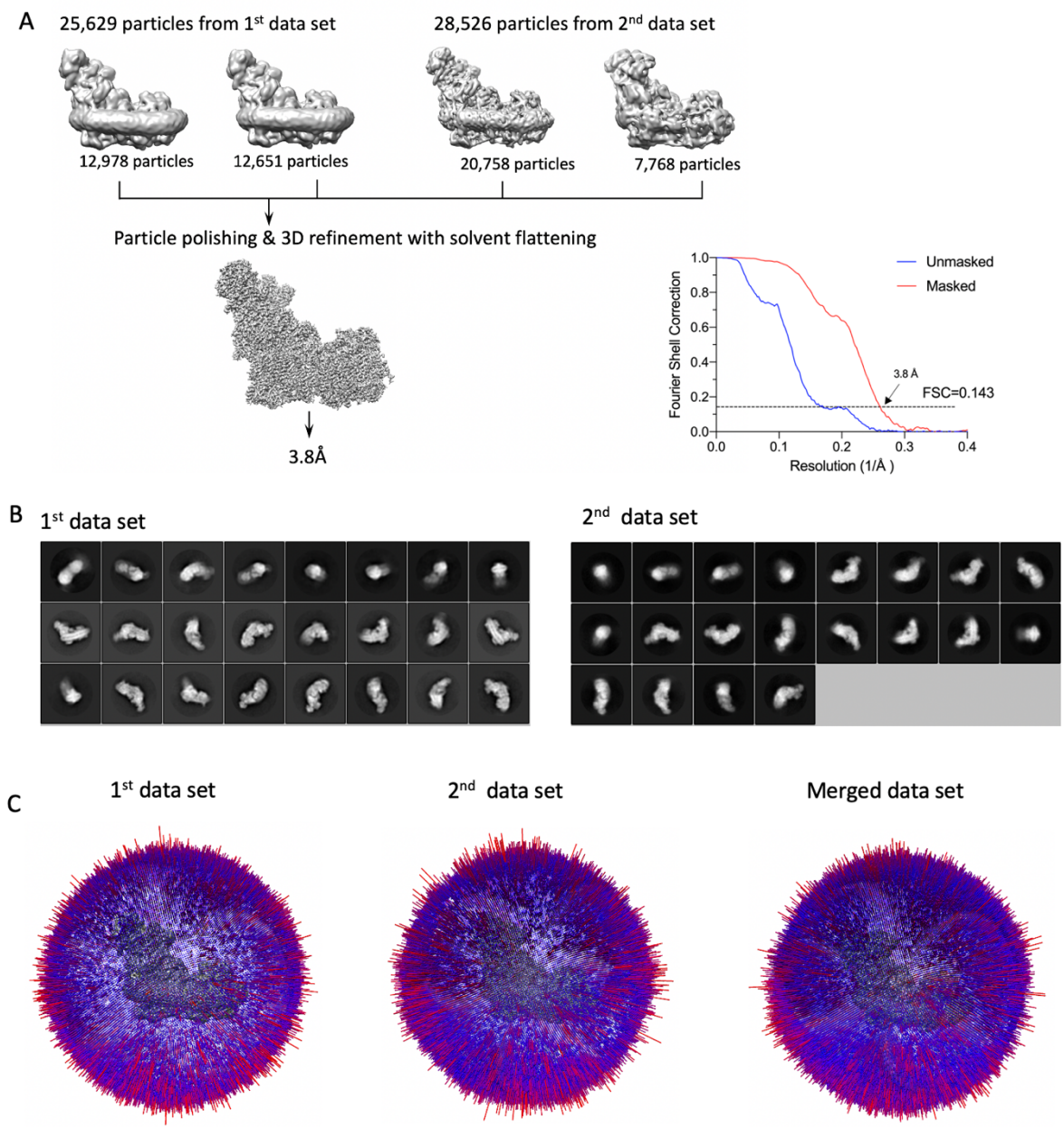

Fig 3.10 Merged data does not improve the resolution (A) Classification and refinement scheme of the merged data sets. (B) Selected good 2D classes for 3D classification in each data set. (C) Orientation distribution efficiency shown on the surface of the density map by angdist.bild file. Blue dots on the surface indicate the coverage of the angle, the red color spikes show a higher particle number in this region.

3.3.5 ND6-P25L-CI model building

With the upgrade of RELION from 2.1 to 3.0 version, the resolution of the active state WT-CI density map has improved from the previously published 3.3 Å to 3.1 Å (Bridges et al., 2020; Agip et al., 2018); The resolution of the deactive state WT-CI map has improved to 3.2 Å. Thus, RELION 3.0 was used to process the ND6-P25L-CI cryo-EM data set. To achieve a better structural comparison between the ND6-P25L-CI and the WT-CI, the deactive state WT-CI

model was rebuilt using the improved density map. Both models were built in Coot 0.9-pre and refined by Phenix with the help of Dr Hannah Bridges. During this process, the unfavoured Ramachandran, rotamers and chiral outliers were manually corrected and minimised in Coot. The final model statistics produced by Phenix-1.16-3549, MolProbity 4.4 and EMRinger-1.0 are shown in Table 3.4.

For model building of the deactive state WT-CI, the active state WT-CI model (PDB: 6ZR2) was used as the initial model to perform rigid-body fitting with the deactive density map. The deactive state WT-CI model was then manually adjusted in Coot 0.9-pre using both the globally sharpened and multibody maps. The model was further refined by phenix real space refinement with secondary structure restraints against the globally sharpened consensus map in Phenix-1.16-3549 (Afonine et al., 2012). The model was subsequently refined in ISOLDE (Croll, 2018) with a molecular-dynamics flexible fitting before a second round of phenix.real_space_refine. ISOLDE improved the modeling resulting in a reduced clash score of 7.25 (from 9.10). The final model and density map were deposited into RCSB PDB with accession codes: EMD-11810, PDB: 7AK5. In comparison to the published deactive mouse model (Agip et al., 2018), the new deactive state WT-CI (PDB: 7AK5) has shown a significant improvement in the percentage of the favorable regions in the Ramachandran plot and clash score as shwon in Table 3.4.

Table 3.4 Cryo-EM data validation statistics comparision

	WT-CI deactive state (PDB: 6G72)*	WT-CI deactive state (PDB: 7AK5)	ND6-P25L-CI (PDB: 7AK6)
Model resolution (Å)	3.9	3.18	3.83
FSC threshold	0.143	0.143	0.143
Model composition			
Nonhydrogen atoms	64,923	65,903	65,341
Protein residues	8,072	8,070	8,063
Ligands	14	28	21
B factors mean (Å^2)			
Protein	71	42.79	58.21
Ligand	67	38.24	57.59
R.m.s. deviations			
Bond lengths (Å)	0.012	0.003	0.004
Bond angles (°)	1.33	0.587	0.605
Validation			
MolProbity score	2.18	1.80	2.1
Clashscore, all atoms	9.10	7.25	10.83
Poor rotamers (%)	0.23	0.01	0
Ramachandran plot			
Favored (%)	82.7	94.05	89.91
Allowed (%)	16.9	5.94	10.07
Disallowed (%)	0.4	0.01	0.01
EMRinger	2.10	2.66	2.19

*The deactive state (PDB: 6G72) data is from the Agip et al. (2018).

Before the ND6-P25L-CI model was built, the ND6-P25L-CI density map was firstly compared with the published density maps of WT active and the new deactive complex I in Chimera by fit-in-map (Bridges et al., 2020). Interestingly, the ND6-P25L-CI map shows a ~94% similarity to the deactive state WT-CI in map-to-map correlation, but only ~71-77% similarity to the active state (see Fig 3.11A). Thus, the ND6-P25L-CI model was built with the deactive state WT-CI (PDB: 7AK5) as the initial model. The ND6-P25L-CI model was built in the same way as deactive state WT-CI (PDB: 7AK5) without the ISOLDE refinement. The final ND6-P25L-CI model was produced with a minimised percentage of unfavoured Ramachandran and clash score. The structure coordinates together with the density maps were deposited into RCSB PDB with accession codes: EMD-11811, PDB ID: 7AK6. The validation statistics for the ND6-P25L-CI map are given in Table 3.4.

No obvious coordination changes of subunits were observed between the deactive state WT-CI and ND6-P25L-CI model. The local resolution estimated using the Local Resolution function in RELION from both models shows similar patterns (Fig 3.11B). The root-mean-square deviation of atomic positions (RMSD), a comparison of Cα atoms between two structures, showed a low value of 0.59 Å, which indicates a close match between ND6-P25L-CI and deactive state WT-CI structure.

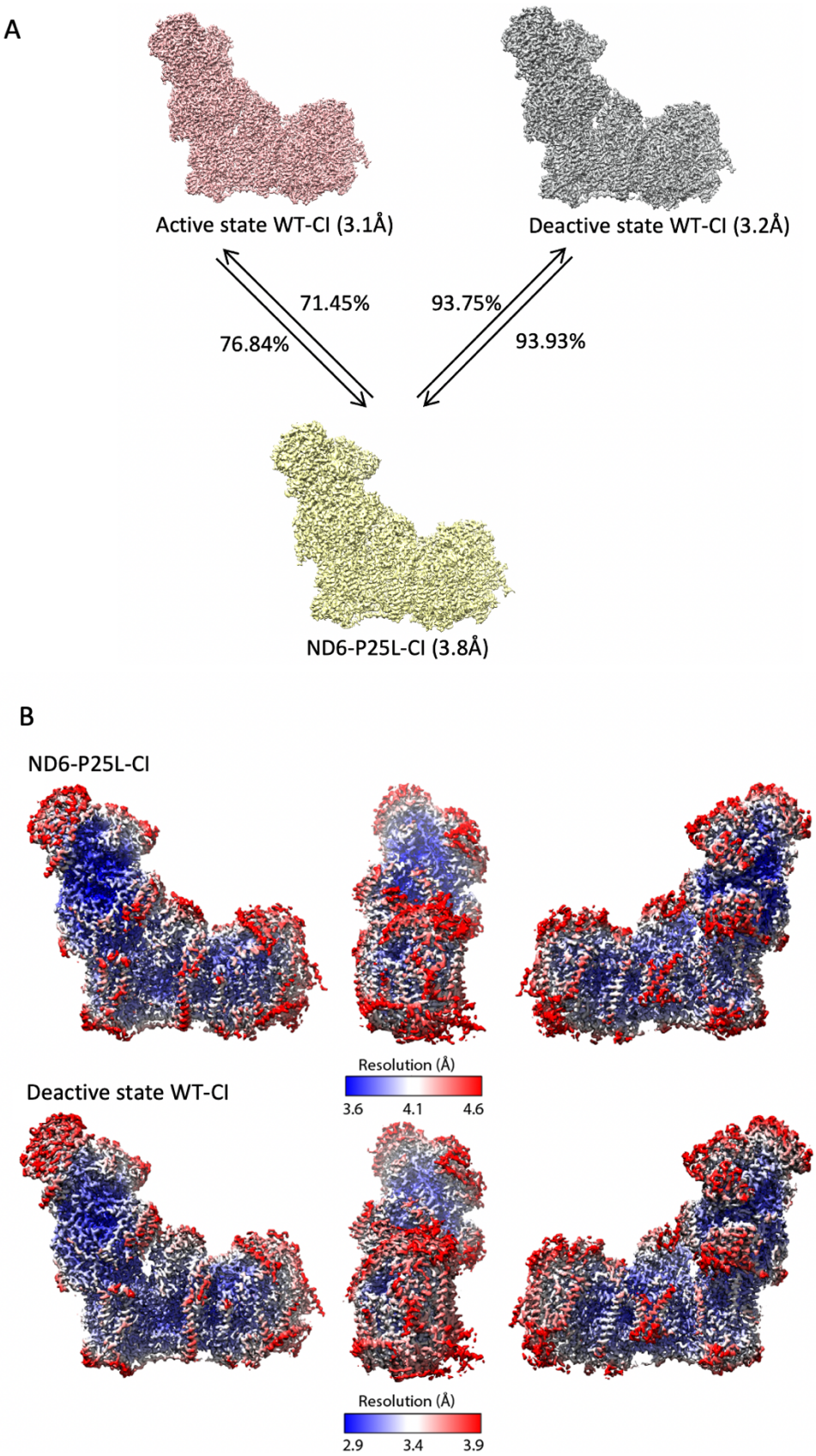

Fig 3.11 Global structral comparison with density maps. (A) Map-to map cross-correlation coefficient calculated from Chimera rigid fitting between active state WT-CI (pink), deactive state WT-CI (gray) and ND6-P25L-CI (yellow) density maps. (B) Local resolution of the density maps for the ND6-P25L-CI and the new deactive state WT-CI.

3.3.6 Analysis of the ND6-P25L-CI model

Structural comparison and analysis was performed with the newly obtained ND6-P25L-CI and WT-CI models. Firstly, the formation of the π-bulge in TMH3 of the ND6 subunit, as a characteristic property of the deactive state mouse complex I structure (Agip et al., 2018), was identified in ND6-P25L-CI (see Fig 3.12A). The models fitted into the density of TMH3 of the ND6 in both WT (active and deactive) and ND6-P25L have shown in Fig 3.12B. Secondly, the relative distance between NDUFA5 and NDUFA10, reflecting the rotation between hydrophilic and membrane domains, is consistent with the distance observed in the deactive state mouse complex I (see Fig 3.12C) (Agip et al., 2018). These lines of evidence have shown that the reconstructed ND6-P25L-CI is a "deactive-like" structure. The ND6 subunits from active, deactive state WT-CI and ND6-P25L-CI models were then compared. TMH2 in each model was superimposed in Fig 3.12D, illustrating that the distance between TMH2 and the top part of TMH3 was longer in the ND6-P25L-CI. The measured distance from P25 to TMH3 in the deactive state WT-CI is approximately 6.6 Å while this is extended to 8.5 Å in ND6-P25L-CI. This single subtle alteration could explain why the ND6-P25L-CI has shown the propensity to take up the deactive state during cryo-EM analysis. The L25 substitution in the mutant could push the upper part of TMH3 further away from TMH2. It is known that during the A/D transition, the bulky residues F67 and Y69 have to transit across the interface between TMH2 and TMH3 (Agip et al., 2018). The potential steric clashing between F67 and the adjacent residues in TMH2 is high for the A/D transition in WT-CI (Fig 3.12E). However, the enlarged interspace in ND6-P25L-CI results in a reduced clashing during rotation and π-bulge formation (Fig 3.12F), thus the energy barrier for the A/D transition in ND6-P25L-CI may be reduced.

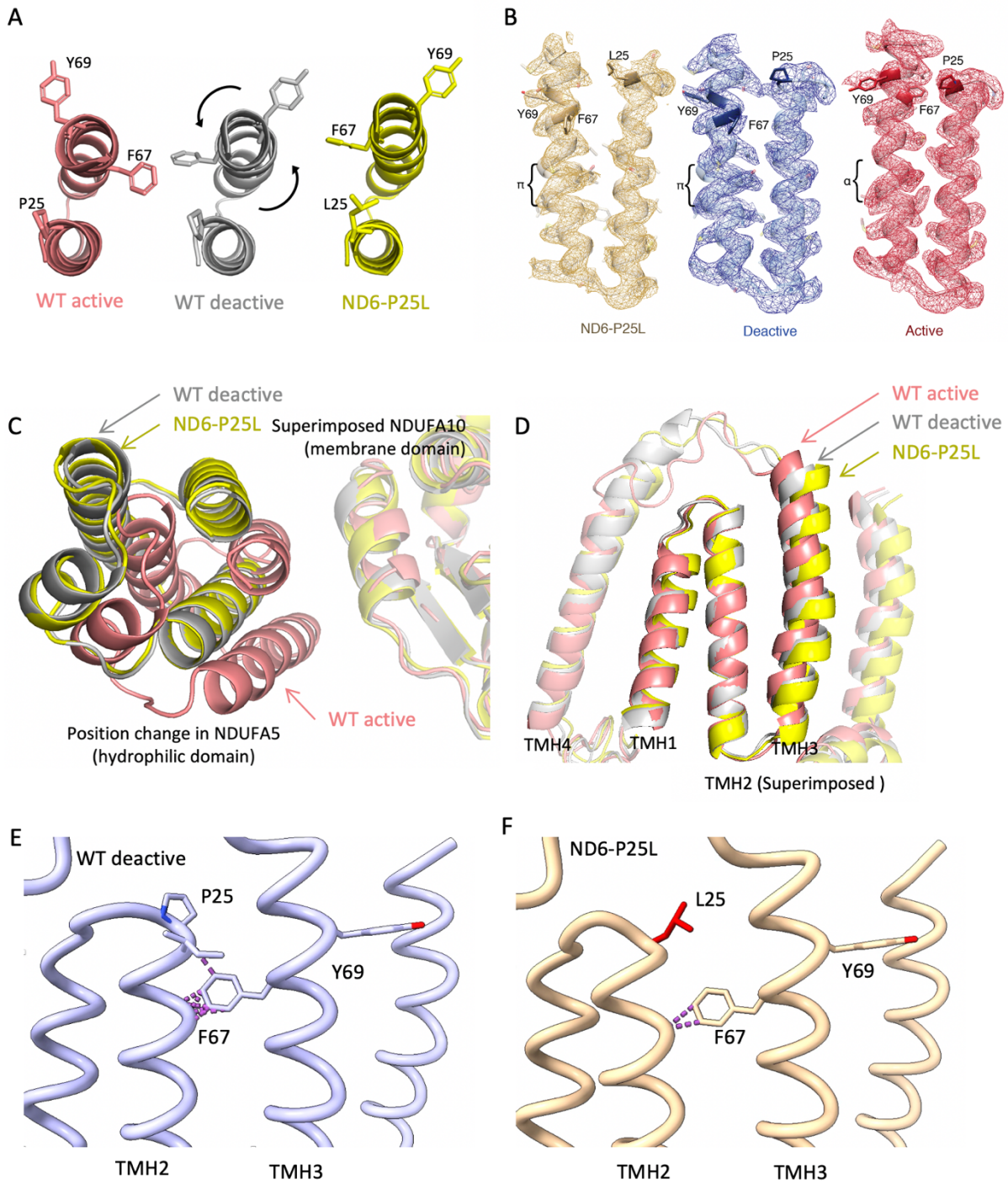

Fig 3.12 Structural comparison between ND6-P25L-CI (PDB: 7AK6), active state (PDB: 6ZR2) and deactive state (PDB: 7AK5) WT-CI. (A) The P25L mutation position in TMH2 and the relative position of two bulky residues F67 and Y69 in TMH3 of the ND6 subunit. (B) The side view of the TMH2 and 3 with the models fitted in the density maps. This figure was generated by Dr Hannah Bridges. The residues in the models are shown as transparent except for P/L25, F67 and Y69. (C) The relative position difference of NDUFA5 and NDUFA10 in the active, deactive state WT-CI and ND6-P25L-CI. The ND6-P25L-CI has a similar relative subunit position to the deactive state WT-CI. (D) The relative distance between TMH2 and TMH3 with superimposed TMH2 in the active/deactive state WT-CI and ND6-P25L-CI. (E) & (F) The potential steric clashes between F67 and the ND6 subunit TMH2 during the A/D transition in WT-CI(E) and ND6-P25L-CI (F). The figure (E) and (F) were generated from the movies made by Mr Daniel Grba (Yin et al., 2021).

3.3.7 ND6 subunit polymorphism

The ND6-P25L mutation has been found in a patient with leigh syndrome onset (Malfatti et al., 2007), while the mouse model has shown no obvious phenotypes (Lin et al., 2012). Therefore, the mtDNA polymorphism around ND6 subunit was investigated. Amino acid residues within 20 Å of the P25 in the ND6 subunit have been compared between human and mouse using Clustal Omega with Gonnet Pam250matrix. As shown in Table 3.5, 8 subunits are present within 20 Å of the mutation. The table column marked with "no similarity" indicates the number of unfavoured substitutions in this subunit within the 20 Å distance. The "strong" and "weak" represent the favoured substitutions. Within the ND6 subunit, there are 10 unfavoured substitutions. In addition to this, ND2 and ND4L each have 2 unfavoured substitutions and ND1 has 1 unfavoured substitution within the selected 20 Å region. The unfavoured substitution positions have been highlighted in yellow in Fig 3.13A. The substitutions in the ND6 subunit have been compared with the reported clinically relevant mutations as shown in Fig 3.13B. The mutations are presented in the highly conservative amino acids, not in the substitution positions. These results suggested that the ND6 subunit is not conserved in sequence between human and mouse, thus the mtDNA polymorphism could be a possible reason for varied phenotypes.

Table 3.5 Residues substitution within 20 Å of the mutation position.

Subunit	Number of amino acids included in 20Å	Similarity (number of amino acids)			
		Identical	Strong	Weak	No
NDUFS2	1	1	0	0	0
ND1	48	37	10	0	1
ND2	13	10	1	0	2
ND3	18	17	1	0	0
ND4L	61	48	10	1	2
ND5	7	4	3	0	0
ND6	60	32	16	2	10
NDUFA9	2	2	0	0	0

A

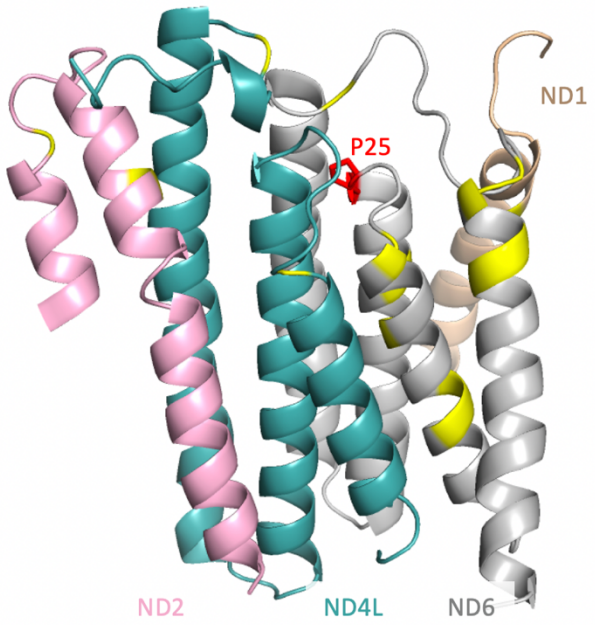

B

```
NU6M_HUMAN   1   MMYALFLLSVGLVMGFVGFSSKPSPIYGGLVLIVSGVVGCVIILNFGGGYMGLMVFLIYL   60
NU6M_MOUSE   1   MNNYIFVLSSLFLVGCLGLALKPSPIYGGLGLIVSGFVGCLMVLGFGGSFLGLMVFLIYL   60
                 *   :*:**  :::* :*:: ********** *****.***:::*.***.::*********

NU6M_HUMAN  61   GGMMVVFGYTTAMAIEEYPEAWGSGVEVLVSVLVGLAMEVGLVLWVKEYDGVVVVVNFNS  120
NU6M_MOUSE  61   GGMLVVFGYTTAMATEEYPETWGSNWLILGFLVLGVIMEVFLICVLNYY-DEVGVINLDG  119
                 ***:********** *****:***.  :*  :::*: *** *:  :: * . * *:*:::.

NU6M_HUMAN 121   VGSWMIYEGEGSGLIREDPIGAGALYDYGRWLVVVTGWTLFVGVYIVIEIARGN        174
NU6M_MOUSE 120   LGDWLMYEVDDVGVMLEGGIGVAAMYSCATWMMVVAGWSLFAGIFIIIEITRD-        172
                 :*.*::** :. *:: *. **..*:*. . *::**:**:**.*::*:***:*.
```

Fig 3.13 Amino acid substitutions around P25. (A) The amino acid substitution positions caused by polymorphism between the human and mouse were colored in yellow on the active mouse model (PDB: 6g2j). The area within 20 Å of the P25 in the ND6 subunit includes four subunits (pink: ND2, cyan: ND4L, gray: ND6, wheat: ND1). (B) ND6 amino acids sequence alignment between human and mouse. Asterisks (*) indicate positions with fully conserved residue. Colon (:) indicates strongly similar properties between groups. Period (.) indicates weakly similar properties between groups. The red squares highlight pathogenic variants according to Marino (2019).

3.4 The A/D transition of ND6-P25L-CI

3.4.1 Deactivation of WT-CI in heart mitochondrial membranes

As the cryo-EM 3D reconstruction structure of ND6-P25L-CI shows high similarity to the deactive state WT-CI, a series of kinetic assays were designed to biochemically verify the conformational state of ND6-P25L-CI and investigate the A/D transition during catalysis. The details of A/D transition assays were shown in Chapter 1.3.4. In this chapter, NEM was used to identify the status of complex I as it has been widely used as a biochemical marker for the deactive state in many studies (Maklashina et al., 2003; Blaza et al., 2018).

In the previous mouse deactivation study, the mouse complex I was only able to achieve 61±7% deactivation in the population by incubating at 37°C for 30 min (Agip et al., 2018). To verify whether mouse complex I could achieve higher deactivation percentage, WT mouse heart mitochondrial membranes were incubated at 37°C for different time lengths (15 to 60 min) in the presence and absence of NEM, as shown in Fig 3.14A. The NADH:O_2 assays on NEM-treated mitochondrial membranes showed 22.21±0.87% complex I were retained in the active state in the membranes regardless of the incubation time. The longer incubation time did not increase the population of deactivated complex I in the mouse WT heart mitochondrial membranes. This suggests that, unlike the bovine membranes which could easily achieve approximately 95% deactive state in 15 min incubation at 37°C (Blaza et al., 2018), it is difficult to achieve complete deactivation of complex I in the WT mouse membrane using the same method. Since the deactivating ratio is not incubation-time dependent, the same deactivating conditions was used as previously in the lab (Agip et al., 2018), which is 30 min incubation at 37°C.

To check the re-activation character of the thermally deactivated complex I, 1 mM NADH was incubated with deactivated membranes at 19°C for different time lengths (10, 30, 60, 120 secs as shown in Fig 3.14B). NEM was then added to the re-activated membranes on ice for 20 min to estimate the proportion of re-activated complex I. The results show that an NADH incubation time as short as 10 sec is sufficient to change deactive complex I into active, while a 30-second

incubation gives the highest activity. Interestingly, none of the incubation times, from 10 to 120 sec, was able to achieve 100% reactivation as shown in Fig 3.14A (white bars, deactivation without NEM). This indicates that a certain percentage of complex I is likely either damaged or remains in D-form during the reactivation process.

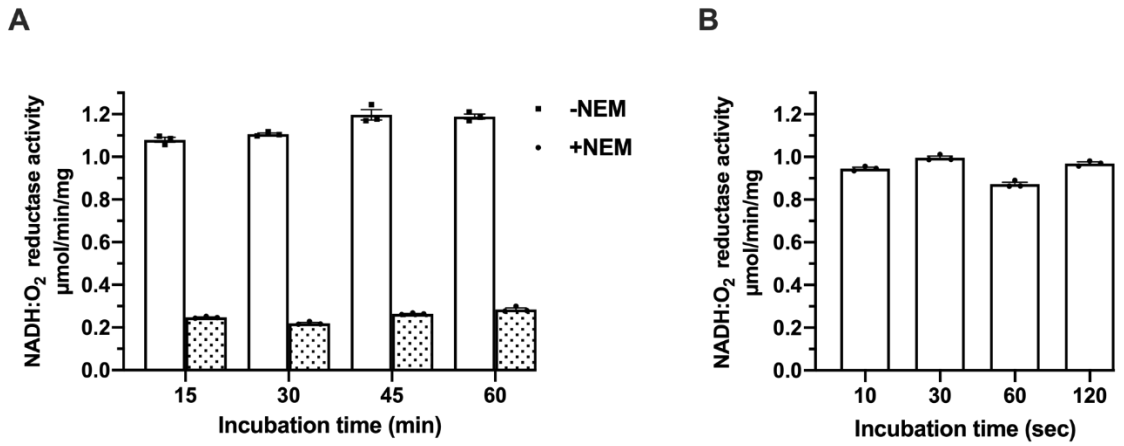

Fig 3.14 Complex I maximum rates assessed by the rotenone-sensitive NADH:O_2 assay on WT mouse heart mitochondrial membranes. (A) Membranes were deactivated at 37°C for different time lengths: 15, 30, 45 or 60 min before NADH:O_2 assay. (B) Deactivated membranes were re-activated by incubating with NADH for 10, 30, 60 or 120 sec. Data in (A) and (B) show the mean values ± SEM, n=3.

3.4.2. Re-activation of ND6-P25L-CI in membranes

To analyse the re-activation capability of ND6-P25L-CI, an experiment was designed as shown schematically in Fig 3.15A. This approach used three types of membranes: the 30-min deactivated WT membranes, as-prepared WT membranes and as-prepared ND6-P25L membranes, which were split into two identical aliquots. One of these aliquots was then treated with 1 mM NADH to re-activate complex I for 10 sec at 19°C; while the other non-NADH treated aliquot was regarded as the control showing the status before reactivation. NEM/DMSO was added to each of the membrane samples to estimate the ratio of A/D states before and after this NADH re-activation process. The results in Fig 3.15B show the proportion of active state complex I in each sample before and after reactivation. From Fig 3.15B, the as-prepared WT was maintained 84.69±1.62% complex I in the active state before NADH reactivation and 85.36±1.44 % after NADH treatment, thus no significant change was observed in the A/D ratio before and after NADH treatment. Both the deactivated membranes and ND6-P25L membranes showed an increased amount of active state complex I after NADH treatment: The percentage

of activated complex I in the deactivated WT membrane increased from 38.64±2.35% to 74.18±1.91%; while a lower increase from 9.95±0.57% to 39.63±1.70% was observed in ND6-P25L membranes following NADH treatement. Thus, the ND6-P25L still has less active state complex I compared to the deactivated and as-prepared WT membrane after NADH re-activation.

To further investigate whether the deactive state complex I observed in ND6-P25L is age-related, heart mitochondria from both young (3 months) and old (12 months) ND6-P25L mice were collected. In a similar experiment to that implemented in Fig 3.15A, mitochondrial membranes from as-prepared WT (3 months old) and ND6-P25L mice (3 months and 12 months old) were incubated with 2 mM NEM on ice for 20 min. As shown in Fig 3.15C, there is about 89% active complex I present in the as-prepared WT membranes. However, in both young and old ND6-P25L mice, complex I activity decreased significantly following treatment with NEM (7% and 6% of the activity to the non-NEM treated enzyme respectively), indicating a majority of complex I is in the deactive state. However, there is no significant difference in the complex I activity between young and old ND6-P25L. These results show that majority of the complex I in ND6-P25L strain remains in the deactive state during the preparation procedure, which is markedly different from the WT complex I. The results also indicate that the high proportion of deactive complex I in the ND6 mutants is not an age-dependent phenomenon.

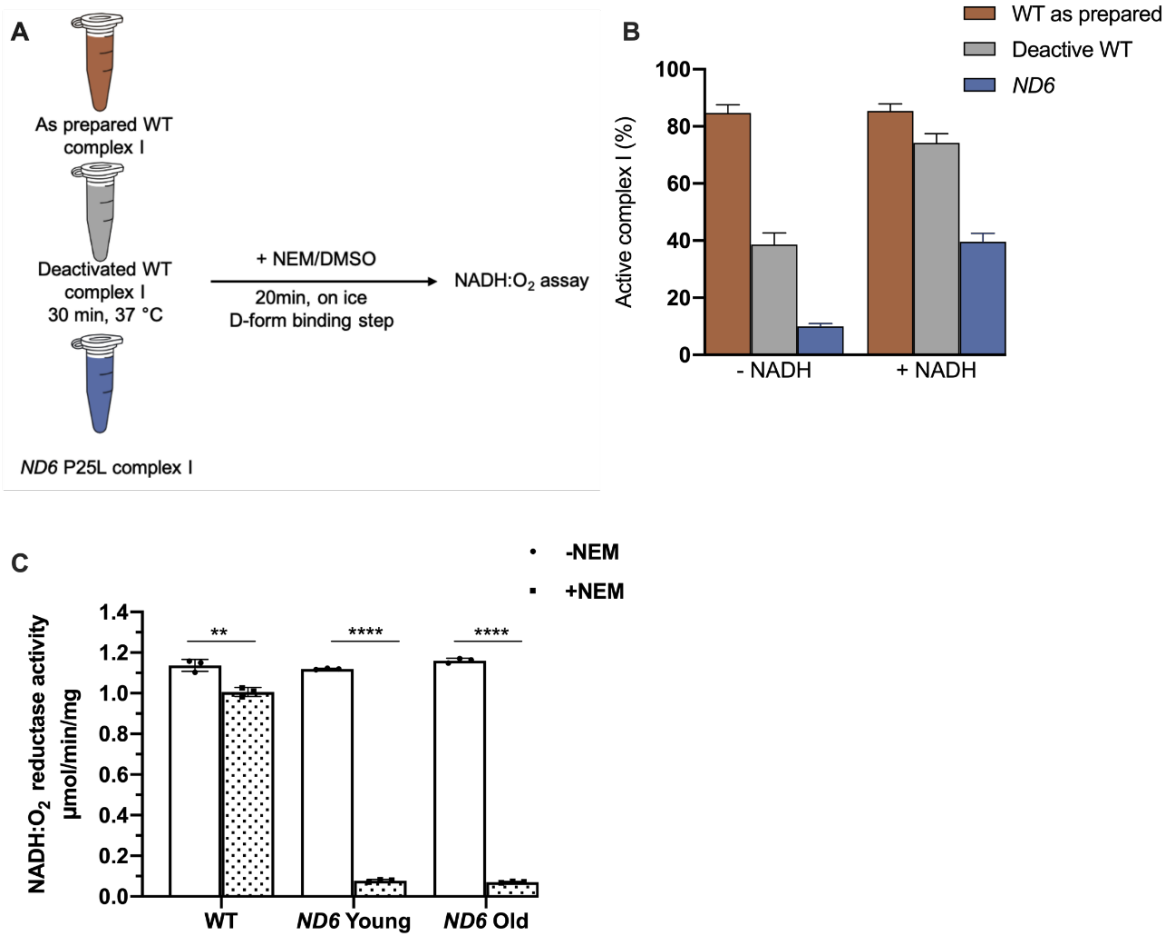

Fig 3.15 Rotenone-sensitive NADH:O_2 oxidoreduction with N-ethylmaleimide (NEM) treatment. (A) A diagram illustrating the NEM treated NADH:O_2 assay. (B) The percentage of active complex I before (left) and after incubation (right) with 1mM NADH for 10 sec at 19°C. The fully activated enzyme (100% activity) was determined by adding DMSO (vehicle control) instead of NEM. (C) The maximum rate of NEM treated NADH:O_2 assay in WT and ND6-P25L mice at two different age stages. Data in (B) and (C) show the mean values ± SEM, n=3 (**p < 0.01; ***p < 0.001;****p < 0.0001).

3.4.3 A/D transition of ND6-P25L-CI during turnover

The re-activation results above showed that ND6-P25L-CI may have a quick transition from A to D and not able to maintain an active state without NADH reactivation. Thus, there is a question as to whether longer re-activation could increase the population of ND6-P25L-CI in the active state. A time-dependent NAD(P)H:O_2 assay with NEM treatment for the ND6-P25L-CI was designed (Fig 3.16A for NADH:O_2 assay and Fig 3.16C for NADPH:O_2 assay). The experiment design with longer re-activation time is illustrated in Fig 3.16A. ND6-P25L and deactivated WT membranes were re-activated by incubating with 1 mM NADH for different lengths of time, followed by the standard NEM treatment. The results in Fig 3.16B shows the

maximum rate of complex I in NADH:O_2 assay with different re-activation times. After a 30 sec NADH re-activation, the deactivated WT-CI returned to a normal level of activity, while the ND6-P25L-CI was only able to re-activate to 52.57±0.83% of WT-CI's maximum activity. The deactivated WT membranes had a slight decreased activity from 10 sec to 2 min but were able to retain 84.50±1.30% activity from 2 to 10 min incubation when the substrates were likely depleted. However, there was a dramatic decrease in ND6-P25L-CI activity after 2 min. The activity is decreased to almost 0 after 6 min. This indicates that the WT-CI is able to maintain its A-form for at least 15 min after NADH is applied. However, the ND6-P25L-CI shows different NEM-sensitivity after NADH is applied and is not able to maintain in the active state during this reactivation process.

To further investigate if the ND6-P25L-CI is able to maintain the active state during turnover, re-activation by NADH incubation was replaced by NADPH. NADPH is a very poor hydride donor; thus, it gives a much lower oxidation rate (Yakovlev & Hirst, 2007). After the re-activation with NADPH, the standard NEM treatment was performed. Fig 3.16B shows the activity of WT-CI dropped by 24.39±0.54% after 5 min incubation with NADPH, following which, the amount of active state complex I remains constant regardless of the incubation time with NADPH. In ND6-P25L-CI, the maximum rate it obtained is only around 59.06±2.92% of the activity on WT membranes which suggests that the ND6-P25L-CI is not able to completely maintain its active state even in the prolonged presence of sufficient substrate.

To understand the A/D transition during the shortage of substrate, a further experiment was performed as shown in Fig 3.16C. The experiment was modified from Fig 3.16B with an extra step of adding ferricyanide to rapidly remove the reducing substrate before NEM treatment. Ferricyanide is an electron acceptor during NADH:FeCN oxidoreduction at the flavin site of complex I, and the reaction is the fastest known reaction for complex I from bovine (Dooijewaard & Slater, 1976). In general, membranes from both ND6-P25L mutant and WT mice were incubated with 1 mM NADPH at 32°C for 5 min for pre-activation. The NADPH was then consumed using the NADPH:FeCN oxidoreduction reaction with 2 mM FeCN for different periods of time until NADPH was fully oxidised. Fig 3.16C shows that the WT-CI

undergoes a gradual transition from active to deactive state when the substrate was insufficient, while the activity of ND6-P25L-CI remained low even after just 5-min incubation with FeCN. This indicates that while the active to deactive transition is a slow process in the WT when substrate is limiting the ND6-P25L-CI is more “sensitive” to the lack of substrate condition and thus the active to deactive transition seems more rapid in this mutant.

Another experiment was performed to further verify if the ND6-P25L-CI is able to maintain its A-state during NADH oxidation catalysis. Complex I was pre-activated with 200 μM NADH at 32°C for 2 min and then 1 mM NEM or the same volume of DMSO (as control) was added during the catalysis. The results from Fig 3.16D show that the ND6-P25L-CI was rapidly inhibited by the NEM during catalysis, whilst no difference in activity of WT-CI was identified in the presence and absence of NEM in the assay. This result, together with the previous data, confirms that ND6-P25L-CI is not able to maintain its A-form as the WT does during turnover. Interestingly, the ND6-P25L-CI without NEM treatment shows a similar initial rate to WT with no obvious lag phase observed during this process. This indicates the D state in the ND6-P25L-CI may be different from the conventional WT deactive state.

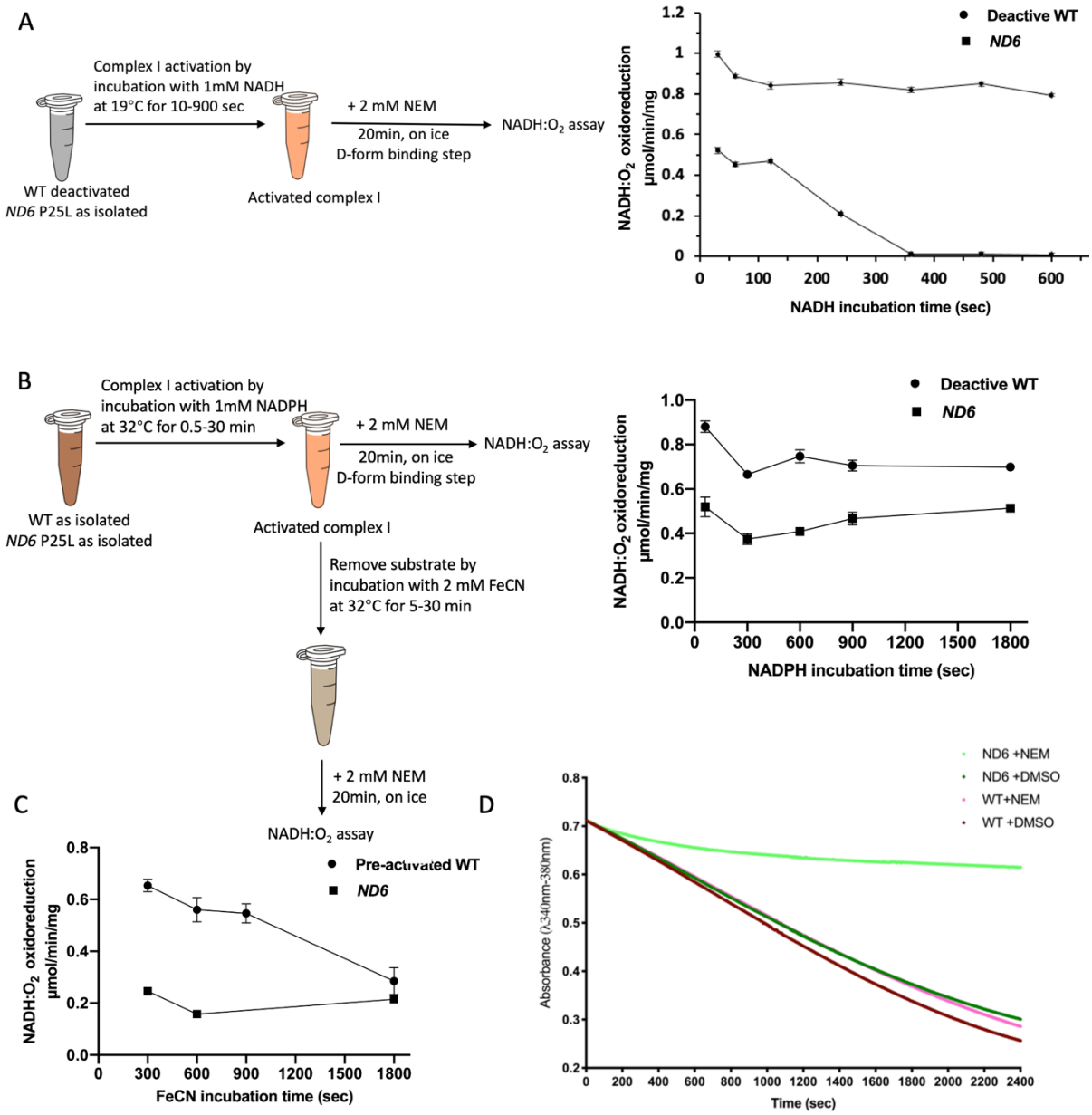

Fig 3.16 Time-dependent oxidoreduction assays on ND6-P25L-CI. (A) A diagram explaining the time-dependent NADH:O_2 assay and NADPH:O_2 assay (B) followed with NEM treatment. The result plot is shown on the right side (mean values ± SEM, n=3). (C) NADH:O_2 activity measured after FeCN treatment. (D) NADH:O_2 assay with 1 mM NEM adding during the catalysis.

To summarise, the results obtained from the biochemical assays indicates that cys39 in ND6-P25L-CI is continuously exposed during catalysis. There are several key characteristics of this mutant complex I. Firstly, the ND6-P25L mutant seems to have a lower energy barrier between active and deactive states which makes the transition more rapid with no lag phase observed. Secondly, the ND6-P25L-CI exists either in an unstable state with cys39 partially exposed or has a continual A/D transition during the catalysis, which is not exhibited in the WT-CI. This phenomenon is further discussed in Chapter 3.7.3.

3.5 ROS production during RET in ND6-P25L in heart mitochondria

The study from Lin et al. reported an increase in forward electron transfer and an absence in reverse electron transfer induced H_2O_2 production in liver mitochondria of the ND6-P25L mouse (Lin et al., 2012). To investigate the ROS production in ND6-P25L complex I in heart mitochondria, a series of experiments assessing ROS production during forward and reverse electron transfer were performed collaborating with Mr Nils Burger together with Dr Andrew M. James, Dr Amin Mottahedin and Dr Hiran A. Prag from Professor Michael P. Murphy's group (MRC MBU, University of Cambridge).

Firstly, the catalytic activity of ND6-P25L-CI as well as the succinate oxidation pathway were assessed on isolated mitochondria by Mr Nils Burger, similar to those experiments have been performed on the heart mitochondrial membrane (Chapter 3.2.3). The membrane result shows a decreased NADH oxidation rate due to the low complex I content on ND6-P25L membrane (Fig 3.5A, C), with the same succinate reduction rate observed between ND6-P25L and WT (Fig 3.5B). In isolated heart mitochondria, the O_2 consumption rate was measured with the addition of glutamate/malate or succinate on both ND6-P25L and WT (Fig 3.17). The results from the isolated heart mitochondria are consistent with the results on the mitochondrial membrane, ND6-P25L show a decreased O_2 consumption rate (Fig 3.17A). This decreasing could be due to less complex I content, however this effect is more difficult to assess in the more complicated isolated mitochondria system. As in the mitochondrial membranes, there was no influence on the O_2 consumption rate with succinate in the mutant mouse mitochondria (Fig 3.17B). Additionally, the glutamate/malate-induced H_2O_2 production rates were similar in ND6-P25L and WT (Fig 3.17C).

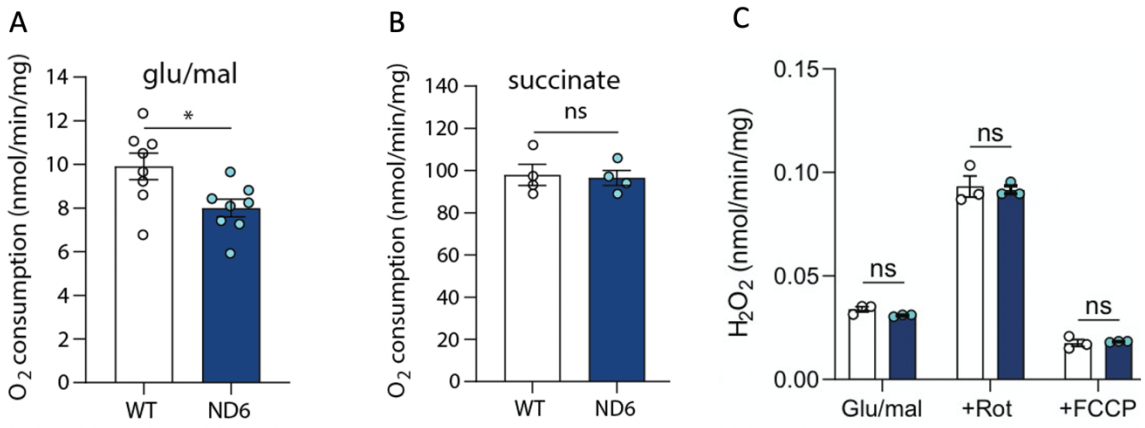

Fig 3.17 Catalytic activity and ROS production of ND6-P25L and WT complex I in isolated heart mitochondria. (A) O_2 consumption rate during glutamate/malate (0.5 mM) respiration. (B) O_2 consumption rate in the presence of succinate (10 mM). The data are mean values ± S.E.M. (n=4–8, *p < 0.05). (C) H_2O_2 production rate by adding glutamate/malate (10 mM of each). FCCP (5 μM) or rotenone (5 μM) were added as indicated. The data are mean values ± S.E.M. (n = 4–8, *p < 0.05).

Secondly, the ROS production by RET was tested by adding succinate to initiate ubiquinone reduction and membrane potential (Δp) (Robb et al., 2018). The following experiments were performed by Mr Nils Burger with assistance from Dr Andrew M. James. As shown in Fig 3.18A, the rotenone-sensitive H_2O_2 production rate was significantly lower in ND6-P25L mitochondria compared to the WT. The rotenone-insensitive rate of H_2O_2 production shows no significant difference between ND6-P25L and WT mitochondria, indicating that the higher H_2O_2 production was ND6-P25L-CI specific. The addition of FCCP abolished Δp on mitochondria, resulted in barely any H_2O_2 production from both ND6-P25L and WT confirmed that the H_2O_2 production were all Δp dependent. To confirm that the lack of ROS production by RET in ND6-P25L is a complex I mutant specific effect rather than other effects in changing the thermodynamic driving force on the membrane, the Δp and redox status of CoQ pool were measured in the presence of succinate (Burger et al., 2020; Ross et al., 2006; Ross et al., 2008) (Fig 3.18B and Fig 3.18C). No significant difference in Δp was observed between ND6-P25L and WT (Fig 3.18B). A higher reduced CoQ pool was accumulated in ND6-P25L (Fig 3.18C), which is due to the lack of RET to oxidise ubiquinol in ND6-P25L-CI. Once the RET was blocked by adding rotenone (Robb et al., 2018), the redox states of CoQ pool became the same in both ND6-P25L and WT mitochondria. These results all indicate that the absence of ROS production through RET in ND6-P25L is due an intrinsic effect of the mutant complex I rather than the change of the thermodynamic driving force. A further experiment was designed to

assess whether ND6-P25L-CI was able to switch from the catalytic active state to the RET condition. The complex I in mitochondria was activated by NADH:O_2 oxidoreduction with glutamate/malate followed by a rapid switching to RET condition by the addition of succinate (Fig 3.18D). The results showed that ND6-P25L mitochondria have similar O_2 consumption level to the WT, but much less increased H_2O_2 production after adding succinate. The result proves that, unlike the WT-CI, ND6-P25L-CI was not able to switch rapidly from catalysing the forward reaction to performing RET.

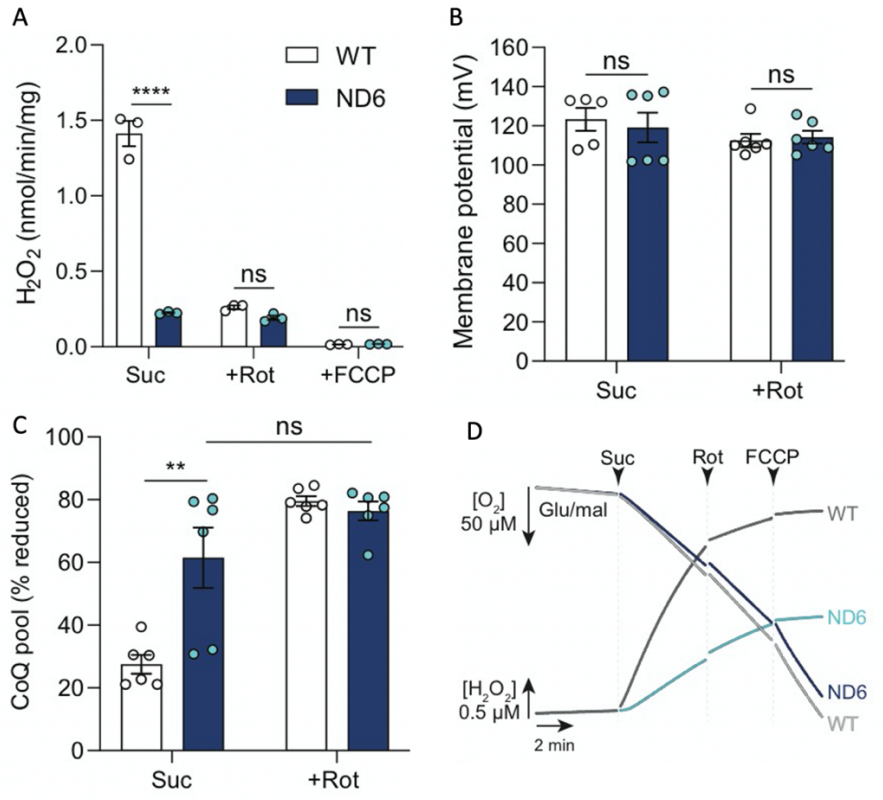

Fig 3.18 Reverse electron transfer in ND6-P25L and WT complex I from isolated heart mitochondria. (A) H_2O_2 production rate measured by adding succinate (10 mM). FCCP (5 µM) or rotenone (5 µM) were added as indicated. The data are mean values ± S.E.M. (n = 3, **** $p < 0.0001$). (B) Membrane potentials calculated from the accumulation of [^{3}H]-TPMP with the presence of succinate. The data are mean values ± S.E.M (n = 6). (C) The redox status of the CoQ pool was assessed by LC-MS. The data are mean values ± S.E.M (n = 6, **$p < 0.01$). (D) O_2 consumption and H_2O_2 production rate measured during glutamate/malate oxidation (0.5 mM). Succinate (10 mM), rotenone (5 µM) and FCCP (5 µM) were subsequently added as indicated.

3.6 Ischemia/reperfusion studies on ND6-P25L mouse heart

It is known that during ischaemia, the impeded blood supply to the tissue decreases the local O_2 level, which results in the accumulation of succinate in mitochondria. During reperfusion, the succinate is oxidised rapidly to drive RET in complex I to produce ROS which generates tissue damage (Chouchani et al., 2013, 2016; Martin et al., 2019). Besides, selective modification of exposed ND3-Cys39 in deactive state is known to have a cardioprotective role of reducing ROS damage during ischaemia-reperfusion (Chouchani et al., 2016). From the results of previous *in vitro* studies, it was identified that ND6-P25L-CI has a preferred deactive state conformation and the ROS production by RET is largely decreased. If the above-mentioned ischaemia-reperfusion model is correct, the ND6-P25L could also be cardioprotective during ischemic injury.

To verify this hypothesis, the complex I conformation status in tissue was checked by measuring the exposure of ND3-Cys39 by Mr Nils Burger and Dr Amin Mottahedin (Fig 3.19A). Ischemic and non-ischemic heart tissue was isolated and snap-frozen after the mice were sacrificed. The tissue was labelled with light and heavy ($^{13}C_2$, 2-d_2) iodoacetamide. The labelled ND3-Cys39 tryptic peptide was then detected by LC-MS/MS. In contrast to the WT-CI, the ND6-P25L-CI shows a higher ND3-Cys39 exposure rate even before the ischemia was initiated, indicating a larger deactive state complex I in ND6-P25L (Fig 3.19A). This is consistent with the results from the *in vitro* membrane studies that the ND6-P25L-CI is predominantly in deactive state. Comparing the ND3-Cys39 exposure rate during the ischemia (Fig 3.19A), the ND6-P25L tissue shows a much greater rate than the WT, indicating a greater complex I deactivation in ND6-P25L during ischemia.

To testify the cardioprotective potential of ND6-P25L-CI further, Dr Duvaraka Kula-Alwar from Dr Thomas Krieg's group (Department of Medicine, University of Cambridge) helped with several *in vivo* experiments mimicking the ischemia-reperfusion process in mouse heart. In brief, female ND6-P25L mice underwent 30-minute heart ischemia by left anterior descending (LAD) followed by 120-minute reperfusion (Antonucci et al., 2019). The image of

the infarct area (white) is highlighted in Fig 3.19B. The result in Fig 3.19C shows that the ND6-P25L mouse heart was significantly protected from ischaemia-reperfusion damage with approximately 50% less damage compared to the WT. Notably, the level of cardiac protection conferred by the ND6-P25L mutation is as good as the current known therapeutic interventions (Pell et al., 2018). Additionally, the succinate level and CoQ redox state measured in heart tissue by Dr Hiran A. Prag showed no significant difference between ND6-P25L and WT, indicating the reduced tissue damage is again an intrinsic effect of mutant complex I rather than a lower level of succinate accumulation in the tissue (Fig 3.19D and E). A global heart ischemia-reperfusion was then performed on isolated Langendorff-perfused hearts after ischemia by Dr Dunja Aksentijevic (Queen Mary University of London). The succinate level was measured, withthe level of succinate in ND6-P25L mouse heart shown to be the same as in the WT during ischemia and following ischemia-reperfusion (Fig 3.19F). This indicates that succinate was not able to drive RET in ND6-P25L mouse heart. The H_2O_2 production measured *in vivo* by MitoB oxidisation (Chouchani et al., 2014; Cochemé et al., 2011) (Fig 3.19F) shows no increase in H_2O_2 production after reperfusion was observed in ND6-P25L heart, while the WT heart had a significant increase of H_2O_2 production upon reperfusion. The *in vivo* study results above provide strong evidence that support this hypothesis. Therefore, the ND6-P25L complex I has cardioprotection potential due to its inability to produce ROS from RET during ischemia-reperfusion.

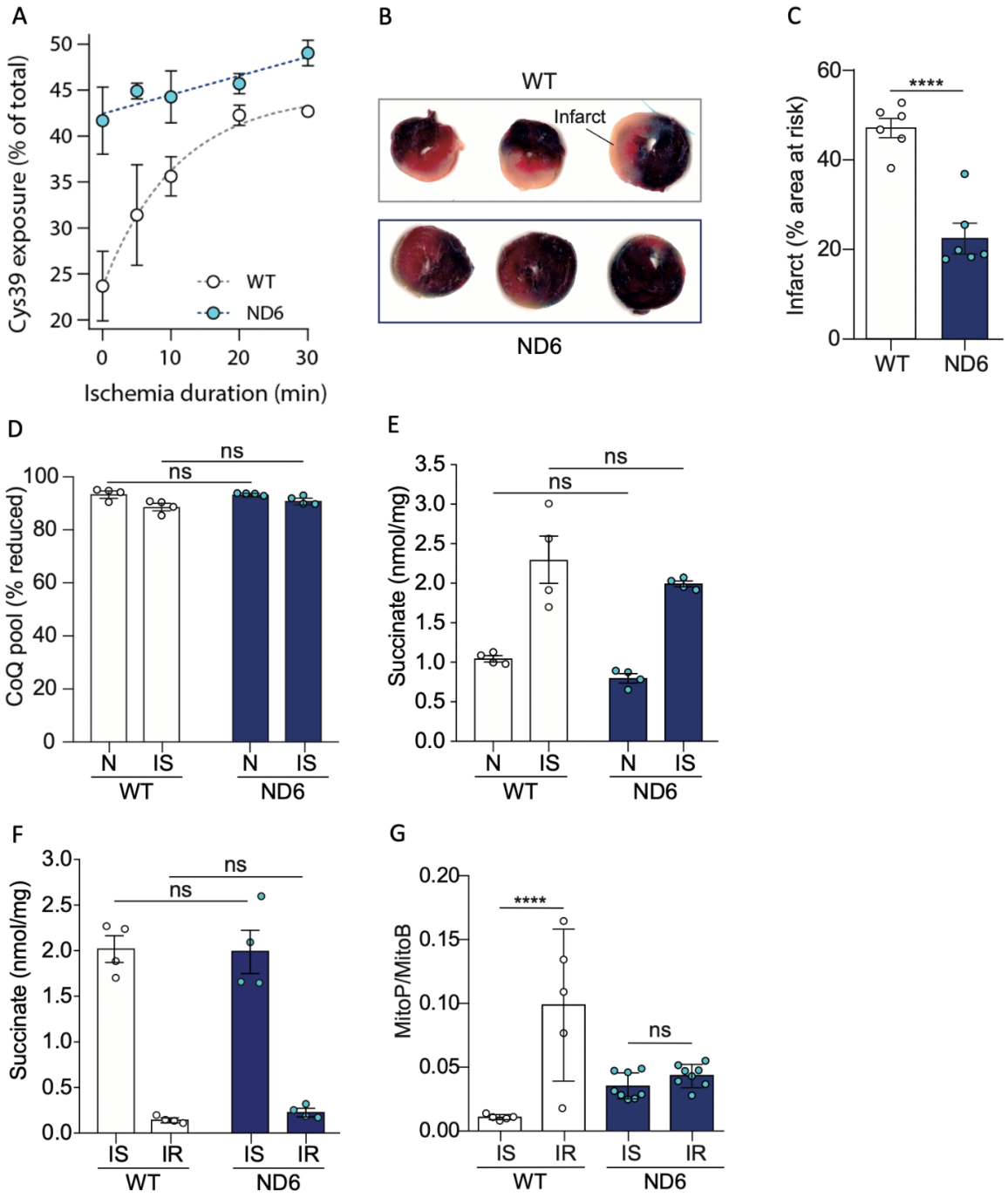

Fig 3.19 The cardioprotection potentional of ND6-P25L-CI during ischemia-reperfusion. (A) Deactivation rate of complex I from WT and ND6-P25L heart tissue during ischemia assessed by ND3-Cys39 exposure rate. The light and heavy ($^{13}C_2$, 2-d_2) labelled ND3-Cys39 peptides were detected by LC-MS/MS. The data are mean values ± S.E.M. (n = 3). (B) Images of heart slices showing cardiac infarct (the white colored areas). (C) The proportions of the cardiac infarct size among the risk area during ischemia-reperfusion. The data are mean values ± S.E.M. (n = 6, ****p < 0.0001). (D, E) Reduction level of the CoQ pool (D) and accumulation level of succinate (E) during normoxia (N) and ischemia (IS). The data are the mean value ± S.E.M. (n = 4). (F) The tissue succinate level after 20 min global ischemia (IS) or 20 min ischemia followed with 5 min reperfusion (IR). The data are mean values ± S.E.M. (n = 4). (G) The H_2O_2 production was assessed by MitoP/B ratio. MitoB was injected into ND6-P25L and WT mice by the tail vein followed with 30 min ischemia (IS) or 30 min ischemia + 15 min reperfusion (IR). The data are mean values ± S.E.M. (n = 5-8, **** p < 0.0001).

3.7 Discussions

3.7.1 ND6-P25L mice have a mild phenotype

The ND6-P25L mouse model was designed to mimic LHON syndrome with a reported decline in central smaller caliber optic nerve fibers and swelling axons (Lin et al., 2012). However, the severity of the phenotype varies between humans and the mouse model with the same amino acid substitution. It has been reported that a patient carrying the same homoplasmic mtDNA variant has severe Leigh syndrome, resulting in premature death (Malfatti et.al, 2007), while the mouse model had much milder phenotype and a normal lifespan (Lin et al., 2012). Although the P25 position is highly conserved across many eukaryotic species, there are mtDNA polymorphisms identified between human and mouse which could possibly alter the tolerance of the substitution and the phenotype severity.

In addition, a secondary factor should be considered besides the primary mutation, such as environmental factors and the nuclear DNA background. It has been reported that ND6-P25L mouse has a unique stress-response with a higher blood glucose level and inflammatory response in the hippocampus (Picard et al., 2015). As it was established that the ND6-P25L shows a lack of RET induced ROS, the abnormal responses of blood glucose level and inflammatory could possibly be due to the abolished RET-ROS signaling. Besides, another study of the ND6-P25L mouse with C57BL/6 (B6) gene background rather than C57BL/6(A/J) has shown enhanced lymphoma development (Hashizume et al., 2015), which suggested a synergistic pathological effect of this point mutation with a specific genetic background required. However, in this study, the point mutation itself on heart tissue has proven to be competent for normal forward catalytic activity. The ND6-P25L mouse heart is physiologically similar to the WT heart according to echocardiography (McManus et al., 2019). These all indicated that the ND6-P25L mutation could be an enhancer of some phenotypes with the presence of second factors (nuclear genetic abnormality or physical stress), but ND6-P25L mutation did not introduce any obvious phenotypes in the mice. Furthermore, the lack of ROS

production by RET in ND6-P25L mouse heart makes it an ideal cardioprotective model against ROS damage during ischemia/reperfusion (IR).

3.7.2. ND6-P25L-CI shows a deactive-like structure

The 3D reconstruction of the ND6-P25L-CI in this study has been shown to adopt a "deactive-like" structure. It is interesting that the ND6-P25L-CI does not need any additional methods to induce a deactive state in contrast with the WT which requires a 30-min, substrate-free incubation at 37 ˚C to achieve deactivation. It is known that the mammalian complex I is predominantly in the active form *in vivo* and the slow A/D transition only occurs under specific conditions, for example in the absence of substrate at a warm temperature (Kotlyar & Vinogradov, 1990; Grivennikova, Kapustin & Vinogradov, 2001), which can also be applied *in vitro* during warm ischemia (Maklashina, 2002).

The complex I in the mouse model shows for the first time that the deactive state mammalian complex I presents in a physiologically relevant condition without inducing treatments. The cryo-EM structure has also shown this point mutation causes subtle conformational changes in the distance between TMH2 and TMH3 in ND6 subunit. It suggests that the proline to leucine substitution increases the space for π-bulge formation which could reduce the steric hindrance during the A/D transition. Thus, the complex I is prone to stay at the lower energy deactive-state in the ND6-P25L mutant. The recent high-resolution cryo-EM study in yeast complex I has reported that the ND6 π-bulge formation could be the onset of deactivation initiating a series of conformational changes in ND1, ND3, NDUFS2, and NDUFS7 (Grba & Hirst, 2020). Together, this suggests that this single mutation has altered the local conformation around ND6 could eventually alter the enzyme catalytic state as a whole.

It is known that the deactive form of complex I is able to prevent the formation of ROS by reverse electron transfer during ischemia/reperfusion (Chochani et al., 2016). The A/D transition in complex I was considered as a target for therapeutic intervention (Galkin & Moncada, 2017). The distinct feature of ND6-P25L-CI being prone to stay in deactive state with a high sensitivity for substrate shortage makes it a perfect model for preventing ROS

damage during ischaemia-reperfusion. The LAD ligation experiment, mimicking the ischaemia-reperfusion process shows a significantly reduced infarct on the ND6-P25L mouse heart, in a result that is as effective as the currently available therapeutic interventions (Pell et al., 2018). These results also suggest that targeting a rapidly reversible deactivation of complex I during reperfusion could be a promising therapeutic strategy in the future.

3.7.3 ND6-P25L-CI is unstable in the active state

The biochemical studies on ND6-P25L-CI in membranes have shown that mutant mitochondria prepared with the same protocol (Agip et al., 2018) contain complex I largely in the deactive state in, while in WT, the majority of CI is in the active state. Interestingly, the ND6-P25L-CI is capable of achieving the same maximum NADH:O_2 oxidoreduction rate as the WT complex I without the typical lag-phase associated with the A/D transition, suggesting a normal functional state during turnover. This showed a unique character of ND6-P25L-CI whereby it is capable of normal forward electron transfer and competent catalytic activity but collapses into the deactive state in the absence of substrate. It is known that the reverse electron transfer was not observed in deactivated bovine complex I using submitochondrial particles (SMP) (Kotlyar & Vinogradov, 1990). If the ND6-P25L is in the deactive state, reverse electron transfer could not be achieved thus the ND6-P25L-CI is incapable of ROS production by RET. Whether ND6-P25L is able to perform RET can be verified in model systems such as SMPs or proteoliposomes (Biner, Fedor, Yin & Hirst, 2020).

The previous study also showed a decreased NADH:ubiquinone oxidoreductase activity in ND6-P25L mice liver (Lin et al., 2012). Similarly, the purified ND6-P25L-CI from mice hearts also showed a decrease in the activity; however, in mitochondrial membranes, the NADH:O_2 oxidoreductase activity and ROS production were decreased but this is due to less complex I content in the ND6-P25L heart mitochondria thant in the WT, which differs from the findings in synaptosomes (Lin et al., 2012). The re-activation experiment on deactivated WT membrane and ND6-P25L indicated that the complex I from the ND6-P25L cannot maintain its active state even with sufficient substrates during prolonged turnover. The time-dependent NADH:O_2 oxidoreduction with NEM showed that while undergoing steady-state NADH oxidation, the

enzyme is still NEM sensitive. In other words, the cysteine-39 in ND3 subunits remains highly solvent accessible in this mutant and thus, the NEM can access it during turnover.

These biochemical results combined with the structural analysis suggest that the ND6-P25L-CI is unstable in its active state. With sufficient substrate, it either rapidly switches between NEM sensitive and insensitive states or it has several intermediate states between active and deactive (Fig 3.20). A recent study by Grivennikova et al. has proposed extra biochemical states of complex I rather than active and deactive states: a cysteine-residue-reactive deactive state and a proton-motive force-induced active state (Grivennikova, Gladyshev & Vinogradov, 2020). It is feasible that some intermediate states exist between the canonical A and D states determined from structural biology. Further studies are required to clarify the conformational changes that take place during the A/D transition and whether intermediate states can be accessed for robust structural analysis.

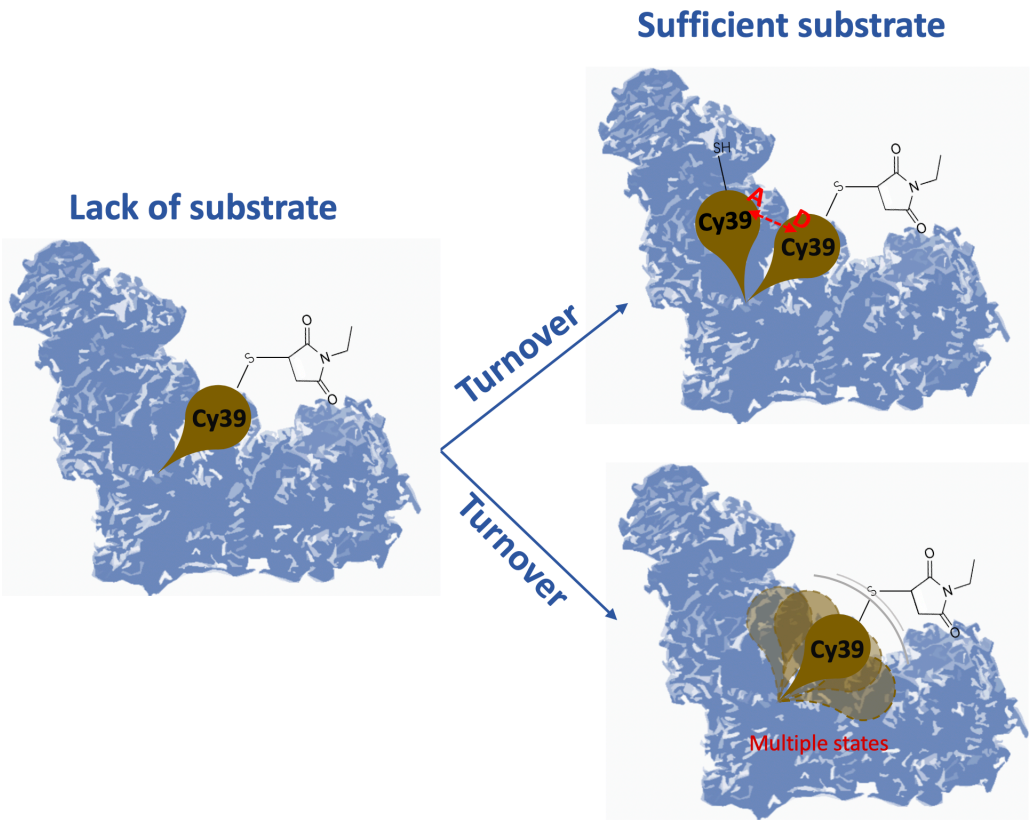

Fig 3.20 The proposed ND6-P25L-CI conformational change during turnover. When lacking of substrate, the ND6-P25L-CI is in the deactive state/cys39 exposing state. During turnover with sufficient substrate, the ND6-P25L-CI can either rapidly switch between A/D state or it stays in multiple intermediate states between A/D states.

3.8 Conclusion and future works

In this chapter, the first high-resolution cryo-EM structure of mammalian complex I with a disease-associated mtDNA point mutation was presented. The single mutation substitution in this structure surprisingly switches the state of the enzyme as a whole: the mutant complex I has a propensity to be in the deactive state. The subtle difference around the ND6 subunit suggests a possible reduction in the energy barrier during the A/D transition, thus the enzyme becomes catalytically unidirectional. The biochemical studies on both mitochondrial membranes and isolated heart mitochondria are in the line with the cryo-EM structure indicating that the ND3-Cys39 in ND6-P25L-CI remains exposed during catalysis. The mutant complex I shows a normal NADH:ubiquinone catalytic activity but significantly decreased ROS production by RET. The *in vivo* IR study on the ND6-P25L mouse suggests that the mutant complex I is cardioprotective against IR injury. The combination of structural, biochemical and *in vivo* experiments in this study together illustrates the effects of the point mutation on the function of complex I and has highlights a promising therapeutic strategy of reversibly targeting deactive state complex I for IR injury in the future.

Chapter 4. High-resolution cryo-EM structure of complex I from the NDUFS4 knockout mouse model

4.1 Introduction

4.1.1 The structure and function of the NDUFS4 subunit

NADH:ubiquinone oxidoreductase iron-sulfur protein 4 (also known as NDUFS4 in mouse and human, 18 kDa in bovine, and NUYM in *Yarrowia*) is a nuclear DNA encoded 18 kDa accessory subunit of mammalian complex I (Carroll et al., 2006). The NDUFS4 protein, alongside two other accessory subunits (NDUFS6 and NDUFA12), is located at the interface between the N module and Q module of the complex I (Fig 4.1A). The C-terminus of NDUFS4 crosses the interface of the N-module, and is positioned close to the iron-sulfur (FeS) cluster N3 in NDUFV1. Interestingly, the orthologs of these three accessory subunits (NDUFS4, NDUFS6, and NDUFA12) have also been identified in complex I from the α-proteobacteria *Paracoccus denitrificans*, which is considered as an ancient predecessor of the mitochondrion (Yip et al., 2011). The NDUFS4 subunit is thought to be added in the final stages of the mammalian complex I assembly, together with NDUFV3, NDUFA12, and NDUFS6 (Guerrero-Castillo et al., 2017). The NDUFS4 subunit has long been regarded as an important accessory subunit for complex I assembly and activity, but how it interacts with other subunits during assembly and how it regulates the complex stability are yet to be conclusively determined.

The *ndufs4* gene was identified in human chromosome 5 where it is comprised of five exons (Emahazion, Beskow, Gyllensten & Brookes, 1998). The *ndufs4* gene product of the NDUFS4 precursor, containing 175 amino acids, is highly conserved in mammalian species (Fig 4.1B). The import and maturation of NDUFS4 is controlled and promoted by phosphorylation of the C-terminal serine (Ser173) at a C-terminal RVSTK consensus site by cAMP-dependent protein kinase (PKA) (Fig 4.1B) (Papa, 1996, Scacco et al., 2000). The mature NDUFS4 subunit contains 133 amino acids in humans, within which, the serine (Ser129) is reported to be

reversibly phosphorylated by PKA and protein phosphatase (Sardanelli et al., 2006; Signorile et al., 2002). The phosphorylation on NDUFS4 was considered as a “rejuvenation” process for mammalian complex I allowing the exchange and replacment of damaged peripheral subunits (Lazarou, McKenzie, Ohtake, Thorburn & Ryan, 2007). However, a proteomic study of the phosphorylation of the complex I from bovine heart mitochondrial membranes and isolated enzyme argued that the phosphorylation occurs on Ser20 of the NDUFB11 subunit instead of the NDUFS4 subunit (Chen, Fearnley, Peak-Chew, & Walker, 2004). This result was then questioned since the small-size C-terminal sample of NDUFS4 digested by trypsin may be not detected by mass spectrometry (De Rasmo, 2010). A further study of immunoblotting with ^{32}P labeling on isolated bovine complex I has shwon the phosphoserine in matured NDUFS4 and its precursor (De Rasmo, 2010). Furthermore, a recent study has shown that decreasing the phosphorylation of NDUFS4 on mouse brain astroglial cells can destabilise complex I, with the mutation of Ser173 to Glu significantly blocking the degradation of the N-module (Jimenez-Blasco et al., 2020). These results provide strong evidence that the phosphorylation on NDUFS4 is physiologically relevant.

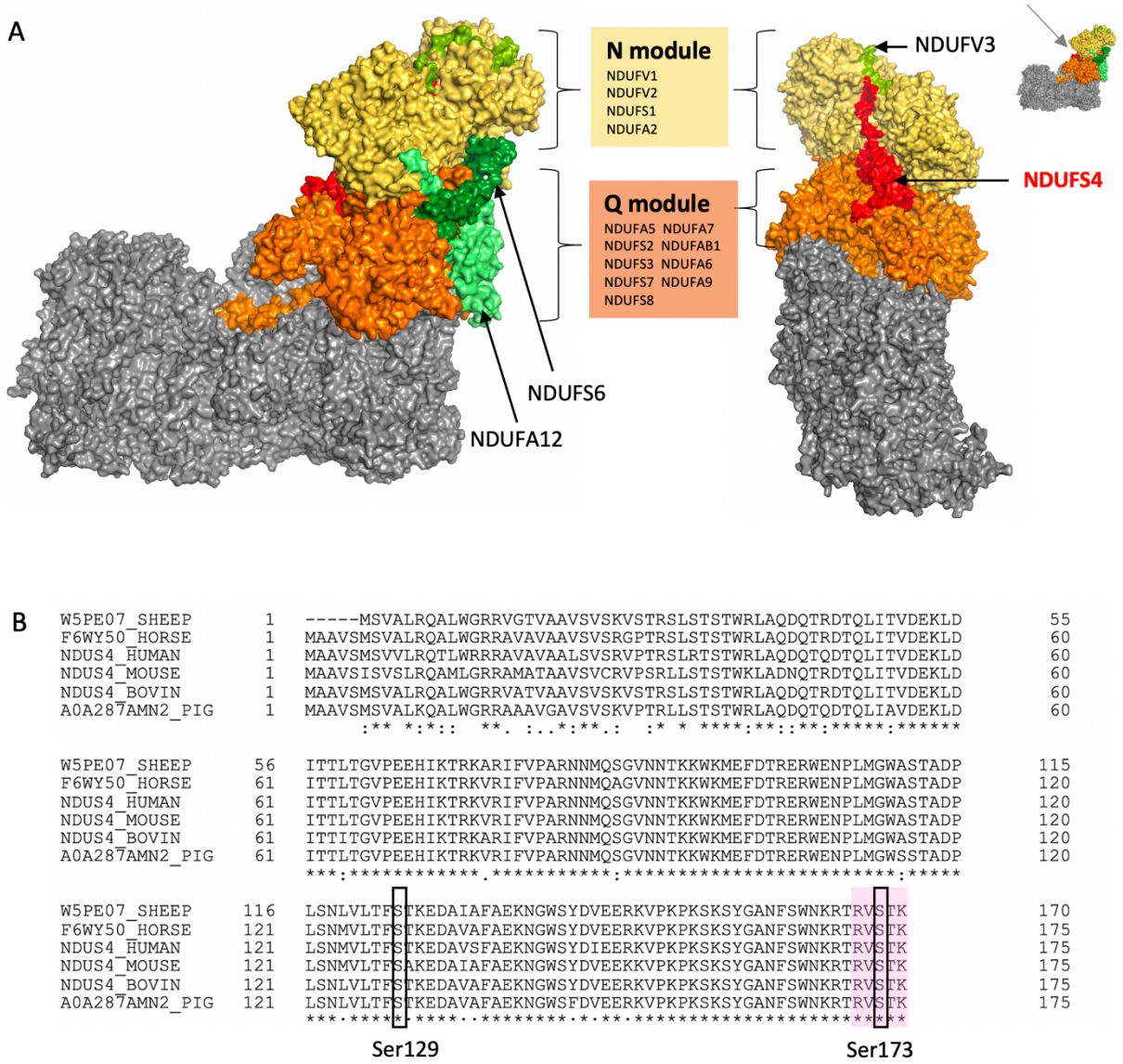

Fig 4.1 The location of the NDUFS4 subunit in complex I and its genetic conservation. (A) NDUFS4 subunit of complex I is highlighted in red, N-module is in yellow; Q module is in orange. Accessory subunits NDUFA12 (light green), NDUFS6 (dark green), and NDUFV3 (pale green) are labeled with arrows. The complex I density map is adapted from the mouse active model (PDB: 6G2J) from Agip et al. (2018). (B) NDUFS4 protein sequence alignment from multiple mammalian species. Sequences were obtained from the Swiss-Prot database and aligned with Clustal Omega (Söding, 2005). The highly conserved c-terminal RVSTK consensus site is indicated by the pink square. Two phosphorylation sites (Ser129 and Ser173) are marked out with squares.

4.1.2 Diseases associated with *ndufs4* mutations

A patient with *ndufs4* pathogenic variant was first reported in 1998 (van den Heuvel et al., 1998). This patient showed non-specific fatal progressive phenotypes, including severe psychomotor retardation and hypotonia leading to death of cardiorespiratory failure at 16 months old. The cerebral magnetic resonance imaging (MRI) revealed brain atrophy and

symmetrical basal ganglia abnormalities. The genetic diagnosis identified a 5-bp duplication, which destroys the C-terminal phosphorylation site and leads to immature NDUFS4 formation. Biochemical studies showed a decrease in NADH:ferricyanide activity in the patient's skeletal muscles and decreased NADH:Q1 activity in fibroblasts (van den Heuvel et al., 1998).

Following the first reported patient with NDUFS4 pathogenic variant, more than 20 cases have since been reported (Ortigoza-Escobar et al., 2016). 13 alterations associated with clinical phenotypes were identified in the NDUFS4 gene. The common clinical presentations include Leigh-syndrome (LS) or severe Leigh-like symptoms (Breuer et al., 2013). LS is a fatal neurological disorder and the NDUFS4 patients succumb to the disease before the age of 3 (Ortigoza-Escobar et al., 2016). However, clinical cases have not been limited to neurological disorders, with some NDUFS4 patients also displayed pathologies associated with high lactate levels in blood plasma, ataxia, and loss of motor skills (Budde et al., 2003; Ortigoza-Escobar et al., 2016). There are some common features displayed in biochemical studies on patients' muscle biopsies and primary skin fibroblasts. Firstly, a significant decrease in complex I activity (more than 50% of the minimal control value) was observed in all reported NDUFS4 patient fibroblasts and muscle (Ortigoza-Escobar et al., 2016). Moreover, a decreased CIII activity was observed in some patients fibroblast which suggests NDUFS4 related complex I deficiency may have an influence on other OXPHOS enzyme activity (Budde et al., 2000). It was still debatable whether the completion of complex I assembly requires the interatction with complex III and IV to form supercomplex (Moreno-Lastres et al., 2012; Enríquez, 2016). Furthermore, the accumulation of an 830-kDa subcomplex and an 830-kDa-CIII3 holocomplex was observed in BN-PAGE analysis instead of the intact complex I in NDUFS4 patients' biopsies (Scacco et al., 2003; Ugalde, Janssen, van den Heuvel, Smeitink & Nijtmans, 2004; Assouline et al., 2012). These clinical studies suggest the NDUFS4 mutant could result in decreased complex I activity and enzyme stability.

4.1.3 Mouse models with *ndufs4* mutations

To further understand the pathogenesis of *ndufs4* mutation-associated diseases, the first NDUFS4 dysfunction mouse model with *ndufs4* whole-body knockout (referred as "*ndufs4* KO"

and “KO” in this chapter) was designed (Kruse et al., 2008). The mice display Leigh-like phenotypes including growth retardation, ataxia, motor dysfunction, and progressive fatal encephalomyopathy resulting in a short life-span of 7 weeks (Kruse et al., 2008). The *ndufs4* KO mouse stops growing at postnatal day 30 (P30) with a maximum bodyweight of 15 g (Fig 4.2A). The *ndufs4* KO mouse has also shown a hair loss cycle starting around P29 with regrowth at P42, and a hunched appearance at P42 (Fig 4.2B).

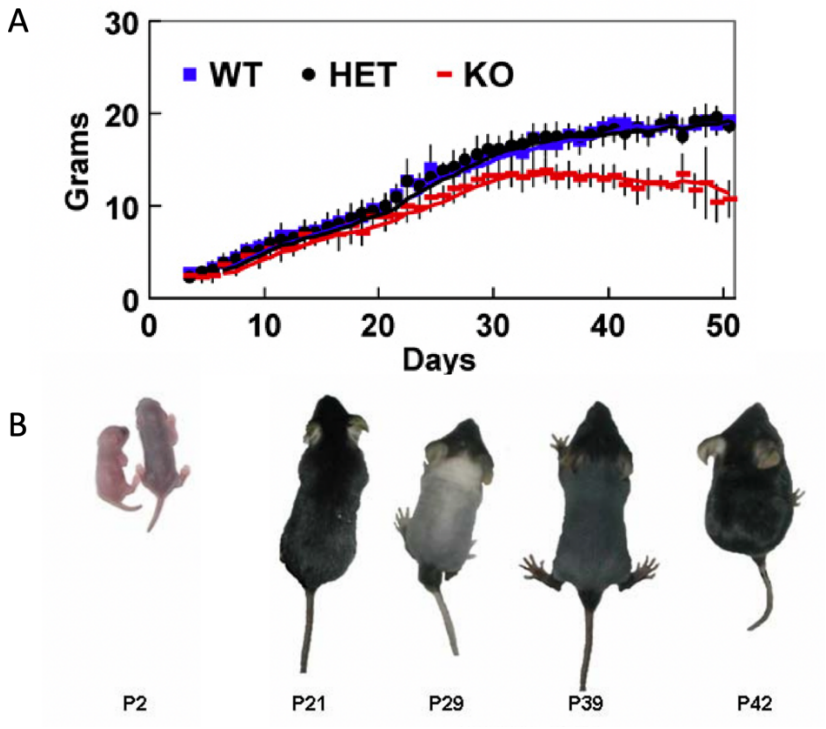

Fig 4.2 Growth rate and phenotype of *ndufs4* KO mice. (A) Growth curves of wild type (WT), heterozygous (HET), and knockout (KO) mice. n = 4–56. (B) Photographs of KO mice at different postnatal days. The figure and images were adapted from Kruse et al. (2008).

The *ndufs4* KO was designed using a frameshift mutation to preclude the synthesis of the mature NDUFS4 protein (Kruse et al., 2008). Exon 2 flanked by loxP sites resulted in the deletion of exon 2 and no production of mature NDUFS4 protein. The in-detailed gene targeting strategy of generating *ndufs4* KO mice was shown in the previous study (Kruse et al., 2008). Subsequently, the activity and stability of the OXPHOS enzymes in the *ndufs4* KO mouse were assessed in several studies (Kruse et al., 2008; Calvaruso et al., 2012). Some of the results are summarised as follows:

1) Complex I activity measured by monitoring oxygen consumption is half that of control in liver tissue and is not detectable in submitochondrial particles (SMPs).

2) The abundance of intact complex I, assessed by BN-PAGE, was decreased in the *ndufs4* KO mice liver and brain. An inactive 830-kDa CI subcomplex was observed in the pancreas, kidney, liver, lung, brain, heart, and muscle tissues.

3) Normal activity of complex II was observed in KO kidney SMPs; normal activity of complex III and IV was identified in the *ndufs4* KO kidney tissue.

4) O2 consumption and ATP levels were unchanged between control and *ndufs4* KO mice in muscle tissue.

After the *ndufs4* whole-body knockout mouse was developed, *ndufs4*-point mutation mice were generated by introducing a stop codon truncating the last 10-15 amino acids on the NDUFS4 protein (Ingraham et al., 2009). The homozygous mutation is embryonic lethal and the heterozygous shows decreased complex I activity and normal complex II activity indicating that the effect of the mutation on NDUFS4 subunit is complex I specific.

Alongside the *ndufs4* whole-body knockout mouse, several tissue-specific *ndufs4* knockout mice have been generated to investigate the tissue-specific pathology associated with the mutation (Roestenberg et al., 2012; Quintana et al., 2010). The neuron-specific knockout mice, and glia-specific *ndufs4* knockout mice have shown clinical phenotypes similar to that of the whole-body *ndufs4* KO which suggests a major influence of the *ndufs4* mutation on the neuron tissue (Quintana et al., 2012; Sterky et al., 2012). The heart-specific *ndufs4* KO mice, with the phenotype of cardiomyopathy, have shown a 50% decrease in complex I activity in heart tissue (Chouchani et al., 2014). Normal cardiac function was abolished under stress conditions with accelerated heart failure (Karamanlidis et al. 2013; Sterky et al., 2012). Taken together, the results from tissue-specific knockout studies suggest that the *ndufs4* associated complex I deficiency has different pathological displays depending on the tissue types. This could explain

the various phenotypes and low genotype-phenotype correlation observed in NDUFS4-mutant patients.

4.1.4 Potential therapies for *ndufs4* associated complex I dysfunction

No specific treatment is available for *ndufs4* associated complex I dysfunction at the moment. However, the animal models designed with *ndufs4* gene mutations have enabled studies to be conducted into potential therapies for combating *ndufs4* deletion-linked pathologies. Treatment of the *ndufs4* KO mouse with a small molecule ROS-redox modulator (KH176) has been reported to confer beneficial effects, including improved rotarod performance and reduced degeneration of the retinal ganglion (De Haas et al., 2017). This new chemical is currently undergoing clinical trials to explore its potency against oxidation stress in mitochondrial disease patients and assess the safety of its use (Janssen et al., 2019). In addition to this, a recent study carried by Ferrari et al. (2017) on *ndufs4* KO mice showed that hypoxia treatment could not only prevent but also reverse the brain damage observed in the mouse model (Ferrari et al., 2017). Although non-invasive hypoxia therapy has proven to be effective in the mouse model, its efficacy and potential side effects are yet to be addressed in humans. Recently, it was determined that supplementation of the NAD^+ precursor, nicotinamide mononucleotide, was capable of extending the lifespan of the *ndufs4* KO mouse, suggesting a degree of therapeutic potential (Lee, Caudal, Abell, Nagana Gowda & Tian, 2019). Moreover, gene replacement techniques using adeno-associated viral (AAV) vectors to reinstate gene expression in the *ndufs4* KO mouse model has shown improved locomotor activity and corrected the pathological phenotype in multiple organs (Reynaud-Dulaurier et al., 2020; Silva-Pinheiro, Cerutti, Luna-Sanchez, Zeviani & Viscomi, 2020). Although therapeutic efficacy and safety should be addressed in future clinical studies, the pre-clinical studies mentioned above have shown promising results and potential therapeutical strategies in rescuing the survival rate of mouse models.

4.1.5 *Ndufs4* deletion in other species

In addition to the mammalian species discussed above, deletion of the NDUFS4 subunit has also been studied in plants (*Arabidopsis thaliana*) and yeast (*Yarrowia lipolytica*) (Kühn et al., 2015; Kahlhöfer, Kmita, Wittig, Zwicker & Zickermann, 2017; Parey et al., 2019). In arabidopsis, the *ndufs4*-deleted complex I has a remarkably low enzyme activity, concomitant with the loss of the NADH:ubiquinone oxidoreductase flavoprotein (NDUFV1) as observed by blue native gel analysis. Unlike in humans, the *ndufs4* deletion in plants does not cause premature death, only showing a mild growth phenotype which could be due to the presence of alternative NADH dehydrogenases (NDH) to compensate for the absense of functional complex I (Meyer et al., 2009).

The study in yeast showed a complex I assembly intermediate which lacks the NUYM subunit (human NDUFS4) but contains the additional assembly factor, N7BML (human NDUFAF2) (Kahlhöfer et al., 2017). The authors of this study identified that the loss of NUYM destabilises the structure of the N1b and N3 iron-sulfur clusters, and they suggested that such distortion at the electron input module is the cause of increased ROS production. Later, a cryo-EM structure of the complex I lacking NDUFS4 was determined (Parey et al., 2019). Contrast to their previous predicted results, the mutant complex I does not show NDUFAF2 attachment. Besides, not shifting of the N1b and N3 clusters was identified in the cryo-EM structure. The comparisons of the mutant structures from yeast and mouse are shown in the disscussion section of this chapter.

4.1.6 Previous studies on complex I from *ndufs4* KO mouse heart

The previous biochemical and proteomic studies undertaken on the *ndufs4* KO mouse heart mitochondrial membranes were performed by Dr Ahmed-Noor Adam Agip and have shown some distinct features (Agip, 2018). Firstly, the complex I-dependent NADH:O2 activity in the membrane and NADH:DQ activity of purified complex I have shown only 10% and 7% of the activity comparing to the WT control, respectively. The NADH:APAD+, NADH:FeCN and NADH:hexammineruthenium (HAR) transhydrogenase reactions on the *ndufs4* KO heart

mitochondrial membranes have shown less than 50% the activity of the WT control. The catalysis through complex II, III and IV shows no change. Secondly, the proteomic BN-PAGE complexome profiling (Fig 4.3) showed a lower abundance of intact complex I in KO mice heart, an 830-kDa subcomplex band, which overlaps with the complex V band on the BN-PAGE; and a 200 kDa flavin complex which co-migrates with complex IV. Interestingly, two assembly factors: ACAD9 and NDUFAF2, which are involved in early and late-stage assembly respectively, were identified within the 830-kDa subcomplex, but not on the intact complex I.

Thirdly, the EPR spectroscopy measurements carried out by Dr John Wright shows removing of the NDUFS4 has diminished signal of the detected four FeS clusters (N1b, N2, N3 and N4) comparing to the WT, indicating altered intramolecular electron transfer. A temperature based flavin association assay showed that the FMN in *ndufs4* KO has the same stability as in the WT. Additionally, an initial crosslinking experiment on 1% DDM solubilised mouse heart mitochondrial membranes with BS3 concentration over a range of 0.1 mM to 1 mM showed a reduced NBT-sensitive flavin complex band on BN-PAGE indicating a promising result for improving *ndufs4* KO complex I integrity on the gel.

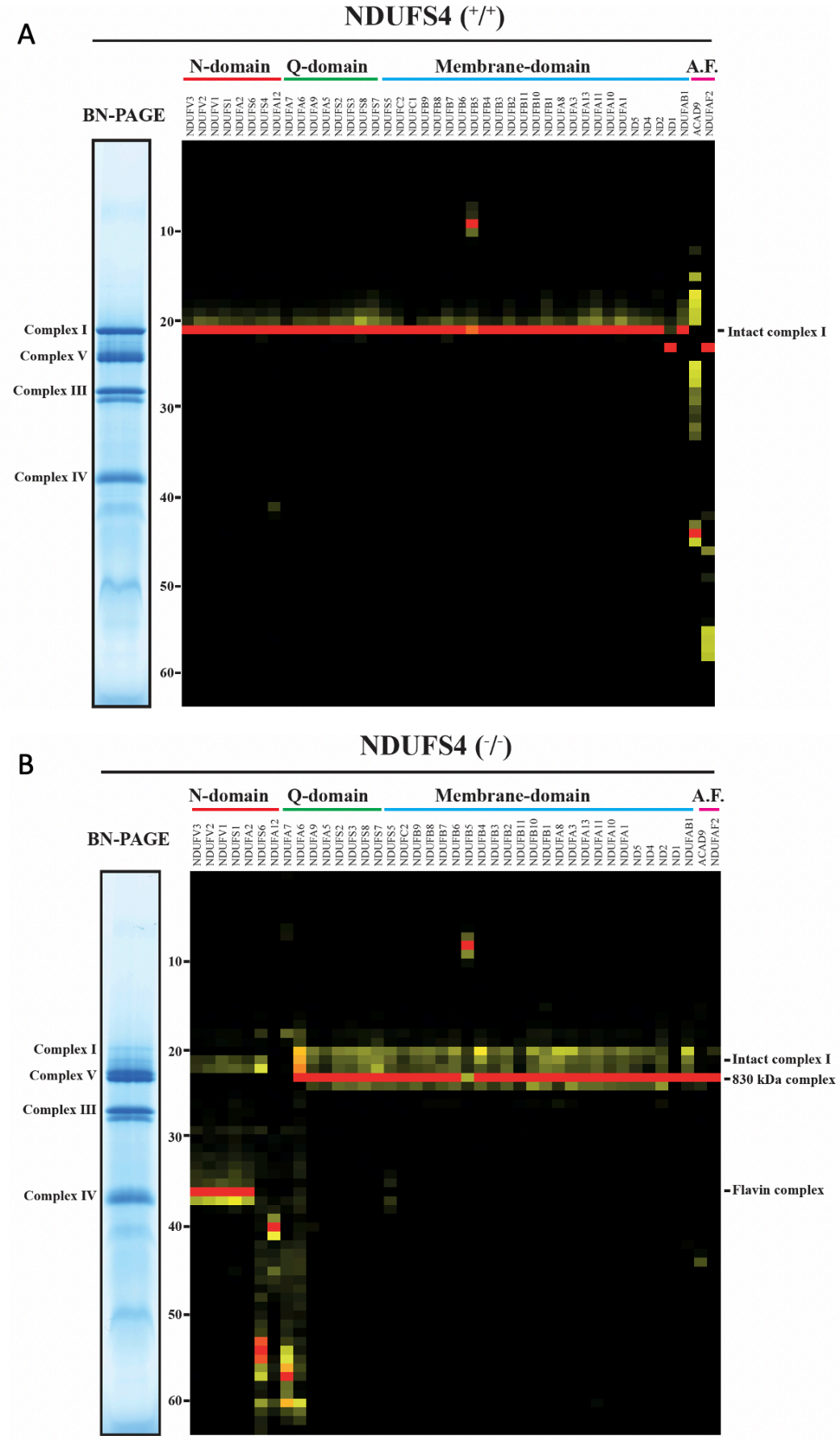

Fig 4.3 Complexome profiles of WT and *ndufs4* KO mouse heart mitochondrial membrane. The heat map indicates the migration pattern of proteins. The images were adapted from Agip (2018).

4.1.7 Aims

The function, structure, and assembly of the NDUFS4 subunit have been studied for over 25 years with mutations on this accessory subunit strongly associated with mitochondrial diseases. To expand the knowledge of the role of NDUFS4 subunit in complex I assembly and disease, a structure-based investigation of the *ndufs4* deletion is required. The mouse models with the *ndufs4* knockout have provided the opportunity to investigate the mechanism behind the pathogenesis. This study aims to understand the molecular basis of NDUFS4-related complex I deficiency and complex I assembly by reconstructing a high-resolution complex I from the *ndufs4* knockout mouse heart using cryo-EM technology.

4.2 Ndufs4 KO mice colony management and mitochondrial membrane preparation

4.2.1 Mouse breeding

The homozygous *ndufs4* KO mouse is not suitable for breeding as it has a progressive lethal phenotype resulting in an average life span of ~7 weeks (Kruse, et al., 2008). Thus, heterozygous (HET, *ndufs4*$^{+/-}$) crossbreeding was required to continuously produce KO (*ndufs4*$^{-/-}$) offspring. The mouse colony was set up with the help of Dr Carlo Viscomi under the project license number: P6C97520A. One male HET mouse and two female HET mice at the age of 8 weeks old were selected for setting up each breeding cage. Five breeding cages were set up for a breeding lifespan of around 24 to 30 weeks. In total, 20 breeding cages were set up for two years.

A summary of the strain characteristics is shown in Table 4.1. Some of the characteristics are compared with the WT mice with the same C57BL/6 genetic background. The average number of litters each HET female can deliver is 5.1±0.57 which is similar to the averaged litter numbers of 5.4 in the WT mice (Lambert, 2007). The average litter size for HET females is 7.1 ±0.28 which is higher than the average WT litter size of 5.6 (Lambert, 2007). After the pups were weaned at 21 days, an additional porridge meal was supplied with the normal food pellets in each newly weaned cage. Two non-productive breeders were identified as producing no litter within 60 days of mating. The male breeder mice were then immediately replaced by older males to improve breeding performance. A total number of 676 mice were produced, of which 45.9% were females, which is close to 47% in the WT (Lambert, 2007). Out of 676 newborns, the successful wean pup number was 581. A total of 95 newborns died before weaning from 14 litters. The wean-to-born ratio is 0.86 which is slightly smaller than that observed in the WT (0.92) (Lambert, 2007). This indicates that the pre-weaning pup mortality is higher in this strain compared to the WT. This could be due to the large litter size produced in this strain and the litter overlap being as there are two females in one breeding cage (Morrello et al., 2020). Whether this high mortality is *ndufs4* knockout related remains unclear.

Table 4.1 Strain characteristics

Breeding stock	40 females (2 female x 1 male /cage**)**
Breeding scheme	Heterozygote x Heterozygote
Breeding lifespan	24 - 30 weeks
Percent non-productive breeders	10% (2 cages)
Number of litters produced	5.1 litters
Litter frequency	1 litter/ 5.7 weeks/ cage
Litter size	7.1 pups
In total offspring	676
Offspring gender ratio	45.9% female; 54.1% male

For the KO offsprings, the noticeable feature of the hair loss cycle starting at 4 weeks old and ending at 6 weeks old was observed, which was also described by Kruse et al. (2008). The KO mouse were smaller in size than their WT/HET siblings at 3 to 4 weeks old. The KO mice were also observed with splayed hind legs, fewer movements, and an unbalanced, hesitant walk starting at 4 weeks old. The KO mice were culled between 4 to 5 weeks old with cervical dislocation before the onset of further severe phenotypes based on the principles of the 3Rs (replacement, reduction, and refinement) to minimise animal suffering.

4.2.2 Mouse genotyping

Although the obvious phenotypes were observed on the KO mouse compared to their HET siblings, genotyping on each offspring was required to verify their genetic identity before conducting any experiments. At the age of 3-4 weeks old, ear punches on each mouse of the litter were performed and the ear biopsy from each mouse was collected separately, and frozen at -20°C by the technicians in the Phenomics Laboratory, University of Cambridge. The biopsies were then collected from the animal facility and transferred to the lab for genotyping the following day.

To genotype the mice, the DNA extraction sample from the mouse earclip biopsy underwent PCR with two different sets of primers (see Fig 4.4A, the sequences are given in Chapter 2.2.1). The WT allele showed a smaller product size compared to the knockout allele. As shown in Fig 4.3 A and B, the wild type (*ndufs4*$^{+/+}$, WT) mouse (lane 1 in Fig 4.3 A and B) only shows the 150 bp band and the KO mouse, only shows the 250 bp band, indicating the removal of exon2

by loxP (lane 2); the HET mouse contains both alleles and so has both the 150 bp and 250 bp bands (lane 3).

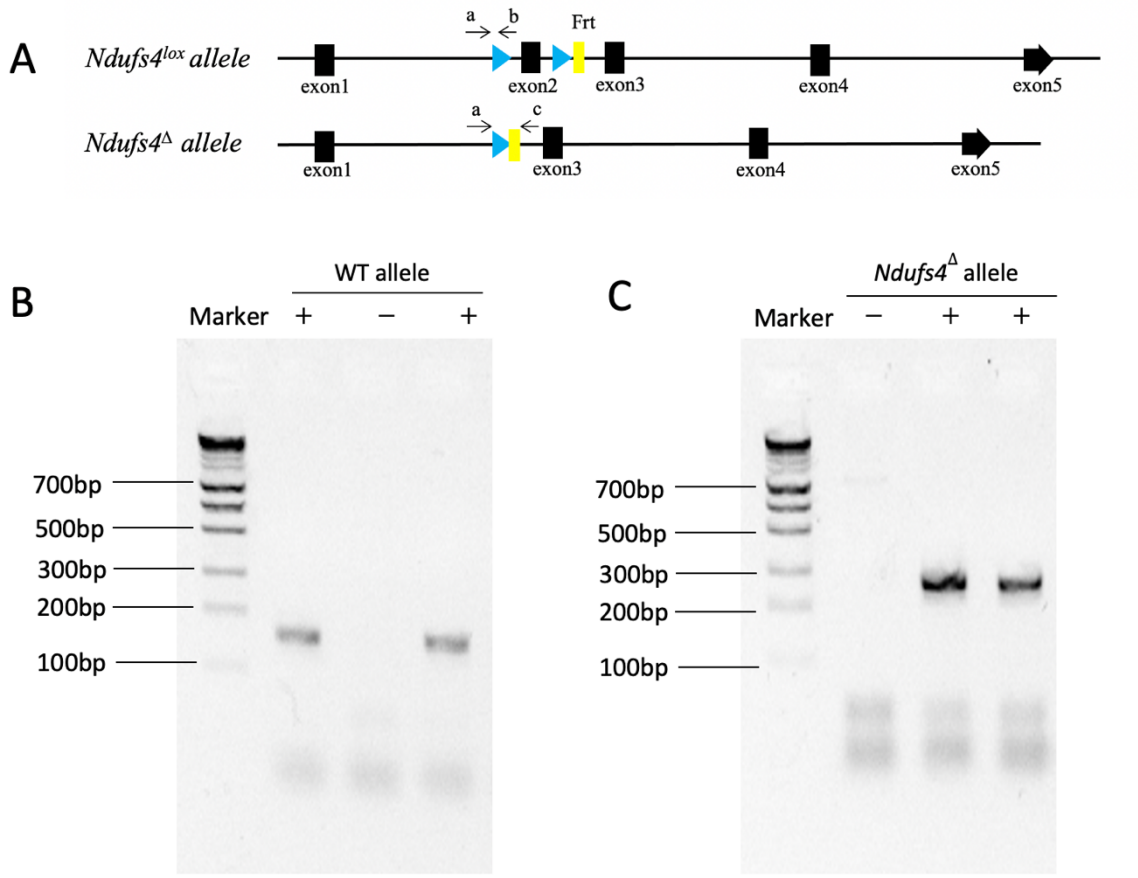

Fig 4.4 Mouse genotyping for ndufs4 deletion. (A) Illustration of the locations of the primers used in genotyping. To identify *the ndufs4*$^{\Delta}$ allele and *ndufs4*^{lox} (WT) allele, the same forward primer sequence (marked as "a") was used. The reverse primer for the WT allele is b, while for the *ndufs4*$^{\Delta}$ allele is c. Then the targeted allele can be identified by PCR using primers a and b giving a 250 bp band for *the ndufs4*$^{\Delta}$ allele and 150 bp band for the WT allele; The *ndufs4*$^{\Delta}$ allele was identified using primers a and c. The black squares represent the location of exons, the blue triangles show the loxP sites, the yellow square shows the Frt site. Frt is the positive selection site for target construction. (B) and (C) are examples of electrophoresis of PCR products from WT, KO, and HET mouse (lanes from left to right) DNA with two different primers to identify different alleles.

The summary of the genotype experiments is shown in Table 4.2 and Fig 4.5. Among 581 offspring mice, 263 (45.3%) are females. Approximately 21.7% of the offspring identified as KO (*ndufs4*$^{-/-}$), and around 50.2% were identified as HET. The percentage of KO mice is lower than the expected Mendelian frequencies (25%). The published genotype ratio of 790 mice from Palmiter's group showed 23% identified as KO mice and is consistent with the result from this study(Kruse et al., 2008). The offspring genotype percentage was further analysed on the basis of sex and showed that out of the total male offspring the percentage of KO mice (19.5%)

is significantly lower than the expected Mendelian frequencies of 25%; while the KO female mice have shown 24.3% which is close to 25%. This interesting observation suggests that there is a sex-related unfavoured inheritance of the mutant allele and a lower survival rate in male homozygous for *ndufs4* deletion.

Table 4.2 The genotypes distribution of offspring from *ndufs4* heterozygous cross

	Female	**Male**	**Total number**
WT	61 (23.2%)	102 (32.1%)	163 (28.1%)
HET	138 (52.5%)	154 (48.4%)	292 (50.2%)
KO	64 (24.3%)	62 (19.5%)	126 (21.7%)
Total number	263 (100.0%)	318 (100.0%)	581 (100.0%)

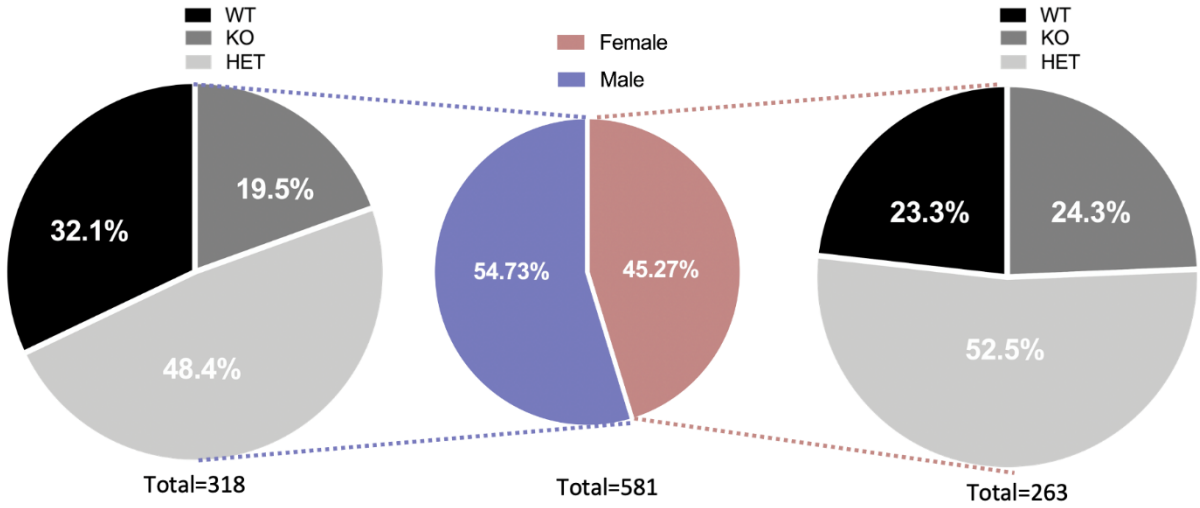

Fig 4.5 Summary of the offspring genotypes among 581 offspring. The central pie chart shows the total male and female percentage of the offspring. The left and right pie charts show the percentage of WT, HET, and KO mice among the male and female offspring respectively. The male KO mice percentage (19.5%) shown on the left panel is much lower than expected Mendelian frequencies (25%).

4.2.3 Tissue collection and membrane preparation

Following the genotyping results, the KO mice and the WT siblings aged 4 to 5 weeks old were culled and several tissues were collected. The tissue collection was performed with the help of Dr Ahmed-Noor Adam Agip and Mr Daniel Grba. In each tissue collection session, a minimum number of 4 KO mice were required for the following mitochondrial preparation. If less than 4 KO mice were obtained, the chopped mice tissue was snap-frozen in isopentane cooled with liquid N_2 and stored at –80°C. The KO kidney tissue was stored as an alternative tissue for optimisation of the purification process, allowing the limited KO heart tissue to be saved for

the cryo-EM study. Besides, the NADH:APAD$^+$ experiment (Table 4.3) on the mitochondrial membranes isolated from different tissues in WT mice have shown that the kidney has the second abundant complex I among the tested tissues. Additionally, the kidney has a similar weight to the heart (Table 4.3). As each mouse has two kidneys and one heart, the kidney material accumulates twice as much as the heart, which makes it the optimum alternative tissue to the heart for optimisation experiments. Other organs (such as the brain and liver) were not considered due to the lower yield of complex I protein in the mitochondrial membranes (Table 4.3).

Table 4.3 WT mice tissue characteristic comparison

Tissue type	Tissue weight (g)*	Complex I content (μmol·min^{-1}·mg^{-1})**
Heart	0.145±0.009	0.732±0.011
Brain	0.550±0.018	0.207±0.007
Kidney	0.145±0.006	0.628±0.017
Liver	1.066±0.095	0.294±0.015

*The data are mean averages ± SEM (n=5 and 6, from 5 or 6 independent preparations each comprising more than 3 mice each).

** The amount of complex I was quantified using NADH:APAD$^+$ assay. The data are mean averages ± SEM (n=3, from 3 independent preparations each comprising 4 mice).

The hearts from both KO and WT mice were collected and weighed, with the KO mice showing a substantial (38.4%) decrease in heart weight (0.092g on average) when compared to the age-matched WT siblings (0.145g on average), as shown in Fig 4.6A. Similar to the heart, the collected kidney tissue (0.103g) showed a 28.6% lower weight compared to the age-matched WT (0.145g), as shown in Fig 4.6B. The KO mouse is known to have a decreased rate of body weight gain from day 20 to 30 with growing ceasing at 30 days old (Kruse et al., 2008). The average body weight at day 30 is approximately 25% less than the WT. The small heart and kidney weight can be associated with the overall smaller body-weight in the KO mouse compared to the WT mouse.

The mitochondria were isolated from the mouse tissue using the method described in Chapter 2.3.1. The concentration of the protein in mitochondria was measured by BCA, and the yield of mitochondrial membrane protein in one gram of tissue was calculated (Fig 4.6C and Fig 4.6D). The average yield of membrane protein in the KO heart is approximately 6.5 mg which

is close to the 6.23 mg obtained from the WT heart. While the average yield of membrane protein in KO kidney is 10.860 mg compared to 8.611 mg in the WT, the difference is not statistically significant. Thus, there is no clear difference in the yield of mitochondrial protein in one gram of tissue between KO and WT in the kidney or heart. The mitochondrial suspension was then concentrated to ~5 mg/mL and frozen at –80°C for at least 24 hr. The freeze-thawed mitochondria were then sonicated to generate mitochondrial membranes (the detailed methods are given in Chapter 2.3.2).

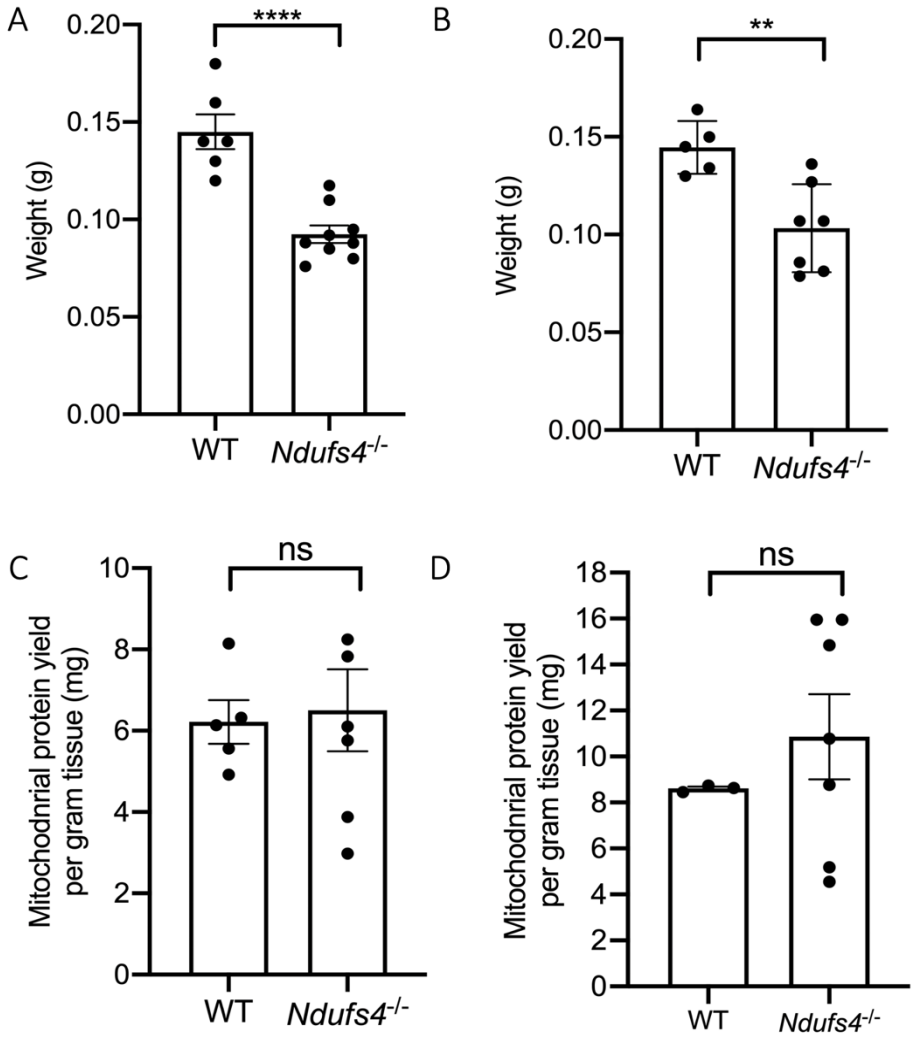

Fig 4.6 Tissue weight and mitochondrial protein weight comparison between WT and KO mice (A) Heart tissue weight comparison between WT and KO mice. (B) Kidney tissue weight comparison between WT and KO mice. (C) Mitochondrial protein yield per gram of heart tissue in WT and KO mice. (D) Mitochondrial protein yield per gram of kidney tissue in WT and KO mice. Each point represents a single tissue collection session of more than 3 mice. The data are mean averages ± SEM (n = 3 to 9, the number of points is shown) with statistical significance determined using Student's t-test (****, $p < 0.0001$; **, $p < 0.005$).

4.2.4 Evaluation of enzyme integrity and activity

To assess the structural integrity of the NDUFS4-lacking complex I, the complexes present in mitochondrial membranes from NDUFS4-lacking complex I and WT heart mitochondria were investigated by BN-PAGE analysis. Fig 4.7 shows the Coomassie blue and NBT in-gel staining of membranes from WT and KO heart mitochondria. A significant difference in complex I content was observed. The KO shows a markedly less intense CI band when compared to the WT, indicating there is less intact complex I present in KO membranes. The BN-PAGE on WT and KO mitochondrial membrane is consistent with the previous complexome studies (Agip, 2018). There is an NBT-insensitive 830-kDa subcomplex identified in KO at the gel position overlapping with the complex V band and an NBT-sensitive NADH dehydrogenase domain overlapping with the complex IV band.

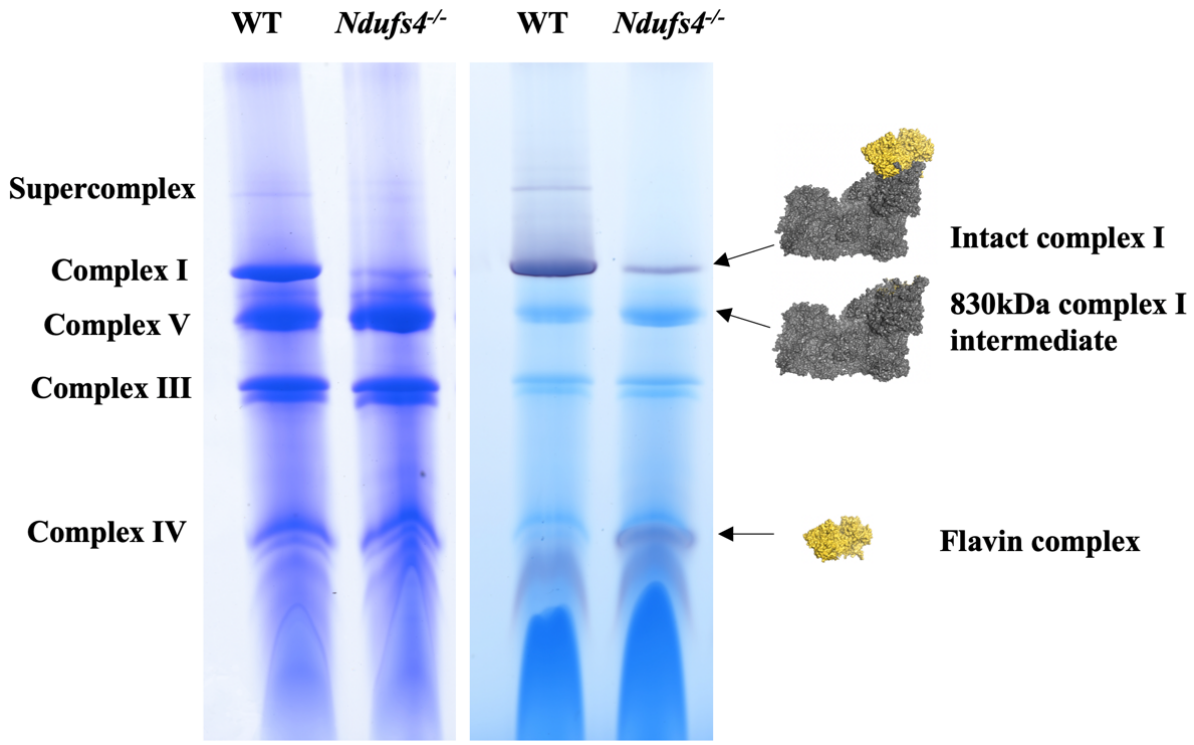

Fig 4.7 Comparison of protein integrity and in-gel activity between KO and WT complex I. BN-PAGE of heart mitochondrial membranes with Coomassie blue staining (left panel) and NBT in-gel staining (right). Membranes were solubilised with 1% DDM and 30 µg of protein from each sample was loaded on the gel.

This result raises the question as to whether an 830-kDa subcomplex exists *in vivo* or only the intact complex I presents in NDUFS4-lacking complex I. The preliminary data from Agip (2018) showed that crosslinking the mitochondrial membranes with *ndufs4* KO could increase the

number of intact complex I present on the BN-PAGE, suggesting that the *ndufs4* KO complex I was dissociating on the BN-PAGE. The observation of a faint intact complex I band on BN-PAGE has also proved the existence of a fully assembled complex I in the mitochondrial membranes. The BN-PAGE of human fibroblasts with *ndufs4* mutations showed a complete absence of an intact complex I band (Scacco et al., 2003; Ugalde et al., 2004; Assouline et al., 2012). Interestingly, complexome profiling on the BN-PAGE of the *ndufs4* KO strain (also known as *nuymΔ*) in *Y. lipolytica* showed a contrasting result: only the intact complex I without the 830-kDa subassembly was observed. Furthermore, N7BML (assembly factor NDUFAF2 in humans) co-migrated with the nuymΔ complex I in the BN-PAGE analysis (Kahlhöfer et al., 2017). From these results, both intact complex I and the 830-kDa intermediate were present, albeit with the former in small amounts, which differs from all the previous studies in either human fibroblast or yeast (Assouline et al., 2012, Kahlhöfer et al., 2017). These contradictory results suggest that the stability of intact complex I and the presence of 830-kDa intermediate may be species specific. The deletion of NDUFS4 may have less influence on the complex I stability in yeast than in mammalian.

The previous catalytic experiments performed by Dr Ahmed-Noor Adam Agip showed that the complex I content measured by non-physiological NADH:HAR and NADH:$APAD^+$ transhydrogenation reactions of KO mouse membranes were only 6% and 25% of the activity of the WT respectively (Agip, 2018), indicating a low level of flavin-containing intact complex I present in KO mouse.

Furthermore, an NBT-sensitive supercomplex band was identified in WT but not observed in KO membranes (Fig 4.7). The loss of such a band in KO but not in WT suggests that the loss of the NDUFS4 subunit could affect the formation and stability of supercomplexes. It is known that the KO complex I can be stabilised by forming a supercomplex with complex III. Both $CI+CIII_2$ and 830-kDa $CI+CIII_2$ were observed in KO muscle tissue and embryonic fibroblast, solubilised with 1% digitonin (Calvaruso et al., 2012; Adjobo-Hermans et al., 2020). In this result, neither $CI+CIII_2$ nor 830-kDa $CI+CIII_2$ were observed in 1% DDM solubilised KO

membranes. However, digitonin is a more mild solubilising agent than DDM, and thus, no supercomplex observed on the gel could possibly be due to the harsh extraction environment.

The complex I and II activities in membranes were assessed in both WT and KO mice (the details of the methods are shown in Chapter 2.6). Fig 4.8A shows a significant decrease (~93%) of complex I activity in the KO membranes in comparison to WT when assessing electron flux through CI-III-IV. Similar to these results, CI from the KO kidney mitochondria has been shown to possess barely any activity (Kruse, et al., 2008). The succinate:O_2 oxidoreduction assay was performed to assess the combined activity of respiratory complexes II, III, and IV using the protocol designed by Jones and Hirst (2013). The detail of the methods is shown in Chapter 2.6.2. Figure 4.8B shows that the succinate:O_2 oxidoreduction does not change in KO, which indicates that the loss of NADH:O_2 activity is a complex I specific effect.

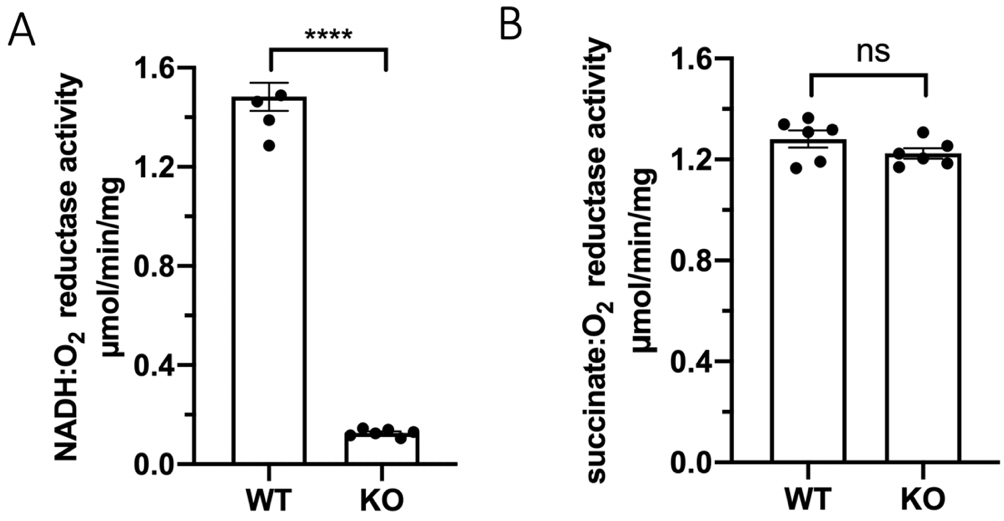

Fig 4.8 Complex I and complex II activity in heart mitochondrial membranes. (A) The rate of inhibitor-sensitive NADH oxidation in WT and KO mitochondrial membranes. Data are mean ± SEM (n= 4 or 6) analysed with Student's t-test (**** $p < 0.0001$). (B) The rate of inhibitor-sensitive succinate oxidation. Data are mean ± SEM (n =6) analysed with Student's t-test. Each point represents an individual membrane preparation from more than 4 mice.

4.3 Optimising complex I purification for the cryo-EM study

4.3.1 Small-scale complex I purification

For cryo-EM single-particle analysis, the KO complex I from heart tissue was chosen for the reason that the published complex I structure from WT mouse heart can be used for a direct comparison (Agip et al., 2018). Based on the knowledge of previous complex I purifications on WT mouse, around 15-17 mg protein-containing KO mouse membrane was used to achieve a 3-5 mg/mL purified complex I, which is an ideal concentration for making complex I cryo-grids with UltrAuFoil gold grids (Blaza et al., 2018; Agip et al., 2018). To obtain 15-17 mg protein-containing membranes, around 2.3 - 2.8 g KO mice heart tissue was required, based on the estimated protein yield of 6.5 mg per one gram of tissue in KO mouse in chapter 4.2.3. As the KO mouse has a relatively smaller heart compared to the WT, the 2.3- 2.8 g heart tissue requires an accumulation of around 25 to 30 KO mice, which took a longer period to accumulate (22 to 26 weeks) than typical WT complex I purifications.

Considering the difficulty of sample accumulation for purification, a small-scale tissue material purification was developed for cryo-EM. A preliminary purification with less material (7.65 mg heart membrane protein prepared from 8 WT mice hearts) resulted in a low concentration (0.33 mg/mL) at the peak fraction with an absorbance of 350 mAU at the wavelength of 280 nm (Fig 4.9A). The purification process was identical to the large-scale WT complex I purification performed by Agip et al. (2018). This two-step chromatography purification using an ÄKTAmicro system is described in Chapter 2.4. However, such a low concentration is not able to achieve good particle distributions on cryo-grids. Therefore, three strategies to improve the protein concentration were employed: 1) Using the alternative kidney tissue from KO mouse which shows similar protein abundance to the WT in the membrane, thus it can be used for method optimisation 2) Concentrating the sample after purification, with several complex I-containing fractions being pooled with an extra concentrating step to improve the final concentration. 3) Grid condition improvement, enabling the low-concentration purification

samples to be directly applied on carbon-coated cryo-EM grids as the carbon support could enhance the particle attaching to the grid surface.

To test the first strategy, small-scale purifications (less than 7 mg membrane) KO kidney tissue was performed to estimate the yield and to compare with the yields from WT heart and WT kidney (Fig 4.9B). The complex I containing-fractions were collected after chromatography, and the amount of purified complex I was estimated. Both kidney and heart mitochondrial membranes from KO mice show a significantly lower yield comparing to the WT heart, showing less intact complex I in KO kidney and heart tissue than in the WT. This result is in agreement with the previous BN-PAGE findings (Fig 4.7) with the fainter band of intact complex I in KO compared to the WT.

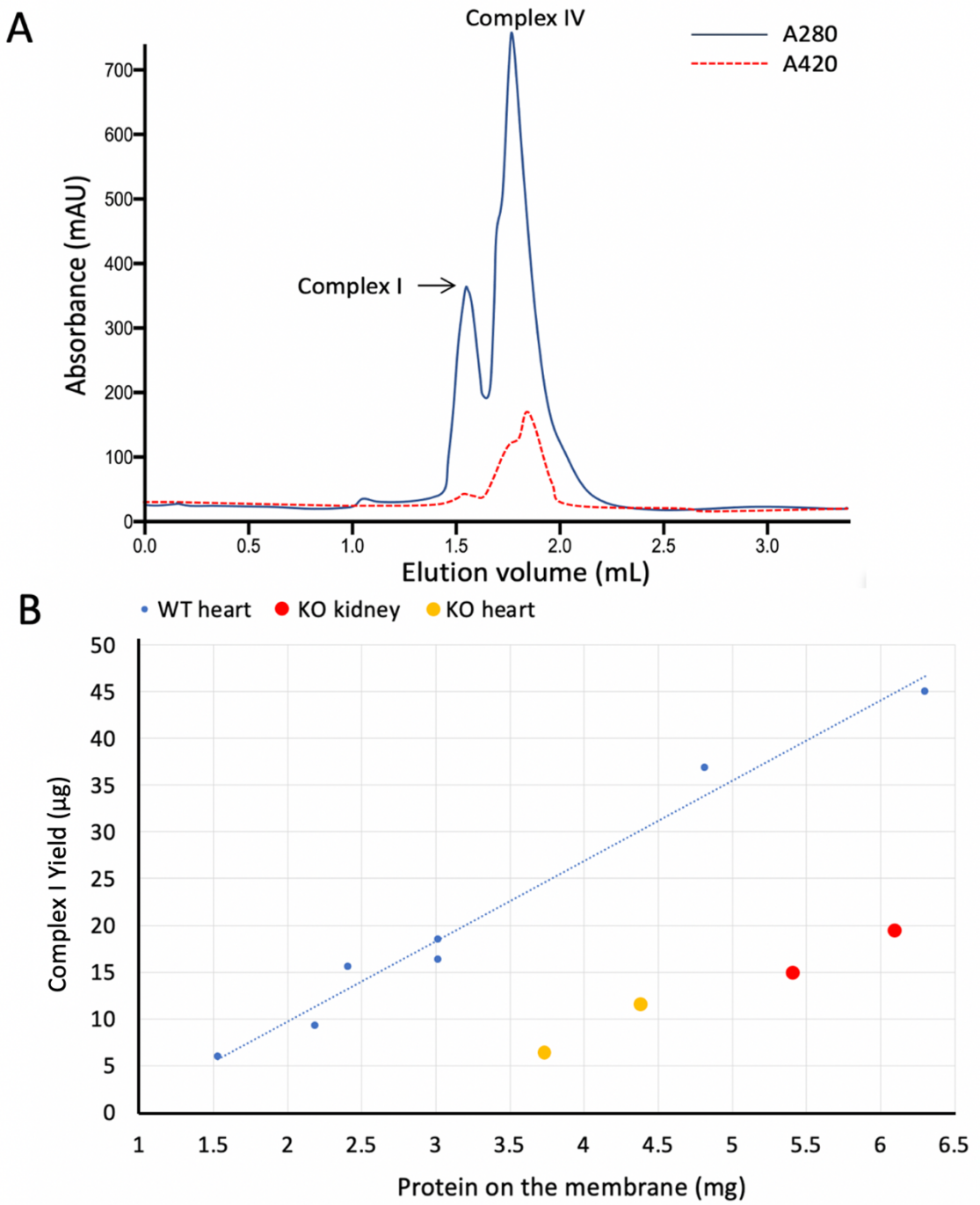

Fig 4.9 Summary of small-scale complex I purifications. (A) WT heart complex I purification elution profile from the size exclusion chromatography. A total of 7.65 mg heart membrane gave a concentration of 0.325 mg/mL at the complex I peak fraction. (B) The small-scale complex I purification yield plot. Each dot represents an individual complex I purification. The yield from WT heart, KO heart, and kidney is shown as blue, yellow, and red dots respectively. The X-axis shows the amount of protein in the mitochondrial membrane for purification. The Y-axis shows the complex I yield from the elution fractions collected under complex I peaks.

To assess the second strategy of concentrating the sample, the WT membrane condition was optimised before using any KO materials. Eluted fractions (0.4 mg/mL) from size-exclusion chromatography were centrifuged with the 100 kDa MWCO Vivaspin 500 concentrator using a benchtop concentrator at ~8,160 xg, and the sample volume was checked after each 30-second

concentrating period to estimate the concentration changes. Approximately 2-, 4-, and 8-fold concentration was performed, after which, the sample was applied on the cryo-EM grid as described in Chapter 2.8. The complex I NADH:DQ activity was measured after centrifugation and showed no difference in concentrated and non-concentrated samples, confirming that the gentle concentrating step does not affect the enzyme activity. Fig 4.10 shows the different degree of complex I aggregation on the cryo-EM grid after concentrating between 2- to 8-fold. This data clearly shows that the 8-fold concentrating step showed more aggregation resulting in larger aggregation clumps. Although the 8-fold concentration achieved the target concentration of 3-5 mg/mL, the grid is usable for cryo-EM studies due to the severe aggregation. This suggests that a gentle concentrating up to 4-fold may help to achieve the target concentration for cryo-EM, but more than 4-fold would increase the risk of aggregation.

The third strategy of applying the WT complex I on the carbon-coated cryo-EM grids was also investigated. Unfortunately, the strong adhesion of the enzyme to the carbon surface damages its structure and leads to an unsuccessful cryo-EM 3D reconstruction. This grid optimisation investigation for low concentration complex I is discussed in Chapter 5.

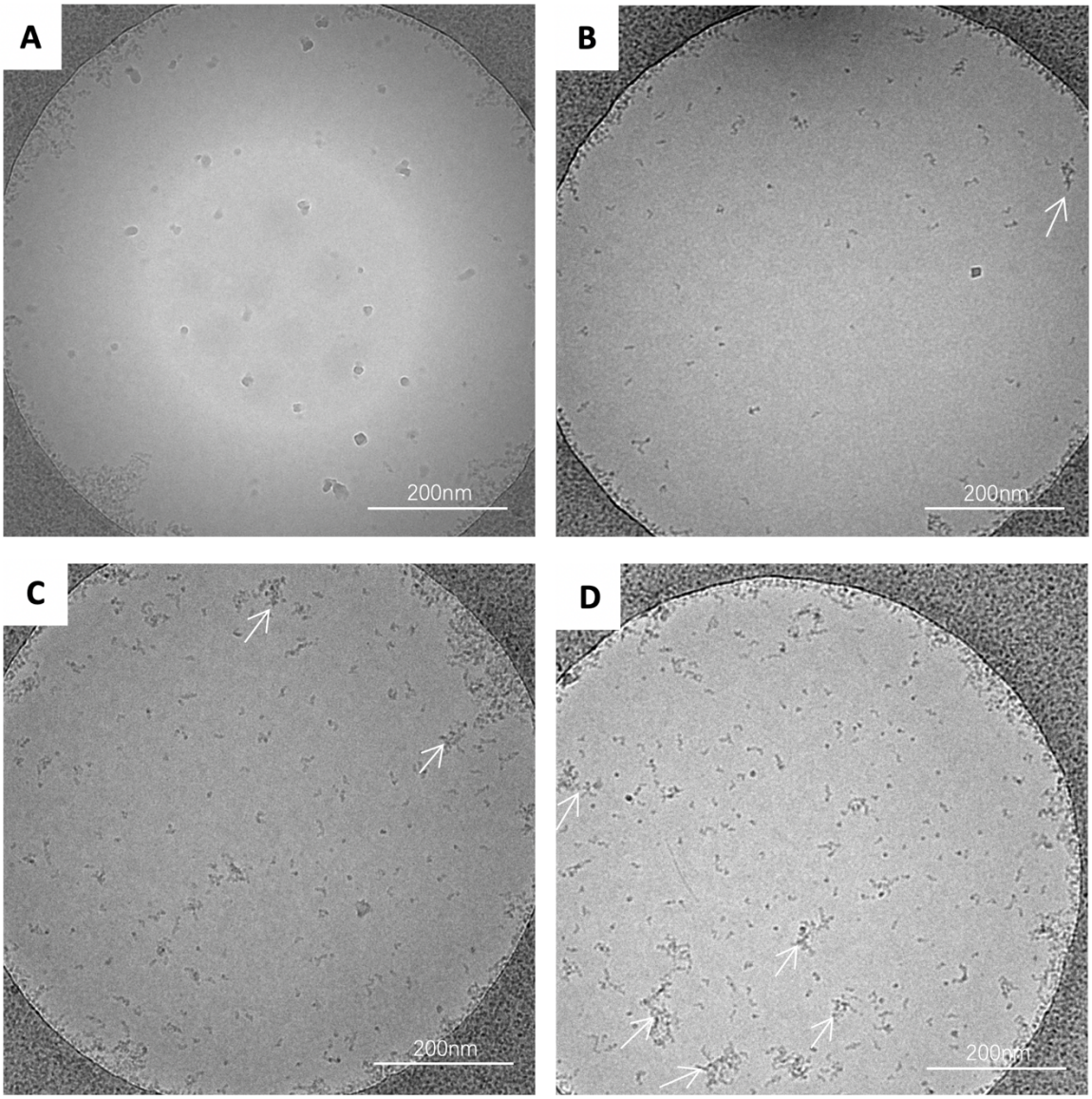

Fig 4.10 Cryo-EM images of grids with different WT complex I concentrations. WT complex I was applied on Quantifoil R1.2/1.3 grids with a blotting time of 10 sec and a blotting force of -10. The complex I was concentrated at 2-fold, 4 -fold, and 8-fold before applying on the grids. The white arrows point out the aggregation points on the images. (A) The complex I was not concentrated, 2.5µL of 0.40 mg/mL was applied on the cryo-EM grid. (B) Cryo-EM grid made with ~2-fold concentrated complex I at 0.88 mg/mL. (C) Cryo-EM grid made with ~4-fold concentrated complex I at 1.50 mg/mL. (D) Cryo-EM grid made with ~8-fold concentrated complex I at 3.23 mg/mL.

Collectively, strategies one and two were decided to apply for the KO complex I cryo-EM purification and its optimization. The *ndufs4* KO kidney mitochondrial membranes were initially used for purification process optimization with a 2- to 4-fold concentrating after purification to achieve ideal concentration for cryo-EM. The concentrating process was performed by several 30-second centrifuge sessions at 10,000 xg with a benchtop centrifuge at 4°C. The volume was checked between sessions to achieve the 2- to 4-fold concentrating. After

the preliminary trial on the kidney, the optimised purification condition would be applied to KO heart tissue.

4.3.2 Complex I purification from *ndufs4* KO mice kidney

10.05 mg of mitochondrial membrane was isolated from 24 *ndufs4* KO mice kidneys (12 mice). The WT complex I purification from the kidney was performed with a similar amount of material (12.16 mg WT kidney mitochondrial membrane) using the same methods except that a 5 mL Hi-Trap Q HP anion exchange column was used rather than 1 mL in the *ndufs4* KO complex I purification. As shown in Fig 4.11A and Fig 4.11B, the complex I containing fractions were collected from anion-exchange chromatography, with the KO kidney showing a lower complex I containing peak. In Fig 4.11C, the WT complex I peak from gel filtration chromatography (peak 1) was shown at ~1.6 mL followed by a similar-size complex IV peak (peak 2), while the mutant complex I elution peak (Fig 4.11D) appeared at the same volume with a proportionally larger complex IV peak. The tail of the complex I peak heavily overlapped with the complex IV peak, with significantly worse separation when compared to the WT complex I.

Peak 1 in Fig 4.11D indicated a low yield of complex I relative to complex IV in KO, where the complex I to complex IV ratio is nearly 1:1 (Fig 4.11C) in WT. This suggests that the intact complex I in the KO kidney is much less than in WT. Additionally, the complex I peak was not well separated from the complex IV. The broadening of the complex I peak indicates the high heterogeneity of the complex I in these fractions. The complex I fractions around peak 1 were collected with an average concentration of 0.81 mg/mL. Following the strategy of two of gentle concentrating steps, a 3-fold concentrated complex I sample (2.55 mg/mL) was applied on the cryo-EM grids.

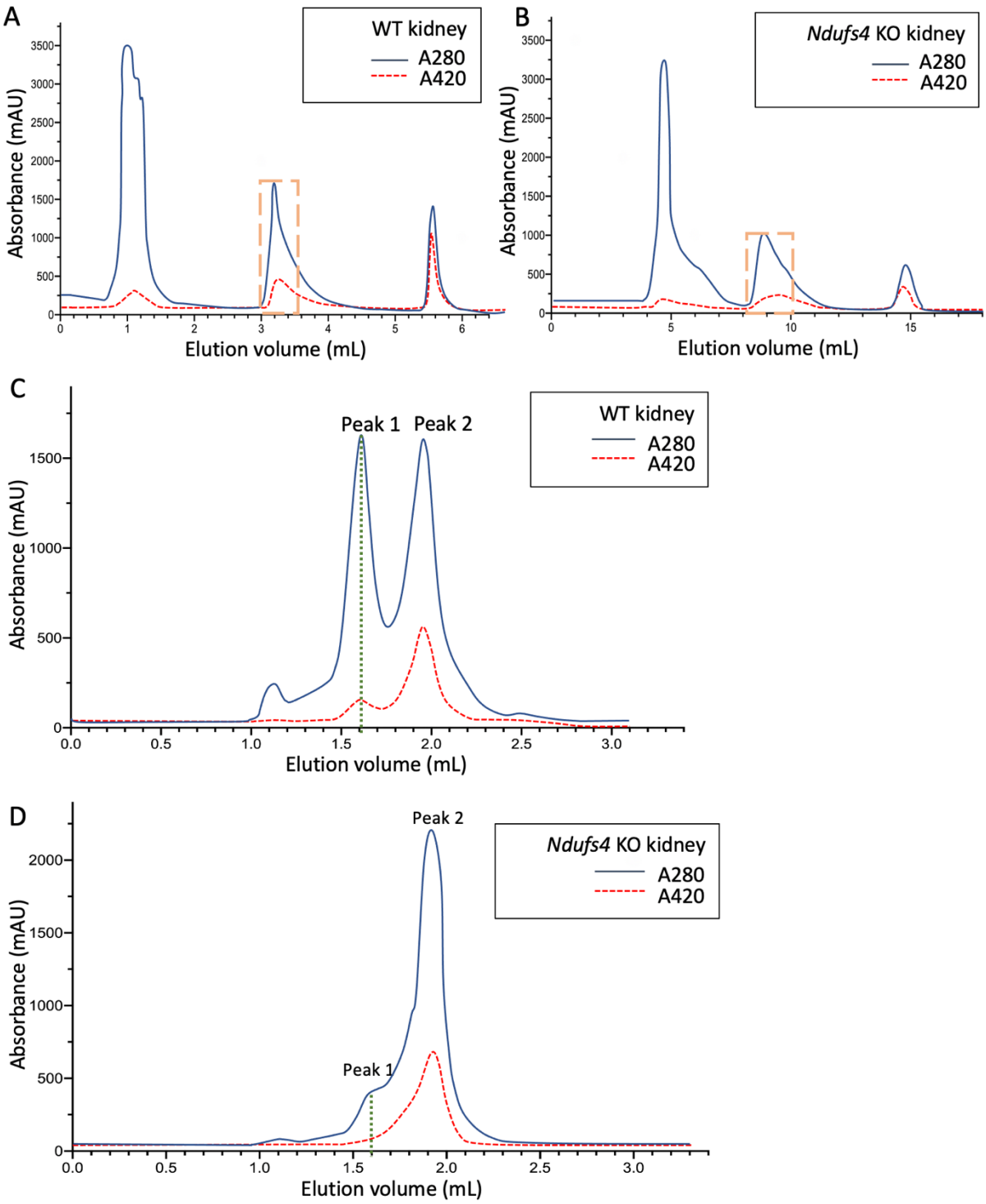

Fig 4.11 Kidney complex I elution profiles from two-step chromatography. (A) & (B) The anion-exchange elution profiles from WT kidney membranes with 5mL Hi-Trap Q HP anion exchange column (A) and *ndufs4* KO kidney membrane with 1mL Hi-Trap Q HP anion exchange column (B). The orange dash squares mark out the complex I-containing fractions. (C) & (D) The elution profiles from the size-exclusion column with WT kidney membranes (C) and *ndufs4* KO kidney membrane (D). Peak 1 and 2 in (C) & (D) indicate the complex I and complex IV elution peaks respectively. The vertical green dash lines highlight the position of the complex I elution peak.

4.3.3 3D reconstruction of complex I from KO mouse kidney

The mutant kidney complex I sample (2.55 mg/mL) was applied onto PEGylated gold grids (R 0.6/1) and plunge-frozen by using the Vitrobot with a blotting force of -10 and blotting time of 10 sec as the standard setup (the detailed descriptions of methods are given in Chapter 2.8.1). The cryo-grids were screened with a T12 Tecnai electron microscope (see Chapter 2.9.1 for T12 imaging). The resulting micrographs are shown in Fig 4.12. During the screening, the particle distribution was found to be highly dependent on ice thickness. A higher density of particles was observed in grid holes with thicker ice, while a low density of particles or no particles was observed with thinner ice. There are three factors of ice thickness that need to be considered (Fig 4.12): the ice gradient across the grid generated by the filter paper blotting before plunge-freezing; the ice gradient across each grid square with thicker ice around the conner and thinner ice in the center; and the ice gradient in each grid hole, where the center of the hole has thinner ice than the edge. The two micrographs in Fig 4.12 were show that the hole in the center of the grid square has overall thinner ice with no particles present. Conversely, the grid hole near the edge of the grid square shows thicker ice in general with more particles in the center of the hole. In such a case, finding the best ice thickness is crucial for taking micrographs with maximum particles. For each selected grid square, a “donut” shaped area of grid holes was selected rather than within the grid square for a better image collection.

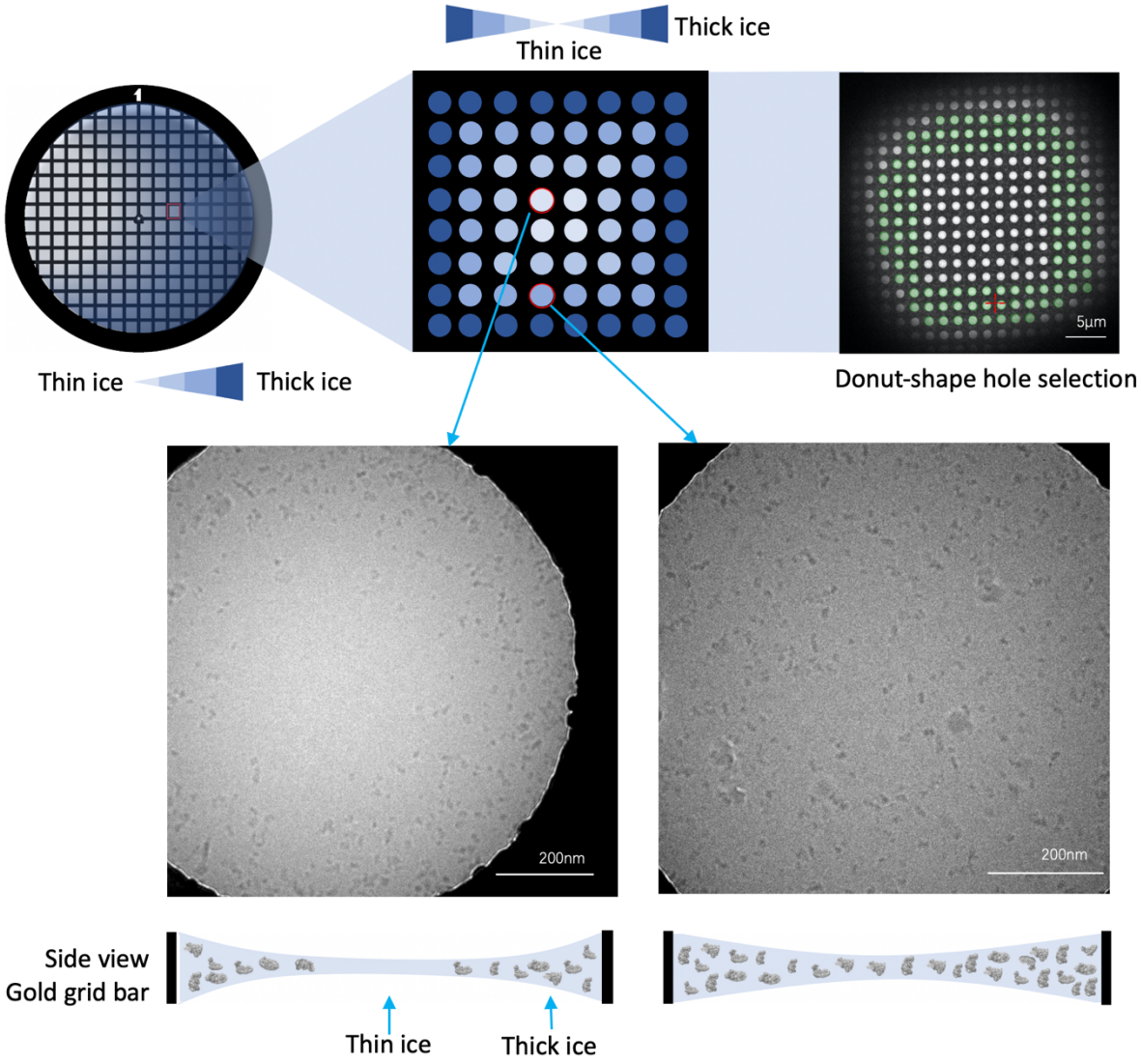

Fig 4.12 Illustration of the ice thickness distribution in cryo-EM grids containing KO complex I. The micrographs were taken using a T12 Tecnai. The hole in the center of the grid square (bottom left) shows fewer particles distributed in the hole center than the the micrograph taken from the near edge of the grid square (bottom right). For data collection, a donut-shaped area of grid holes was selected to satisfy the ice thickness required for complex I. The image on the top right is an example of a donut shape (green colored holes) selection for data collection.

After grid screening, the cryo-EM data of one of the best grids were collected using a Titan Krios (300 kV) at the UK National Electron Bio-Imaging Centre at Diamond Light Source with help from Dr Yuriy Chaban. To acquire as much valid data (more particles) as possible in a limited timeframe, several alterations on the setup of the microscope were made to maximize the utilization of the data collection time. (1) For capturing more particles in one image, a larger pixel size (1.46 Å/pix) and a low magnification (59,000x) were applied to enlarge the acquisition field. (2) The Falcon III camera was set to integrating mode which has a faster collection speed than the counting mode, while use of the K2 camera was not considered as its

integrating mode has a lower DQE comparing to Falcon III integrating mode (Chang, Dwyer, Barthel, Boothroyd & Dunin-Borkowski, 2016; Song et al., 2019). (3) The "donut" shape was selected in each grid square for imaging. The cryo-EM data collection parameters are shown in Table 4.4. In brief, a total dose of 49.24 $e^-/Å^2$ was applied for 1.5-sec exposure. The defocus was set at a range of -2.1 to -3.3 µm with a step of 0.3 µm. In total 3,373 micrographs were collected in 50 hours. The average speed of ~67 micrographs/hr is significant faster compared to the K2 counting mode speed of 32-34 micrographs/hr (the K2 data collection of ND6-P25L-CI in Chapter 3.3.3).

Table 4.4 NDUFS4 deleted complex I cryo-EM data collection microscope setup

Microscope	Titan Krios
Detector	Falcon III integrating
Voltage (kV)	300
Magnification	59,000
Gun lens	4
Spot size	6
C2 aperture (µm)	50
Objective aperture (µm)	100
Pixel size (Å)	1.46
Exposure time (sec)	1.5
Electron exposure ($e^-/Å^2$)	49.24
Dose rate ($e^-/Å^2$/sec)	32.83
Defocus range (µm)	-2.1, -2.4, -2.7 -3.0, -3.3
Number of fractions	59
Number of initial images	3,373

The 3D reconstruction of the KO kidney complex I was performed by using RELION 2.1 with the help of Dr Hannah Bridges. The reconstruction scheme is given in Fig 4.13. Firstly, the imported images in RELION were corrected using whole-frame micrograph movie-alignment with MotionCor2 (Zheng et al., 2017), and the CTF of the motion-corrected images were estimated using Gctf. 1,391 out of 3,373 micrographs which displayed few particles (similar to Fig 4.14A) were discarded. Following this, automatically particle picking was performed on 1,982 micrographs with ~112,000 selected particles. Fig 4.14B shows the micrograph with the particles at different orientations. The particles were then extracted and cleaned with two rounds of 2D classification resulting in ~38,000 particles remaining. Only the "good" 2D classes with

less background and strong features were chosen for 3D classification. As shown in Fig 4.14C, 24 good classes were selected from 100 2D classes, after which, the selected particles from those 24 2D classes were split into five classes during 3D classification based on their homogeneity. The WT mouse complex I density map was low pass filtered to 60 Å as the reference for 3D classification. The five classes showed high heterogeneity (Fig 4.13), with four classes being shown to be incomplete complex I. Only 12.2% of the particles (~ 5,000) in class 5 are shown intact complex I-like, suggesting that the majority of the particles shown on the micrographs are broken or incomplete. Thus, only particles in class 5 were taken for 3D auto-refinement. The 3D class density map from class 5 was used as the reference for the 3D refinement. A mask was the generated from the 3D refined density map with a soft edge of 8 pixels and an extended binary of 2 pixels for the final 3D refinement. Ultimately, the final refinement density map was reconstructed with ~5,000 good particles with a global resolution of 8.3 Å determined by gold-standard Fourier shell correlation (Fig 4.14D). The angular distribution (Fig 4.14E) of the complex I reconstruction showed a few empty spaces highlighted by the blue dots and several regions with strong red spikes, suggesting that several angles were missing. This uneven orientation distribution, as well as limited particle numbers, is likely the cause of the low resolution obtained.

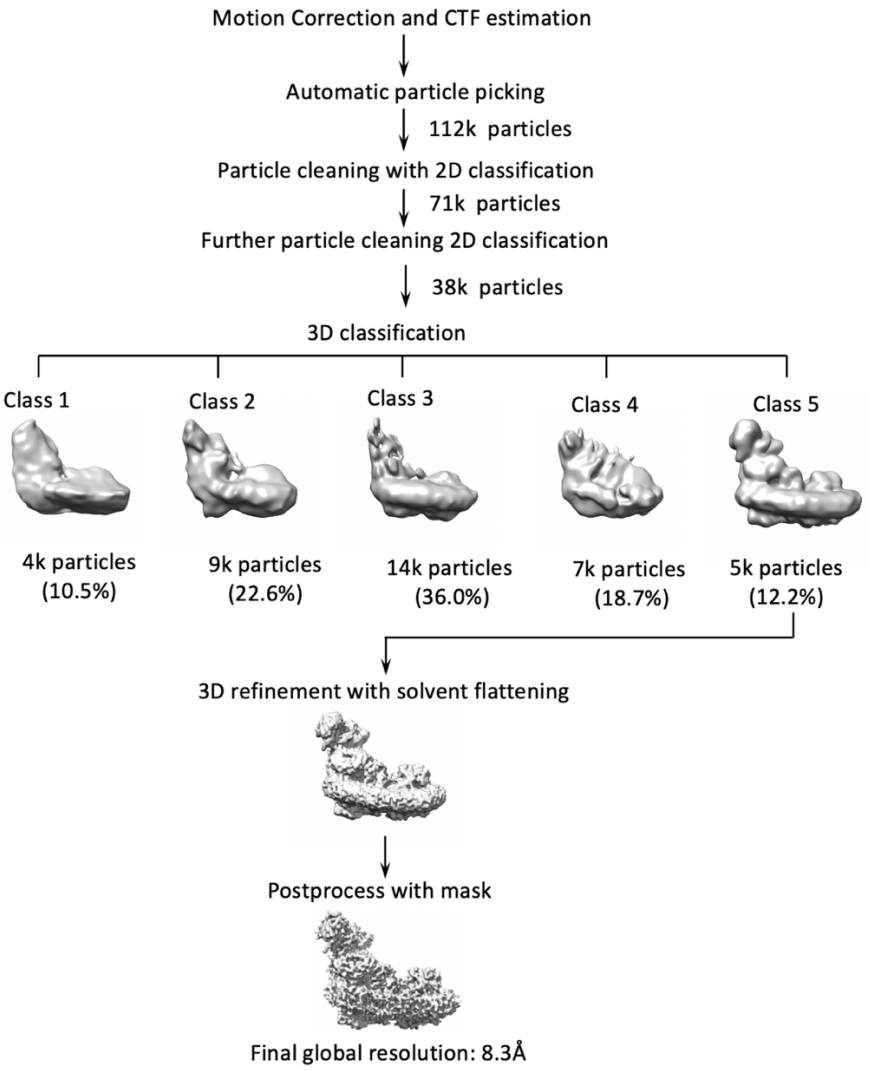

Fig 4.13 Cryo-EM data processing flow of mutant complex I structure reconstruction. The micrographs were motion corrected and the particles were auto-picked and cleaned in RELION. The selected 38k particles were further 3D-classfied into 5 classes, within which only class 5 containing about 5000 particles showed a intact complex I-like shape. The structure from class 5 was further 3D-refiened and a density map was determined at 8.3 Å resolution.

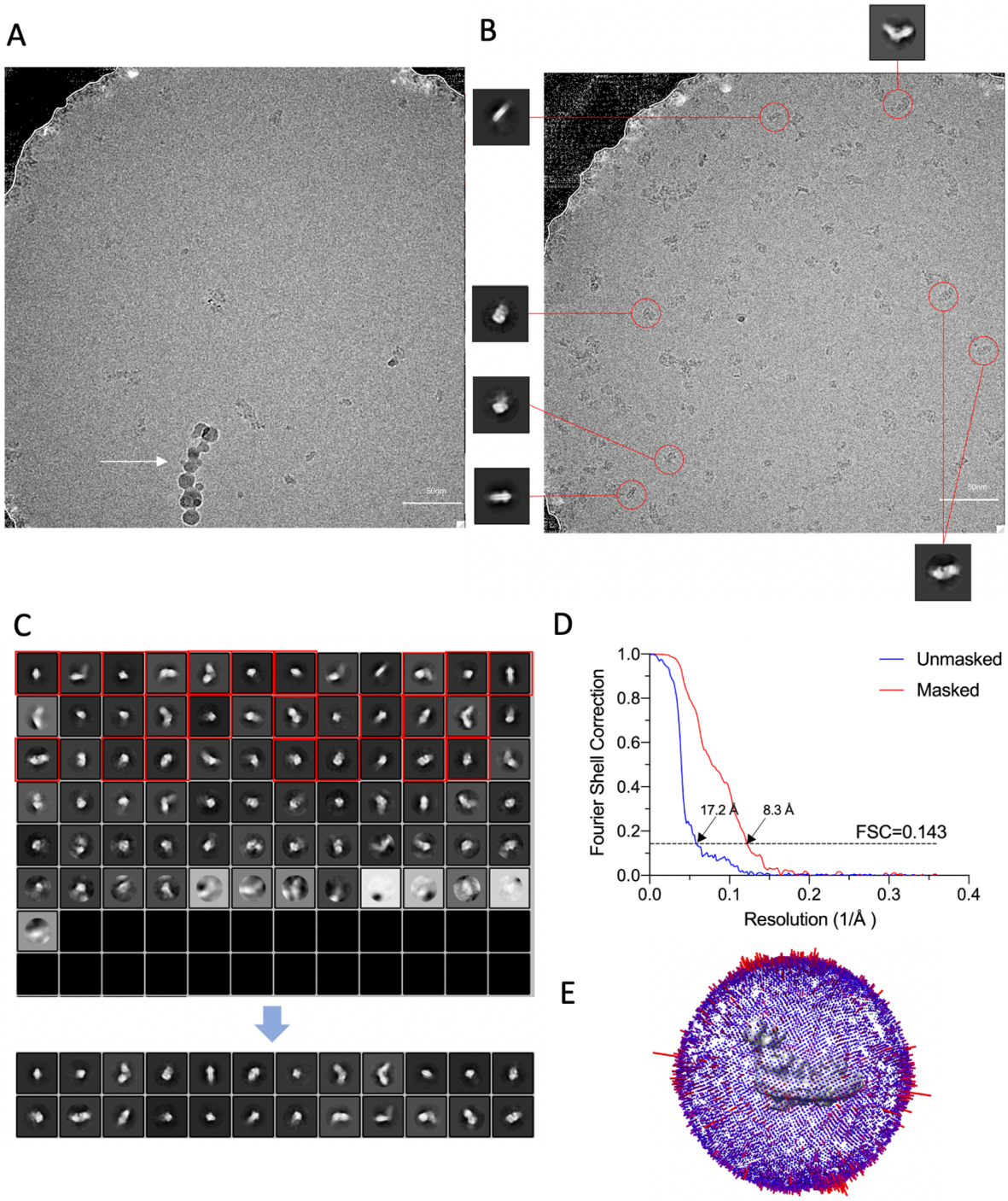

Fig 4.14 Cryo-EM analysis of the mutant complex I from KO mouse kidney. (A) & (B) Two micrographs representing the particle distribution. (A) A micrograph showing fewer particles with non-protein containment marked with a white arrow. (B) A micrograph with more particles of different orientations marked out with red circles. (C) Selected 2D classes in red squares were used for 3D classification. (D) FSC curves of two refined maps with (red) and without (blue) mask after post-processing in RELION 3.1. (E) The angular distribution of the mutant complex I reconstruction. Blue dots indicate the coverage of the 2D projection angle , the red color spikes show a higher particle number in this region.

To check the mutant complex I conformation states, the density map was compared with the published WT complex I structures, both in the active and deactive state (Agip et al., 2018).

WT density maps were generated at the same resolution using the molmap command in Chimera and the active mouse model (PDB: 6G2J) and deactive mouse model (PDB: 6G72) with a low pass filter to 8.3 Å. The mutant complex I was then cross-correlated with these two density maps by fit-in-map in Chimera (Fig 4.15A). The correlation score shown in Fig 4.15A suggested that the mutant complex I structure has a higher similarity to the active than the deactive state.

Due to the limited resolution of the map, only a rigid body fit with an initial model from active state complex I (PDB: 6G2J) was performed using fit-in-map in Chimera without further modeling. The NDUFA5 and NDUFA10 subunits of the mutant complex I fit better to the active model than in the deactive model (Fig 4.15B), which also suggested that the mutant complex I is in the active state. Futhermore, the comparison between the rigid body fitted mutant complex I model, and the WT active model shows a slight shift of N-module (Fig 4.15C). The mutant complex I structure shows an overall intact complex I structure lacking NDUFS4 subunit (Fig 4.15D). Several subunits (NDUFS6, NDUFA12, and NDUFA7) seem to have partially lost density as the part of the model was not able to fit into any density during the rigid body fit (Fig 4.15E). NDUFS6 and NDUFA12 are considered as late-onset subunits during assembly together with NDUFS4 (Guerrero-Castillo et al., 2017). The deletion of NDUFS4 seems to influence the stability and location of these two subunits assembling onto complex I. However, the observation and comparison were limited by the current resolution. To confirm the change of conformation and loss of densities mentioned above, a high-resolution map was required for more clear observations.

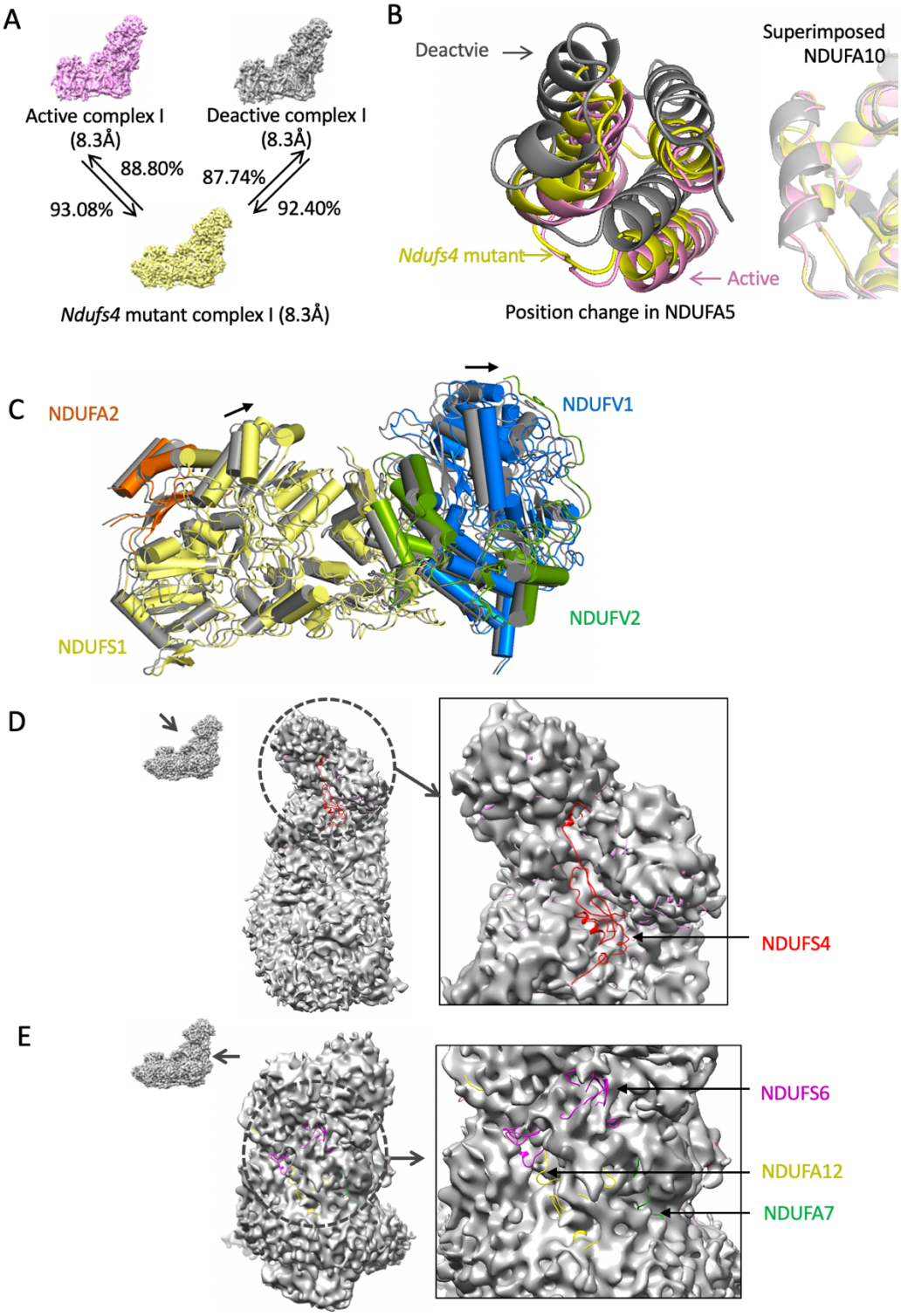

Fig 4.15 Structure analysis of mutant complex I from *ndufs4* KO mouse kidney mitochondria. (A) Fit-in-map cross-correlation calculated from Chimera between WT active (pink), WT deactive (gray), and the NDUFS4- lacking complex I (yellow). (B) The relative position difference of NDUFA5 with superimposed NDUFA10 in the active (pink), deactive (gray), and mutant complex I (yellow). The NDUFA5 of mutant complex I takes up a similar position to the active state complex I. (C) Overlay of WT active (gray) and mutant complex I (color) N-module with aligned membrane arm. The arrow indicates the shift direction of the N-module. (D) The active complex I model (PDB: 6G2J) docked into the mutant complex I density map (gray), the location of NDUFS4 (red) shows no density. (E) The subunits with poor density. The model of NDUFS6 (magenta), NDUFA12 (yellow), and NDUFA7 (green) show a partially unmatched density.

4.3.4 Improving complex I stability by crosslinking

The low number of intact complex I particles and the high numbers of degraded complex I-like particles observed from previous cryo-EM micrographs have suggested that complex I damage during sample freezing could limit the particle number and subsequent resolution for 3D reconstruction of the intact complex. To improve the stability of the mutant complex I for grid freezing, a water-soluble cross-linker, bis(sulfosuccinimidyl)suberate (BS3), was applied. The BS3 reacts with primary amino groups (-NH2) to form stable amide bonds. In proteins, BS3 specifically targets lysine sidechains and the N-terminus of polypeptide within the distance of its spacer arm (11.4 Å). BS3 crosslinking has been successfully integrated with cryo-EM for protein complex structural studies, and several large protein complexes (550 kDa to 2 MDa) have been solved with BS3 treatment (Liu et al., 2018; Poepsel, Kasinath & Nogales, 2018; Fica et al., 2019). Although other crosslinkers such as glutaraldehyde have also been applied in cryo-EM studies, the activity of the proteins was highly inhibited and the solubilisation of the protein with a high surface content of lysine was sometimes limited (Chui & Wan, 1997; Migneault et al., 2004; Parvate et al., 2020). A further reason to choose BS3 over other crosslinkers is that the long spacer arm of BS3 makes it ideal for mono-linking and could avoid potential aggregation. Additionally, the BS3 has high reaction specificity to protein-surface lysine and lacks reaction by-products (Rozbeský et al., 2018).

It has been previously demonstrated that a high concentration of BS3 (100 to 500-fold molar excess of the protein concentration) may affect enzymatic activity (Rozbeský et al., 2018). Low crosslinker concentrations usually result in intramolecular rather than intermolecular crosslinking (Shi et al., 2017). Low concentrations do not affect protein structure especially in proteins containing multiple lysine residues on the solvent-accessible surfaces (Rozbeský et al., 2018). The previously published protein complex structure studies with BS3 have shown a concentration range of 0.5 to 3 mM with a purified protein concentration of 1-2 mg/mL (Liu et al., 2018; Fica et al., 2019). To find the optimum concentration for the mutant complex I sample, various BS3 concentrations were applied to ensure effective cross-linking but also minimizing the negative effects on enzyme activity.

To identify appropriate cross-linking conditions, bovine heart membranes, KO mouse kidney, and heart mitochondrial membranes were prepared in resuspension buffer with 20 mM Tris-HCl replaced by HEPES, to avoid Tris buffer reacting with BS3. To allow the water-soluble BS3 to react with membrane proteins, the mitochondrial membranes (5 mg/mL) were firstly solubilised in 1% DDM at 4°C for 5 min before the addition of BS3 (0.1 mM to 25 mM). The membranes were then continuously solubilised for a further 25 min in the presence of BS3. The remaining unreacted BS3 reagent in the sample was then quenched by the addition of 40 mM Tris buffer (pH 7.5). A total amount of 30 µg protein was loaded onto a BN-PAGE with coomassie blue or in-gel NBT staining. Alongside this, the complex I activity was assessed using the NADH:DQ oxidoreduction assay. The BS3 in different concentrations was initially tested with solubilised bovine heart membranes (Fig 4.16A & Fig 4.16B). The BN-PAGE shows no effect of the treatment of BS3 on the bovine complex I band, but an increased density of supercomplexes with higher cross-linker concentrations was observed (Fig 4.16A). The activity of complex I in bovine membranes decreased dramatically with increasing concentrations of BS3 treatment (Fig 4.16B). Moreover, the bands of complexes I and V shifted towards a lower position following cross-linker incubation. Interestingly, the complex V dimer (ATP synthase) showed the biggest shift when compared to other OXPHOS proteins treated with cross-linker (Fig 4.16A). This is because the intramolecular crosslinking reaction between BS3 and the side chain of lysine shields the positive charges on the protein surface giving a more negative net charge (Rozbeský et al., 2018), thus it could influence the electrophoretic mobility of the protein. Furthermore, a strong band of NBT-sensitive supercomplex had been identified in the WT mouse heart membranes in the previous study (Agip, 2018) and bovine heart membranes but not observed in KO membranes. This raises the question as to whether the loss of the NDUFS4 subunit affects the formation and stability of complex I-containing supercomplexes. It has been proposed that the formation of a supercomplex could stabilise the mutant complex I (Calvaruso et al., 2012). It has shown that in the KO mice the supercomplex was formed by complex I intermediate with complex III in the form of 830-kDa CI+ CIII2 (Calvaruso et al., 2012). This is consistent with the previous finding that only the NBT-insensitive supercomplex was identified in KO mice.

Kidney and heart membranes from mutant mice were solubilised for BS3 treatment with a smaller concentration gradient (0-5 mM) due to the observed effect on NADH:DQ activity in bovine membranes. As shown in Fig 4.16C and E, the kidney and heart membranes showed significant preservation of intact complex I after BS3 treatment. Activity assays (Fig 4.16D) on kidney membranes seem to show an initial increase of complex I activity with the treatment of BS3 from 0.25 to 0.5 mM, after which the activity again decreases with higher cross-linker concentrations. However, the increase of activity from 0 to 0.5 mM is not statistically significant, suggesting a minimum effect on enzyme activity with up to 0.5 mM BS3 treatment. In the mutant heart complex I (Fig 4.16F), the NADH:DQ activity without BS3 treatment for mutant complex I is about 1.84 μmol/min/mg compared to a typical WT complex I activity of 10-12 μmol/min/mg (Agip et al., 2018). The BN-PAGE analysis together with the NADH:DQ assays suggest that BS3 at low concentration has no effect on the complex I activity but stabilises the structure. Thus, the optimum BS3 concentration of 0.25 mM was established for the mutant complex I purification from *ndufs4* KO mouse kidney and heart.

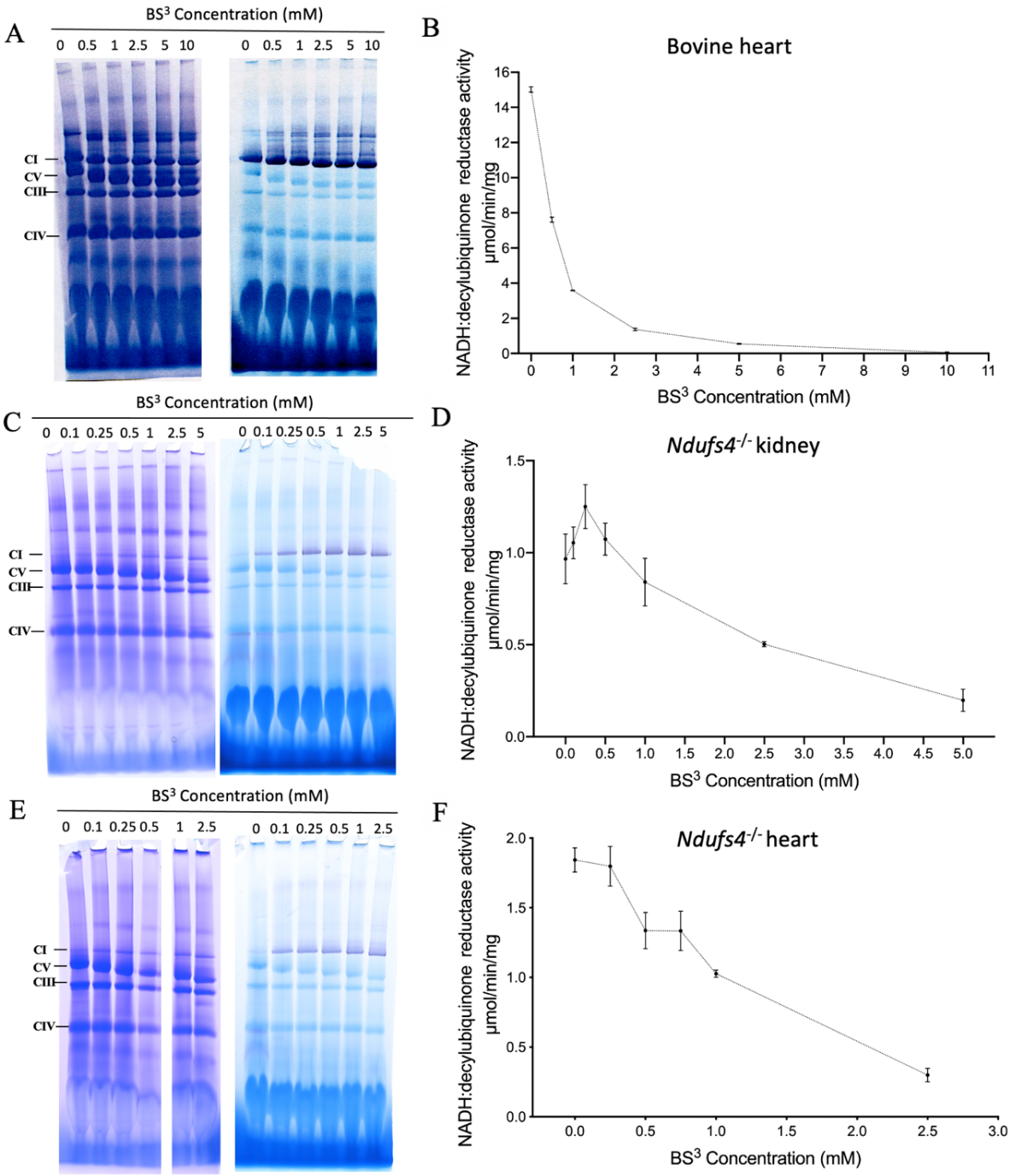

Fig 4.16 Optimising BS^3 concentration on solubilized mitochondrial membranes. (A), (C) and (E) Blue native PAGE gels of solubilized bovine heart (A), KO mouse kidney (C), and KO mouse heart (E) mitochondrial membranes incubated with BS^3 at different concentrations. The left panel shows the Coomassie blue staining and the right panel shows the in-gel activity staining of complex I by NBT. (B), (D) and (F) complex I activity in the bovine heart (B), KO mouse kidney (D), and KO mouse heart membrane (F) assessed by NADH:decylubiquinone assay. Data in (B) (D) and (F) are mean ± SEM ($n \geq 3$).

4.3.5 Preparation of mutant complex I from *ndufs4* KO mouse kidney with BS^3

Kidney membranes were crosslinked with 0.25 mM BS^3 during solubilization with 1% DDM. As shown in Fig 4.17A, an extra peak was observed in the 280 nm absorbance compared to the elution profiles from the non-BS^3 treated WT and mutant kidney complex I purification with anion-exchange column (Fig 4.11A and Fig 4.11B), suggesting a crosslinking-caused peak. BN-PAGE of peak 2 showed no bands indicating this peak is the result of a non-protein component. It is known that the free N-Hydroxysuccinimide (NHS) ester hydrolysed in the solution can be measured at 260 to 280 nm (Mattson, Conklin, Desai, Nielander, Savage & Morgensen, 1993). In the process of purification, the cross-linking reaction was quenched by conjugating with Tris buffer. Thus, the extra peak at 280 nm is likely a result of the sulfonate-N-hydroxysuccinimide (sulfo-NHS) byproducts released from the amide bond-forming reaction with BS^3 or the free BS^3 in solutions conjugated by Tris buffer (Miron & Wilchek, 1982). The complex I was eluted at peak 2, where the BN-PAGE suggested that the majority of the complex I eluted from the peak was intact. Only a small, less intense 830-kDa subcomplex band below complex I was observed compared to the heavy 830-kDa subcomplex band shown in previous non-BS^3 treated *ndufs4* KO kidney mitochondrial membrane BN-PAGE gel (Fig 4.16B). These results indicate that the majority complex I was intact during purification and was able to remain intact on the BN-PAGE after gentle crosslinking. Four elution fractions around peak 3 were collected and concentrated to 100 µL and the sample was then injected onto the size-exclusion column.

As shown in Fig 4.17B, the complex I peak of the gel filtration (peak 1) shows a relatively low absorbance compared to the complex IV peak which is similar to the non-BS^3 treated mutant complex I purification (Fig 4.11D). However, the BN-PAGE of peak 2 showed good separation of complex IV from the complex I in peak 1, which indicates the improvement in the integrity and homogeneity of complex I following the BS^3 treatment. The BN-PAGE of fractions from peak 1 still showed a small portion of the molecular weight NBT-sensitive smear and the faint band of 830-kDa subcomplex. This suggests that the majority crosslinked mutant complex I

was able to maintain intact in the size-exclusion column, but still some un-crosslinked complex I can break on the gel. The yield of the mutant complex I from the kidney was increased by 2-fold when compared to the non-BS^3 treated sample (from 6.4 μg complex I per 1 mg membrane protein to 13.6 μg complex I per 1 mg membrane protein), but still a lower yield than the WT. Considering the further complex I concentrating step for cryo-EM study, an extra step of gentle cross-linking after size-exclusion purification was performed and tested on BN-PAGE. Fig 4.16C shows the gently concentrated elution fraction (2-fold) from size-exclusion chromatography was cross-linked with 0 to 10 mM of BS^3 to improve the protein stability of the KO complex I. 2.5 mM BS^3 showed a significant improvement of KO complex I integrity. The results overall demonstrate that a low concentration crosslinker treatment can preserve the enzyme integrity during the purification process and therefore producing higher yields of high-quality protein for further studies.

These results led to the optimised purification process for the unstable mutant complex I. In brief, the mitochondrial membrane was solublised with 1% DDM for 30 min. When the mitochondrial membrane has been solublising for 5 min, 0.25 mM BS^3 was added to the suspension. The reaction was quenched after 25 min. After two-step chromatography, the eluted complex I-containing fractions were gently concentrated and a second crosslinking of 2.5 mM BS^3 was added 30 min before the cryo-EM grid preparation.

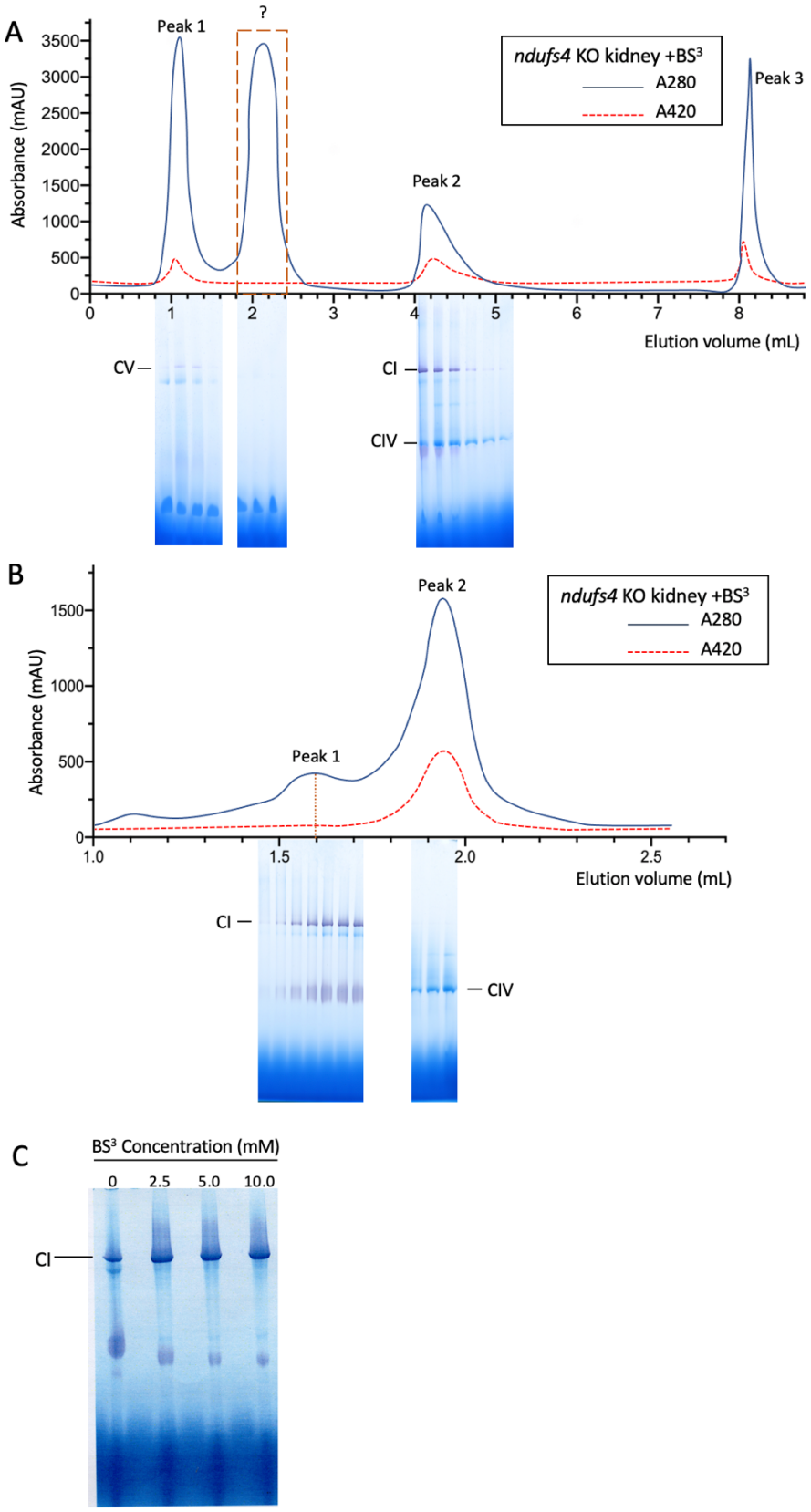

Fig 4.17 Purification of complex I from KO mice kidney mitochondria with cross-linker BS^3. (A) The elution profile with 0.25 mM BS^3 from an anion-exchange column. The orange square marked out the location of the unexpected peak. (B) The size-exclusion column elution profile of mutant complex I. (C) The in-gel activity of complex I from selected elution fractions is shown below the elution plots.

4.3.6 Preparation of *ndufs4* KO mouse heart complex I with BS^3

The *ndufs4* KO mouse has a smaller heart by weight than the WT mice (see Chapter 4.2.3) and only 25% (21.7% in reality) offspring are theoretically homozygous from the heterozygous breeding pairs. Thus, sufficient heart tissue was difficult to accumulate for the cryo-EM structure study. Eventually, 22 mg of mitochondrial membrane from 29 *ndufs4* KO mouse hearts was collected for purification. The heart mitochondrial membrane was solubilised and crosslinked in the same way as the kidney membranes and quenched by the addition of 40 mM Tris buffer (pH 7.5).

Fig 4.18A shows the complex I purification through the anion-exchange column. Similar to BS^3 treated KO kidney membranes, an extra peak is observed and attributed to the sulfo-NHS byproduct. The elution fractions at peak 2 were concentrated to 100 µL and injected onto the size-exclusion column for further purification and desalting. The spiky peaks shown in Fig 4.18 appear because of the detector reaching the limit of its linear dynamic range due to the high concentration of the injected sample. After size-exclusion chromatography, the elution fractions from peak 1 were collected. Following gentle concentration of two of the peak fractions together, a final concentration of 3.82 mg/mL was obtained before the second stage of BS^3 cross-linking. Fig 4.18C shows the purified complex I from KO mice was then crosslinked with 2.5 mM BS^3 for 30 min on ice, after which the sample was ready for cryo-EM grids preparation.

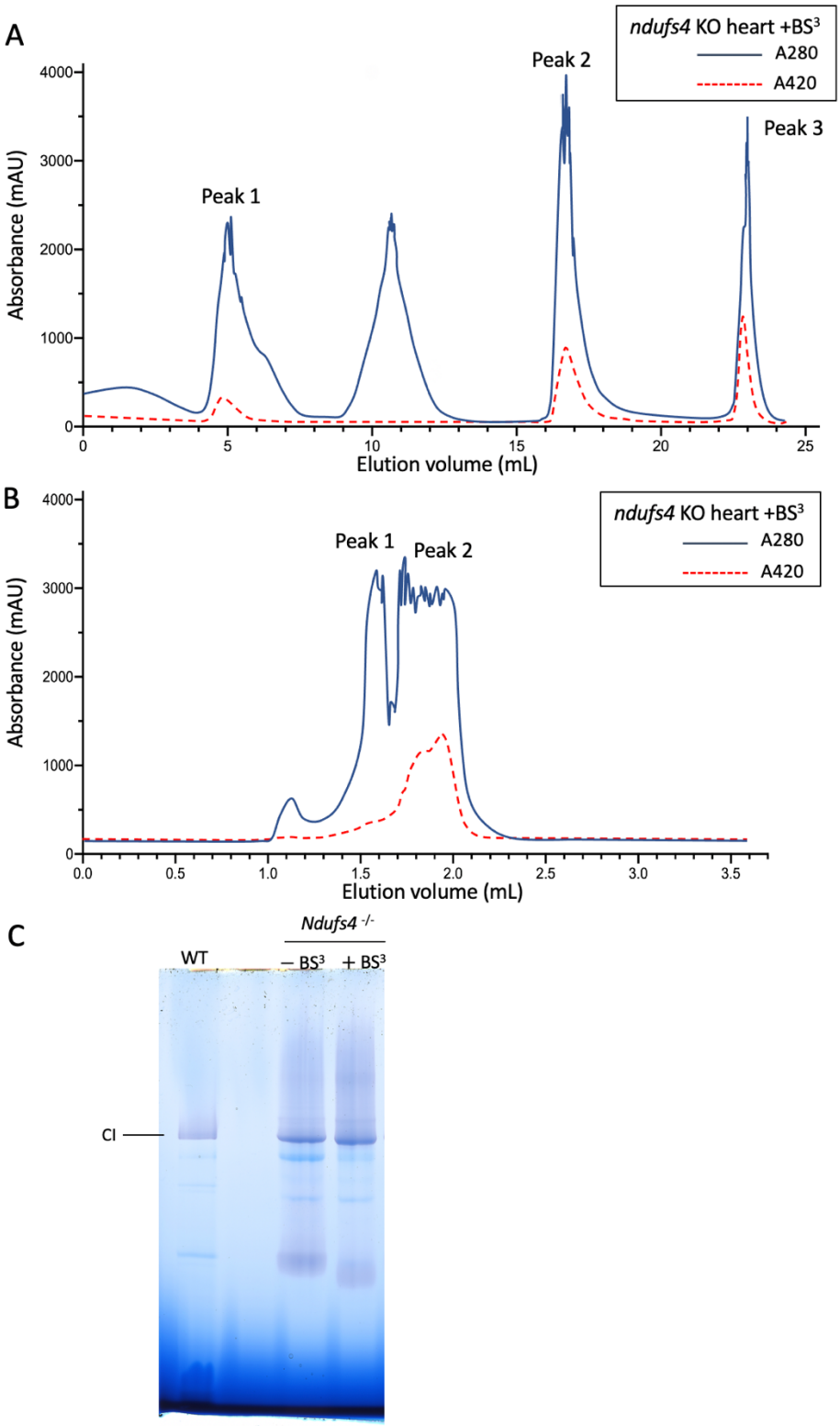

Fig 4.18 Purification of mutant complex I from mouse heart with the treatments of BS^3 crosslinker. (A) & (B) The elution profile of mutant complex I with 0.25 mM BS^3 from anion-exchange (A) and size-exclusion column (B). Fractions at Peak 2 in (A) were collected for further size-exclusion chromatography. The unlabeled peak in (A) showed the byproduct of crosslinking reaction. Fractions of peak 1 in (B) were collected for cryo-EM study. (C) In-gel activity staining on BN-PAGE. The WT mouse heart complex I from a frozen sample was loaded as control (left). The right two lanes showed the complex I from KO mice following purification with and without 2.5 mM BS^3 crosslinking. The BN-PAGE and in-gel NBT staining was performed by Dr Hannah Bridges.

4.4 Cryo-EM study of mutant complex I structure from ndufs4 KO mouse heart

4.4.1 Cryo-EM data collection

Cryo-grids with the crosslinked mutant complex I from *ndufs4* KO mouse heart were prepared in the same way as the kidney complex I, except the complex I concentration is higher in the crosslinked sample. 12 cryo-grids were made and screened with a Talos Arctica microscope using automatic atlas screening to exclude the grids with thick ice. The grids with reasonable ice thickness were further evaluated by the size of ice contaminations and broken areas. As the complex I particle distribution is highly sensitive to the ice thickness, the "donut" shape selection strategy was also applied for data collection.

The cryo-EM data was collected on a Titan Krios microscope at the UK National Electron Bio-Imaging Centre at Diamond Light Source. A Gatan K3 camera instead of K2 was used for the following reasons: K3 camera has a faster speed and can take approximately 4 times more micrographs with the same session length in comparison to the K2 (Myasnikov, Zheng, Bulkley, Cheng & Agard, 2018).The K3 camera has a larger field of view (5,760 x 4,092) compared to the K2 (4,000 x 4,000). Furthermore, the K3 camera has higher dose tolerance, thus with the same total electron dose, the exposure time was reduced without compromise the image quality (Myasnikov et al., 2018). The micrographs were taken by K3 camera in compressed non-gain corrected tiff mode. To include more particles in one image, a larder image filed was required, thus a smaller magnification was selected. The magnification for the collection was 64,000 x with a calibrated pixel size of 1.352 Å/pixel. In this data collection session, a similar total dose (45 $e^-/Å^2$) to previous data collection on WT complex I was applied with a shorter exposure time (5.4 s) compared to previous data collected by K2 (10 s) (Agip et al., 2018). The electrons were captured into 25 frames, the C2 aperture and the objective aperture were set at 50 μm and 100 μm respectively which are also the same as in the previous study (Agip et al., 2018). The collection model setup with aberration-free image shift (AFIS) and hole clustering in the EPU2.5 has saved time by minimising the movement of the stage during data collection.

Throughout 45-hours of data collection sessions, 7,309 micrographs were collected at a speed of ~162 micrographs/hr, which is approximately 5-time faster than the counting mode of K2 used in ND6-P25L-CI data collection (32 to 34 micrographs/hr, see Chapter 3.3.4).

Table 4.5 KO heart complex I cryo-EM data collection microscope setup

Microscope	Titan Krios
Detector	K3 counting (super resolution mode)
Voltage (kV)	300
Magnification	64,000
Gun lens	4
Spot size	4
C2 aperture (µm)	50
Objective aperture (µm)	100
Energy filter slit size (eV)	20
Pixel size (Å/pixel)	0.676 (in super-resolution mode), 1.352 (in real)
Exposure time (sec)	5.4
Electron exposure (e^{-}/Å^2)	45
Dose rate (e^{-}/Å^2/sec)	8.29
Defocus range (µm)	-1.5, -1.7, -1.9, -2.1, -2.3, -2.5, -2.7, -2.9
Number of fractions	25
Number of initial images	7,309

4.4.2 Reconstruction of mutant complex I

As the K3 camera is 5-times faster in data collection than the K2, the data size (7,309 micrographs in 45 hours) is ~5-times larger than for the K2 (1,519 micrographs collected in 45 hours in chapter 3.6.2). The micrographs captured through the K3 camera is in a rectangle shape (Fig 4.19A). To improve the data processing efficiency, the reconstruction was performed in a combination of RELION 3.1 and cryoSPARC v2 (Fig 4.19B). The micrographs were first imported into RELION 3.1 for motion correction by using MOTIONCOR2. The micrographs collected in super-resolution mode which has a large pixel size of 0.676 Å/pixel would result in a large box size of particles and a less efficient refinement process with limited RAM. Thus, the micrographs are two times binned during motion correction to reduce the box size. Considering a large number of micrographs (7,309 micrographs) could contribute to a large number of particles, the motion-corrected micrographs were exported from RELION 3.1 into

cryoSPARC v2 to achieve a better particle picking efficiency and a reduced demand on the central processing unit (CPU) for processing a large dataset (Punjani et al., 2017).

The CTF was estimated by using Gctf in cryoSPARC v2. As shown in Fig 4.19B, a subset of 354 micrographs were selected as the template for automatic particle picking. Within those micrographs, 2,385 particles were manually selected, and after 2D classification 2,012 particles were cleaned out for an *ab-initio* 3D reconstruction (known as the template-free 3D map reconstruction). Then the 3D map was back-projected into 2D projections as the picking template. The auto-picking process was initially tested on a smaller subset of 1,000 micrographs, with aggregated particles were largely avoided during this process (Fig 4.19C). Within the 1,000 micrographs, 11,051 good particles out of 147,298 auto-picked particles were selected for 3D classifications. One of the three 3D classes, containing 7263 particles, was able to generate a map at the resolution of 4.28 Å. With the success of the small subset data processing, the template was then used for the whole dataset of 7,309 micrographs.

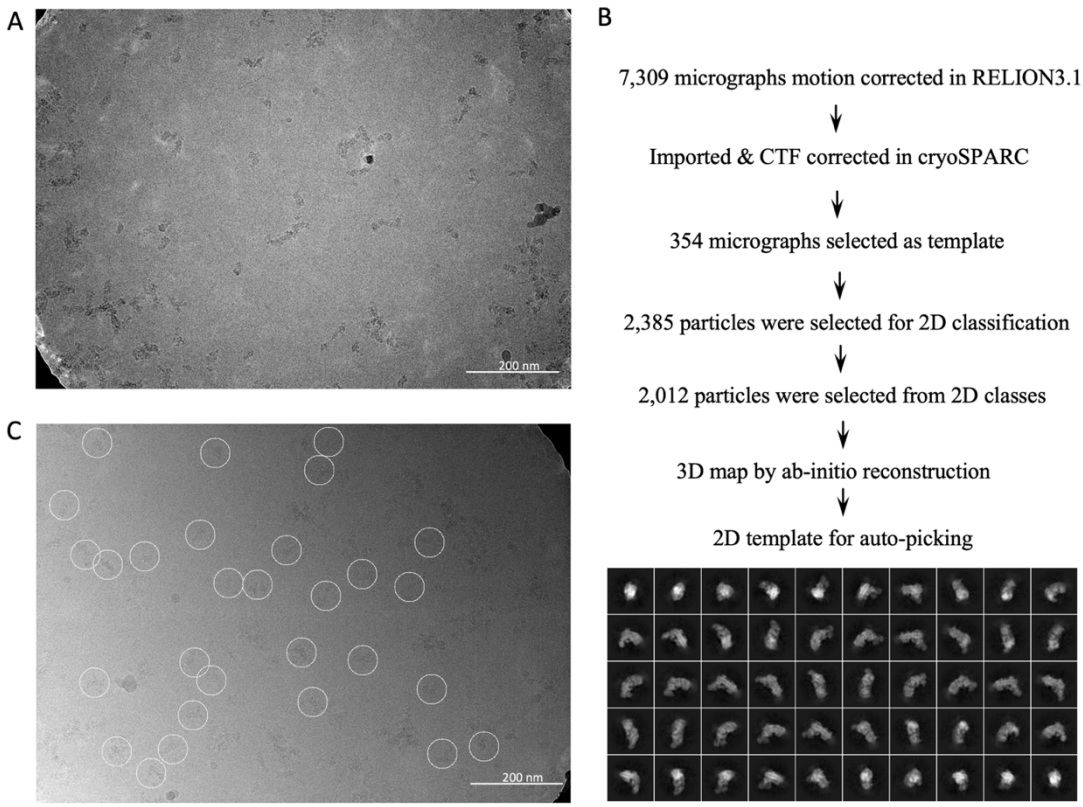

Fig 4.19 Cryo-EM analysis of K3 dataset (A) A representative K3 micrograph of mutant complex I. (B) The particle picking template selection in cryoSPARC. (C) An example of auto-picked particles on the micrograph with the template. The aggregated particles were successfully avoided by the auto-picking process.

The auto-picking in cryoSPARC gave an initial 1,141,407 particles. Following two rounds of 2D classification with 250 classes in each round, the particles were further cleaned resulting in 84,141 particles for a reference-free ab-initio 3D classification with three classes. As shown in Fig 4.20A, class 1 depicts a broken complex I with low electron density at the peripheral arm, while the other two classes (class 2 and 3) contained particle subsets with intact complex I. A quick rigid-body fitting of class 1 with a WT mouse model (PDB: 6G2J) in Chimera with a contour level of 0.287 was performed (Fig 4.20B). The class 1 has shown that there is nearly no density at N-module (NDUFV1, NDUFV2, NDUFV3, NDUFS1, NDUFA2) and the Q module has a poor density with NDUFA12 density completely absent. Considering the sample applied to the grid was collected from the homogenous peak fraction of the size-exclusion chromatography, the broken complex in class 1 could be an artefact generated during the plunge-freezing process rather than intermediate-assembly complex I. Further comparison of class 2 and 3 in Chimera shows that the two complex I maps have different handedness, but the map-to-map correlation showed a 99.49% similarity indicating the two classes belong to the same subset. Thus, the particles from class 2 and 3 were merged as one subset and further homogeneous 3D refinement was performed, giving a global resolution of 3.42 Å. To improve the resolution of the map, the particles were imported into RELION 3.1 for further analysis.

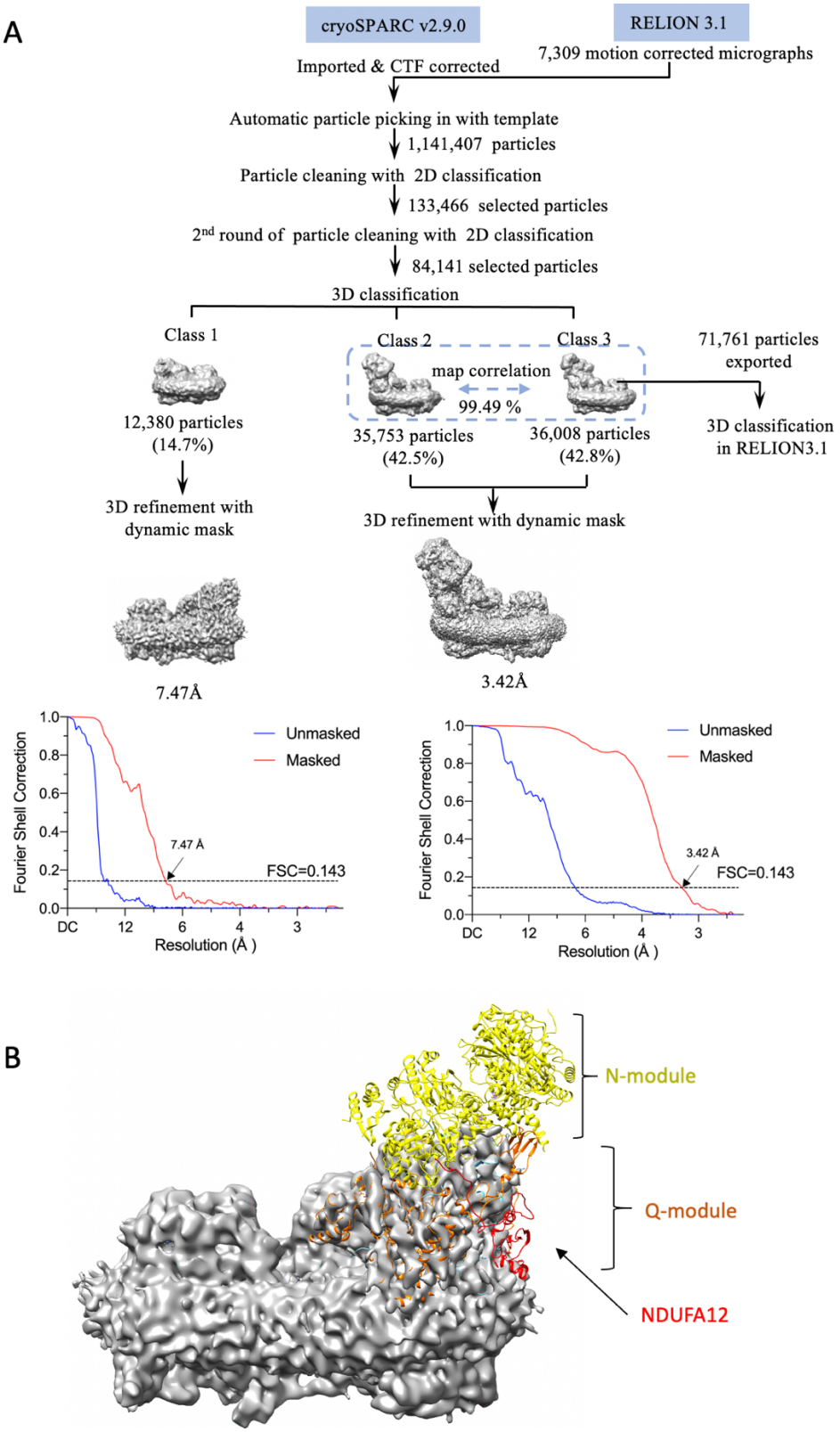

Fig 4.20 Data processing in cryoSPARC. (A) A total of 84,141 particles were selected for 3D classification from 7,309 micrographs. The 71,761 particles were reconstructed to an intact complex I with a global resolution of 3.42Å; while the remaining 12,380 particles were reconstructed into an incomplete complex I with only the membrane domain presented at a resolution of 7.47 Å. The FSC curves have shown the estimated global map resolution defined where the black dotted FSC line = 0.143. (B) Rigid body fitting of WT complex I (PDB: 6G2J) into class 1. The N-module subunits are coloured in yellow, the Q-module is in orange and the NDUFA12 subunit is in red.

The 84,141 particles were imported, and 3D classification was performed with a 60 Å low-pass filtered complex I map (class 2 from 3D classification in cryoSPARC) as the reference. However, in contrast to the 3D classification in cryoSPARC, which is an *ab initio* reconstruction, the 3D classification with the reference in RELION produced 4 classes with similar structures (Fig 4.21A). The map-to-map fit scores calculated from chimera showed a range of 95.87% to 98.34% similarity between the 4 classes. Due to the different classification methods between cryoSPARC and RELION, class 1 with broken complex I in cryoSPARC was not shown in RELION 3D classification. Thus, only 71,761 particles from class 2 and 3 from cryoSPARC were imported. By taking advantage of CTF refinements, together with particle polishing, the 3D refinement of this subset resulted in a final map of 2.9 Å in RELION. As the data was collected in super-resolution mode by K3, the data was able to be unbinned to further improve the resolution. The particles were unbinned during the polishing process by rescaling the box size in pixels of unbinned micrographs. The final resolution was slightly improved in the unbinned data, and the density of the map has been significantly improved as it showed more details during modeling (Fig 4.21B).

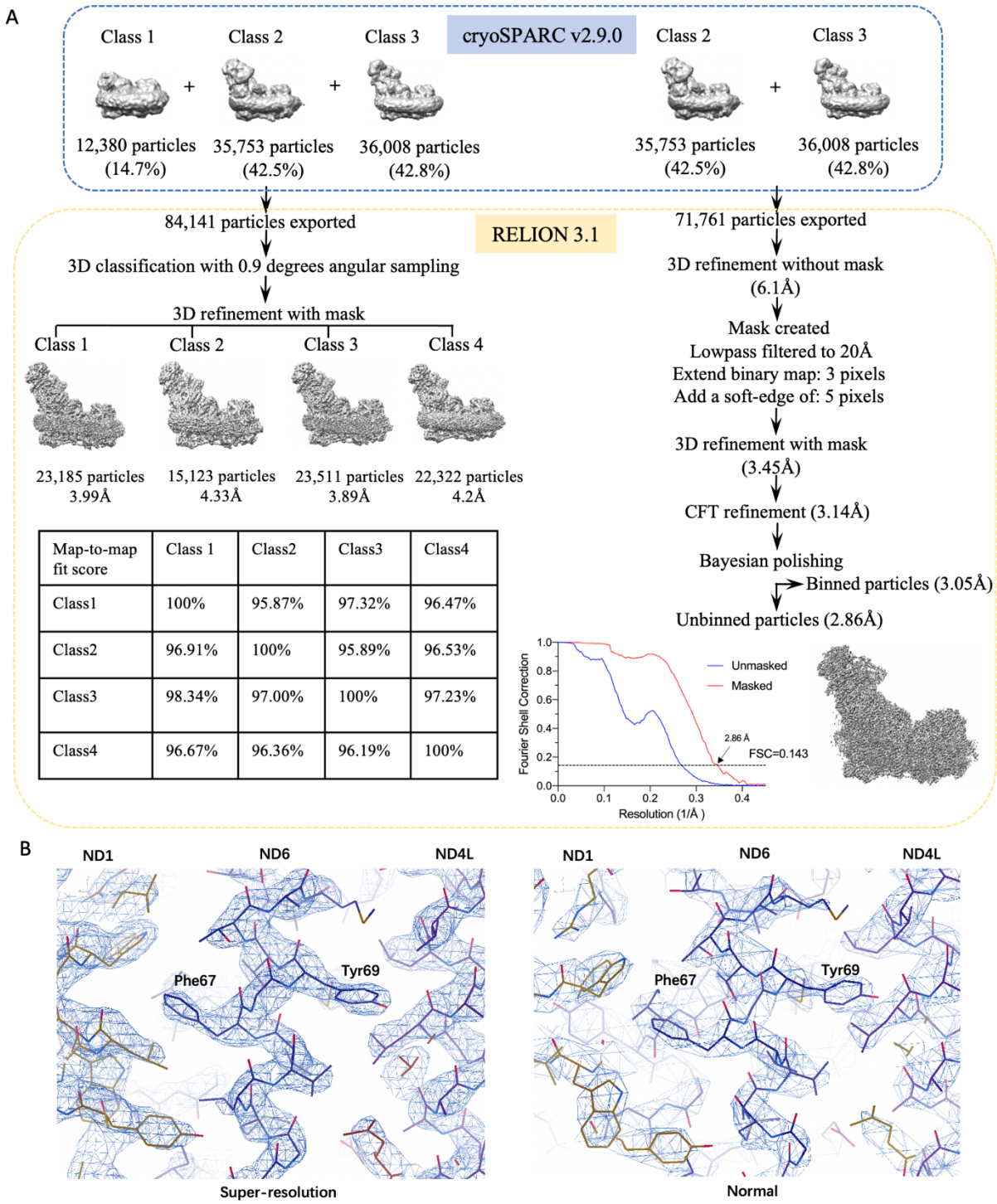

Fig 4.21 Classification and refinement scheme in RELION 3.1 for the mutant complex I. (A) 3D classifications and refinements of selected particles imported from cryoSPARC. In the left panel, 84,141 particles were classified again in RELION into 4 classes. The density maps from these 4 classes were further 3D-refined individually. The refined density maps were cross-correlated by map-to-map function in Chimera, the fit scores were shown in the table. In the right panel, 71,761 particles from the selected 2 classes from cryoSPARC were directly refined with a mask generated. Then the particles were CTF refined and Bayesian polished. The final maps were obtained at 3.05 Å for binned data and 2.9 Å for unbinned super-resolution mode data. The FSC curve shows the estimated global map resolution defined where the black dotted FSC line = 0.143. (B) A comparison of the map in super-resolution (left) and normal resolution (right). The images show the map density around the ND6 subunit with the same threshold.

4.4.3 Structural analysis of the mutant complex I

The 3D structure of complex I from KO mouse heart mitochondria (called as "the mutant complex I" in this chapter) was reconstructed with a global resolution of 2.9 Å. The local resolution shows a relatively low resolution (~ 4.5 Å) in the flavin-containing N-module (Fig 4.22A). A global conformational comparison between the mutant complex I, WT active and deactive complex I density maps is given in Fig 4.22B. The mutant complex I map shows a higher correlation to the active map than the deactive, indicating the complex I structure in *ndufs4* KO mice likely represents the active state. This result is in line with the previous findings from mutant complex I from kidney. Thus, the active mouse model (PDB: 6G2J) was rigid body fitted into the the mutant complex I density map, and the fit of each subunit was checked manually in COOT (Emsley et al., 2010). The mutant complex I possesses a series of local conformational hallmarks that indicate that it is in the active state. with the *ndufs4* KO having the same arrangement of the NDUFA5 and NDUFA10 domains as the active state rather than the deactive state (Fig 4.22C), as well as a full α-helical conformation in the ND6-TMH3.

Some densities are weak or absent in the mutant complex I. Specifically, the expected location of subunit NDUFA12 shows barely any density, indicating the absence of this subunit (see Fig 4.22D). The absence of NDUFA12 is in line with the complexome studies in different mouse tissues (Adjobo-Hermans et al., 2020; Agip, 2018). Interestingly, NDUFA12 was identified in the mutant structure of the *Y. lipolytica ndufs4* KO strain (Parey et al., 2019). This difference indicates the possibility of variation in assembly pathways between species.

The assembly factor NDUFAF2 is a paralog of accessory subunit NDUFA12 (Ogilvie, Kennaway, & Shoubridge, 2005), which was identified in previous complexome profiling (Agip, 2018). However, it was not identified in the mutant complex I structure. The NDUFAF2 was believed to be associated with the 830-kDa subcomplex for stabilisation (Calvaruso et al., 2012; Ogilvie et al., 2005). It seems likely that the NDUFAF2 identified in the complexome study is associated with the 830-kDa subcomplex I rather than the mature complex I. In addition to the loss of NDUFA12, another two subunits show poor density – NDUFS6, and NDUFA7 (see Fig 4.22D). In NDUFS6, density for the first 37 amino acids is lost, but the rest of the

subunit possesses a strong density, including the bound Zn^{2+} cofactor. In NDUFA7, amino acids 17 to 35 have low density relative to the active mouse structure. It is known that NDUFS4 is involved in the late stages of the mammalian complex I assembly, together with NDUFV3, NDUFA12, and NDUFS6 (Guerrero-Castillo et al., 2017). These subunits closely interact with NDUFA12 in the WT structure (see Fig 4.22D). Thus, it was expected that the loss of NDUFA12 influences the stability of the adjacent subunits.

In the *Y. lipolytica ndufs4* KO strain, the N-terminus of NDUFA11 was observed with poor density, and TMH 16 of ND5 was weak or absent (Parey et al., 2019). However, in the mouse mutant complex I map, those mentioned positions show strong densities with ordered helices. NDUFA11 was reported to interact with complex III in mammalian supercomplex (Wu et al., 2016), with complex III determined to stabilize complex I in the *ndufs4* KO mouse model in the supercomplex forms of CI+CIII2 and 830-kDa CI + CIII2 (Calvaruso et al., 2012). In the *Y. lipolytica* study, the distortion of NDUFA11 was believed to be associated with a complex III interaction for stabilising the complex I; however, there is no direct evidence showing the presence of complex III in their structure. The clear density of NDUFA11 in this study has shown that NDUFA11 in the mouse *ndufs4* KO strain was undamaged, and the surrounding structure also showed ordered arrangements. The results provide another possibility that the complex I lacking NDUFS4 could also be stabilised without the help of complex III.

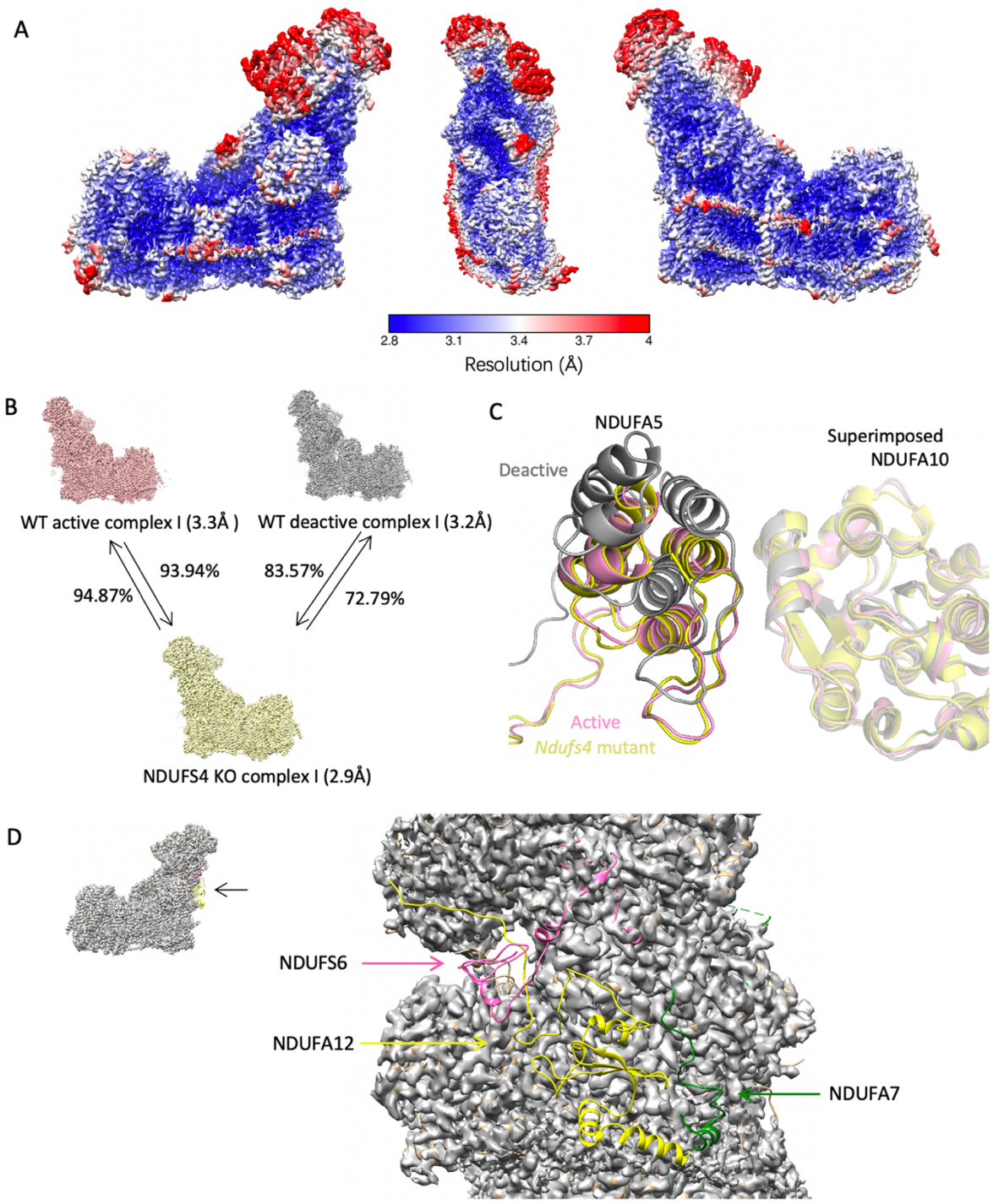

Fig 4.22 The mutant complex I is in the active state. (A) Local resolution of mutant complex I. (B) The map-to-map cross-correlation coefficient calculated from Chimera rigid fitting between active state WT complex I (pink), deactive state WT complex I (gray), and mutant complex I (yellow) density maps. (C) The relative position difference of NDUFA5 and NDUFA10 in the active, deactive state WT and mutant complex I. (D) the rigid body fit model in the mutant complex I density map shows no density of NDUFA12, with poor density for NDUFA7 and NDUFS6.

Interestingly, the local resolution has shown that the deletion of the NDUFS4 subunit left a deep groove at the location of NDUFS4 with relatively good resolution around it, suggesting that the local conformation does not seem disturbed by the absence of the NDUFS4 subunit.

However, the loss of the NDUFS4 subunit can expose the iron-sulfur clusters (N1b and N3) adjacent to the C-terminus of NDUFS4 to the solvent environment (Fig 4.23A). This solvent exposure area was calculated in *Y. lipolytica ndufs4* KO strain, which is about 2.6-fold higher than the WT (Parey et al., 2019). FMN was found and fitted with a strong density in COOT (Fig 4.23B). The previous temperature-based flavin association study also showed that the FMN in the mutant complex I has the same stability as in the WT (Agip, 2018). Additionally, there is no indication of any major change in the position of the FeS clusters in this mutant complex I model, and the results is different from the previous EPR spectroscopy measurement, where the signal from the detected four clusters is diminished (Agip, 2018). As the solvent exposure can affect the FeS clusters in the yeast mutant (Parey et al., 2019), the EPR spectrum of crosslinked mutant complex I should be measured to verify whether the crosslinker influenced the solvent exposure. Interestingly, the N-module (NDUFV1, NDUFV2, NDUFS1, and NDUFA2) in the KO structure shows a slight shift compared to the WT structure (Fig 4.23C). The same shift was also observed in the mutant complex I structure from the mouse kidney. In the yeast complex I, a similar shift was identified and described as 1° backward tilt (Parey et al., 2019). This evidence indicates that rather than disrupting the local arrangement, the loss of NDUFS4 could cause an instability in the N-module attachment. Considering the decreased NADH:O2 oxidoreduction activity of the mutant complex, the unstable N-module and the exposure of iron-sulfur clusters could be the reasons for the decreased electron transfer activity during this process.

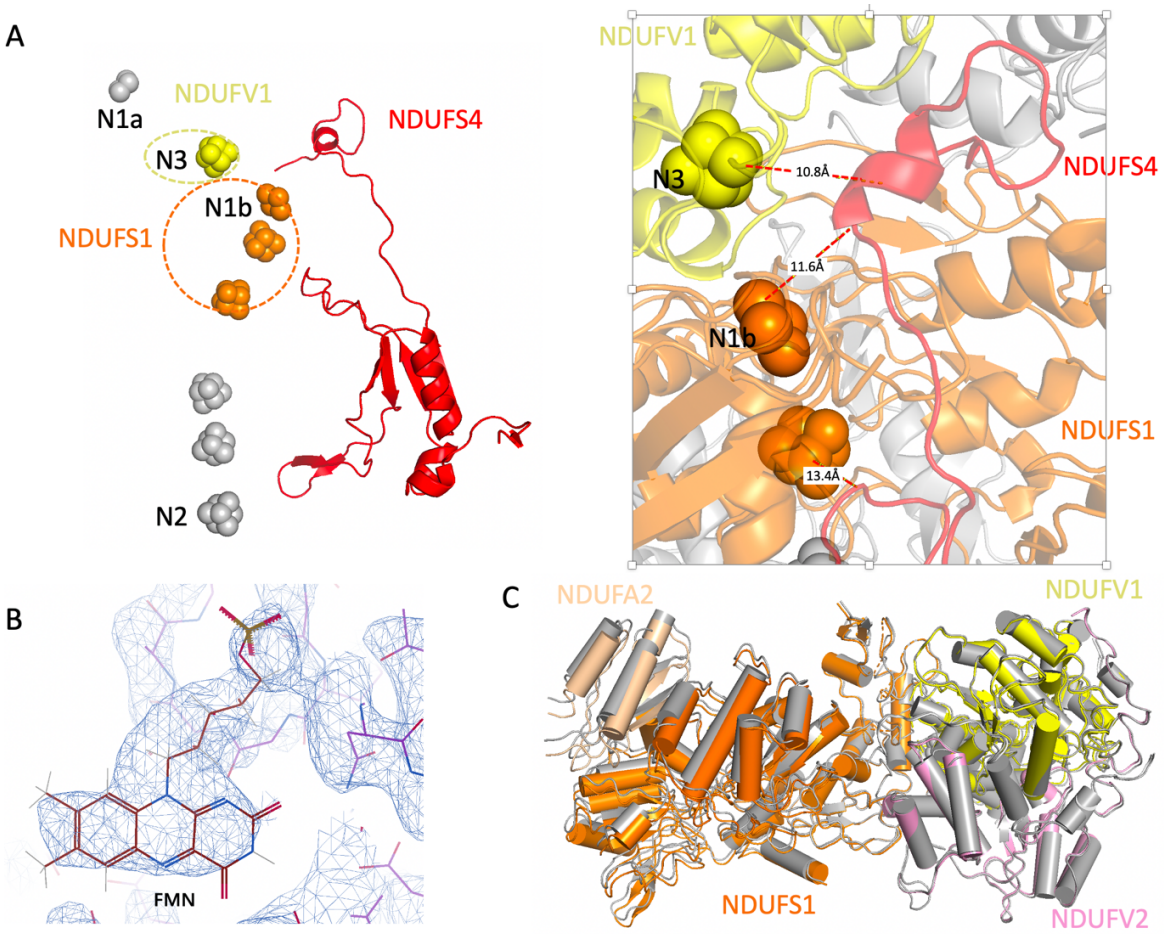

Fig 4.23 The mutant complex I structure around the position of NDUFS4. (A) The location of FeS clusters to the NDUFS4 subunit. The distance from the adjacent iron-sulfur clusters to the NDUFS4 subunit was measured as indicated in the right panel. (B) The FMN shows a clear density in the mutant. (C) The overlay of and mutant complex I (color) N-module and WT (gray) with aligned membrane arm (not shown).

Interestingly, a clear density of ubiquinone was identified in the Q binding tunnel (Fig 4.24A). The head position is close to Tyr108 in NDUFS7 (3.9 Å) and the tail shows a continuous density until the last isoprenyl units (Fig 4.24A). The quinone head group is 14.1 Å away from the N2 cluster (Fig 4.24B), and the main subunits forming the tunnel have not changed compared to those observed in the WT active structure. The binding position is similar to the proposed ubiquinone-binding cavity in mice and also to the published piericidin A binding position, where the head group is 3.4 Å from the Tyr108 (Agip et al., 2018; Bridges et al., 2020). There is a "ring" of density in the kink region of the isoprenoids, which is possibly due to averaging of two positions. Comparing to the continous density of the isoprenoids chain, the benzoquinone head group has show weak density suggesting multiple possible positions of the head group. Surprisingly, the continuous ubiquinone density was not observed in the unpublished high-resolution (2.5 Å) WT mouse density map, which raises the question if the

presence of ubiquinone in the binding tunnel is due to the mutation or whether the crosslinker has enhanced the ubiquinone binding in the cavity. Further cryo-EM study of WT mice with crosslinker treatment is required to answer such a question.

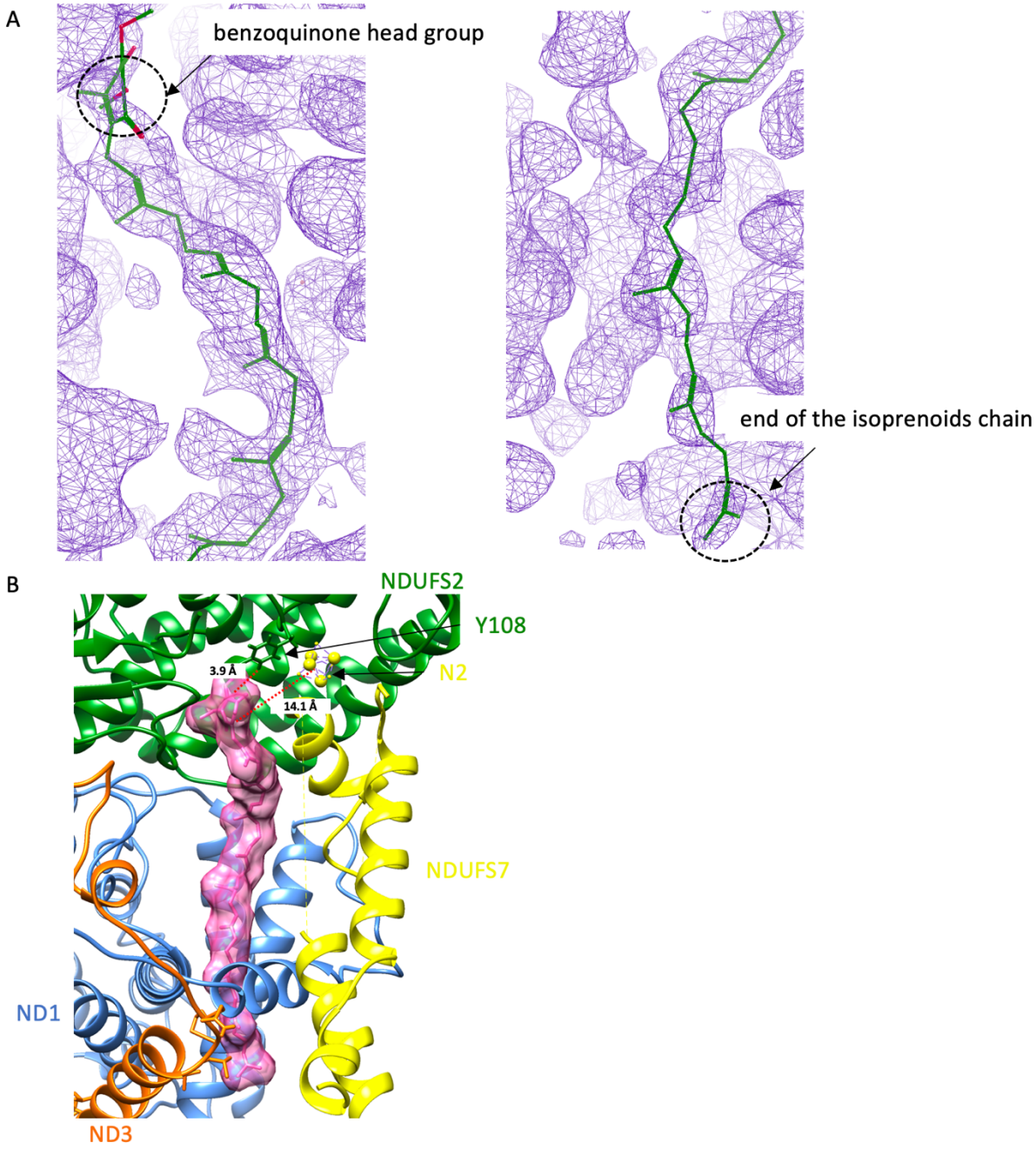

Fig 4.24 A clear ubiquinone density identified in the mutant complex I structure. (A) The continuous density with a Q9 model fitted as shown in COOT. The left panel shows the density of head group and the first four isoprene units. The right panel shows the density of the last five isoprene units. The density map is generated by Phenix with automated map sharpening. (B) The position of the modelled Q9 (hot pink) with the surrounding subunits. The distance from the Q9 head group toY108 anf N2 cluster is about 3.9 Å and 14.1 Å respectively.

4.5 Discussion

Patients with pathogenic variants on *ndufs4* have been reported with severe neurodegenerative disorders (Budde et al., 2000). The common characteristics of complex I deficiency caused by the loss of the NDUFS4 subunit are low enzyme activity and stability (Kruse, et al., 2008; Kühn et al., 2015; Kahlhöfer et al., 2017). Although, the mutant complex I structure from the yeast was reported (Parey et al., 2019), this high-resolution mammalian complex I structure from *ndufs4* KO mouse heart has illustrated for the first time a deficient complex I structure from a clinical phenotype-based animal model. The structure shows distinct differences from the healthy WT mouse complex I, indicating a possible pathogenic mechanism behind the mutant structure.

4.5.1 A combination of mature and immature CI in *ndufs4* KO mouse heart mitochondria

At the protein level, the catalytic activity of complex I from KO heart mitochondria was proven to be remarkably low when compared to the WT complex I. This low activity of complex I had previously been reported across a range of tissues in KO mice including liver, kidney, brain, heart, and muscle and also patients' muscle and fibroblast (Budde et al., 2002; Breuer et al., 2013; Calvaruso et al., 2012; Kruse, et al., 2008). These results are consistent with these studies, showing a general low complex I activity in the *ndufs4* KO mouse. The succinate oxidoreduction activity was unchanged from the WT in this study, also in agreement with other studies which indicate that normal oxidoreduction through complex II-III-IV proceeds with no negative effects arising from the complex I deficiency (Kruse, et al., 2008; Agip, 2018). These results confirm that the pathologies associated with NDUFS4 deficiency are the direct consequence of the impaired complex I activity rather than being a downstream effect on OXPHOS complexes.

Several possibilities have been considered to explain the low enzyme activity in the mutant mouse. The first possible situation is that the complex I quantity in the membrane is decreased. The catalytic experiments measuring complex I content by non-physiological NADH:HAR and

NADH:APAD$^+$ transhydrogenation reactions showed 6% and 25% activity in comparison to the WT (Agip, 2018), indicated a largely decreased mature complex I. The purification yield after crosslinking also showed a reduced yield of intact complex I in comparison to the WT. However, SDS-PAGE analysis with antibodies has shown that the individual subunits of complex I were presented at comparable amounts (Krus et al., 2008). These compositional studies have also shown unchanged subunit quantities but an increase in the NDUFAF2 present (Adjobo-Hermans et al., 2020). These results all suggested that the production of complex I was not influenced but the amount of intact complex I is possibly decreased.

The second possibility is that the KO complex I in the mutant mouse is in an immature subcomplex form. The NDUFS4-absent patients' fibroblasts have shown no complex I activity with only 830-kDa subcomplex observed on BN-PAGE (Breuer et al., 2013). Many other studies from different species, organs, and cell lines, highlight a subcomplex I with a size of ~830 kDa which was also identified in BN-PAGE analysis from this study (Kahlhöfer et al., 2017; Stroud, et al., 2016, Adjobo-Hermans et al., 2020). However, whether the subcomplex of KO complex I identified by electrophoresis studies is a reflection of the situation *in vivo* is still controversial. The mutant complex may break on the BN-PAGE due to its weak connection between the N-module and the main complex. The results from crosslinker studies on the KO mitochondrial membranes showed that after applying crosslinker, the intact complex I band was shown on BN-PAGE and the 830-kDa subcomplex I is much decreased, which proves that the dissociation of the N-module in the mutant complex was caused by the electrophoresis process. This indicates the possibilty of the co-existence of a fully assembled complex I without the NDUFS4 subunit and the immature 830-kDa subcomplex in the mitochondrial membrane. Further evidence of the NDUFAF2 associated 830-kDa subcomplex identified in the mutant mouse embryonic fibroblasts (MEFs) and patient fibroblast has also suggested the existence of an immature complex I (Adjobo-Hermans et al., 2020; Calvaruso et al., 2012). It is known that the mammalian complex I may exchange and re-assemble the N-module to maintain homeostasis (Lazarou et al., 2007). The unstable assembly process of the mutant complex I could affect the homeostasis and alter the efficiency of exchange and re-assembly of the N-

module. Thus, both mature and immature complex I could be present in the mitochondria of the *ndufs4* KO mouse.

The third possibility is that the mature complex I has a decreased activity. This study of the NADH:DQ oxidoreductase reaction on the crosslinked mutant membrane still shows no improvement in the activity. This suggests that the intact mutant complex I has low activities as well. The purified mutant complex I shows a NADH:DQ activity of 0.86 μmol/min/mg (Agip, 2018). Similar results were also reported in *Y. lipolytica*, where the mutant complex I was intact on the BN-PAGE but the NADH:DQ activity is only 30% of the WT (Kahlhöfer et al., 2017).

The results outlined in this chapter combined with this literature data suggest the co-existance of immature complex I intermediates and mature mutant complex I in the mitochondrial membrane, and the mature complex I has a decreased activity. The NDUFS4 subunit is proposed to facilitate and stabilise the anchoring of the N-module, thus, the absence of NDUFS4 could decrease the assembly efficiency resulting in the presence of immature subcomplex and also unstable mature complex I.

4.5.2 *Ndufs4* gene deletion results in complex I instability and the loss of the NDUFA12 subunit

Complex I purification and cryo-EM reconstruction was initially performed and optimised using KO mice kidney tissue. The density map obtained from the KO mice kidney showed the intact mature complex I without the NDUFS4 subunit. The optimised crosslinking treatment of complex I from KO mouse hearts with BS3 allowed for an effective and homogenous chromatographic purification. The resulting 2.9 Å high-resolution structure of the mutant complex I further showed the absence of NDUFA12 with weak density for both the NDUFS6 and NDUFA7 subunits. The loss of NDUFA12 in the mutant complxe I structure from this study is consistent with the compositional studies of KO mouse brain tissue, KO mouse embryonic fibroblasts, and NDUFS4-mutated human cells (Stroud et al., 2016; Adjobo-Hermans, et al., 2020). On the contrary, the loss of NDUFA12 is not observed in the structure of the *Y. lipolytica ndufs4* KO strain (Parey et al., 2019). It was expected that this is mainly due

to the difference between yeast and mammalian tissue; however, this also suggests the possibility of variations in the assembly pathway between species. Collectively, the results described here, along with these previous studies all demonstrate that the deletion of NDUFS4 in mammalian complex I hampers the assembly of NDUFA12 onto the mature complex.

Previous compositional studies from KO mouse brain tissue and LS patient cells demonstrated an increased level of specific assembly factors including NDUFAF2 (Adjobo-Hermans, et al., 2020). NDUFAF2, a paralog of NDUFA12, is known as an assembly factor involved in the final phase of complex I assembly, where it is associated with the insertion of FeS cluster N4 between the Q- and N-modules (Ogilvie et al., 2005; Vogel et al., 2007; Lazarou et al., 2007). The mouse NDUFAF2 is 13.1/22.0% identical/similar to mouse NDUFA12 in sequence. Similarly, the NDUFAF2 was also found to be retained in the complex I of yeast *ndufs4* KO strain, albeit with a weak interaction between the assembly factor and the main complex (Kahlhöfer et al., 2016). Interestingly, the complexome study of KO mouse mitochondrial membrane has shown the presence of NDUFAF2 and NDUFA12 in both KO and WT hearts (Agip, 2018), specifically an increased level of NDUFAF2 and decreased level of NDUFA12 in the KO mouse brain tissue (Adjobo-Hermans et al., 2020).

However, these previous complexome profiling studies are all based on electrophoresis gel analysis of mitochondrial membranes, which does not present direct evidence showing the attachment and association of NDUFAF2 with mature complex I. The recent cryo-EM study of yeast NDUFS4-lacking complex I shows a structure lacking NDUFAF2 binding, which was explained as the loss of the weak interaction of NDUFAF2 with complex I during solubilising and chromatographic purification (Parey et al., 2019). This study with crosslinker treatment on membrane-associated CI showed no appearance of the NDUFA12 or NDUFAF2 with intact complex I, suggesting the absence of NDUFAF2 is not due to the purification process in mouse tissue. The mouse embryonic fibroblasts have shown an association of NDUFAF2 with an 830-kDa subcomplex in both WT and KO (Adjobo-Hermans et al., 2020). Thus, it is debatable as to the extent that NDUFAF2 is associated with the mature KO complex I, raising questions as to how it interacts with complex I and other complex I intermediates. Based on the current

information, a late-stage assembly pathway as shown in Fig 4.25 was proposed. It is envisaged that the presence of NDUFS4 is not the trigger for NDUFAF2 disassociation as proposed in *Y. lipolytica* (Parey et al., 2019), but instead, NDUFS4 helps to anchor NDUFA12 and the surrounding subunits.

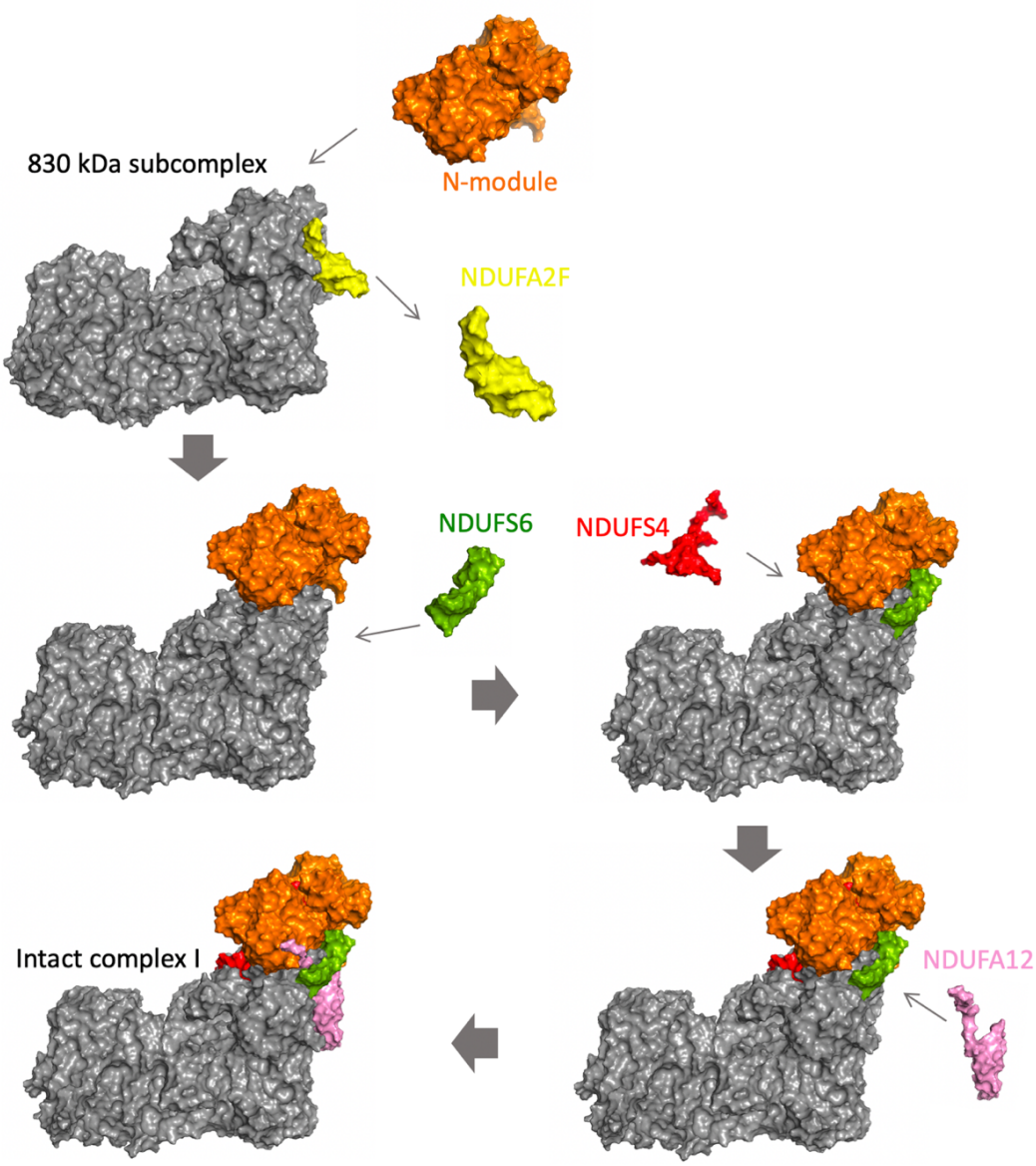

Fig 4.25 Proposed late stahe assembly pathway of complex I. NDUFAF2 binds to 830-kDa subcomplex. Anchoring of the N-module was achieved by the release of NDUFAF2 and mounting of NDUFS6. NDUFS4 is then attached to the complex to fix the position of N-terminus of NDUFS6. NDUFA12 then associats to the complex in the last step. NDUFAF2 model was generated using using the Phyre^2 server (Kelly, Mezulis, Yates, Wass & Sternberg, 2015).

Comparing the complex I structures obtained here from KO mouse kidney and heart tissue, both showed a weak density of N-terminus in NDUFS6 subunit. NDUFS6 contains a Zn-

binding site of unknown function (Kmita et al., 2015). It was reported that knockouts of NDUFS6 led to the dissociation of the N-module from complex I (Stroud, et al., 2016). The crosslinked structure showed the presence of the NDUFS6 subunit with the first 37 amino acids absent, while the rest of the structure including the Zn-binding position remains the same as the WT structure. These missing amino acids are close to the expected position of the NDUFS4 subunit, which suggests the NDUFS4 subunit deletion disturbs the arrangement of part of the NDUFS6 on complex I. The deletion of the NDUFS6 subunit in yeast has shown an intact structure of NDUFS4 (Adjobo-Hermans, et al., 2020). Therefore, these findings together with the previous study also refer to the NDUFS4 influence the stability of the NFUDS6 subunit onset but not *vice versa*.

4.5.3 Pathogenesis of the *ndufs4* KO mouse complex I

The *ndufs4* KO mouse shows a severe Leigh-like phenotype (Kruse et al., 2008). One of the recognised explanations of this pathogenesis is the instability of the mutant complex I causes a low enzyme activity and high ROS production which both are toxic to OXPHOS metabolism and such cellular aberrations are correlated with the phenotypes in the patient (Adjobo-Hermans et al., 2020; Breuer et al., 2013; Ortigoza-Escobar et al., 2016). The *ndufs* KO mouse complex I in line with the yeast structure has shown no change in coordination of any iron-sulfur clusters but indeed the loss of NDUFS4 has exposed a larger solvent-accessible area near N1b and N3 (Parey et al., 2019). Such exposure could potentially increase the possibility of electron leakage resulting in the production of ROS. Interestingly, it has been shown that a hypoxia environment could mitigate the phenotypes (Jain et al., 2016), which also suggested that the oxygen damage in this mutant could be the main cause of the disease. Additionally, the mutant structure shows a shifted N-module with low resolution indicating that an unstable positioning of the N-module which could also be a cause of electron leakage. Furthermore, the structure has shown a continuous density of ubiquinone at the Q-binding tunnel which is not observed in the yeast mutant structure. It makes us consider whether the NDUFS4 deletion could cause a local conformational change around Q-tunnel which results in a strong binding at the Q site and blocked the Q reduction. However, the Q-tunnel has shown a similar arrangement to that in the

active state WT complex I, which makes us consider another possibility that the Q is binding for a longer time to compromise the less efficient electron transfer due to the shift of the N-module. A detailed structural analysis around Q-tunnel is needed supplemented with robust biochemical evidence to support this idea and confirm any potential effects the NDUFS4 mutation has on Q binding at the spatially separated Q binding site.

4.6 Conclusion and future works

In this chapter, a high-resolution cryo-EM structure of the highly unstable mutant complex I from the clinically relevant *ndufs4* KO mouse heart model was presented. The structure of the mutant complex I without NDUFS4 has shown a complete loss of NDUFA12 subunit, a shifted N-module, and increased solvent exposure of the N1b and N3 FeS clusters. Together with the previous enzymology study and complexome profiles, the important roles of NDUFS4 in the late stage of complex I assembly including N-module anchoring was revealed. The compromised enzyme activity in the mutant complex I could be caused disturbed by a decreased electron transfer efficiency and an increased ROS production due to the structural changes. The results provide an opportunity to investigate promising therapeutic strategies to stabilise or restore complex I and decrease the ROS damage for NDUFS4-linked complex I disorder in the future.

Chapter 5. Improving complex I distribution on cryo-EM grids by grid surface modification

5.1 Introduction

5.1.1 Carbon coated grids

The carbon-coated grids (continuous amorphous carbon grids) have been widely used for negative staining in traditional EM and routinely used in cryo-EM (Grassucci, Taylor & Frank, 2007). The carbon-coated grids can be either made in-house with continuous carbon film or purchased as holy carbon-coated grids, such as Quantifoil™ and C-flat™ grids. However, there are limitations to the holey carbon-supported grids.

Firstly, the holy carbon grids require high protein concentration which is sometimes difficult to achieve. For a traditional sample preparation with the holey carbon-supported grid, 2 to 4 μL of the purified sample (1MDa) with a concentration of 0.5 to 10 mg/mL is needed (Fig 5.1A) (Vinothkumar & Henderson, 2016). The larger size of the protein, the higher concentration it needs to achieve a reasonable number of particles on the grid. For complex I, ~1 MD in size, 3 to 4.5 mg/mL was used (Vinothkumar et al., 2014; Zhu et al.,2016; Agip et al., 2018). For each grid preparation session, multiple grids (usually 10-12 grids) are made to allow screening for the best grid. This means that, for each grid screening session, a minimum of ~75 μg complex I protein are required. However, for some purified protein samples, it is difficult to achieve the required concentration or amount. For example, the protein purification from 4 liters of human cell culture ended up at a concentration of 0.2 mg/mL (Guo et al., 2017). Besides, specimens like the unstable mutant complex I, are not suitable to concentrate considering its fragility and instability for aggregation.

Secondly, the ideal grids should contain particles evenly distributed with various orientations (Fig5.1B), however, the carbon surface could result in an uneven distribution of particles. It has been shown that the majority of the protein populations can be easily stuck on either the

amorphous carbon supporting film (Fig 5.1C) or the edge of the grid hole (Fig 5.1D) where the ice is thick after bolting and plunge freezing (Drulyte et al., 2018). And this phenomenon is even more significant in low concentration samples (Drulyte et al., 2018).

A

Number of particles in projection/μm² in 800 Å thick ice film (separation)

	Concentration				
M.W.	10mg/ml	2mg/ml	0.5mg/ml	0.1mg/ml	20μg/ml
10 kD	48000 (45Å)	10000 (100Å)	2500 (200Å)	500 (450 Å)	100 (1000 Å)
50 kD	10000 (100Å)	2000 (220Å)	500 (400Å)	100 (1000Å)	20 (0.2μm)
250kD	2000 (220Å)	400 (500 Å)	100 (1000 Å)	20 (0.2μm)	4 (0.5μm)
1 MD	500 (400Å)	100 (1000Å)	25 (0.2μm)	5 (0.4μm)	1 (1μm)
5 MD	100 (1000Å)	20 (0.2μm)	5 (0.4μm)	1 (1μm)	0.2 (2.2μm)
25 MD	20 (0.2μm)	4 (0.5μm)	1 (1μm)	0.2 (2.2μm)	0.04 (5μm)

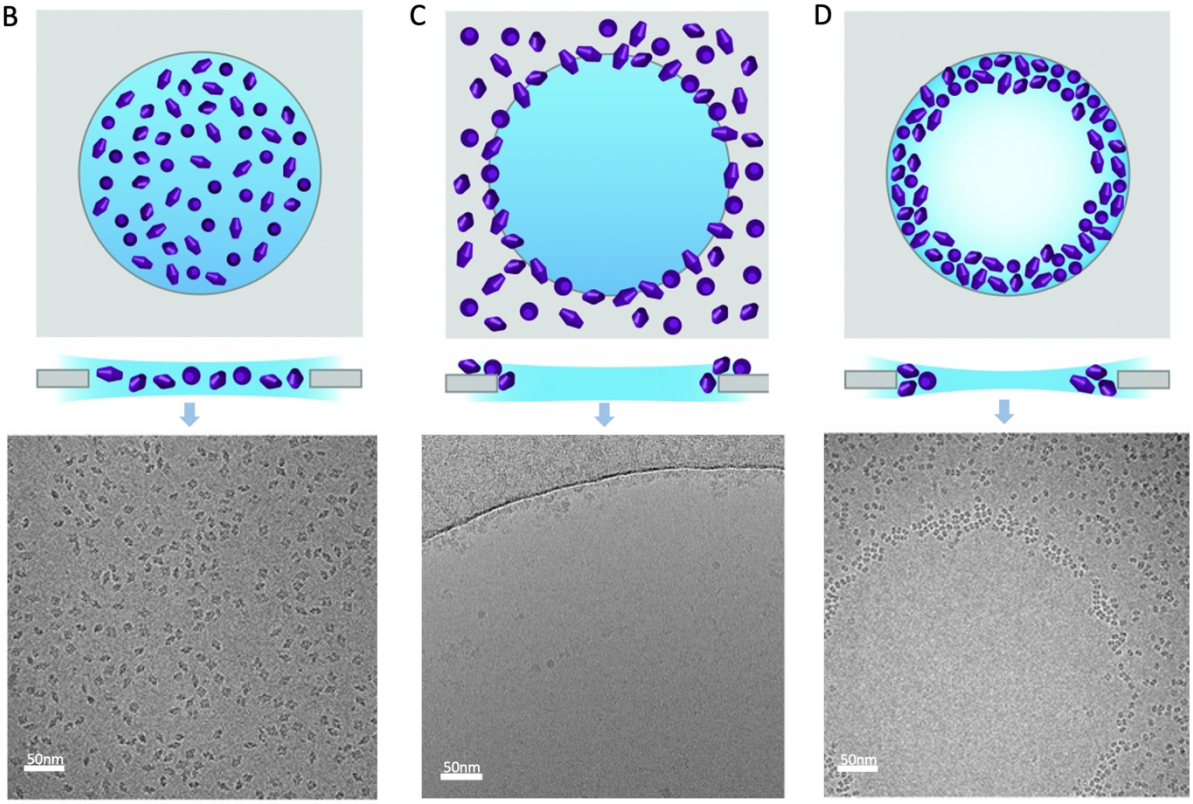

Fig 5.1 Particle distributions on holey grids. (A) The expected number of particles and separations will be seen on the grids with the given concentrations and molecular weight of interests. The table was adopted from Vinothkumar & Henderson (2016). The numbers in green color represent reasonable number of particles per μm^2. The numbers in red are too condensed, those in blue are too separate. (B) to (D) the schematic representations (top) and micrographs (bottom) of the protein distributions in the vitrified grids. (B) An ideal sample with well-dispersed particles. The particles in the micrograph are β-galactosidase, MW ~480 kDa. (C) The particles have a high affinity to the carbon film. The micrograph showed the grid with oligomeric proteins, MW ~600 kDa. (D) The empty center of the hole with very thin ice pushing the particles to the edge. The particles in the micrograph are Human erythrocyte catalase, MW ~240 kDa. The images in (B) to (D) were adapted from Vinothkumar & Henderson (2016) and Drulyte et al. (2018) with some modifications.

To tackle the problem of dealing with low concentration unstable complexes, the common approach is to coat a continuous carbon layer onto the grids (Williams & Glaeser, 1972). It has recently been reported that as low as 0.2mg/mL mammalian respirasomes (human and porcine) applied on the continuous carbon layer coated Quantifoil grids can be used in cryo-EM (Guo et al., 2017; Gu et al., 2016). Even though the carbon film can produce a background noise from electron scattering (poorer signal to noise ratio) and particle movements during imaging (Brilot et al., 2012), the continuous carbon layer can improve the particle distribution in the hole. The effect of movement induced by carbon film can later be minimised by a motion-correction algorithm during the image process (Zheng et al., 2017). Besides, it was known that a thin layer of continuous carbon film could improve the particle orientations by pulling particles away from the air-water interface (Cheng, Grigorieff, Penczek & Walz, 2015).

5.1.2 Graphene and graphene oxide grids

Although continuous carbon film has been successfully used as sthe ample supporting material for the cryo-EM study of macromolecules, this type of carbon film has several disadvantages: it is often semiconducting which could result in background noise, and the fabrication of consistent good-quality thin layers carbon-coated grids by evaporation is difficult (Glaeser & Han, 2017). Compared to the traditional amorphous carbon, graphene is considered as a better substitution.

Graphene has a single-layered carbon crystalline lattice with a flexible three-dimensional structure (Fig 5.2A). It also has a higher electron conductivity and a thinner layer compared with traditional carbon film (Russo & Passmore, 2014b). The monolayered graphene has barely any contrast under EM (Russo & Passmore, 2014b; Han et al., 2020). Thus, the diffraction mode of EM was used to identify the crystalline lattice of graphene monolayer (Fig 5.2B) (Russo & Passmore, 2014b). These favorable characters over amorphous carbon make graphene a promising sample supporting substrate. There are a few protein structures solved by cryo-EM that have used graphene-coated grids and the results showed a significantly reduced background noise on the micrograph (Russo & Passmore, 2014b; Han et al., 2020). However during their experiments, only soluble proteins such as the ribosome, GroEL, and apoferritin

were tested. Whether the membrane protein such as complex I is suitable for this method is still unknown.

At the moment, graphene is still not widely used as the graphene-coated grids is not usually feasible in-house. The graphene layer deposition on grids requires specific equipment (Russo & Passmore, 2014b; Han et al., 2020). Besides, the purchased graphene-coated grids are available but pricy. The sample optimisation process usually requires several dozens of grids to find out the best conditions which make the whole process even costly.

The alternative option is graphene oxide (GO) (Fig 5.2C and D), which has a hydrophilic surface and reduced background contrast (Pantelic et al., 2010). Fabricating GO-coated holey carbon grids is less expensive and more feasible without any specific equipment (Palovcak, et al., 2018). Recent studies also showed that the GO-coated grids can be used to improve particle distributions and orientations to achieve near-atomic resolutions (Bokori-Brown et al., 2016; Boland, et al., 2017).

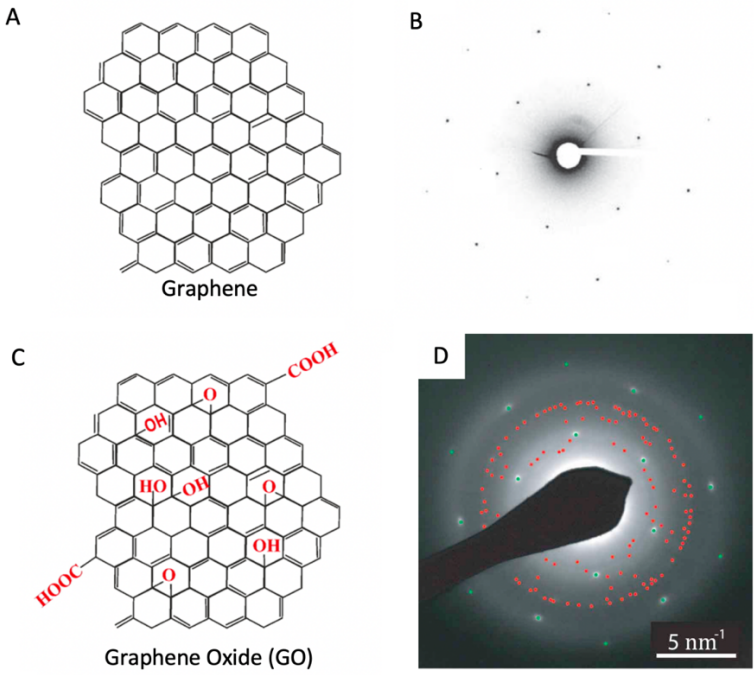

Fig 5.2 The structures of graphene and graphene oxide. (A) & (C) The crystal structure of graphene and graphene oxide. The images were adapted from Priyadarsini, Mohanty, Mukherjee, Basu & Mishra (2018). (B) The electron diffraction pattern of the graphene monolayer. The image was adapted from Russo& Passmore (2014b). (D) The electron diffraction pattern of graphene oxide monolayer (green) with the ferritin peaks (red). The image was adapted from Wilson et al. (2009).

5.1.3 Other grid surface modifications

There are many other proposed methods to improve particle distribution or to tackle the problem of preferred particle orientations. These include acquiring tilted data for more orientations (Mindell & Grigorieff, 2003; Tan et al., 2017); changing the carbon surface characteristics by applying glow discharge with hydrogen gas to control particle number (Russo & Passmore, 2014b); or increasing ice thickness by applying sample droplet from the matte side rather than the shiny side of the grid as a "back-side injection" (Fig 5.3A) to improve particle number (Palovcak et al., 2018). Further more, modifying the grid surface to reduce the hydrophobicity is also a way of controlling particle distribution. For example, PEGylated gold grids (Fig 5.3B) can decrease contact angle and allow particles to enter grid holes (Meyerson et al., 2014). Polylysine (Fig 5.3C) was also reported to increase the particle affinity to the carbon surface (Williams, 1977; Cheung et al., 2013). Polylysine is a cationic polymer with two amino groups in a repeating unit, it can form a positively charged a thin layer to attract particles (Guo and Jiang, 2014).

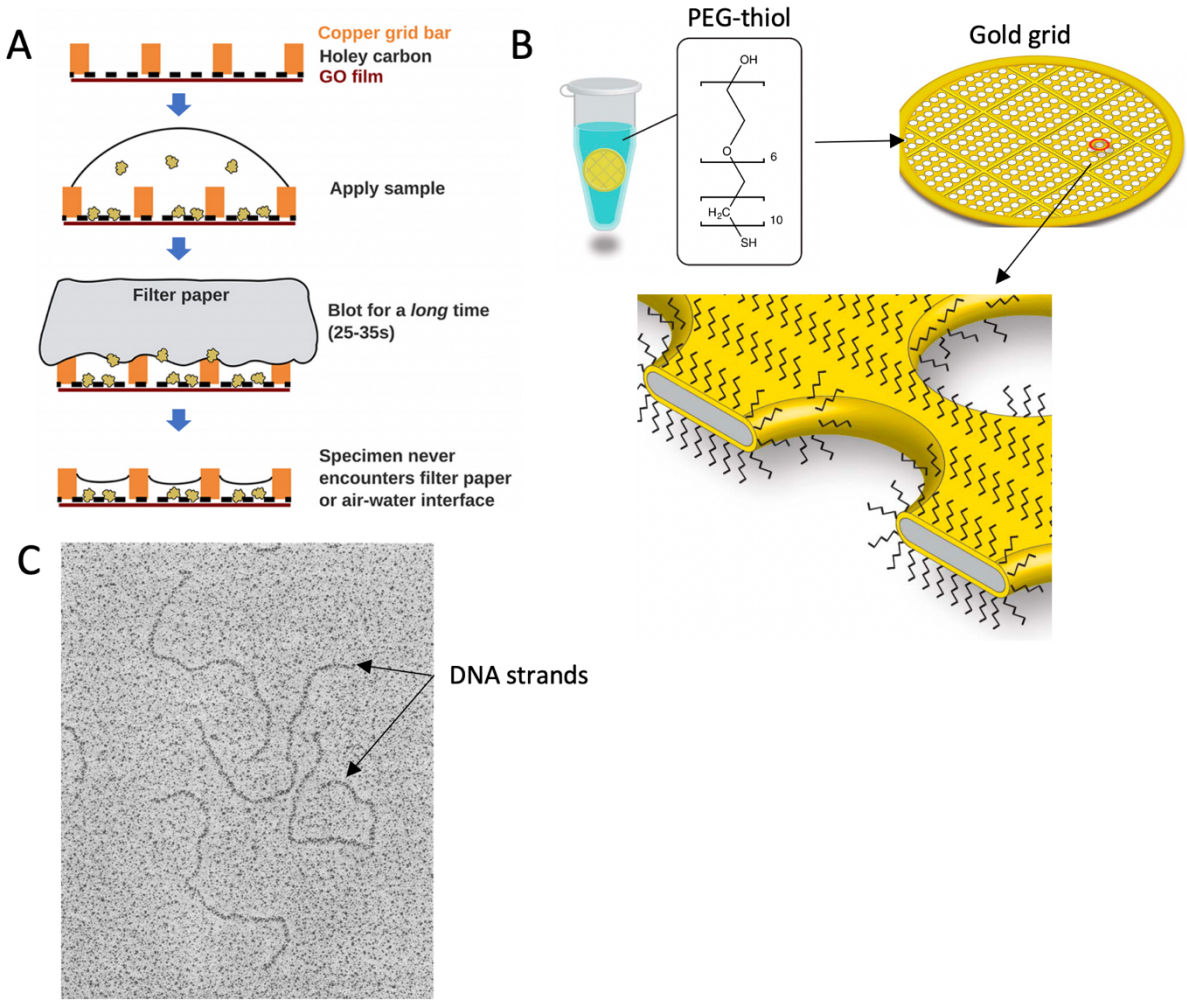

Fig 5.3 Other grid surface modifications. (A) The sample was "back-side injected" and was protected by the grid bars from blotting. The image was adapted from Palovcak et al. (2018). (B) PEGylated gold grid surface. The image was adapted from Meyerson et al. (2014) with some modifications. (C) A micrograph of polylysine treated carbon film with negatively stained DNA. The image was adapted from Williams (1977).

However, the published methods either require specific equipment or experienced skills to achieve producing good cryo-grids. These methods are highly specimen-specific and may not be suitable for complex I considering its unique shape and flexibility. Thus, optimising the grid preparation conditions for complex I was performed in this study.

5.1.4 Aims

In this chapter, the aim is to find out the optimised grid condition to generate high-quality cryo-EM data for complex I structure in the situation of limited complex I sample and low concentration.

5.2 GO coating grids

5.2.1 GO grids fabrication

Graphene oxide (GO)-coated Quantifoil grids were made based on the protocol from Bokori-Brown et al. (2016) with some alterations. In brief, holey carbon grids (Quantifoil grids R1.2/1.3) were plasma cleaned and a drop of GO solution was applied, blotted and air-dried. Different GO concentrations were applied to achieve the best monolayer GO sheet coverage on the grid surface. Due to GO's good electron conductivity, the single layer of GO has barely any imaging contrast under the EM. The coating can only be observed on partially coated broken holes with a scrolled edge (as shown in Fig 5.4A). At higher magnification (Fig 5.4B), the winkles on the single-layered GO can be observed. It is known that the single monolayer of GO shows a 6-fold diffraction pattern consistent with its crystalline order (Wilson, et al., 2009). Thus, to identify whether the grid hole was covered with GO, the 6-fold diffraction spots were searched under Tecnai T12 with the diffraction mode. Three grids with identical preparation process were made, 20 holes were randomly selected from each grid and screened under the diffraction mode. The coverage was estimated by the observation of the diffraction pattern of these holes. The grids were glow-discharged at 20 mA, 0.1 mBar for 90 s, and 2.5 μL of GO solution (0.2 mg/mL) was applied on the grids as suggested (Bokori-Brown et al., 2016). In addition, two more concentrations (0.1 mg/mL, 0.4 mg/mL) were tested to find out the best coating concentration. Under each condition, three grids were prepared, and 20 random holes were selected and screened on each grid. The grid hole was regarded as "single layer" GO coverage if the 6-fold diffraction pattern was shown (as in Fig 5.4C); The grid hole was regarded as "multi-layer " GO coverage if more than 6-fold diffraction pattern was shown (Fig 5.4D); The grid hole was regarded as "broken " if a scrolled edge was identified; the grid hole was regarded as "empty" if no diffraction pattern was shown. Then the number of grid holes with different coverage conditions was counted.

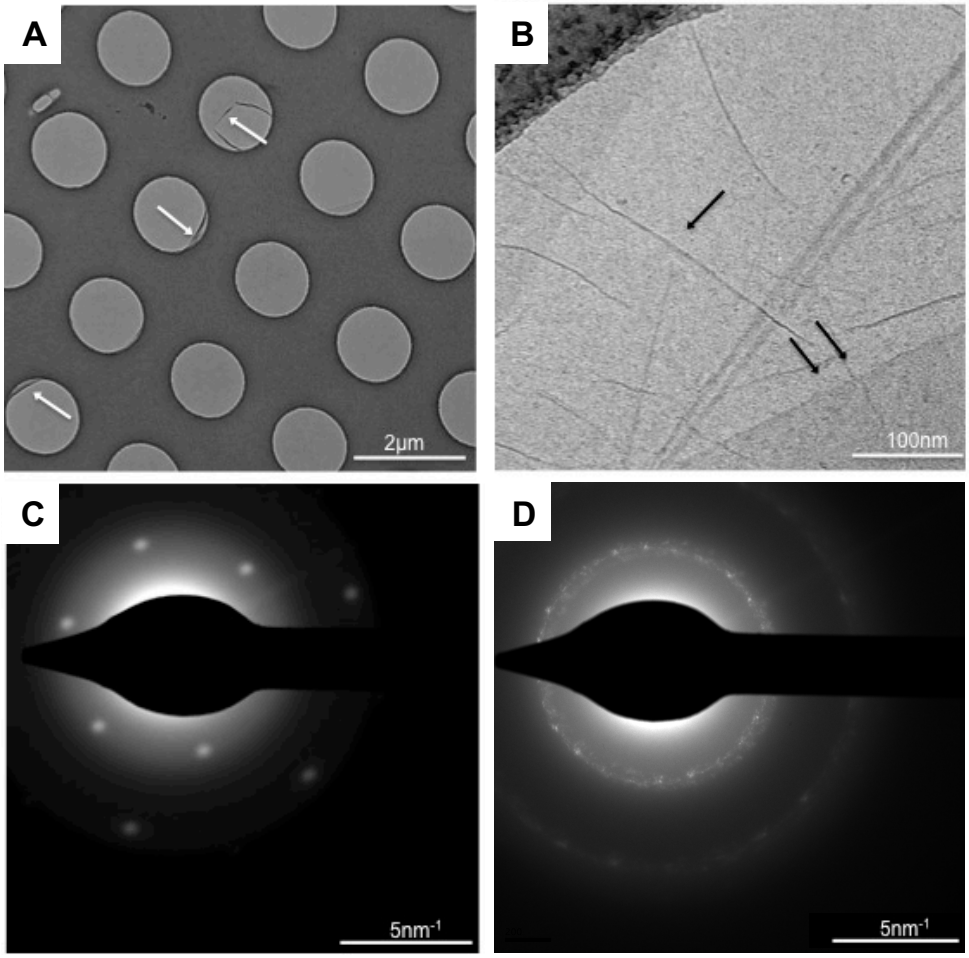

Fig 5.4 Quantifoil grids coated with GO sheets. (A) Low magnification image of a Quantifoil grid (R1.2/1.3) covered with GO film. The white arrows show the scrolled edge of the GO sheet, without which the thin GO film was not able to be identified under EM. (B) A higher magnification image of GO-coated grid hole. The black single arrow marks the winkles on the single-layered GO; the black double arrows mark the position of the multiple-layered GO. (C) and (D) Electron diffraction patterns of the hole with single-layered GO (C) and multiple-layered GO (D).

As shown in Table 5.1, the grids with 0.1 mg/mL GO had only 6.67% coverage with all broken holes. 0.2 mg/mL GO gives a higher coverage of single layers GO (21.67%), whereas 0.4 mg/mL gives the highest single layer converge, up to 51.67%. The higher the concentration of GO, the larger the proportion of multilayered GO was also observed. To remove the multilayered GO, a 30 s sonication of the GO suspension was introduced before coating. The same GO concentration with the sonication step can achieve a 61.67% of single-layered GO coverage and 91.67% overall coverage. The alterations in the GO concentration have significantly increased the GO coverage on the grid surface. Another method to generate GO grids has been published by Palovcak et al. (2018). Instead of blotting away the excessive GO suspension from the grids, the GO deposition requires a customised water-containing dish for

the GO flakes to float at the surface of the water. By draining the water, the GO flakes are lower onto the surface of the grids. They have shown an 80% overall coverage with 7% multilayers. The result has shown better overall coverage, besides there is no need for any customised tools in this method.

Table 5.1 GO coverage on grids

GO concentration / GO coverage	0.1 mg/mL	0.2 mg/mL	0.4 mg/mL	0.4 mg/mL with sonication
Single layer	0.00%	21.67%	51.67%	61.67%
Multilayer	0.00%	13.33%	33.33%	20.00%
Broken	6.67%	5.00%	6.67%	10.00%
No coverage (empty hole)	93.33%	50.00%	8.33%	8.33%

5.2.2 Optimisation of complex I concentration on GO grids

The purified complex I with different concentrations were applied on the optimised GO grid. 4 mg/mL purified mouse complex I was diluted 10 and 40 times with gel-filtration buffer before applying on the GO grids. Then the grids were blotted and plunge-frozen by Vitrobot and screened on a Tecnai T12 with a side-entry cryo-holder.

The grids with a sample concentration of 4 mg/mL showed fully saturated complex I particles on the grid surface (Fig5.5A). There were protein particles observed even in the grid hole without any carbon support (Fig5.5A). The grids with a sample concentration of 0.4 mg/mL showed a saturated GO surface with proteins while nothing in the holes which have no GO supporting film (Fig 5.5B). The further 40 times dilution of the complex I sample to 0.1 mg/mL was applied, the complex I protein shows a less crowded distribution on the grids with space between particles and no aggregation (Fig 5.5C). While comparing to the non-GO-coated Quantifoil grids, the same concentration of complex I (0.1 mg/mL) gave barely any particles to distribute in the hole. There are only a few particles that could be seen at the edge of the hole as shown in Fig 5.5D.

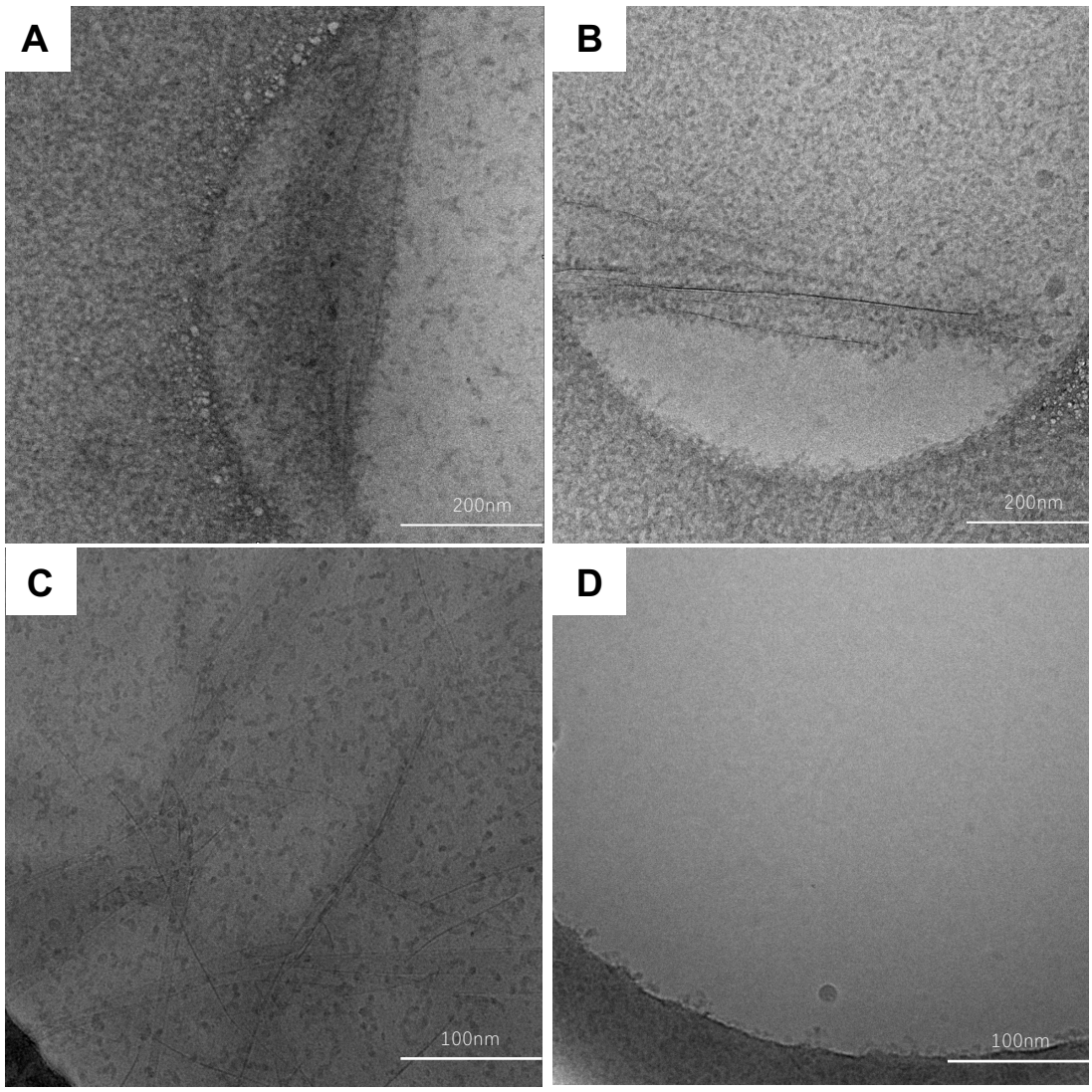

Fig 5.5 Cryo-EM images of grids applied with complex I sample at different concentrations. (A) 4 mg/mL mouse complex I was applied on a GO coated grid. (B) 0.4 mg/mL mouse complex I was applied on the GO-coated grid. (C) and (D) 0.1 mg/mL complex I sample applied on GO-coated (C) and non-GO-coated (D) grid.

5.2.3 Optimisation of ice thickness on GO grids

During plunge freezing with Vitrobot, the blotting time and force can be adjusted to control the thickness of the vitrified ice on the grid. With a fixed blotting force of –10, the blotting time was varied during sample freezing to observe the best ice thickness. Figure 5.6 shows the ice thickness and particle distribution difference by applying different blotting time. The ice thickness was estimated based on the image contrast of particles with the same amount of electron exposure dose and defocus. A blotting time of 10 s resulted in the GO film breaking for most of the grid holes (Fig 5.6A1), and the few intact grid holes showed good distribution of complex I (Fig 5.6A2). This means that 10 s blotting is so intensive that the GO film has

been damaged. On the 5 s blotting grids (Fig 5.6B2), more intact grid holes were identified with a nice particle distribution. The grid with 1.5 s blotting time also showed a reasonable number of particles but a lower contrast compared to 5 and 10 s (Fig 5.6C2) suggesting the thicker ice. Therefore, the blot time of 5 s was considered as the ideal condition for GO grids.

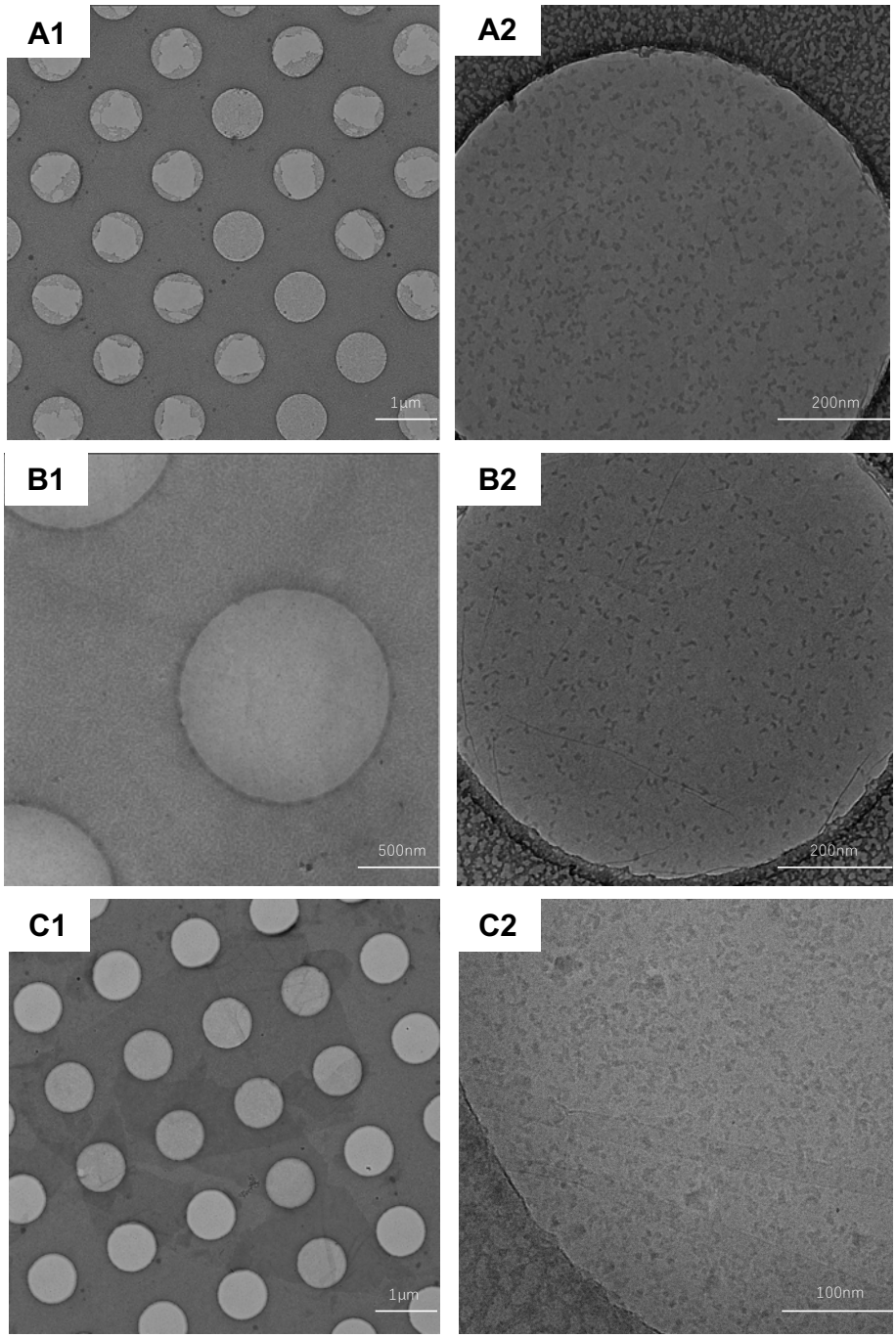

Fig 5.6 Cryo-EM images of grids with different blotting times. The micrographs were taken from T12 Tecnai with different magnifications. (A) Low (A1) and high (A2) magnification cryo-EM images of the grid with 10s blotting time. (B) Medium (B1) and high (B2) magnification micrographs with 5s blotting time. (C) Low (C1) and high (C2) magnification micrographs with 1.5s blotting time. Multi-layered GO sheets were shown in (C1). A single-layered GO sheet with wrinkles was shown in (C2).

5.2.4 Cryo-EM data collection and processing using optimised GO grids

The GO-coated grids with the optimised conditions mentioned above were made with 0.1mg/mL complex I protein. The cryo-EM data collection session was performed on a 300kV Titan Krios electron microscope with an FEI Falcon III detector in linear mode for a rapid data collection at the Nanoscience Centre, University of Cambridge with the help from Dr Dima Chirgadze and Dr Jamie Blaza. The pixel size was 1.43 Å /pixel with a total dose of 80 $e^-/Å^2$ in 2s exposure time. The size of objective aperture was 100 μm and the size of C2 aperture was 50 μm. The defocus range was set from -1.8 μm to -3 μm. In total, 818 micrographs were collected.

The RELION 2.1 was used for further data process. Beam induced motion was corrected for micrographs before particle picking. As shown in Fig 5.7A, 98,887 particles were automatically picked with a template from 8,978 manually picked good particles. The particles were extracted with a box size of 460 pixels. The 2D classification was performed and 25 good classes were selected containing 84,060 particles (Fig 5.7B). However, the majority of the 2D classes were shown the side view of the protein indicating a preferred orientation, and the other views were barely identified. The selected particles were further 3D-classified. In particular, class 4 contains 38,818 particles showed an intact complex I structure while the other 3 classes showed the structure of incomplete complex I. In class 1 and 3, there is a flat disk shape surrounding the protein which could be because the particles were partially exposed in the air-water interface due to the thin ice layer. This suggests that the ice film formed on the GO surface through the blotting process was too thin to hold complex I. Class 2 shows that 31.45% of the particles were damaged and the N-module could be missing. Only the class 4, with 38,810 particles, was used for 3D refinement. However, the two half-maps converged early at 14 Å, which indicates the resolution could be limited by the biased orientational information. The heat map in Fig 5.7C presents the particle distribution by tilting angles along X and Y access. The map shows a strong orientation bias with barely any information at tilt angle from 0° to 50°. This missing information of certain angles resulted in an incomplete reconstruction and limited resolution. Therefore, the GO surface needs to be modified to improve the orientation.

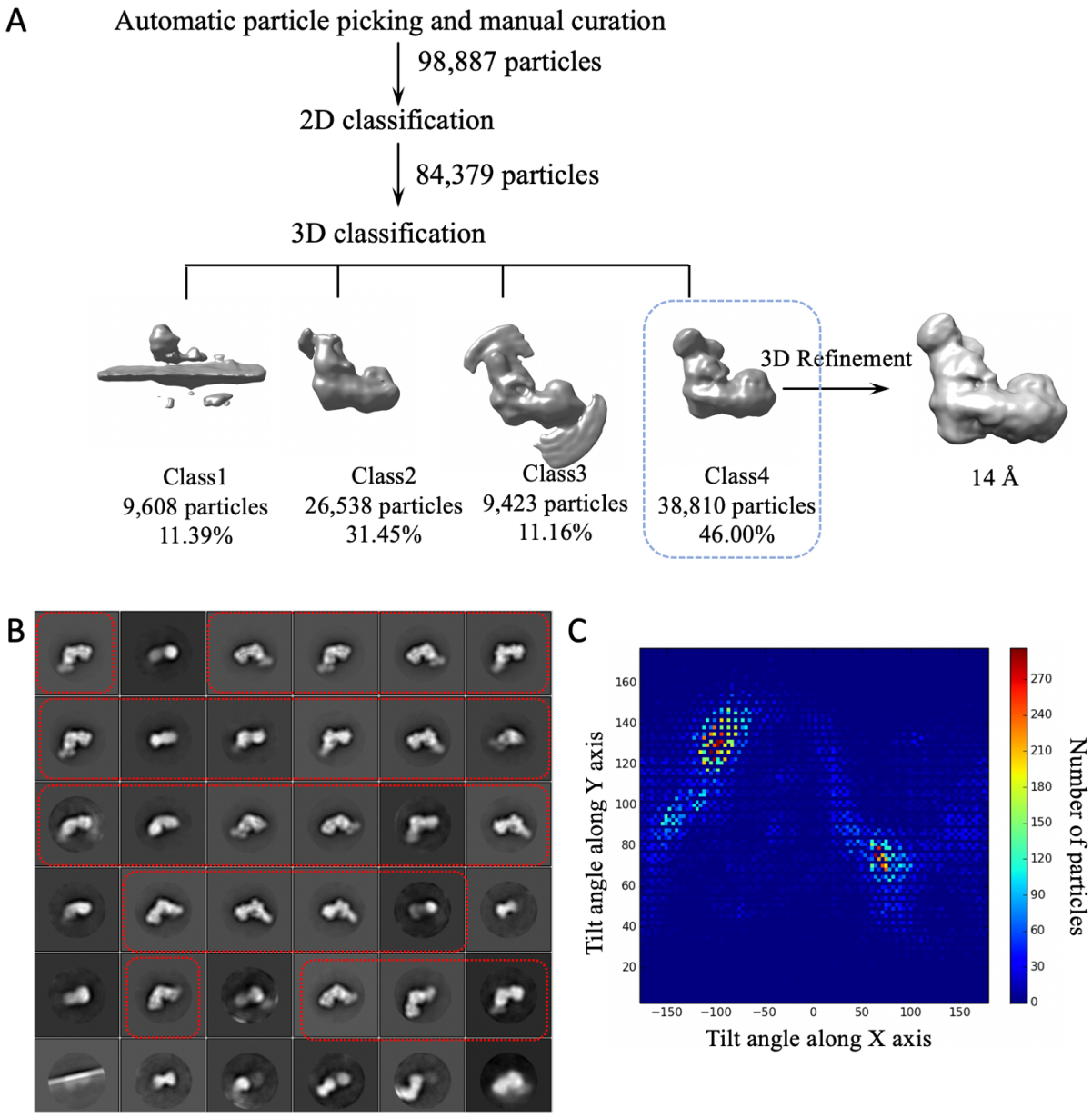

Figure 5.7 Cryo-EM data processing for mouse complex I on GO grids. (A) the classification and refinement scheme for GO grid data. (B) The selected 25 good classes (in red dotted squares). (C) The heatmap shows the particle orientation distribution of 38,810 particles for 3D refinement.

5.3 Baked-GO coating grids

The GO film is a single sheet of carbon with a mixture of carboxyl, epoxy, and hydroxyl groups attached to the surface (as illustrated in Fig 5.8A). These functional groups on the GO sheet can potentially react with the substrates attaching to its surface. The hydroxyl groups on the surface could form hydrogen bonds between GO and the protein surface leading to a preferred orientation (Wilson et al., 2009). However, the GO coated surface can be partially reduced by simply baking at a high temperature which can remove water and some active functional groups from the GO (Fig 5.8B) (Pantelic et al., 2010).

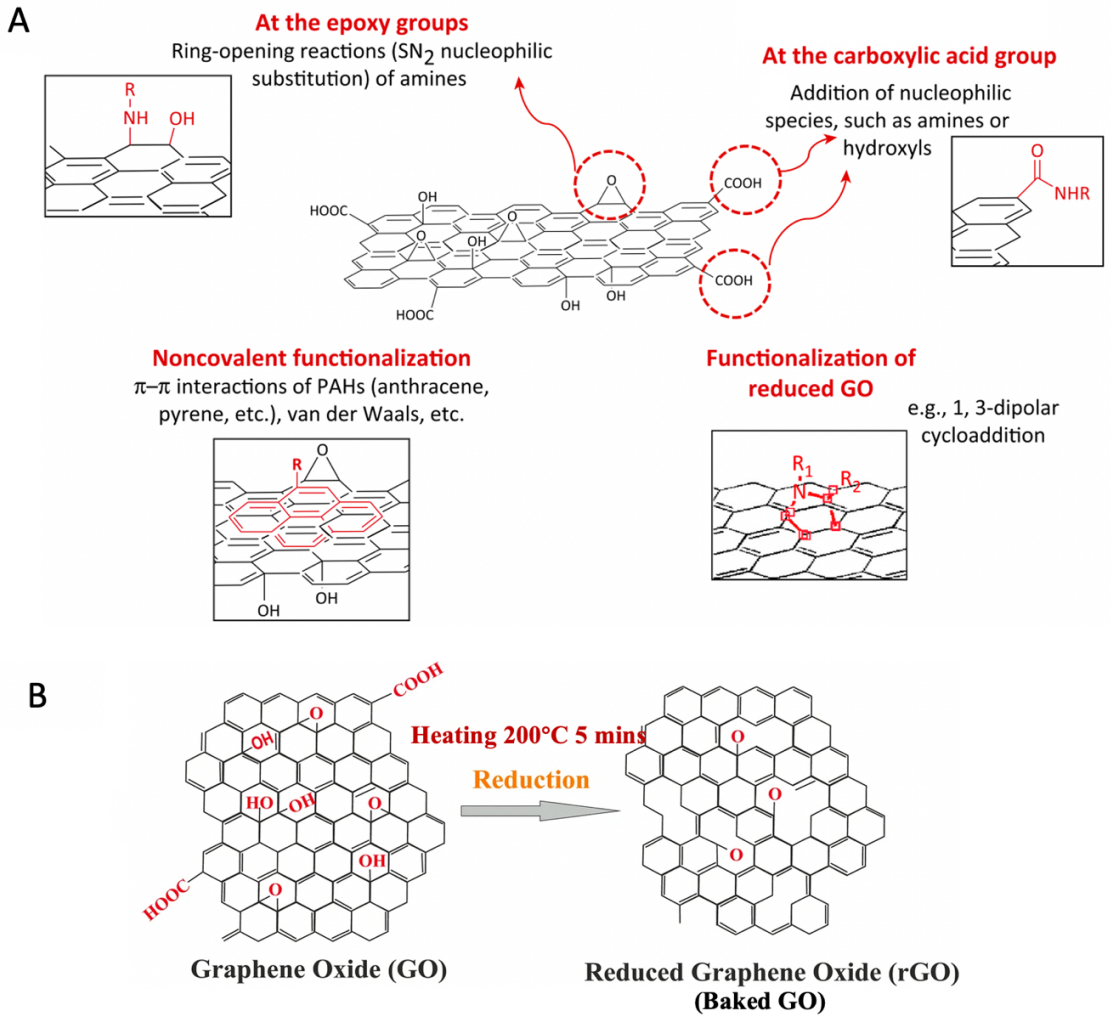

Fig 5.8 Graphene oxide surface functionalities and modification. (A) GO surface reaction groups. This figure was adapted from Pavlidis et al. (2014). (B) The conversion of GO to reduced GO by heating. This figure was adapted from Priyadarsini et al. (2018) with some modifications.

The GO-grids were baked at 200°C for 5min by following the protocol (Pantelic et al., 2010). Since the 5s blotting time used on the non-baked GO grids gave biased orientations, the blotting time of 2 s were applied this time for a thicker ice. Then the cryo-EM data collection session on the baked GO grids was performed with the same microscope and the same setup (300kV Titan Krios electron microscope with the FEI Falcon III detector on linear mode). The pixel size, the dose, and the defocus range were not changed to the last data collection with the non-baked GO grid. A total of 803 micrographs were collected overnight. Then the micrographs were motion-corrected before particle picking. As shown in Fig 5.9A, 30,567 particles were automatically picked with the same box size (460 pixels). With the same protein concentration applied (0.1 mg/mL), the micrographs from the baked GO grid have shown less particle density comparing to the non-baked GO grid. This is also reflected by the averaged automatically picked particles per micrograph on baked GO grid (38 particles/micrograph) were less than that on non-baked GO grid (121 particles/micrograph), which indicates the reduced surface "stickiness" by baking. The 2D classification was performed and 25,270 good particles were selected for 3D classification. Comparing the 2D classes of the baked-GO to the non-baked GO grids, a few top- and end-on views (red circles in Fig 5.9A) were shown. This also indicates that the baking process could decrease the complex I orientational bias on GO surface. The class 1 which had 10, 877 particles showed an intact structure and were selected for 3D refinement. The particle distribution heat map (Fig 5.9A) shows the presence of particles at the tilt angle of 0° to 50°, even though this population is still small. After 3D refinement and post-process, a density map with a resolution of 7.4 Å was successfully generated.

To analyse the density map further, the active mouse model (PDB: 6G2J) was fitted into the density map. As shown in Fig 5.9B, the model fits well in the overall density map except for NDUFA12 which shows a fragmented density. NDUFA12 is one of the supernumerary subunits with a long loop wrapping around the domain surface (Zhu et al., 2016). The fragmented density indicates the flexible and unstable status of this subunit. This result is consistent with the porcine complex I cryo-EM map made with the traditional continuous amorphous carbon-coated grids, which has shown a fragmented density of NDUFA12 in their map (Wu et al., 2016). Comparing to the active mouse complex I structure, the complex I map from the baked

GO grid has less density for the lipid belt, despite the purification process of complex I being identical. As NDUFA12 is partially anchoring above the membrane, the loss of the membrane support could increase its flexibility.

Considering the short overnight data collection session (less than 12 h), a quick data processing with about 10,000 particles could achieve a resolution of 7.4 Å which is good enough for identifying major structural changes. Overall, the baked-GO grid is a promising method that could generate a cryo-EM map for macromolecules with a limited sample concentration, but still, there are preferred orientation to some extent and weak density of NDUFA12 subunit.

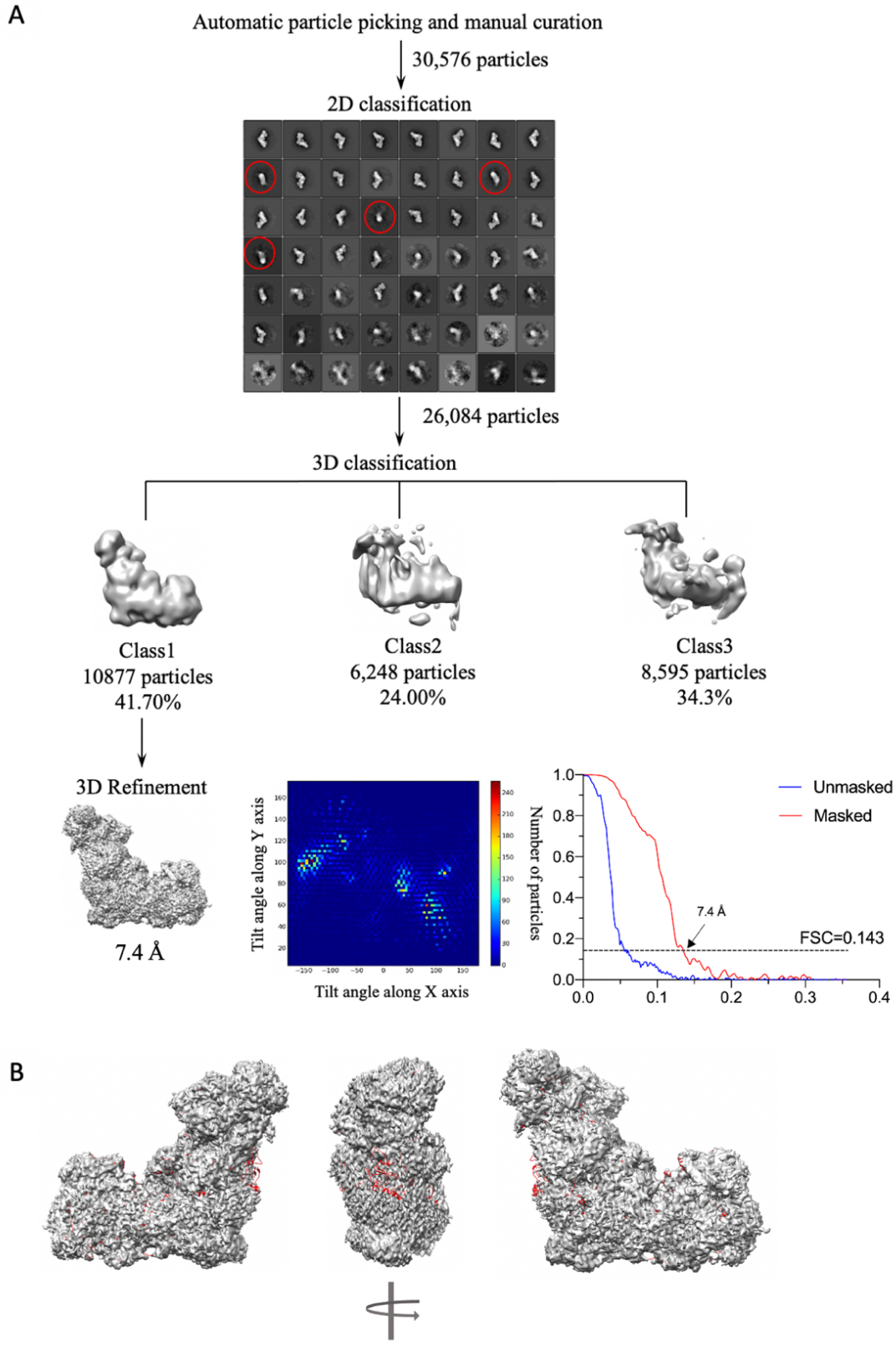

Figure 5.9 Cryo-EM data processing for mouse complex I on baked GO grid. (A) Classification and refinement scheme for cryo-EM data processing for mouse complex I on baked GO grids. The top- and end-on views from the 2D classification are circled in red. The heatmap shows the particle orientation distribution. The FSC curve defines an estimated global resolution of 7.4 Å at FSC = 0.143. (B) Complex I density map fitted with complex I mouse model (Red, PDB:6G2J) shown using UCSF Chimera in three differently rotated views along the membrane.

5.4 Graphene-coated gold grids

It was known that the baked-GO grids were able to be used as a support substrate. The GO grids after baking had a graphene-like surface with many functional groups removed. In this study, the graphene grids were investigated as an alternative supporting substrate for complex I.

The home-made graphene grids are not easily feasible as they require specific equipment for chemical vapor deposition (Hao et al., 2013; Han et al., 2020). Thus, in this study, commercially-available Au Quantifoil R 2/4 grids coated with graphene were purchased from Agar scientific. Grids were brief glow-discharged for 20 s at 20 mA immediately before usage to clean the surface without damage. 2.5µL of 0.1 mg/mL freshly purified mouse complex I was applied on the graphene surface. The blotting force and blotting time were unchanged (–10 and 2 s). The data set was collected on the same microscope with the same setup in the Nanoscience Center. An overnight data collection on the Titan Krios electron microscope with the FEI Falcon III detector on linear mode provided 694 micrographs. Micrographs were motion-corrected, and 12,088 particles were manually picked (Fig 5.10A). The result of 2D classification showed multiple views of complex I which means that the graphene can improve the particle orientation. However, a few classes were showing a bright dot (Fig 5.10B) associated with the 2D projection which sabotaged the alignment of complex I in these classes. These dots contaminants were also identified on the micrographs background which could be the detergent formed micelles attached to the graphene surface. 5,935 particles from the contamination-free classes were picked for 3D classification and refinement. The heatmap of class 3 shows unevenly distributed particle numbers among tilting angles. However, class 3 with only 3,013 particles was able to be reconstructed and refined into a complex I structure with a resolution of 8.4 Å. The further map-to-model fitting analysis shows the low density of NDUFA12 which is similar to the result from baked GO. The particle distribution heat map shows the absence of particles at the tilt angle of -50 to 50°, indicating a lack of 2D projection information at such angles.

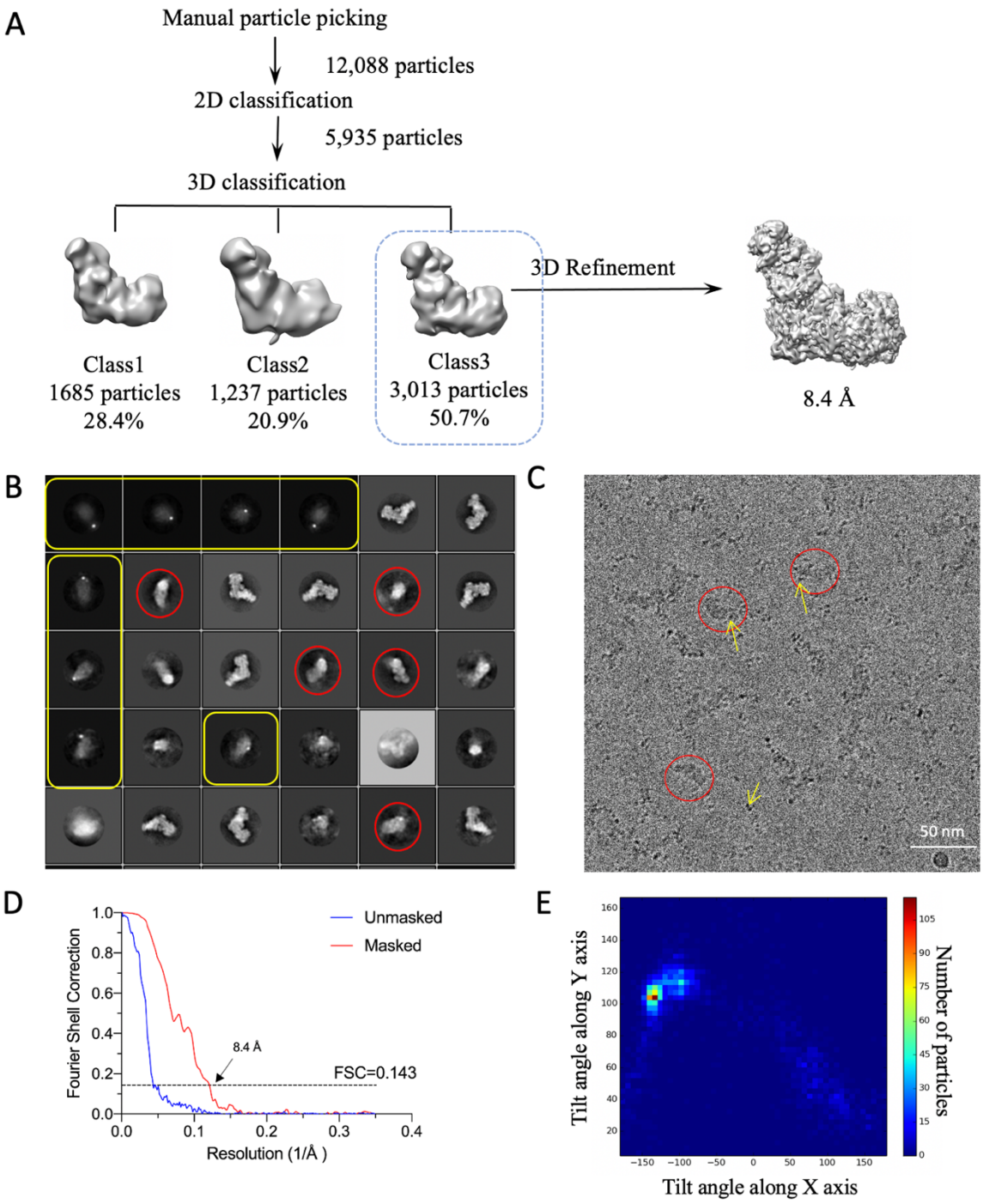

Fig 5.10 Cryo-EM data processing for mouse complex I on the graphene-coated gold grid. (A) Classification and refinement scheme for cryo-EM data processing. The 3D refinement of 3,103 particles resulted in a density map of 8.4 Å. (B) Classes in the 2D classification. The classes with red circles show the orientations that are different from the side view. The classes in yellow squares represent the 2D projections misaligned with micelles. (C) A representative micrograph with complex I particles marked in red circles. The yellow arrows point out the dot-shaped micelles attached to graphene and complex I. (D) The FSC curve defines an estimated global resolution of 8.4 Å at FSC = 0.143. (E) The heatmap shows the particle orientation distribution from class 3 in (A). The tilt angles from -50 to 0 degrees have shown very few particles.

5.5 Polylysine treated grids

The polylysine-treated carbon films have been used as a supportive substrate for negatively charged particles (Williams, 1977; Guo and Jiang, 2014). However, the polylysine adds extra background noise to the carbon film. This study aims to test whether complex I on polylysine-treated Quantifoil or GO-coated grids could achieve better particle distribution and less background noise.

According to a previous successful study (Guo and Jiang, 2014), a drop (~2.5μL) of 0.1% (w/v) polylysine was applied on the surface of glow discharged Quantifoil R1.2/1.3 or GO-coated Quantifoil grids. The excess solution was gently blotted from the edge of the grids. Once the grids were air-dried, 0.1 mg/mL complex I was applied on the grids, and the sample was plunge-frozen. Four different grid conditions with 0.1 mg/mL mouse complex I were compared as in Fig 5.11: the Quantifoil grids, baked GO-coated Quantifoil grids, polylysine coated Quantifoil grids, and baked GO-coated Quantifoil grids with polylysine.

The Quantifoil grids with 0.1mg/mL complex I have shown barely any particles within the grid hole (Fig 5.11A1). Some particles are aggregated around the edge (Fig 5.11A2). For the baked-GO grids, good particle distribution with slight background noise was shown compared to the ice-only background in Fig 5.11A. Fig 5.11C1 and C2 show the best 0.1% polylysine covered hole with the polylysine layer partially broken. Within the three polylysine-coated Quantifoil grids, it was noticed that the coverage of polylysine on the Quantifoil grid was poor (less than 10% of grids holes were found to be covered by polylysine during the screening). The polylysine coated grid squares show a reasonable number of particles. Some particles were even saturated on the edge of the polylysine film and aggregates inside the holes. Still, the background noise is obvious comparing to the ice-only background and the GO background. The GO-coated polylysine grids were generated by applying 0.1% polylysine on baked-GO grids (Fig 5.11D1 and D2). It shows a reduced background signal and a good number of particles. However, aggregations of complex I were identified, and a spherical shaped contaminant was also observed on grids along with the complex I particles. The complex I

protein samples applied on all four types of grids was from the same protein preparation batch, but neither the Quantifoil grids nor the baked-GO grids have shown any contaminant. This indicates that this contaminant is not an artefact from protein purification. This kind of contaminant is similar to what was observed on graphene grids (Chapter 5.4). One possibility is that the detergent monomers, which suppose to cover the air-water interface, anchored on the graphene and polylysine-coated GO surface or formed micelles (Hauer et al., 2015, Rubinstein, 2007).

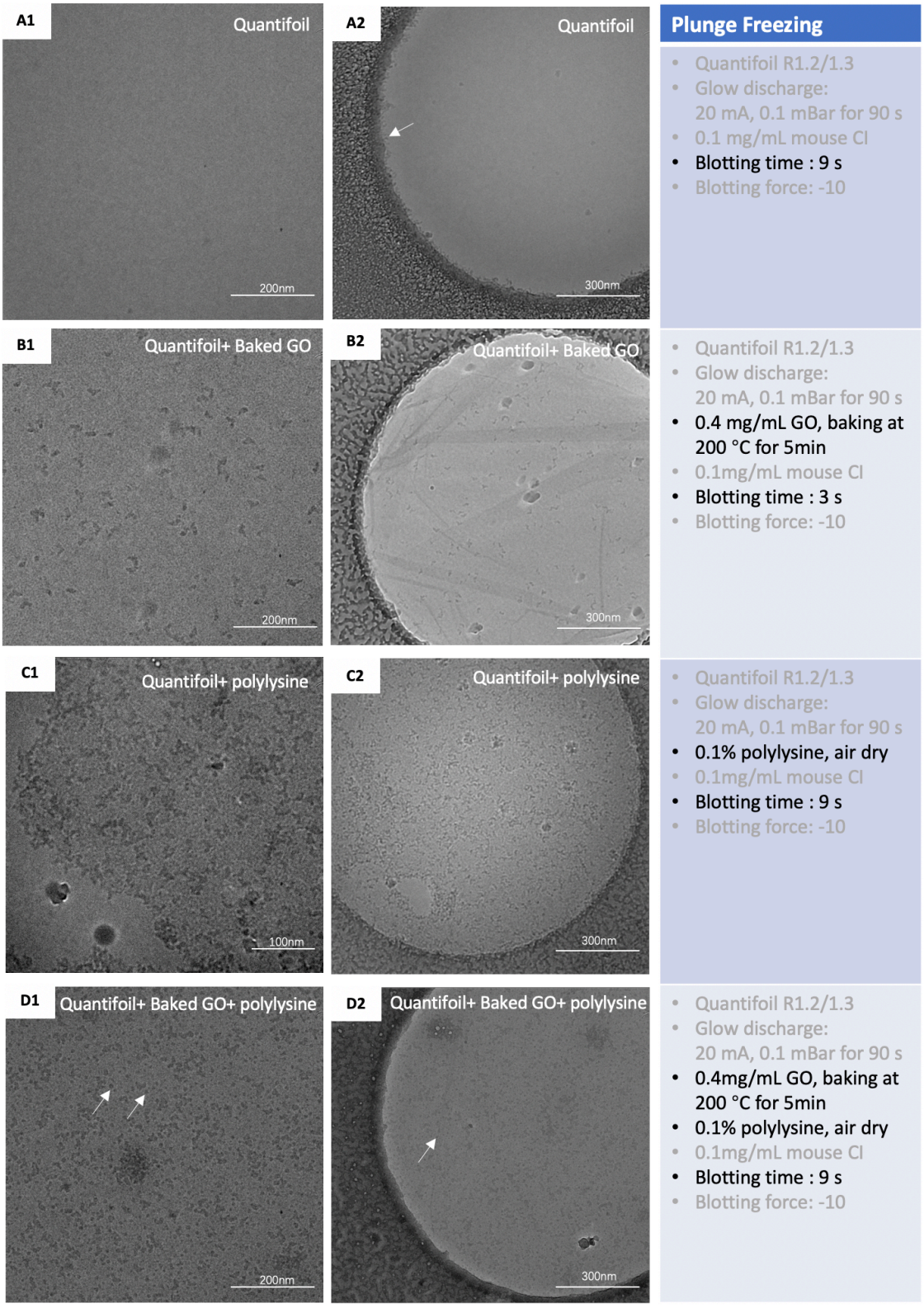

Fig 5.11 Cryo-EM images of Quantifoil grids with different treatments. The micrographs were taken from T12 Tecnai with different magnifications. The column on the right panel shows the plunge freezing conditions for the images on the left. The identical parameters among the four conditions are coloured in grey. The different conditions are shown in black. (A1) &(A2) Quantifoil grids applied with 0.1 mg/mL mouse complex I. The white arrow in (A2) shows the complex I particles attached at the edge. (B1) &(B2) Quantifoil grids coated with baked-GO. (C1)& (C2) Quantifoil grids coated with 0.1% polylysine. (C) & (D) GO-coated Quantifoil grids applied with polylysine. The white arrows point out the location of contaminants.

5.6 Thiol-PEG grids

Gold has been successfully used as a support substrate to fabricate cryo-EM grids, as the gold can significantly reduce the specimen movement during irradiation, contributing to a high-resolution structure (Russo and Passmore, 2016). However, the hydrophobic surface of the gold grid makes it difficult to have a nice distribution of particles into the grid hole, especially for membrane bound macromolecules. Meyerson and colleagues suggested introducing a hydrophilic self-assembled monolayer onto the hydrophobic gold surface (Meyerson et al., 2014). The thiol-PEG attached gold grids were successfully used for acquiring high-resolution complex I structure (Blaza et al., 2018; Agip et al., 2018; Grba & Hirst, 2020; Bridges et al., 2020). In this study, I aimed to investigate alternative thiol-PEG reagents to optimise the grid conditions.

5.6.1 Particle distribution on thiol-PEG grids

Although thiol-PEG reagent allows a lower concentration of complex I sample applied on grids, the particle distribution is still highly ice-thickness sensitive. To make PEGylated grids, the thiol-GEG was diluted into 5mM with ethanol and incubated with glow discharged gold grids for 48 h in an anaerobic glove box (Blaza et al., 2018). In Fig 5.12, within the same grid square, the centre holes with thinner ice support give barely any particles in the hole, while the hole at the edge which is less than 15 μm in distance, had a satisfying number of particles. Even within the same hole, the centre, with the thinner ice compare to the edge, has fewer particles. This indicates that the complex I distribution is highly dependent on ice thickness on thiol-PEG grids. This analysis suggests that during the automatic cryo-EM data collection session, the pre-sessional grid square and hole selection is crucial. Within a grid square, the holes should be selected as a “donut” shape, which means that the centre of the hole and the very edge part should all be avoided due to the undesired ice thickness.

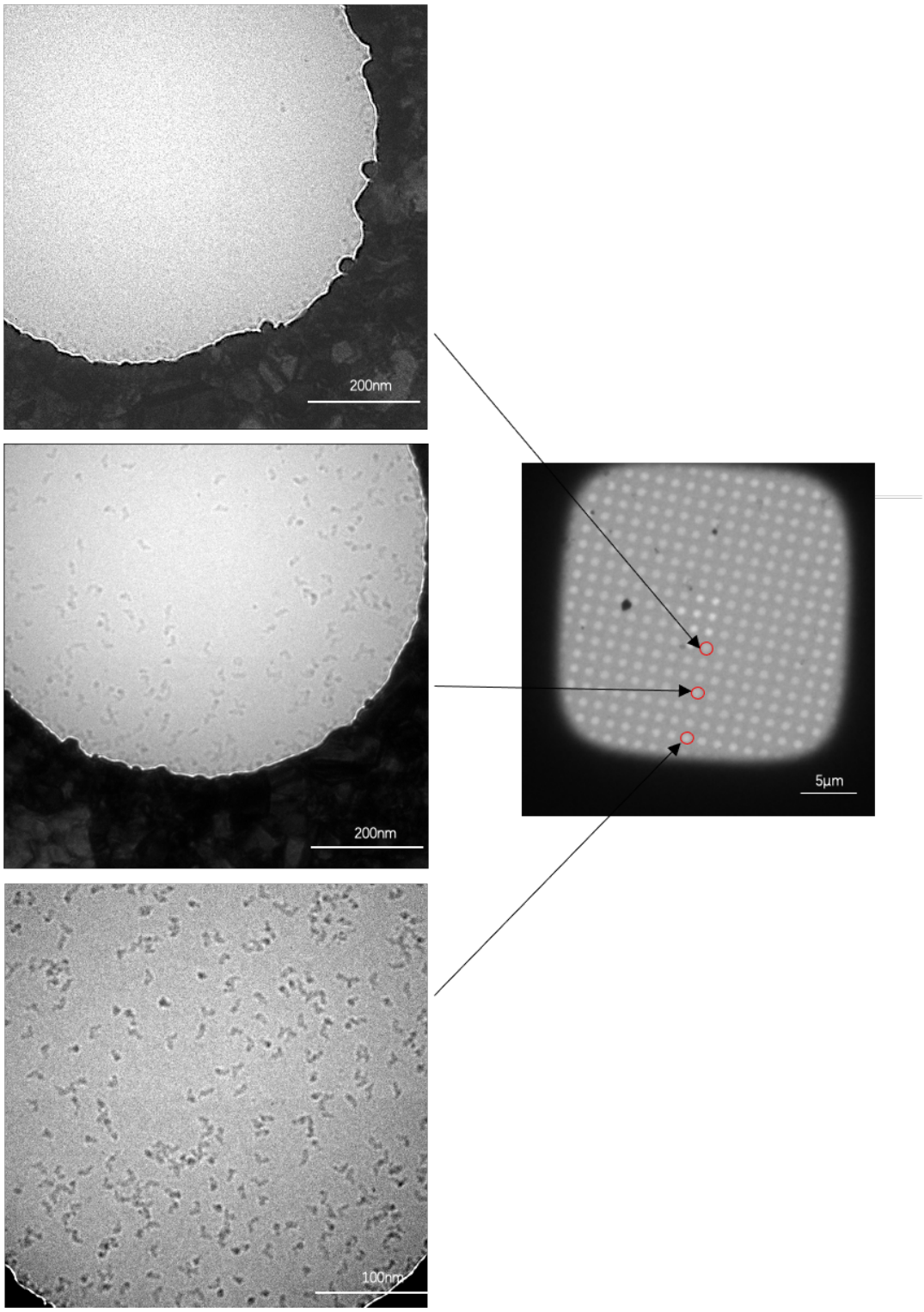

Fig 5.12 Complex I particle distribution in different holes with different ice thickness on one thiol-PEG grid square. 3.5mg/mL bovine complex I was applied on the GEGylated gold grids. The left panel has shown three micrographs taken from different locations within the same grid square (the right panel image). The particle number within the grid holes increases from the center of the grid to the edges.

5.6.2 The long- and short-PEG coated gold grids

Two different thiol-PEG reagents in length were tested (Fig 5.13A). A regular 10 s blotting time with a blotting force of –10 was applied during plunge freezing. Mouse complex I sample concentration was 2.5 mg/mL. Three repeat grids with the same type of thiol-PEG were screened. The micrographs taken from two kinds of thiol-PEG grids show a very similar particle distribution (Fig 5.13B and C). The highest particle numbers of holes around the edge in the grid square were counted. Three holes from three random grid squares on each grid were recorded (see Fig 5.13D). There is no significant difference in the number of particles between these two thiol-PEG.

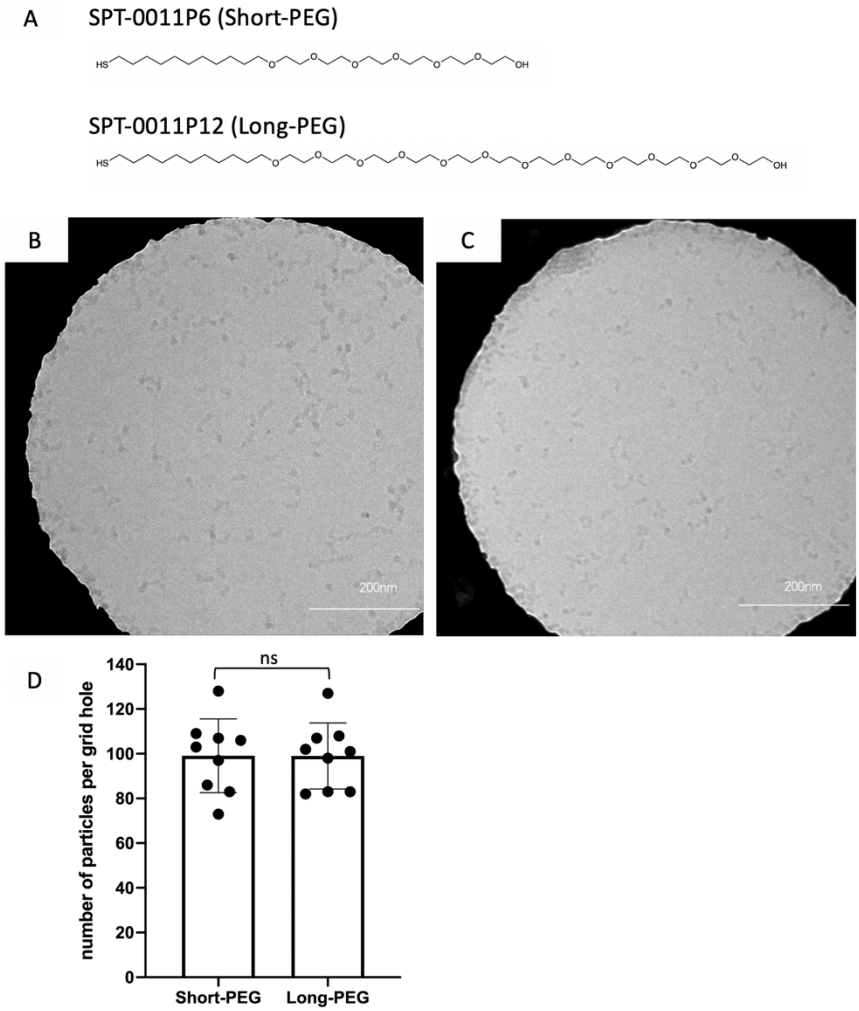

Fig 5.13 The comparison of short-PEG and long-PEG coated gold grids. (A) the chemical formulas of long- and short-PEG. (B) &(C) Representative micrographs show particle distribution on the short- (B) and long-PEG (C) coated girds. (D) The number of particles in each hole from grids with different PEG treatments (n=3). Data are mean averages ± SEM (n=3, from 3 independent grid preparations) with statistical significance determined using Student's t-test.

5.7 Discussions and conclusion

With the help of developments in detectors and data processing software, the number and quality of micrographs were no longer the limitations to determine a high-resolution cryo-EM structure. However, the specimen-specific grid preparation and optimisation remain the crucial steps for producing good-quality data. Many aspects should be considered to achieve optimum grid conditions, such as sample compatibility with the grid surface, sample concentration, and ice thickness. In some cases, the sample concentration was limited, such as complex I purified from KO mouse samples (*ndufs4* KO mouse in Chapter 4) or human cell cultures (Guo et al., 2017). Thus, grid surface modifications were tried to compensate for the low concentration. The method of fabricating GO-coated grids by fine-tuning the GO concentration with an additional sonication step has shown a 91.67% overall coverage with 61.67% single-layered GO. This method is better than the commercially produced GO grids, which have an overall coverage of ~80% with ~50% single-layered GO coverage. Furthermore, the in-house fabricated GO-coated grids have shown better coverage and more feasible approaches comparing to the published coating method with the customised water-containing dish (Palovcak et al., 2018).

The complex I concentration required for the GO grid (0.1 mg/mL) was about 30 times less than the conventional Quantifoil grids (3–5 mg/mL). Thus, this method solves the problem of using a low concentration sample to generate reasonable particle-distributed cryo-grids. However, a highly biased particle orientations during this process was found, suggesting the GO surface has selective high affinity to certain orientations. The specimens that have been sucessfuly applied on the GO grids were soluble proteins with globular shapes (Palovcak et al., 2018). Considering complex I is a membrane protein with a special L-shape, the GO grids must be modified before use. In such a case, the GO grid was baked at 200°C for 5 min before applying the 0.1 mg/mL sample to remove some active functional groups from the GO surface. During this time, a density map was determined at a resolution of 7.4 Å with about 10,000 particles from 600 micrographs collected overnight. This mid-resolution reconstruction shows a feasible approach to collect preliminary information of protein structure with limited sample

concentration and collection time. However, the preferred orientation was not eliminated on baked-GO grids. A tilt angle data collection may reduce the orientational bias (Mindell & Grigorieff, 2003; Tan et al., 2017). Besides, a weak density of NDUFA12 was identified. The same weak density of NDUFA12 in complex I was also observed from the graphene-coated Au grids and the traditional caron-coated grids (Wu et al., 2016), but not reported in the non-carbon-coated grids (Vinothkumar et al., 2014; Fiedorczuk et al., 2016; Agip et al., 2018), indicating an artefacts of applying complex Ion carbon film. The further non-carbon coated grids, such as polylysine-coated grids and PEGylated grids, were tested. The polylysine grids have shown compatibility of low concentration complex I sample but with background noise and unexpected contaminants. The thiol-PEG reagents been used in the lab with many studies (Blaza et al., 2018; Agip et al., 2018; Grba & Hirst, 2020; Bridges et al., 2020), and this study has shown that the long-PEG have identical affect on particle distributions as the short-PEG, which provides alternative options for PEGylation.

Many other methods should be considered in the future. For example, affinity grids using specific interactions such as His-tag to anchor targeted protein without purification by chromatography have been successfully used in cryo-EM (Benjamin et al., 2016). Besides, stabilising protein by nanodiscs with a further concentration step can also be considered to improve particle numbers on the micrographs (Denisov & Sligar, 2016).

Chapter 6. General Discussion

NADH:ubiquinone oxidoreductase (complex I), as the largest enzyme of the OXPOHS system and one of the electron entry points, has a series of essential roles in the system including oxidation of NADH, reduction of ubiquinone and translocation of protons across the IMM (Berrisford & Sazanov, 2009; Baradaran et al. 2013; Efremov & Sazanov, 2011).

Mitochondrial disease can be caused by pathogenic variants in genes encoded by both nuclear DNA and mitochondrial DNA, with isolated complex I deficiency being one of the most frequent cause of mitochondrial disease (Ng & Turnbull, 2016). Therapeutic approaches for such diseases are limited due to the lack of sufficient understanding of the pathogenic mechanism. In the last two decades, the complex I structure from different organisms have been well studies by crystallography and cryo-EM (Hinchliffe and Sazanov, 2005; Efremov & Sazanov, 2011; Zickermann et al., 2015). Besides, the structures of complex I from gene-edited yeast strains were investigated (Parey et al., 2018), as the structural analysis of mutated complex I is a fundamental approach to understanding the mechanism. These studies have all contributed to the knowledge of complex I pathogenesis and provide insight into complex I function and assembly.

It was the near-atomic cryo-EM maps of the complex I from bovine and mouse that have provided a platform to investigate complex I pathogenesis in mamalian species based on their structures (Vinothkumar, Zhu & Hirst, 2014; Agip et al., 2018). Therefore, the aim of my work was to acquire structural information of the complex I from the gene-edited mouse models to investigate its function in health and disease. Two mouse models with the genetic mutations on either nuclear DNA or mitochondrial DNA were selected and studies described in Chapter 3 and Chapter 4 of this thesis.

Chapter 3 focused on the structural study of complex I of a mouse model with a homoplasmic variant in the ND6 subunit (m.13997G >A MT-ND6) that encodes the P25L subsitution. The mouse was reported with abnormal mitochondrial morphologies and a reduced ROS production in reversed electron transfer (Lin et al., 2012). The cryo-EM structure of ND6-P25L complex I

has shown subtle structural changes that drive the whole complex into a confirmation that is similar to the deactive state wild-type complex I. Besides, the biochemical assays have shown the complex is fully active for NADH oxidation, but exhibit deactive-like characteristics, such as sensitive to NEM, even during the catalysis activity. Furthermore, the ND6-P25L mitochondria was incapable of generating ROS by RET and this phenomenon was proved to be the mutation-specific. In collaboration with the groups of Professor Michael Murph, Dr Thomas Krieg and Dr Dunja Aksentijevic, *in vivo* experiments have shown that the ROS production was eliminated on ND6-P25L mouse, and consequently the cardiac tissue was prevented from the damage during IR. The results suggest the central role of complex I in pathological ROS production and provide a promising therapeutic direction of reversible deactivation of complex I against heart injury during IR.

Chapter 4 focused on generating the high-resolution cryo-EM structure of complex I from *ndufs4*$^{-/-}$ mouse. NDUFS4, as a nuclear DNA encoded accessory subunit, was considered to play a role in connecting N- and Q-module of complex I (Guerrero-Castillo et al., 2017). Patients with pathogenic *NDUFS4* variants have been reported with non-specific fatal progressive phenotypes and a decreased complex I activities in fibroblasts (Ortigoza-Escobar et al., 2016). Complex I from *ndufs4*$^{-/-}$ mouse heart has been shown to have low activity and integrity in this study. The cryo-EM structure of complex I without NDUFS4 was obtained with a resolution of 2.9 Å. The mutant complex has a highly unstable N-module with the absence of NDUFA12 subunit, which is confirmed by the proteomic BN-PAGE complexome profiling (Agip, 2018). This is different from the complex I structure obtained from yeast strain with *ndufs4* deletion, where the assembly factor NDUFAF2 was identified on the structure (Kahlhöfer et al., 2017). This finding suggests a possible species-specific assembly pathway in mammalian species comparing to the yeast. Besides, the mutant complex I has shown an active state with a ubiquinone identified in the proposed Q-binding tunnel. All the findings, including the loosely bound N-module and absence of NDUFA12, have revealed the important role of NDUFS4 in the complex I assembly and maintaining the N-module stability. These findings support the proposed pathogenesis that structurally unstable complex I could cause low activity and high ROS production due to the leak of electrons, which eventually cause the damage

(Parey et al., 2019). The active state of the enzyme together with the tightly bound ubiquinone provide another perspective that the loss of NDUFS4 could cause less efficient electron transfer, which could possibly elongate the binding time of ubiquinone in Q-binding tunnel. In this way, the complex I activity was decreased, and the ROS production was enhanced.

The cryo-EM study in Chapter 4 required the isolation of mitochondrial from mouse heart tissue and the purification of homogenous complex I from solubilised mitochondrial membrane. However, in this chapter, the sample size is limited and it is difficult to achieve the required protein concentration for preparing the satisfied cryo-EM grids. This is due to the mouse heart in *ndufs4*$^{-/-}$ mouse being smaller than that of the WT, and mutant complex I disassociating during purification. Thus, several strategies including mild crosslinking and sample concentrating have been successfully applied to optimise the sample condition. Besides, several promising grid-surface optimisation approaches for samples with a small volume have been investigated in Chapter 5.

Different types of surface coating reagents including carbon layers, thiol-PEF as well as polylysine were considered in Capter 5 for the low concentration cryo-EM samples. Specifically, the graphene oxide coated grids were able to downscale the sample concentration up to 30 folds. The continued baking treatment on the graphene oxide grids modified the surface reaction groups and improved the particle orientation. The fast image collecting and processing of a small set of micrographs demonstrated in this chapter has achieved a good resolution for identifying major structural changes. This successful 3D reconstruction of the complex I makes it possible to apply this technique to more challenging samples with limited sample volume and low concentrations such as the human cell lines and patient samples.

The studies in this thesis were dedicated to the investigation of the clinically relevant complex I variants in genetic modified mouse models. The high resolution cryo-EM maps of the complex I from ND6-P25L and *ndufs4*$^{-/-}$ mouse together with the biochemical studies have revealed the mutation-induced structural changes on this macromolecule and offered clues on the pathological mechanism of complex I deficiency. The invented grid optimisation techniques for complex I cryo-EM structural study have removed the bottleneck of studing the small-scale

and unstable samples. Together, this work has demonstrated a possible way of investigating pathology by bring the structural, biochemical and *in vivo* studies together. Visualisation of protein with mutations and its confirmational alteration will sharpen our ability to identify novel therapeutic targets and shed light on the structure-based drug design. Furthermore, the microscaling of techniques I have validated and developed in this work makes the structural study of marcormolecues from human cell lines and even patient biopsy samples feasible. The rapid structural screening by cryo-EM on patient samples could assist the molecular diagnosis and development of personalised medicine in the future.

Chapter 7. References

Adamus, K., Le, S. N., Elmlund, H., Boudes, M., & Elmlund, D. (2019). AgarFix: Simple and accessible stabilization of challenging single-particle cryo-EM specimens through crosslinking in a matrix of agar. *Journal of structural biology,* 207(3), 327–331. https://doi.org/10.1016/j.jsb.2019.07.004

Adam-Vizi, V., & Chinopoulos, C. (2006). Bioenergetics and the formation of mitochondrial reactive oxygen species. *Trends in pharmacological sciences*, 27 (12), 639–645. https://doi.org/10.1016/j.tips.2006.10.005

Adjobo-Hermans, M., de Haas, R., Willems, P., Wojtala, A., van Emst-de Vries, S. E.,Wagenaars, J. A., van den Brand, M., Rodenburg, R. J., Smeitink, J., Nijtmans, L. G., Sazanov, L. A., Wieckowski, M. R., & Koopman, W. (2020). NDUFS4 deletion triggers loss of NDUFA12 in *Ndufs4*$^{-/-}$ mice and Leigh syndrome patients: A stabilizing role for NDUFAF2. *Biochimica et biophysica acta*. Bioenergetics, 1861(8), 148213. https://doi.org/10.1016/j.bbabio.2020.148213

Afonine, P. V., Grosse-Kunstleve, R. W., Echols, N., Headd, J. J., Moriarty, N. W., Mustyakimov, M., Terwilliger, T. C., Urzhumtsev, A., Zwart, P. H., & Adams, P. D. (2012). Towards automated crystallographic structure refinement with phenix.refine. Acta crystallographica. Section D, *Biological crystallography*, 68(Pt 4), 352–367. https://doi.org/10.1107/S0907444912001308

Afonine, P. V., Poon, B. K., Read, R. J., Sobolev, O. V., Terwilliger, T. C., Urzhumtsev, A., & Adams, P. D. (2018). Real-space refinement in PHENIX for cryo-EM and crystallography. Acta crystallographica. Section D, *Structural biology,* 74(Pt 6), 531–544. https://doi.org/10.1107/S2059798318006551

Agip, A. N. A., Blaza, J. N., Bridges, H. R., Viscomi, C., Rawson, S., Muench, S. P.,& Hirst, J. (2018). Cryo-EM structures of complex I from mouse heart mitochondria in two biochemically defined states. *Nature Structural and Molecular Biology*, 25(July),1–9. https://doi.org/10.1038/s41594-018-0073-1

Agip, A. (2018). Developing mouse complex I as a model system: structure, function and implications in mitochondrial diseases. (*Doctoral thesis*). https://doi.org/10.17863/CAM.30568

Ahn, C. S., & Metallo, C. M. (2015).Mitochondria as biosynthetic factories for cancer proliferation. *Cancer & metabolism,* 3(1), 1. https://doi.org/10.1186/s40170-015-0128-2

Alston, C. L., Rocha, M. C., Lax, N. Z., Turnbull, D. M., & Taylor, R. W. (2017). The genetics and pathology of mitochondrial disease. *The Journal of pathology*, 241(2), 236–250. https://doi.org/10.1002/path.4809

Anderson, S., Bankier, A. T., Barrell, B.G., de Bruijn, M. H., Coulson, A. R., Drouin,J., Eperon, I. C., Nierlich, D. P., Roe, B. A., Sanger, F., Schreier, P. H., Smith, A. J., Staden, R.,& Young, I.G. (1981). Sequence and organization of the human mitochondrial genome. Nature, 290(5806), 457–465. https://doi.org/10.1038/290457a0

Andrews, B., Carroll, J., Ding, S., Fearnley, I. M., & Walker, J. E. (2013). Assembly factors for the membrane arm of human complex I. *Proceedings of the National Academy of Sciences of the United States of America,* 110(47), 18934–18939. https://doi.org/10.1073/pnas.1319247110

Angerer H. (2015). Eukaryotic LYR Proteins Interact with Mitochondrial Protein Complexes. *Biology,* 4(1), 133–150. https://doi.org/10.3390/biology4010133

Angerer, H., Zwicker, K., Wumaier, Z., Sokolova, L., Heide, H., Steger, M., Kaiser, S., Nübel, E., Brutschy, B., Radermacher, M., Brandt, U., & Zickermann, V. (2011). A scaffold of accessory subunits links the peripheral arm and the distal proton-pumping module of

mitochondrial complex I. *The Biochemical journal*, 437(2), 279–288. https://doi.org/10.1042/BJ20110359

Antonucci, S., Mulvey, J. F., Burger, N., Di Sante, M., Hall, A. R., Hinchy, E. C., Caldwell, S. T., Gruszczyk, A. V., Deshwal, S., Hartley, R. C., Kaludercic, N., Murphy,M. P., Di Lisa, F., & Krieg, T. (2019). Selective mitochondrial superoxide generation in vivo is cardioprotective through hormesis. *Free radical biology & medicine,* 134, 678–687. https://doi.org/10.1016/j.freeradbiomed.2019.01.034

Arnold, S. A., Albiez, S., Bieri, A., Syntychaki, A., Adaixo, R., McLeod, R. A., Goldie, K. N., Stahlberg, H., & Braun, T. (2017). Blotting-free and lossless cryo-electron microscopy grid preparation from nanoliter-sized protein samples and single-cell extracts. *Journal of structural biology*, 197(3), 220–226. https://doi.org/10.1016/j.jsb.2016.11.002

Assouline, Z., Jambou, M., Rio, M., Bole-Feysot, C., de Lonlay, P., Barnerias, C., Desguerre, I., Bonnemains, C., Guillermet, C., Steffann, J., Munnich, A., Bonnefont, J. P.,Rötig, A., & Lebre, A. S. (2012). A constant and similar assembly defect of mitochondrial respiratory chain complex I allows rapid identification of NDUFS4 mutations in patients with Leigh syndrome. *Biochimica et biophysica acta*, 1822(6), 1062–1069. https://doi.org/10.1016/j.bbadis.2012.01.013

Babot, M., Birch, A., Labarbuta, P., & Galkin, A. (2014). Characterisation of the active/de-active transition of mitochondrial complex I. *Biochimica et biophysica acta*, 1837(7), 1083–1092. https://doi.org/10.1016/j.bbabio.2014.02.018

Bachi, A., Dalle-Donne, I., & Scaloni, A. (2013). Redox proteomics: chemical principles, methodological approaches and biological/biomedical promises. *Chemical reviews*, 113(1), 596–698. https://doi.org/10.1021/cr300073p

Baertling, F., Rodenburg, R. J., Schaper, J., Smeitink, J. A., Koopman, W. J., Mayatepek, E., Morava, E., & Distelmaier, F. (2014). A guide to diagnosis and treatment of Leigh

syndrome. *Journal of neurology, neurosurgery, and psychiatry*, 85(3), 257–265. https://doi.org/10.1136/jnnp-2012-304426

Baradaran, R., Berrisford, J. M., Minhas, G. S., & Sazanov, L. A. (2013). Crystal structure of the entire respiratory complex I. *Nature*, 494(7438), 443–448. https://doi.org/10.1038/nature11871

Bayrhuber, M., Meins, T., Habeck, M., Becker, S., Giller, K., Villinger, S., Vonrhein, C., Griesinger, C., Zweckstetter, M., & Zeth, K. (2008). Structure of the human voltage-dependent anion channel. *Proceedings of the National Academy of Sciences of the United States of America*, 105(40), 15370–15375. https://doi.org/10.1073/pnas.0808115105

Belevich, I., Gorbikova, E., Belevich, N. P., Rauhamäki, V., Wikström, M., & Verkhovsky, M. I. (2010). Initiation of the proton pump of cytochrome c oxidase. *Proceedings of the National Academy of Sciences of the United States of America*, 107(43), 18469–18474. https://doi.org/10.1073/pnas.1010974107

Belevich, N., Belevich, G., Chen, Z., Sinha, S. C., & Verkhovskaya, M. (2017). Activation of respiratory Complex I from Escherichia coli studied by fluorescent probes. *Heliyon*, 3(1), e00224. https://doi.org/10.1016/j.heliyon.2016.e00224

Bendory, T., Bartesaghi, A., & Singer, A. (2020). Single-particle cryo-electron microscopy: Mathematical theory, computational challenges, and opportunities. *IEEE signal processing magazine*, 37(2), 58–76. https://doi.org/10.1109/msp.2019.2957822

Benjamin, C. J., Wright, K. J., Hyun, S. H., Krynski, K., Yu, G., Bajaj, R., Guo, F., Stauffacher, C. V., Jiang, W., & Thompson, D. H. (2016). Nonfouling NTA-PEG-Based TEM Grid Coatings for Selective Capture of Histidine-Tagged Protein Targets from Cell Lysates. *Langmuir: the ACS journal of surfaces and colloids*, 32(2), 551–559. https://doi.org/10.1021/acs.langmuir.5b03445

Berg, J., Tymoczko, J., & Stryer, L. (2002). The Respiratory Chain Consists of Four Complexes: Three Proton Pumps and a Physical Link to the Citric Acid Cycle. *In Biochemistry* (5th ed.). New York: W H Freeman. Retrieved from https://www.ncbi.nlm.nih.gov/books/NBK22505/

Berman, H. (2000). The Protein Data Bank. *Nucleic Acids Research,* 28(1), 235-242. https://doi.org/10.1093/nar/28.1.235

Berrisford, J. M., & Sazanov, L. A. (2009). Structural basis for the mechanism of respiratory complex I. *The Journal of biological chemistry*, 284(43), 29773–29783. https://doi.org/10.1074/jbc.M109.032144

Berrisford, J. M., Baradaran, R., & Sazanov, L. A. (2016). Structure of bacterial respiratory complex I. *Biochimica et biophysica acta*, 1857(7), 892–901. https://doi.org/10.1016/j.bbabio.2016.01.012

Billups, B., & Forsythe, I. D. (2002). Presynaptic mitochondrial calcium sequestration influences transmission at mammalian central synapses. *The Journal of neuroscience: the official journal of the Society for Neuroscience,* 22(14), 5840–5847. https://doi.org/10.1523/JNEUROSCI.22-14-05840.2002

Biner, O., Fedor, J. G., Yin, Z., & Hirst, J. (2020). Bottom-Up Construction of a Minimal System for Cellular Respiration and Energy Regeneration. *ACS synthetic biology*, 9(6), 1450–1459. https://doi.org/10.1021/acssynbio.0c00110

Birrell, J. A., Yakovlev, G., & Hirst, J. (2009). Reactions of the flavin mononucleotide in complex I: a combined mechanism describes NADH oxidation coupled to the reduction of $APAD^+$, ferricyanide, or molecular oxygen. *Biochemistry*, 48(50), 12005–12013. https://doi.org/10.1021/bi901706w

Blaza, J. N., Serreli, R., Jones, A. J., Mohammed, K., & Hirst, J. (2014). Kinetic evidence against partitioning of the ubiquinone pool and the catalytic relevance of respiratory-chain

supercomplexes. *Proceedings of the National Academy of Sciences of the United States of America*, 111(44), 15735–15740. https://doi.org/10.1073/pnas.1413855111

Blaza, J. N., Vinothkumar, K. R., & Hirst, J. (2018). Structure of the Deactive State of Mammalian Respiratory Complex I. *Structure*, 26(2), 312–319.e3. https://doi.org/10.1016/j.str.2017.12.014

Blum, T. B., Hahn, A., Meier, T., Davies, K. M., & Kühlbrandt, W. (2019). Dimers of mitochondrial ATP synthase induce membrane curvature and self-assemble into rows. *Proceedings of the National Academy of Sciences of the United States of America*, 116(10), 4250–4255. https://doi.org/10.1073/pnas.1816556116

Body weight information for C57BL/6J (000664) (2020). Retrieved from https://www.jax.org/jax-mice-and-services/strain-data-sheet-pages/body-weight-chart-000664)

Bokori-Brown, M., Martin, T. G., Naylor, C. E., Basak, A. K., Titball, R. W., & Savva, C. G. (2016). Cryo-EM structure of lysenin pore elucidates membrane insertion by an aerolysin family protein. *Nature communications*, 7, 11293. https://doi.org/10.1038/ncomms11293

Boland, A., Martin, T. G., Zhang, Z., Yang, J., Bai, X. C., Chang, L., Scheres, S. H. & Barford, D. (2017). Cryo-EM structure of a metazoan separase-securin complex at near-atomic resolution. *Nature structural & molecular biology*, 24(4), 414–418. https://doi.org/10.1038/nsmb.3386

Brand, M. D., Goncalves, R. L., Orr, A. L., Vargas, L., Gerencser, A. A., Borch Jensen, M., Wang, Y. T., Melov, S., Turk, C. N., Matzen, J. T., Dardov, V. J., Petrassi, H. M., Meeusen, S. L., Perevoshchikova, I. V., Jasper, H., Brookes, P. S., & Ainscow, E. K. (2016). Suppressors of Superoxide-H_2O_2 Production at Site I_Q of Mitochondrial Complex I Protect against Stem Cell Hyperplasia and Ischemia-Reperfusion Injury. *Cell metabolism*, 24(4), 582–592. https://doi.org/10.1016/j.cmet.2016.08.012

Brandt U. (2006). Energy converting NADH:quinone oxidoreductase (complex I). *Annual review of biochemistry*, 75, 69–92. https://doi.org/10.1146/annurev.biochem.75.103004.142539

Bratic, A., & Larsson, N. (2013). The role of mitochondria in aging. *Journal of Clinical Investigation*, 123(3), 951–957. https://doi.org/10.1172/JCI64125

Brenner, S., & Horne, R. W (1959). A negative staining method for high resolution electron microscopy of viruses. *Biochimica et biophysica acta*, 34, 103–110. https://doi.org/10.1016/0006-3002(59)90237-9

Breuer, M. E., Willems, P. H., Smeitink, J. A., Koopman, W. J., & Nooteboom, M. (2013). Cellular and animal models for mitochondrial complex I deficiency: a focus onthe NDUFS4 subunit. *IUBMB life*, 65(3), 202–208. https://doi.org/10.1002/iub.1127

Bridges, H. R., Bill, E., & Hirst, J. (2012). Mössbauer spectroscopy on respiratory complex I: the iron-sulfur cluster ensemble in the NADH-reduced enzyme is partially oxidized. *Biochemistry*, 51(1), 149–158. https://doi.org/10.1021/bi201644x

Bridges, H. R., Fedor, J. G., Blaza, J. N., Di Luca, A., Jussupow, A., Jarman, O. D., Wright, J. J., Agip, A. A., Gamiz-Hernandez, A. P., Roessler, M. M., Kaila, V., & Hirst, J. (2020). Structure of inhibitor-bound mammalian complex I. *Nature communications*, 11(1), 5261. https://doi.org/10.1038/s41467-020-18950-3

Brilot, A. F., Chen, J. Z., Cheng, A.,Pan, J., Harrison, S. C., Potter, C. S., Carragher, B., Henderson, R., & Grigorieff, N. (2012). Beam-induced motion of vitrified specimen on holey carbon film. *Journal of structural biology*, 177(3), 630–637. https://doi.org/10.1016/j.jsb.2012.02.003

Broun G. B. (1976). Chemically aggregated enzymes. *Methods in enzymology*, 44, 263–280. https://doi.org/10.1016/s0076-6879(76)44022-3

Budde, S. M., van den Heuvel, L. P., & Smeitink, J. A. (2002). The human complex I NDUFS4 subunit: from gene structure to function and pathology. *Mitochondrion*, 2(1-2), 109–115. https://doi.org/10.1016/s1567-7249(02)00035-1

Budde, S. M., van den Heuvel, L. P., Janssen, A. J., Smeets, R. J., Buskens, C. A., DeMeirleir, L., Van Coster, R., Baethmann, M., Voit, T., Trijbels, J. M., & Smeitink, J. A. (2000). Combined enzymatic complex I and III deficiency associated with mutations in the nuclear encoded NDUFS4 gene. *Biochemical and biophysical research communications*, 275(1), 63–68. https://doi.org/10.1006/bbrc.2000.3257

Burger, N., Logan, A., Prime, T. A., Mottahedin, A., Caldwell, S. T., Krieg, T., Hartley, R. C., James, A. M., & Murphy, M. P. (2020). A sensitive mass spectrometric assay for mitochondrial CoQ pool redox state in vivo. *Free radical biology & medicine*, 147, 37–47. https://doi.org/10.1016/j.freeradbiomed.2019.11.028

Calvaruso, M. A., Willems, P., van den Brand, M., Valsecchi, F., Kruse, S., Palmiter, R., Smeitink, J., & Nijtmans, L. (2012). Mitochondrial complex III stabilizes complex I in the absence of NDUFS4 to provide partial activity. *Human molecular genetics*, 21(1), 115–120. https://doi.org/10.1093/hmg/ddr446

Cannell, M. B., Cheng, H., & Lederer, W. J. (1995). The control of calcium release in heart muscle. *Science,* 268(5213), 1045–1049. https://doi.org/10.1126/science.7754384

Carroll, J., Fearnley, I. M., Skehel, J. M., Shannon, R. J., Hirst, J., & Walker, J. E. (2006). Bovine complex I is a complex of 45 different subunits. *Journal of Biological Chemistry*, 281(43), 32724–32727. https://doi.org/10.1074/jbc.M607135200

Chang, S., Dwyer, C., Barthel, J., Boothroyd, C. B., & Dunin-Borkowski, R. E. (2016). Performance of a direct detection camera for off-axis electron holography. *Ultramicroscopy*, 161, 90–97. https://doi.org/10.1016/j.ultramic.2015.09.004

Chen, L., Cui, Y., Jiang, D., Ma, C. Y., Tse, H. F., Hwu, W. L., & Lian, Q. (2018).Management of Leigh syndrome: Current status and new insights. *Clinical genetics*, 93(6), 1131–1140. https://doi.org/10.1111/cge.13139

Chen, R., Fearnley, I. M., Peak-Chew, S. Y., & Walker, J. E. (2004). The phosphorylation of subunits of complex I from bovine heart mitochondria. *The Journal of biological chemistry*, 279(25), 26036–26045. https://doi.org/10.1074/jbc.M402710200

Cheng, Y., Grigorieff, N., Penczek, P. A., & Walz, T. (2015). A primer to single-particle cryo-electron microscopy. *Cell*, 161(3), 438–449. https://doi.org/10.1016/j.cell.2015.03.050

Cheung, M., Kajimura, N., Makino, F., Ashihara, M., Miyata, T., Kato, T., Namba, K.,& Blocker, A. J. (2013). A method to achieve homogeneous dispersion of large transmembrane complexes within the holes of carbon films for electron cryomicroscopy. *Journal of structural biology*, 182(1), 51–56. https://doi.org/10.1016/j.jsb.2013.01.004

Chinnery, P. F., Brown, D. T., Andrews, R. M., Lindley, J., Applegarth, D. A., Turnbull, D. M., & Howell, N. (2001). The mitochondrial ND6 gene is a hot spot for mutations that cause Leber's hereditary optic neuropathy. *American Journal of Ophthalmology*, 131(5), 687–688. https://doi.org/10.1016/S0002-9394(01)00948-5

Chouchani, E. T., Methner, C., Nadtochiy, S. M., Logan, A., Pell, V. R., Ding, S., James, A. M., Cochemé, H. M., Reinhold, J., Lilley, K. S., Partridge, L., Fearnley, I. M., Robinson, A. J., Hartley, R. C., Smith, R. A., Krieg, T., Brookes, P. S., & Murphy, M. P. (2013). Cardioprotection by S-nitrosation of a cysteine switch on mitochondrial complex I. *Nature medicine*, 19(6), 753–759. https://doi.org/10.1038/nm.3212

Chouchani, E. T., Pell, V. R., Gaude, E., Aksentijević, D., Sundier, S. Y., Robb, E. L., Logan, A., Nadtochiy, S. M., Ord, E., Smith, A. C., Eyassu, F., Shirley, R., Hu, C. H., Dare, A. J., James, A. M., Rogatti, S., Hartley, R. C., Eaton, S., Costa, A., Brookes, P. S., … Murphy, M. P. (2014). Ischaemic accumulation of succinate controls reperfusion injury

through mitochondrial ROS. *Nature*, 515(7527), 431–435. https://doi.org/10.1038/nature13909

Chouchani, E. T., Pell, V. R., James, A. M., Work, L. M., Saeb-Parsy, K., Frezza, C.,Krieg, T., & Murphy, M. P. (2016). A Unifying Mechanism for Mitochondrial Superoxide Production during Ischemia-Reperfusion Injury. *Cell metabolism*, 23(2), 254–263. https://doi.org/10.1016/j.cmet.2015.12.009

Chui, W. K., & Wan, L. S. (1997). Prolonged retention of cross-linked trypsin in calcium alginate microspheres. *Journal of microencapsulation*, 14(1), 51–61. https://doi.org/10.3109/02652049709056467

Cochemé, H. M., Quin, C., McQuaker, S. J., Cabreiro, F., Logan, A., Prime, T. A., Abakumova, I., Patel, J. V., Fearnley, I. M., James, A. M., Porteous, C. M., Smith, R.A., Saeed, S., Carré, J. E., Singer, M., Gems, D., Hartley, R. C., Partridge, L., & Murphy, M. P. (2011). Measurement of H2O2 within living Drosophila during aging using a ratiometric mass spectrometry probe targeted to the mitochondrial matrix. *Cell metabolism*, 13(3), 340–350. https://doi.org/10.1016/j.cmet.2011.02.003

Croll T. I. (2018). ISOLDE: a physically realistic environment for model building intolow-resolution electron-density maps. Acta crystallographica. Section D, *Structural biology*, 74(Pt 6), 519–530. https://doi.org/10.1107/S2059798318002425

Cronan, J. E., Fearnley, I. M., & Walker, J. E. (2005). Mammalian mitochondria contain a soluble acyl carrier protein. *FEBS letters*, 579(21), 4892–4896. https://doi.org/10.1016/j.febslet.2005.07.077

Dandey, V., Budell, W., Wei, H., Bobe, D., Maruthi, K., & Kopylov, M. et al. (2020). Time-resolved cryo-EM using Spotiton. *Nature Methods*. https://doi.org/0.1038/s41592-020-0925-6

Dang, Q. L., Phan, D. H., Johnson, A. N., Pasapuleti, M., Alkhaldi, H. A., Zhang, F.,& Vik, S. B. (2020). Analysis of Human Mutations in the Supernumerary Subunits of Complex I. *Life* (Basel, Switzerland), 10(11), 296. https://doi.org/10.3390/life10110296

Darin, N., Oldfors, A., Moslemi, A. R., Holme, E., & Tulinius, M. (2001). The incidence of mitochondrial encephalomyopathies in childhood: clinical features and morphological, biochemical, and DNA abnormalities. *Annals of neurology*, 49(3), 377–383.

Davies, K. M., Blum, T. B., & Kühlbrandt, W. (2018). Conserved in situ arrangement of complex I and III2 in mitochondrial respiratory chain supercomplexes of mammals, yeast, and plants. *Proceedings of the National Academy of Sciences of the United States of America*, 115(12), 3024–3029. https://doi.org/10.1073/pnas.1720702115

Davies, K. M., Strauss, M., Daum, B., Kief, J. H., Osiewacz, H. D., Rycovska, A., Zickermann, V., & Kühlbrandt, W. (2011). Macromolecular organization of ATP synthase and complex I in whole mitochondria. *Proceedings of the National Academy of Sciences of the United States of America*, 108(34), 14121–14126. https://doi.org/10.1073/pnas.1103621108

de Haas, R., Das, D., Garanto, A., Renkema, H. G., Greupink, R., van den Broek, P.,Pertijs, J., Collin, R., Willems, P., Beyrath, J., Heerschap, A., Russel, F. G., & Smeitink, J. A. (2017). Therapeutic effects of the mitochondrial ROS-redox modulator KH176 in a mammalian model of Leigh Disease. *Scientific reports*, 7(1), 11733. https://doi.org/10.1038/s41598-017-09417-5

De Rasmo, D., Palmisano, G., Scacco, S., Technikova-Dobrova, Z., Panelli, D., Cocco,T., Sardanelli, A. M., Gnoni, A., Micelli, L., Trani, A., Di Luccia, A., & Papa, S. (2010). Phosphorylation pattern of the NDUFS4 subunit of complex I of the mammalianrespiratory chain. *Mitochondrion*, 10(5), 464–471. https://doi.org/10.1016/j.mito.2010.04.005

Denisov, I. G., & Sligar, S. G. (2016). Nanodiscs for structural and functional studies of membrane proteins. *Nature structural & molecular biology*, 23(6), 481–486. https://doi.org/10.1038/nsmb.3195

Devenish, R. J., Prescott, M., Boyle, G. M., & Nagley, P. (2000).The oligomycin axisof mitochondrial ATP synthase: OSCP and the proton channel. *Journal of bioenergetic and biomembranes*, 32(5), 507–515. https://doi.org/10.1023/a:1005621125812

Doerr A. (2016). Single-particle cryo-electron microscopy. *Nature methods*, 13(1), 23. https://doi.org/10.1038/nmeth.3700

Dooijewaard, G., & Slater, E. (1976). Steady-state kinetics of high molecular weight (type-I) NADH dehydrogenase. *Biochimica Et Biophysica Acta (BBA)* - Bioenergetics, 440(1), 1-15. https://doi.org/10.1016/0005-2728(76)90109-2

Drulyte, I., Johnson, R. M., Hesketh, E. L., Hurdiss, D. L., Scarff, C. A., Porav, S. A., Ranson, N. A., Muench, S. P., & Thompson, R. F. (2018). Approaches to alteringparticle distributions in cryo-electron microscopy sample preparation. *Acta crystallographica*. Section D, Structural biology, 74(Pt 6), 560–571. https://doi.org/10.1107/S2059798318006496

Du, M., Wei, X., Xu, P., Xie, A., Zhou, X., Yang, Y., Li, D., Lyu, J., & Fang, H. (2020). A novel mitochondrial m.14430A>G (MT-ND6, p.W82R) variant causes complex I deficiency and mitochondrial Leigh syndrome. *Clinical chemistry and laboratory medicine*, 58(11), 1809–1817. https://doi.org/10.1515/cclm-2020-0150

Dubochet, J., & McDowall, A. (1981).Vitrification of pure water for electron microscopy. *Journal Of Microscopy*, 124(3), 3-4. https://doi.org/10.1111/j.1365-2818.1981.tb02483.x

Duochet, J., Adrian, M., Chang, J. J., Homo, J. C., Lepault, J., McDowall, A. W., & Schultz, P. (1988).Cryo-electron microscopy of vitrified specimens. *Quarterly review of biophysics,* 21(2), 129–228. https://doi.org/10.1017/s0033583500004297

Efremov, R. G., & Sazanov, L. A. (2011). Structure of the membrane domain of respiratory complex I. *Nature,* 476(7361), 414–421. https://doi.org/10.1038/nature10330

Efremov, R. G., Baradaran, R., & Sazanov, L. A. (2010). The architecture of respiratory complex I. *Nature*, 465(7297), 441–445. https://doi.org/10.1038/nature09066

Eltzschig, H. K., & Eckle, T. (2011). Ischemia and reperfusion--from mechanism to translation. *Nature medicine,* 17(11), 1391–1401. https://doi.org/10.1038/nm.2507

Elurbe, D. M., & Huynen, M. A. (2016). The origin of the supernumerary subunits and assembly factors of complex I: A treasure trove of pathway evolution. *Biochimica etbiophysica acta,* 1857(7), 971–979. https://doi.org/10.1016/j.bbabio.2016.03.027

Emahazion, T., Beskow, A., Gyllensten, U., & Brookes, A. J. (1998). Intron based radiation hybrid mapping of 15 complex I genes of the human electron transport chain. *Cytogenetics and cell genetics,* 82(1-2), 115–119. https://doi.org/10.1159/000015082

Emsley, P., Lohkamp, B., Scott, W. G., & Cowtan, K. (2010). *Features and development of Coot. Acta crystallographica. Section D, Biological crystallography*, 66(Pt 4), 486–501. https://doi.org/10.1107/S0907444910007493

Enríquez J. A. (2016). Supramolecular Organization of Respiratory Complexes. *Annual review of physiology*, *78*, 533–561. https://doi.org/10.1146/annurev-physiol-021115-105031

Ettema, T. J. G. (2016). Mitochondria in the second act. *Nature*, 531(7592), 39–40. https://doi.org/10.1038/nature16876

Fassone, E., & Rahman, S. (2012). Complex I deficiency: clinical features, biochemistry and molecular genetics. *Journal of medical genetics*, 49(9), 578–590. https://doi.org/10.1136/jmedgenet-2012-101159

Fedor, J. G., & Hirst, J. (2018). Mitochondrial Supercomplexes Do Not Enhance Catalysis by Quinone Channeling. *Cell metabolism*, 28(3), 525–531.e4. https://doi.org/10.1016/j.cmet.2018.05.024

Fedor, J. G., Jones, A. J. Y., Di Luca, A., Kaila, V. R. I., & Hirst, J. (2017). Correlating kinetic and structural data on ubiquinone binding and reduction by respiratory complex I. *Proceedings of the National Academy of Sciences of the United States of America*, 114(48), 12737–12742. https://doi.org/10.1073/pnas.1714074114

Fernández-Vizarra, E., Ferrín, G., Pérez-Martos, A., Fernández-Silva, P., Zeviani, M., & Enríquez, J. A. (2010). Isolation of mitochondria for biogenetical studies: An update. *Mitochondrion*, 10(3), 253–262. https://doi.org/10.1016/j.mito.2009.12.148

Ferrari, M., Jain, I. H., Goldberger, O., Rezoagli, E., Thoonen, R., Cheng, K. H., Sosnovik, D. E., Scherrer-Crosbie, M., Mootha, V. K., & Zapol, W. M. (2017). Hypoxia treatment reverses neurodegenerative disease in a mouse model of Leigh syndrome. *Proceedings of the National Academy of Sciences of the United States of America*, 114(21), E4241–E4250. https://doi.org/10.1073/pnas.1621511114

Fica, S. M., Oubridge, C., Wilkinson, M. E., Newman, A. J., & Nagai, K. (2019). A human postcatalytic spliceosome structure reveals essential roles of metazoan factors for exon ligation. *Science*, 363(6428), 710–714. https://doi.org/10.1126/science.aaw5569

Fiedorczuk, K., & Sazanov, L. A. (2018). Mammalian Mitochondrial Complex I Structure and Disease-Causing Mutations. *Trends in Cell Biology*, 28(10), 835–867. https://doi.org/10.1016/j.tcb.2018.06.006

Fiedorczuk, K., Letts, J. A., Degliesposti, G., Kaszuba, K., Skehel, M., & Sazanov, L.A. (2016). Atomic structure of the entire mammalian mitochondrial complex I. N*ature,* 538(7625), 406–410. https://doi.org/10.1038/nature19794

Forbes, J. M., Ke, B. X., Nguyen, T. V., Henstridge, D. C., Penfold, S. A., Laskowski, A., Sourris, K. C., Groschner, L. N., Cooper, M. E., Thorburn, D. R., & Coughlan,M. T. (2013). Deficiency in mitochondrial complex I activity due to Ndufs6 gene trapinsertion induces renal disease.*Antioxidants & redox signaling*, 19(4), 331–343. https://doi.org/10.1089/ars.2012.4719

Formosa, L. E., Mimaki, M., Frazier, A. E., McKenzie, M., Stait, T. L., Thorburn, D. R., Stroud, D. A., & Ryan, M. T. (2015). Characterization of mitochondrial FOXRED1 in the assembly of respiratory chain complex I. *Human molecular genetics*, 24(10), 2952–2965. https://doi.org/10.1093/hmg/ddv058

Frank J. (2016).Generalized single-particle cryo-EM-a historical perspective. *Microscopy* (Oxford, England), 65(1), 3–8. https://doi.org/10.1093/jmicro/dfv358

Froschauer, E. M., Schweyen, R. J., & Wiesenberger, G. (2009). The yeast mitochondrial carrier proteins Mrs3p/Mrs4p mediate iron transport across the inner mitochondrial membrane. *Biochimica et biophysica acta*, 1788(5), 1044–1050. https://doi.org/10.1016/j.bbamem.2009.03.004

Galkin, A., & Moncada, S. (2017). Modulation of the conformational state of mitochondrial complex I as a target for therapeutic intervention. *Interface focus*, 7(2), 20160104. https://doi.org/10.1098/rsfs.2016.0104

Galkin, A., Dröse, S., & Brandt, U. (2006). The proton pumping stoichiometry of purified mitochondrial complex I reconstituted into proteoliposomes. *Biochimica et biophysica acta*, 1757(12), 1575–1581. https://doi.org/10.1016/j.bbabio.2006.10.001

Galkin, A., Meyer, B., Wittig, I., Karas, M., Schägger, H., Vinogradov, A., & Brandt, U. (2008). Identification of the mitochondrial ND3 subunit as a structural component involved in the active/deactive enzyme transition of respiratory complex I. *The Journal of biological chemistry,* 283(30), 20907–20913. https://doi.org/10.1074/jbc.M803190200

Garone, C., & Viscomi, C. (2018). Towards a therapy for mitochondrial disease: an update. *Biochemical Society transactions*, 46(5), 1247–1261. https://doi.org/10.1042/BST20180134

Garrido, C., Galluzzi, L., Brunet, M., Puig, P. E., Didelot, C., & Kroemer, G. (2006). Mechanisms of cytochrome *c* release from mitochondria. *Cell death and differentiation*, 13(9), 1423–1433. https://doi.org/10.1038/sj.cdd.4401950

Geim, A. K., & Novoselov, K. S. (2007). The rise of graphene. *Nature materials*, 6(3),183–191. https://doi.org/10.1038/nmat1849

Ghiselli, F., & Milani, L. (2020). Linking the mitochondrial genotype to phenotype: a complex endeavour. Philosophical transactions of the Royal Society of London. *Series B, Biological sciences*, 375(1790), 20190169. https://doi.org/10.1098/rstb.2019.0169

Giorgi, C., Marchi, S., & Pinton, P. (2018). The machineries, regulation and cellular functions of mitochondrial calcium. Nature reviews. *Molecular cell biology*, 19(11), 713–730. https://doi.org/10.1038/s41580-018-0052-8

Glaeser R. M. (2018). Proteins, interfaces, and cryo-EM grids. *Current opinion in colloid & interface science,* 34, 1–8. https://doi.org/10.1016/j.cocis.2017.12.009

Glaeser, R. M., & Han, B. G. (2017). Opinion: hazards faced by macromolecules when confined to thin aqueous films. *Biophysics reports*, 3(1),1–7. https://doi.org/10.1007/s41048-016-0026-3

Glick, B. S., Beasley, E. M., & Schatz, G. (1992). Protein sorting in mitochondria. *Trends in biochemical sciences*, 17(11), 453–459. https://doi.org/10.1016/0968-0004(92)90487-t

Gnandt, E., Schimpf, J., Harter, C., Hoeser, J., & Friedrich, T. (2017). Reduction of the off-pathway iron-sulphur cluster N1a of Escherichia coli respiratory complex I restrains

NAD^+ dissociation. *Scientific reports,* 7(1), 8754. https://doi.org/10.1038/s41598-017-09345-4

Gonzalez-Halphen, D., Ghelli, A., Iommarini, L., Carelli, V., & Esposti, M. D. (2011).Mitochondrial complex I and cell death: A semi-automatic shotgun model. *Cell Death and Disease*, 2(10). https://doi.org/10.1038/cddis.2011.107

Gorman, G. S., Chinnery, P. F., DiMauro, S., Hirano, M., Koga, Y., McFarland, R., Suomalainen, A., Thorburn, D. R., Zeviani, M., & Turnbull, D. M. (2016). Mitochondrial diseases. *Nature reviews*. Disease primers, 2,16080. https://doi.org/10.1038/nrdp.2016.80

Gorman, G. S., Schaefer, A. M., Ng, Y., Gomez, N., Blakely, E. L., Alston, C. L., Feeney, C., Horvath, R., Yu-Wai-Man, P., Chinnery, P. F., Taylor, R. W., Turnbull, D. M., & McFarland, R. (2015). Prevalence of nuclear and mitochondrial DNA mutations related to adult mitochondrial disease. *Annals of neurology*, 77(5),753–759. https://doi.org/10.1002/ana.24362

Gostimskaya, I. S., Grivennikova, V. G., Zharova, T. V., Bakeeva, L. E., & Vinogradov, A. D. (2003). In situ assay of the intramitochondrial enzymes: Use of alamethicin for permeabilization of mitochondria. *Analytical Biochemistry,* 313(1), 46–52. https://doi.org/10.1016/S0003-2697(02)00534-1

Grant G. A. (2012). Contrasting catalytic and allosteric mechanisms for phosphoglycerate dehydrogenases. *Archives of biochemistry and biophysics*, 519(2), 175–185. https://doi.org/10.1016/j.abb.2011.10.005

Grassucci, R. A., Taylor, D. J., & Frank, J. (2007). Preparation of macromolecular complexes for cryo-electron microscopy. *Nature protocols*, 2(12), 3239–3246. https://doi.org/10.1038/nprot.2007.452

Grba, D. N., & Hirst, J. (2020). Mitochondrial complex I structure reveals ordered water molecules for catalysis and proton translocation. *Nature structural & molecular biology*, 10.1038/s41594-020-0473-x. https://doi.org/10.1038/s41594-020-0473-x

Greggio, C., Jha, P., Kulkarni, S. S., Lagarrigue, S., Broskey, N. T., Boutant, M., Wang, X., Conde Alonso, S., Ofori, E., Auwerx, J., Cantó, C., & Amati, F. (2017). Enhanced Respiratory Chain Supercomplex Formation in Response to Exercise in Human Skeletal Muscle. *Cell metabolism*, 25(2), 301–311. https://doi.org/10.1016/j.cmet.2016.11.004

Grivennikova, V. G., Gladyshev, G. V., & Vinogradov, A. D. (2020). Deactivation of mitochondrial NADH:ubiquinone oxidoreductase (respiratory complex I): Extrinsically affecting factors. *Biochimica et biophysica acta. Bioenergetics,* 1861(8),148207. https://doi.org/10.1016/j.bbabio.2020.148207

Grivennikova, V. G., Kapustin, A. N., & Vinogradov, A. D. (2001). Catalytic activity of NADH-ubiquinone oxidoreductase (complex I) in intact mitochondria. evidence for the slow active/inactive transition. *The Journal of biological chemistry*, 276(12), 9038–9044. https://doi.org/10.1074/jbc.M009661200

Grivennikova, V. G., Maklashina, E. O., Gavrikova, E. V., & Vinogradov, A. D. (1997). Interaction of the mitochondrial NADH-ubiquinone reductase with rotenone as related to the enzyme active/inactive transition. *Biochimica et biophysica acta,* 1319(2-3), 223–232. https://doi.org/10.1016/s0005-2728(96)00163-6

Gu, J., Wu, M., Guo, R., Yan, K., Lei, J., Gao, N., & Yang, M. (2016). The architecture of the mammalian respirasome. *Nature*, 537(7622), 639–643. https://doi.org/10.1038/nature19359

Guarani, V., Paulo, J., Zhai, B., Huttlin, E. L., Gygi, S. P., & Harper, J. W. (2014). TIMMDC1/C3orf1 functions as a membrane-embedded mitochondrial complex I assembly factor through association with the MCIA complex. *Molecular and cellular biology,* 34(5), 847–861. https://doi.org/10.1128/MCB.01551-13

Guerrero-Castillo, S., Baertling, F., Kownatzki, D., Wessels, H. J., Arnold, S., Brandt, U., & Nijtmans, L. (2017). The Assembly Pathway of Mitochondrial Respiratory Chain Complex I. *Cell metabolism,* 25(1), 128–139. https://doi.org/10.1016/j.cmet.2016.09.002

Gueven, N. (2014). Optic Neurodegeneration: Time to Act. *Biology And Medicine,* 01(S1). https://doi.org/10.4172/0974-8369.s1-001

Guo, C., Sun, L., Chen, X., & Zhang, D. (2013). Oxidative stress, mitochondrial damage and neurodegenerative diseases. *Neural regeneration research*, 8(21), 2003–2014. https://doi.org/10.3969/j.issn.1673-5374.2013.21.009

Guo, F., & Jiang, W. (2014). Single particle cryo-electron microscopy and 3-D reconstruction of viruses. *Methods in molecular biology* (Clifton, N.J.), 1117, 401–443. https://doi.org/10.1007/978-1-62703-776-1_19

Guo, R., Zong, S., Wu, M., Gu, J., & Yang, M. (2017). Architecture of Human Mitochondrial Respiratory Megacomplex I2III2IV2. *Cell*, 170(6), 1247-1257.e12. https://doi.org/10.1016/j.cell.2017.07.050

Habeeb, A. J., & Hiramoto, R. (1968). Reaction of proteins with glutaraldehyde. *Archives of biochemistry and biophysics,*126(1), 16–26. https://doi.org/10.1016/0003-9861(68)90554-7

Hägerhäll, C. (1997). Succinate: quinone oxidoreductases. Variations on a conserved theme. *Biochimica et biophysica acta,* 1320(2), 107–141. https://doi.org/10.1016/s0005-2728(97)00019-4

Hall, C., Jakus, M., & Schmitt, F. (1945). The Structure of Certain Muscle Fibrils as Revealed by the Use of Electron Stains. *Journal Of Applied Physics*, 16(8), 459-465. https://doi.org/10.1063/1.1707615

Han, B. G., Watson, Z., Kang, H., Pulk, A., Downing, K. H., Cate, J., & Glaeser, R.M. (2016). Long shelf-life streptavidin support-films suitable for electron microscopy of biological macromolecules. *Journal of structural biology,* 195(2), 238–244. https://doi.org/10.1016/j.jsb.2016.06.009

Han, Y., Fan, X., Wang, H., Zhao, F., Tully, C. G., Kong, J., Yao, N., & Yan, N. (2020). High-yield monolayer graphene grids for near-atomic resolution cryoelectron microscopy. *Proceedings of the National Academy of Sciences of the United States of America*, 117(2), 1009–1014. https://doi.org/10.1073/pnas.1919114117

Hao, Y., Bharathi, M. S., Wang, L., Liu, Y., Chen, H., Nie, S., Wang, X., Chou, H., Tan, C., Fallahazad, B., Ramanarayan, H., Magnuson, C. W., Tutuc, E., Yakobson, B. I., McCarty, K. F., Zhang, Y. W., Kim, P., Hone, J., Colombo, L., & Ruoff, R. S. (2013). The role of surface oxygen in the growth of large single-crystal graphene on copper. *Science* (New York, N.Y.), 342(6159), 720–723. https://doi.org/10.1126/science.1243879

Hashizume, O., Shimizu, A., Yokota, M., Sugiyama, A., Nakada, K., Miyoshi, H., Itami, M., Ohira, M., Nagase, H., Takenaga, K., & Hayashi, J. (2012). Specific mitochondrial DNA mutation in mice regulates diabetes and lymphoma development. *Proceedings of the National Academy of Sciences of the United States of America,* 109(26), 10528–10533. https://doi.org/10.1073/pnas.1202367109

Hashizume, O., Yamanashi, H., Taketo, M. M., Nakada, K., & Hayashi, J. I. (2015). A specific nuclear DNA background is required for high frequency lymphoma development in transmitochondrial mice with G13997A mtDNA. *PLoS ONE,* 10(3), 1–13. https://doi.org/10.1371/journal.pone.0118561

Hauer, F., Gerle, C., Fischer, N., Oshima, A., Shinzawa-Itoh, K., Shimada, S., Yokoyama, K., Fujiyoshi, Y., & Stark, H. (2015). GraDeR: Membrane Protein Complex Preparation for Single-Particle Cryo-EM. *Structure* (London, England: 1993), 23(9), 1769–1775. https://doi.org/10.1016/j.str.2015.06.029

Hausenloy, D. J., & Yellon, D. M. (2013). Myocardial ischemia-reperfusion injury: a neglected therapeutic target. *The Journal of clinical investigation*, 123(1), 92–100. https://doi.org/10.1172/JCI62874

He, S. (2018). Helical Reconstruction in RELION (*Doctoral thesis*). https://doi.org/10.17863/CAM.31456

Hebert-Chatelain, E., Jose, C., Gutierrez Cortes, N., Dupuy, J. W., Rocher, C., Dachary-Prigent, J., & Letellier, T. (2012). Preservation of NADH ubiquinone-oxidoreductase activity by Src kinase-mediated phosphorylation of NDUFB10. *Biochimica et biophysicaacta,* 1817(5), 718–725. https://doi.org/10.1016/j.bbabio.2012.01.014

Heide, H., Bleier, L., Steger, M., Ackermann, J., Dröse, S., Schwamb, B., Zörnig, M., Reichert, A. S., Koch, I., Wittig, I., & Brandt, U. (2012). Complexome profiling identifies TMEM126B as a component of the mitochondrial complex I assembly complex. *Cell metabolism*, 16(4), 538–549. https://doi.org/10.1016/j.cmet.2012.08.009

Hell, K., Neupert, W., & Stuart, R. A. (2001). Oxa1p acts as a general membrane insertion machinery for proteins encoded by mitochondrial DNA. *The EMBO journal,* 20(6), 1281–1288. https://doi.org/10.1093/emboj/20.6.1281

Henderson, R., & Unwin, P. N. (1975). Three-dimensional model of purple membrane obtained by electron microscopy. *Nature*, 257(5521), 28–32. https://doi.org/10.1038/257028a0

Henderson, R., Baldwin, J. M., Ceska, T. A., Zemlin, F., Beckmann, E., & Downing, K. H. (1990). Model for the structure of bacteriorhodopsin based on high-resolution electron cryo-microscopy. *Journal of molecular biology*, 213(4), 899–929. https://doi.org/10.1016/S0022-2836(05)80271-2

Henderson, R., Sali, A., Baker, M. L., Carragher, B., Devkota, B., Downing, K. H., Egelman, E. H., Feng, Z., Frank, J., Grigorieff, N., Jiang, W., Ludtke, S. J., Medalia, O., Penczek,

P. A., Rosenthal, P. B., Rossmann, M. G., Schmid, M. F., Schröder, G. F., Steven, A. C., Stokes, D. L., … Lawson, C. L. (2012). Outcome of the first electron microscopy validation task force meeting. *Structure (London, England : 1993)*, 20(2), 205–214. https://doi.org/10.1016/j.str.2011.12.014

Hinchliffe, P., & Sazanov, L. A. (2005). Biochemistry: Organization of iron-sulfur clusters in respiratory complex I. *Science*, 309(5735), 771–774. https://doi.org/10.1126/science.1113988

Hinkle, P. C., Butow, R. A., Racker, E., & Chance, B. (1967). Partial resolution of the enzymes catalyzing oxidative phosphorylation. XV. Reverse electron transfer in the flavin-cytochrome beta region of the respiratory chain of beef heart submitochondrial particles. *The Journal of biological chemistry*, 242(22), 5169–5173.

Hirano, M., Emmanuele, V., & Quinzii, C. M. (2018). Emerging therapies for mitochondrial diseases. *Essays in biochemistry*, 62(3), 467–481. https://doi.org/10.1042/EBC20170114

Hirst J. (2010). Towards the molecular mechanism of respiratory complex I. *The Biochemical journal,* 425(2), 327–339. https://doi.org/10.1042/BJ20091382

Hirst J. (2011). Why does mitochondrial complex I have so many subunits? *The Biochemical journal*, 437(2), e1–e3. https://doi.org/10.1042/BJ20110918

Hirst J. (2018). Open questions: respiratory chain supercomplexes-why are they there and what do they do?. *BMC biology*, 16(1), 111. https://doi.org/10.1186/s12915-018-0577-5

Hirst, J., King, M. S., & Pryde, K. R. (2008). The production of reactive oxygen species by complex I. *Biochemical Society transactions*, 36(Pt 5), 976–980. https://doi.org/10.1042/BST0360976

Hofhaus, G., Weiss, H., & Leonard, K. (1991). Electron microscopic analysis of the peripheral and membrane parts of mitochondrial NADH dehydrogenase (complex I). J*ournal of molecular biology*, 221(3),1027–1043. https://doi.org/10.1016/0022-2836(91)80190-6

Horvath, S. E., & Daum, G. (2013). Lipids of mitochondria. *Progress in Lipid Research,* 52(4), 590–614. https://doi.org/10.1016/j.plipres.2013.07.002

Howell, N., Bindoff, L. A., McCullough, D. A., Kubacka, I., Poulton, J., Mackey, D., Taylor, L., & Turnbull, D. M. (1991). Leber hereditary optic neuropathy: identificationof the same mitochondrial ND1 mutation in six pedigrees. *American journal of human genetics*, 49(5), 939–950.

Hu, H., Nan, J., Sun, Y., Zhu, D., Xiao, C., Wang, Y., Zhu, L., Wu, Y., Zhao, J., Wu, R., Chen, J., Yu, H., Hu, X., Zhu, W., & Wang, J. (2017). Electron leak from NDUFA13 within mitochondrial complex I attenuates ischemia-reperfusion injury via dimerized STAT3. *Proceedings of the National Academy of Sciences of the United States of America,* 114(45), 11908–11913. https://doi.org/10.1073/pnas.1704723114

Huiskonen, J. T., Overby, A. K., Weber, F., & Grünewald, K. (2009). Electron cryo-microscopy and single-particle averaging of Rift Valley fever virus: evidence for GN-GC glycoprotein heterodimers. *Journal of virology,* 83(8), 3762–3769. https://doi.org/10.1128/JVI.02483-08

Hunte, C., Zickermann, V., & Brandt, U. (2010). Functional modules and structural basis of conformational coupling in mitochondrial complex I. *Science* (New York, N.Y.), 329(5990), 448–451. https://doi.org/10.1126/science.1191046

Huxley, H. E., & Zubay, G (1961). Preferential staining of nucleic acid-containing structures for electron microscopy. *The Journal of biophysical and biochemical cytology,* 11(2), 273–296. https://doi.org/10.1083/jcb.11.2.273

Idelchik, M., Begley, U., Begley, T. J., & Melendez, J. A. (2017). Mitochondrial ROScontrol of cancer. *Seminars in cancer biology*, 47, 57–66. https://doi.org/10.1016/j.semcancer.2017.04.005

Igamberdiev, A. U., & Kleczkowski, L. A. (2015). Optimization of ATP synthase function in mitochondria and chloroplasts via the adenylate kinase equilibrium. *Frontiers in plant science*, 6, 10. https://doi.org/10.3389/fpls.2015.00010

Ingraham, C. A., Burwell, L. S., Skalska, J., Brookes, P. S., Howell, R. L., Sheu, S. S., & Pinkert, C. A. (2009). NDUFS4: creation of a mouse model mimicking a Complex I disorder. *Mitochondrion,* 9(3), 204–210. https://doi.org/10.1016/j.mito.2009.02.001

Irwin, M. H., Parameshwaran, K., & Pinkert, C. A. (2013). Mouse models of mitochondrial complex I dysfunction. *The international journal of biochemistry & cell biology*, 45(1), 34–40. https://doi.org/10.1016/j.biocel.2012.08.009

Irwin, M. J., Gupta, R., Gao, X. Z., Cahill, K. B., Chu, F., & Cote, R. H. (2019). The molecular architecture of photoreceptor phosphodiesterase 6 (PDE6) with activated G protein elucidates the mechanism of visual excitation. *The Journal of biological chemistry*, 294(51), 19486–19497. https://doi.org/10.1074/jbc.RA119.011002

Ishikawa, K., Imanishi, H., Takenaga, K., & Hayashi, J. (2012). Regulation of metastasis; mitochondrial DNA mutations have appeared on stage. J*ournal of bioenergetics and biomembranes,* 44(6), 639–644. https://doi.org/10.1007/s10863-012-9468-6

Iwata, S., Lee, J. W., Okada, K., Lee, J. K., Iwata, M., Rasmussen, B., Link, T. A., Ramaswamy, S., & Jap, B. K. (1998). Complete structure of the 11-subunit bovine mitochondrial cytochrome bc1 complex. *Science* (New York, N.Y.), 281(5373), 64–71. https://doi.org/10.1126/science.281.5373.64

Jain, I. H., Zazzeron, L., Goli, R., Alexa, K., Schatzman-Bone, S., Dhillon, H., Goldberger, O., Peng, J., Shalem, O., Sanjana, N. E., Zhang, F., Goessling, W., Zapol, W. M., &

Mootha, V. K. (2016). Hypoxia as a therapy for mitochondrial disease. *Science* (New York, N.Y.), 352(6281), 54–61. https://doi.org/10.1126/science.aad9642

Jain, T., Sheehan, P., Crum, J., Carragher, B., & Potter, C. S. (2012). Spotiton: a prototype for an integrated inkjet dispense and vitrification system for cryo-TEM. J*ournal of structural biology,* 179(1), 68–75. https://doi.org/10.1016/j.jsb.2012.04.020

Janssen, M., Koene, S., de Laat, P., Hemelaar, P., Pickkers, P., Spaans, E., Beukema, R., Beyrath, J., Groothuis, J., Verhaak, C., & Smeitink, J. (2019). The KHENERGY Study: Safety and Efficacy of KH176 in Mitochondrial m.3243A>G Spectrum Disorders. *Clinical pharmacology and therapeutics*, 105(1), 101–111. https://doi.org/10.1002/cpt.1197

Jimenez-Blasco, D., Busquets-Garcia, A., Hebert-Chatelain, E., Serrat, R., Vicente-Gutierrez, C., Ioannidou, C., Gómez-Sotres, P., Lopez-Fabuel, I., Resch-Beusher, M., Resel, E., Arnouil, D., Saraswat, D., Varilh, M., Cannich, A., Julio-Kalajzic, F., Bonilla-Del Río, I., Almeida, A., Puente, N., Achicallende, S., Lopez-Rodriguez, M. L., … Marsicano, G. (2020). Glucose metabolism links astroglial mitochondria to cannabinoid effects. *Nature,* 583(7817), 603–608. https://doi.org/10.1038/s41586-020-2470-y

Jonckheere, A. I., Smeitink, J. A., & Rodenburg, R. J. (2012). Mitochondrial ATP synthase: architecture, function and pathology. *Journal of inherited metabolic disease*, 35(2),211–225. https://doi.org/10.1007/s10545-011-9382-9

Jones, A. J., & Hirst, J. (2013). A spectrophotometric coupled enzyme assay to measure the activity of succinate dehydrogenase. *Analytical biochemistry*, 442(1), 19–23. https://doi.org/10.1016/j.ab.2013.07.018

Jones, A. J., Blaza, J. N., Varghese, F., & Hirst, J. (2017). Respiratory Complex I in Bos taurus and Paracoccus denitrificans Pumps Four Protons across the Membrane for Every NADH Oxidized. *The Journal of biological chemistry,* 292(12), 4987–4995. https://doi.org/10.1074/jbc.M116.771899

Jun, A. S., Brown, M. D., & Wallace, D. C. (1994). A mitochondrial DNA mutation at nucleotide pair 14459 of the NADH dehydrogenase subunit 6 gene associated with maternally inherited Leber hereditary optic neuropathy and dystonia. *Proceedings of the National Academy of Sciences*, 91(13), 6206–6210. https://doi.org/10.1073/pnas.91.13.6206

Kadenbach, B., & Hüttemann, M. (2015). The subunit composition and function of mammalian cytochrome c oxidase. *Mitochondrion,* 24, 64–76. https://doi.org/10.1016/j.mito.2015.07.002

Kahlhöfer, F., Kmita, K., Wittig, I., Zwicker, K., & Zickermann, V. (2017). Accessorysubunit NUYM (NDUFS4) is required for stability of the electron input module and activity of mitochondrial complex I. *Biochimica et Biophysica Acta (BBA) - Bioenergetics,* 1858(2), 175–181. https://doi.org/10.1016/j.bbabio.2016.11.010

Kampjut, D., & Sazanov, L. A. (2020). The coupling mechanism of mammalian respiratory complex I. *Science*, 370(6516), eabc4209. https://doi.org/10.1126/science.abc4209

Kane D. A. (2014). Lactate oxidation at the mitochondria: a lactate-malate-aspartate shuttle at work. *Frontiers in neuroscience*, 8, 366. https://doi.org/10.3389/fnins.2014.00366

Kao, M. C., Di Bernardo, S., Nakamaru-Ogiso, E., Miyoshi, H., Matsuno-Yagi, A., & Yagi, T. (2005). Characterization of the membrane domain subimit NuoJ (ND6) of theNADH-quinone oxidoreductase from Escherichia coli by chromosomal DNA manipulation. *Biochemistry,* 44(9), 3562–3571. https://doi.org/10.1021/bi0476477

Karamanlidis, G., Lee, C. F., Garcia-Menendez, L., Kolwicz, S. C., Jr, Suthammarak, W., Gong, G., Sedensky, M. M., Morgan, P. G., Wang, W., & Tian, R. (2013). Mitochondrial complex I deficiency increases protein acetylation and accelerates heart failure. *Cell metabolism,* 18(2), 239–250. https://doi.org/10.1016/j.cmet.2013.07.002

Kasinath, V., Faini, M., Poepsel, S., Reif, D., Feng, X. A., Stjepanovic, G., Aebersold, R., & Nogales, E. (2018). Structures of human PRC2 with its cofactors AEBP2 and JARID2. *Science*, 359(6378), 940–944. https://doi.org/10.1126/science.aar5700

Kastner, B., Fischer, N., Golas, M. M., Sander, B., Dube, P., Boehringer, D., Hartmuth, K., Deckert, J., Hauer, F., Wolf, E., Uchtenhagen, H., Urlaub, H., Herzog, F., Peters, J. M., Poerschke, D., Lührmann, R., & Stark, H. (2008). GraFix: sample preparation for single-particle electron cryomicroscopy. *Nature methods*, 5(1), 53–55. https://doi.org/10.1038/nmeth1139

Ke, B. X., Pepe, S., Grubb, D. R., Komen, J. C., Laskowski, A., Rodda, F. A., Hardman, B. M., Pitt, J. J., Ryan, M. T., Lazarou, M., Koleff, J., Cheung, M. M., Smolich, J. J., & Thorburn, D. R. (2012). Tissue-specific splicing of an Ndufs6 gene-trap insertion generates a mitochondrial complex I deficiency-specific cardiomyopathy. *Proceedings of the National Academy of Sciences of the United States of America,* 109(16), 6165–6170. https://doi.org/10.1073/pnas.1113987109

Kelley, L. A., Mezulis, S., Yates, C. M., Wass, M. N., & Sternberg, M. J. (2015). The Phyre2 web portal for protein modeling, prediction and analysis. *Nature protocols,* 10(6), 845–858. https://doi.org/10.1038/nprot.2015.053

Kim, L. Y., Rice, W. J., Eng, E. T., Kopylov, M., Cheng, A., Raczkowski, A. M., Jordan, K. D., Bobe, D., Potter, C. S., & Carragher, B. (2018). Benchmarking cryo-EM Single Particle Analysis Workflow. *Frontiers in molecular biosciences,* 5, 50. https://doi.org/10.3389/fmolb.2018.00050

Kirby, D. M., Crawford, M., Cleary, M. A., Dahl, H. H., Dennett, X., & Thorburn, D.R. (1999). Respiratory chain complex I deficiency: an underdiagnosed energy generation disorder. *Neurology*, 52(6), 1255–1264. https://doi.org/10.1212/wnl.52.6.1255

Kirby, D. M., Salemi, R., Sugiana, C., Ohtake, A., Parry, L., Bell, K. M., Kirk, E. P.,Boneh, A., Taylor, R. W., Dahl, H. H., Ryan, M. T., & Thorburn, D. R. (2004). NDUFS6

mutations are a novel cause of lethal neonatal mitochondrial complex I deficiency. *The Journal of clinical investigation,* 114(6), 837–845. https://doi.org/10.1172/JCI20683

Kirches, E. (2011). LHON: Mitochondrial Mutations and More. *Current Genomics*, 12(1), 44–54. https://doi.org/10.2174/138920211794520150

Kispal, G., Csere, P., Prohl, C., & Lill, R. (1999). The mitochondrial proteins Atm1p and Nfs1p are essential for biogenesis of cytosolic Fe/S proteins. *The EMBO journal*, 18(14), 3981–3989. https://doi.org/10.1093/emboj/18.14.3981

Klein, J. A., Longo-Guess, C. M., Rossmann, M. P., Seburn, K. L., Hurd, R. E., Frankel, W. N., Bronson, R. T., & Ackerman, S. L. (2002). The harlequin mouse mutation downregulates apoptosis-inducing factor. *Nature,* 419(6905), 367–374. https://doi.org/10.1038/nature01034

Klopstock, T., Metz, G., Yu-Wai-Man, P., Büchner, B., Gallenmüller, C., Bailie, M., Nwali, N., Griffiths, P. G., von Livonius, B., Reznicek, L., Rouleau, J., Coppard, N., Meier, T., & Chinnery, P. F. (2013). Persistence of the treatment effect of idebenone in Leber's hereditary optic neuropathy. *Brain: a journal of neurology*, 136(Pt 2), e230. https://doi.org/10.1093/brain/aws279

Klug, A., & Finch, J. T. (1965). Structure of viruses of the papilloma-polyoma type: I. human wart. *Journal of molecular biology*, 11, 403–423. https://doi.org/10.1016/s0022-2836(65)800663

Kmita, K., & Zickermann, V. (2013). Accessory subunits of mitochondrial complex I. *Biochemical Society transactions*, 41(5), 1272–1279. https://doi.org/10.1042/BST20130091

Kmita, K., Wirth, C., Warnau, J., Guerrero-Castillo, S., Hunte, C., Hummer, G., Kaila,V. R., Zwicker, K., Brandt, U., & Zickermann, V. (2015). Accessory NUMM (NDUFS6) subunit harbors a Zn-binding site and is essential for biogenesis of mitochondrial complex

I. *Proceedings of the National Academy of Sciences of the United States of America,* 112(18), 5685–5690. https://doi.org/10.1073/pnas.1424353112

Koene, S., Rodenburg, R. J., van der Knaap, M. S., Willemsen, M. A., Sperl, W., Laugel, V., Ostergaard, E., Tarnopolsky, M., Martin, M. A., Nesbitt, V., Fletcher, J., Edvardson, S., Procaccio, V., Slama, A., van den Heuvel, L. P., & Smeitink, J. A. (2012). Natural disease course and genotype-phenotype correlations in Complex I deficiency caused by nuclear gene defects: what we learned from 130 cases. *Journal of inherited metabolic disease,* 35(5), 737–747. https://doi.org/10.1007/s10545-012-9492-z

Konstantinov A. A. (2012). Cytochrome c oxidase: Intermediates of the catalytic cycle and their energy-coupled interconversion. *FEBS letters*, 586(5), 630–639. https://doi.org/10.1016/j.febslet.2011.08.037

Kotlyar, A. B., & Vinogradov, A. D. (1990). Slow active/inactive transition of the mitochondrial NADH-ubiquinone reductase. *Biochimica et biophysica acta*, 1019(2), 151–158. https://doi.org/10.1016/0005-2728(90)90137-s

Kotlyar, A. B., Albracht, S. P., & van Spanning, R. J. (1998). Comparison of energization of complex I in membrane particles from Paracoccus denitrificans and bovine heart mitochondria. *Biochimica et biophysica acta*, 1365(1-2), 53–59. https://doi.org/10.1016/s0005-2728(98)00042-5

Kotlyar, A. B., Sled, V. D., & Vinogradov, A. D. (1992). Effect of Ca^{2+} ions on theslow active/inactive transition of the mitochondrial NADH-ubiquinone reductase. *Biochimica et biophysica acta*, 1098(2), 144–150. https://doi.org/10.1016/s0005-2728(05)80329-9

Kruse, S. E., Watt, W. C., Marcinek, D. J., Kapur, R. P., Schenkman, K. A., & Palmiter, R. D.(2008). Mice with mitochondrial complex I deficiency develop a fatal encephalomyopathy. *Cell metabolism*, 7(4), 312–320. https://doi.org/10.1016/j.cmet.2008.02.004

Kühlbrandt, W. (2015). Structure and function of mitochondrial membrane protein complexes. *BMC Biology,* 13(1), 1–11. https://doi.org/10.1186/s12915-015-0201-x

Kühn, K., Obata, T., Feher, K., Bock, R., Fernie, A. R., & Meyer, E. H. (2015). Complete Mitochondrial Complex I Deficiency Induces an Up-Regulation of Respiratory Fluxes That Is Abolished by Traces of Functional Complex I. *Plant Physiology,* 168(4), 1537–1549. https://doi.org/10.1104/pp.15.00589

Kussmaul, L., & Hirst, J. (2006). The mechanism of superoxide production by NADH:ubiquinone oxidoreductase (complex I) from bovine heart mitochondria. *Proceedings of the National Academy of Sciences of the United States of America,* 103(20), 7607–7612. https://doi.org/10.1073/pnas.0510977103

Lake, N. J., Compton, A. G., Rahman, S., & Thorburn, D. R. (2016). Leigh syndrome: One disorder, more than 75 monogenic causes. *Annals of neurology,* 79(2), 190–203. https://doi.org/10.1002/ana.24551

Lambert, R. (2007). Breeding Strategies for Maintaining Colonies of Laboratory Mice. *The Jackson Laboratory*.

Lane, N., & Martin, W. (2010). The energetics of genome complexity. *Nature,* 467(7318), 929–934. https://doi.org/10.1038/nature09486

Lazarou, M., McKenzie, M., Ohtake, A., Thorburn, D. R., & Ryan, M. T. (2007). Analysis of the assembly profiles for mitochondrial- and nuclear-DNA-encoded subunits into complex I. *Molecular and cellular biology*, 27(12), 4228–4237. https://doi.org/10.1128/MCB.00074-07

Leber, T. (1871). Ueber hereditäre und congenital-angelegte Sehnervenleiden. *Albrecht von Graefes Archiv Für Ophthalmologie*, 17(2), 249–291. https://doi.org/10.1007/BF01694557

Lee, C. F., Caudal, A., Abell, L., Nagana Gowda, G. A., & Tian, R. (2019). Targeting NAD^+ Metabolism as Interventions for Mitochondrial Disease. *Scientific reports*, 9(1), 3073. https://doi.org/10.1038/s41598-019-39419-4

Leigh D. (1951). Subacute necrotizing encephalomyelopathy in an infant. J*ournal of neurology, neurosurgery, and psychiatry*, 14(3), 216–221. https://doi.org/10.1136/jnnp.14.3.216

Leong, D. W., Komen, J. C., Hewitt, C. A., Arnaud, E., McKenzie, M., Phipson, B., Bahlo, M., Laskowski, A., Kinkel, S. A., Davey, G. M., Heath, W. R., Voss, A. K., Zahedi, R. P., Pitt, J. J., Chrast, R., Sickmann, A., Ryan, M. T., Smyth, G. K., Thorburn, D. R., & Scott, H. S. (2012). Proteomic and metabolomic analyses of mitochondrial complex I-deficient mouse model generated by spontaneous B2 short interspersed nuclear element (SINE) insertion into NADH dehydrogenase (ubiquinone) Fe-S protein 4 (Ndufs4) gene. *The Journal of biological chemistry*, 287(24), 20652–20663. https://doi.org/10.1074/jbc.M111.327601

Letts, J. A., Fiedorczuk, K., Degliesposti, G., Skehel, M., & Sazanov, L. A. (2019). Structures of Respiratory Supercomplex $I+III_2$ Reveal Functional and Conformational Crosstalk. *Molecular cell,* 75(6), 1131–1146.e6. https://doi.org/10.1016/j.molcel.2019.07.022

Lin, C. S., Sharpley, M. S., Fan, W., Waymire, K. G., Sadun, A. A., Carelli, V., Ross-Cisneros, F. N., Baciu, P., Sung, E., McManus, M. J., Pan, B. X., Gil, D. W., Macgregor, G. R., & Wallace, D. C. (2012). Mouse mtDNA mutant model of Leber hereditary optic neuropathy. *Proceedings of the National Academy of Sciences of the United States of America,* 109(49), 20065–20070. https://doi.org/10.1073/pnas.1217113109

Liu, X., Farnung, L., Wigge, C., & Cramer, P. (2018). Cryo-EM structure of a mammalian RNA polymerase II elongation complex inhibited by α-amanitin. T*he Journal of biological chemistry,* 293(19), 7189–7194. https://doi.org/10.1074/jbc.RA118.002545

Llopis, J., McCaffery, J. M., Miyawaki, A., Farquhar, M. G., & Tsien, R. Y. (1998). Measurement of cytosolic, mitochondrial, and Golgi pH in single living cells with green fluorescent proteins. *Proceedings of the National Academy of Sciences of the United States of America,* 95(12), 6803–6808. https://doi.org/10.1073/pnas.95.12.6803

Loskovich, M. V., Grivennikova, V. G., Cecchini, G., & Vinogradov, A. D. (2005). Inhibitory effect of palmitate on the mitochondrial NADH:ubiquinone oxidoreductase (complex I) as related to the active-de-active enzyme transition. *The Biochemical journal,* 387(Pt 3), 677–683. https://doi.org/10.1042/BJ20041703

Louvet, A., & Mathurin, P. (2015). Alcoholic liver disease: mechanisms of injury and targeted treatment. *Nature reviews.* Gastroenterology & hepatology, 12(4), 231–242. https://doi.org/10.1038/nrgastro.2015.35

MacPherson, L., & Tokatlidis, K. (2017). Protein trafficking in the mitochondrial intermembrane space: Mechanisms and links to human disease. *Biochemical Journal,* 474(15), 2533–2545. https://doi.org/10.1042/BCJ20160627

Maklashina, E., Kotlyar, A. B., & Cecchini, G. (2003). Active/de-active transition of respiratory complex I in bacteria, fungi, and animals. *Biochimica et biophysica acta,* 1606(1-3), 95–103. https://doi.org/10.1016/s0005-2728(03)00087-2

Maklashina, E., Sher, Y., Zhou, H. Z., Gray, M. O., Karliner, J. S., & Cecchini, G. (2002). Effect of anoxia/reperfusion on the reversible active/de-active transition of NADH-ubiquinone oxidoreductase (complex I) in rat heart. *Biochimica et biophysica acta,* 1556(1), 6–12. https://doi.org/10.1016/s0005-2728(02)00280-3

Malfatti, E., Bugiani, M., Invernizzi, F., de Souza, C. F., Farina, L., Carrara, F., Lamantea, E., Antozzi, C., Confalonieri, P., Sanseverino, M. T., Giugliani, R., Uziel, G., & Zeviani, M. (2007). Novel mutations of ND genes in complex I deficiency associated with mitochondrial encephalopathy. *Brain: a journal of neurology,* 130(Pt 7), 1894–1904. https://doi.org/10.1093/brain/awm114

Man, P. Y. W., Turnbull, D. M., & Chinnery, P. F. (2002). Leber hereditary optic neuropathy. *Journal of Medical Genetics,* 39(3), 162–169. https://doi.org/10.1136/jmg.39.3.162

Marino P. (2019). Studies on assembly and genetic variation in mitochondrial respiratory complex I *(Doctoral thesis*). https://doi.org/10.17863/CAM.36634

Martin W. F. (2017). Physiology, anaerobes, and the origin of mitosing cells 50 years on. *Journal of theoretical biology*, 434, 2–10. https://doi.org/10.1016/j.jtbi.2017.01.004

Martin, J. L., Costa, A., Gruszczyk, A. V., Beach, T. E., Allen, F. M., Prag, H. A., Hinchy, E. C., Mahbubani, K., Hamed, M., Tronci, L., Nikitopoulou, E., James, A. M., Krieg, T., Robinson, A. J., Huang, M. M., Caldwell, S. T., Logan, A., Pala, L., Hartley, R. C., Frezza, C., … Murphy, M. P. (2019). Succinate accumulation drives ischaemia-reperfusion injury during organ transplantation. *Nature metabolism*, 1, 966–974. https://doi.org/10.1038/s42255-019-0115-y

Martinou, J. C., & Youle, R. J. (2011). Mitochondria in apoptosis: Bcl-2 family members and mitochondrial dynamics. *Developmental cell,* 21(1), 92–101. https://doi.org/10.1016/j.devcel.2011.06.017

Marton, L. (1934). Electron Microscopy of Biological Objects. *Nature*, 133(3372), 911-911. https://doi.org/10.1038/133911b0

Mattson, G., Conklin, E., Desai, S., Nielander, G., Savage, M. D., & Morgensen, S. (1993). A practical approach to crosslinking. *Molecular biology reports*, 17(3), 167–183. https://doi.org/10.1007/BF00986726

Mckenzie, M., & Ryan, M. T. (2010). Assembly factors of human mitochondrial complex I and their defects in disease. *IUBMB life*, 62(7), 497–502. https://doi.org/10.1002/iub.335

McManus, M. J., Picard, M., Chen, H. W., De Haas, H. J., Potluri, P., Leipzig, J., Towheed, A., Angelin, A., Sengupta, P., Morrow, R. M., Kauffman, B. A., Vermulst, M., Narula, J.,

& Wallace, D. C. (2019). Mitochondrial DNA Variation Dictates Expressivity and Progression of Nuclear DNA Mutations Causing Cardiomyopathy. *Cell metabolism,*29(1), 78–90.e5. https://doi.org/10.1016/j.cmet.2018.08.002

Meyerson, J. R., Rao, P., Kumar, J., Chittori, S., Banerjee, S., Pierson, J., Mayer, M. L., & Subramaniam, S. (2014). Self-assembled monolayers improve protein distribution on holey carbon cryo-EM supports. *Scientific reports,* 4, 7084. https://doi.org/10.1038/srep07084

Migneault, I., Dartiguenave, C., Bertrand, M. J., & Waldron, K. C. (2004). Glutaraldehyde: behavior in aqueous solution, reaction with proteins, and application to enzyme crosslinking. *BioTechniques,* 37(5), 790–802. https://doi.org/10.2144/04375RV01

Milenkovic, D., Blaza, J. N., Larsson, N. G., & Hirst, J. (2017). The Enigma of the Respiratory Chain Supercomplex. *Cell metabolism*, 25(4), 765–776. https://doi.org/10.1016/j.cmet.2017.03.009

Millett, F., Havens, J., Rajagukguk, S., & Durham, B. (2013). Design and use of photoactive ruthenium complexes to study electron transfer within cytochrome bc1 and from cytochrome bc1 to cytochrome c. *Biochimica et biophysica acta*, 1827(11-12), 1309–1319. https://doi.org/10.1016/j.bbabio.2012.09.002

Minakami, S., Schindler, F.J., & Estabrook, R.W. (1964). Hydrogen transfer between reduced diphosphopyridine nucleotide dehydrogenase and the respiratory chain. II. An initial lag in the oxidation of reduced diphosphopyridine nucleotide. *The Journal of biological chemistry*, 239, 2049–2054

Mindell, J. A., & Grigorieff, N. (2003). Accurate determination of local defocus and specimen tilt in electron microscopy. *Journal of structural biology,* 142(3), 334–347. https://doi.org/10.1016/s1047-8477(03)00069-8

Miron, T., & Wilchek, M. (1982). A spectrophotometric assay for soluble and immobilized N-hydroxysuccinimide esters. *Analytical biochemistry,* 126(2), 433–435. https://doi.org/10.1016/0003-2697(82)90540-1

Morais, V. A., Haddad, D., Craessaerts, K., De Bock, P. J., Swerts, J., Vilain, S., Aerts, L., Overbergh, L., Grünewald, A., Seibler, P., Klein, C., Gevaert, K., Verstreken, P., & De Strooper, B. (2014). PINK1 loss-of-function mutations affect mitochondrial complex I activity via NdufA10 ubiquinone uncoupling. *Science* (New York, N.Y.), 344(6180), 203–207. https://doi.org/10.1126/science.1249161

Morello, G. M., Hultgren, J., Capas-Peneda, S., Wiltshire, M., Thomas, A., Wardle-Jones, H., Brajon, S., Gilbert, C., & Olsson, I. (2020). High laboratory mouse pre-weaning mortality associated with litter overlap, advanced damage, small and large litters. *PloS one*, 15(8), e0236290. https://doi.org/10.1371/journal.pone.0236290

Moreno-Lastres, D., Fontanesi, F., García-Consuegra, I., Martín, M. A., Arenas, J., Barrientos, A., & Ugalde, C. (2012). Mitochondrial complex I plays an essential role in human respirasome assembly. Cell metabolism, 15(3), 324–335. https://doi.org/10.1016/j.cmet.2012.01.015

Muramoto, K., Ohta, K., Shinzawa-Itoh, K., Kanda, K., Taniguchi, M., Nabekura, H., Yamashita, E., Tsukihara, T., & Yoshikawa, S. (2010). Bovine cytochrome c oxidase structures enable O2 reduction with minimization of reactive oxygens and provide a proton-pumping gate. *Proceedings of the National Academy of Sciences of the United States of America*, 107(17), 7740–7745. https://doi.org/10.1073/pnas.0910410107

Murphy M. P. (2009). How mitochondria produce reactive oxygen species. *The Biochemical journal*, 417(1), 1–13. https://doi.org/10.1042/BJ20081386

Myasnikov, A., Zheng, S., Bulkley, D., Cheng, Y., & Agard, D. (2018). K3 - A FirstLook at The New Direct Electron Detection Camera from Gatan Company. *Microscopy and Microanalysis,* 24(S1), 890–891. https://doi.org/10.1017/s1431927618004944

Nunnari, J., & Suomalainen, A. (2012). Mitochondria: In Sickness and in Health. *Cell,*148(6), 1145–1159. https://doi.org/10.1016/j.cell.2012.02.035

Nicholson, D. W., Hergersberg, C., & Neupert, W. (1988). Role of cytochrome c heme lyase in the import of cytochrome c into mitochondria. *The Journal of biological chemistry*, *263*(35), 19034–19042.

Ng, Y. S., & Turnbull, D. M. (2016). Mitochondrial disease: genetics and management. *Journal of neurology*, *263*(1), 179–191. https://doi.org/10.1007/s00415-015-7884-3

Ogilvie, I., Kennaway, N. G., & Shoubridge, E. A. (2005). A molecular chaperone formitochondrial complex I assembly is mutated in a progressive encephalopathy. *The Journal of clinical investigation,* 115(10), 2784–2792. https://doi.org/10.1172/JCI26020

Ohnishi, T., & Salerno, J. C. (2005). Conformation-driven and semiquinone-gated proton-pump mechanism in the NADH-ubiquinone oxidoreductase (complex I). *FEBS letters,* 579(21), 4555–4561. https://doi.org/10.1016/j.febslet.2005.06.086

Onur, S., Niklowitz, P., Fischer, A., Metges, C. C., Grune, T., Menke, T., Rimbach, G., & Döring, F. (2014). A comparative study into alterations of coenzyme Q redox status in ageing pigs, mice, and worms. *BioFactors* (Oxford, England), 40(3), 346–354. https://doi.org/10.1002/biof.1160

Ortigoza-Escobar, J. D., Oyarzabal, A., Montero, R., Artuch, R., Jou, C., Jiménez, C., Gort, L., Briones, P., Muchart, J., López-Gallardo, E., Emperador, S., Pesini, E. R., Montoya, J., Pérez, B., Rodríguez-Pombo, P., & Pérez-Dueñas, B. (2016). *Ndufs4* relatedLeigh syndrome: A case report and review of the literature. *Mitochondrion*, 28, 73–78. https://doi.org/10.1016/j.mito.2016.04.001

Ott, M., Robertson, J. D., Gogvadze, V., Zhivotovsky, B., & Orrenius, S. (2002). Cytochrome *c* release from mitochondria proceeds by a two-step process. *Proceedings of the National*

Academy of Sciences of the United States of America, 99(3), 1259–1263. https://doi.org/10.1073/pnas.241655498

Pagniez-Mammeri, H., Loublier, S., Legrand, A., Bénit, P., Rustin, P., & Slama, A. (2012). Mitochondrial complex I deficiency of nuclear origin I. Structural genes. *Molecular genetics and metabolism,* 105(2), 163–172. https://doi.org/10.1016/j.ymgme.2011.11.188

Palade G. E. (1952). The fine structure of mitochondria. *The Anatomical record,* 114(3),427–451. https://doi.org/10.1002/ar.1091140304

Palmisano, G., Sardanelli, A. M., Signorile, A., Papa, S., & Larsen, M. R. (2007). The phosphorylation pattern of bovine heart complex I subunits. *Proteomics,* 7(10), 1575–1583. https://doi.org/10.1002/pmic.200600801

Palovcak, E., Wang, F., Zheng, S. Q., Yu, Z., Li, S., Betegon, M., Bulkley, D., Agard, D. A., & Cheng, Y. (2018). A simple and robust procedure for preparing graphene-oxide cryo-EM grids. *Journal of structural biology,* 204(1), 80–84. https://doi.org/10.1016/j.jsb.2018.07.007

Pantelic, R. S., Meyer, J. C., Kaiser, U., Baumeister, W., & Plitzko, J. M. (2010). Graphene oxide: a substrate for optimizing preparations of frozen-hydrated samples. *Journal of structural biology,* 170(1), 152–156. https://doi.org/10.1016/j.jsb.2009.12.020

Papa S. (1996). Mitochondrial oxidative phosphorylation changes in the life span. Molecular aspects and physiopathological implications. *Biochimica et biophysica acta,* 1276(2), 87–105. https://doi.org/10.1016/0005-2728(96)00077-1

Parey, K., Brandt, U., Xie, H., Mills, D. J., Siegmund, K., Vonck, J., Kühlbrandt, W.,& Zickermann, V. (2018). Cryo-EM structure of respiratory complex I at work. *eLife,* 7, e39213. https://doi.org/10.7554/eLife.39213

Parey, K., Haapanen, O., Sharma, V., Köfeler, H., Züllig, T., Prinz, S., Siegmund, K., Wittig, I., Mills, D. J., Vonck, J., Kühlbrandt, W., & Zickermann, V. (2019). High-resolution cryo-EM structures of respiratory complex I: Mechanism, assembly, and disease. *Science advances*, 5(12), eaax9484. https://doi.org/10.1126/sciadv.aax9484

Parvate, A. D., Vago, F., Hasan, S. S., Lee, J., Williams, E. P., Lanman, J., & Jonsson, C. B. (2020). A new inactivation method to facilitate cryo-EM of enveloped, RNAviruses requiring high containment: A case study using Venezuelan Equine EncephalitisVirus (VEEV). *Journal of virological methods*, 277, 113792. https://doi.org/10.1016/j.jviromet.2019.113792

Parvate, A., Sengupta, R., Williams, E. P., Xue, Y., Chu, Y. K., Stahelin, R. V., & Jonsson, C. B. (2020). Cryofixation of Inactivated Hantavirus-Infected Cells as a Method for Obtaining High-Quality Ultrastructural Preservation for Electron Microscopic Studies. *Frontiers in cellular and infection microbiology*, 10, 580339. https://doi.org/10.3389/fcimb.2020.580339

Passmore, L. A., & Russo, C. J. (2016). Specimen Preparation for High-Resolution Cryo-EM. *Methods in enzymology,* 579, 51–86. https://doi.org/10.1016/bs.mie.2016.04.011

Pätsi, J., Kervinen, M., Finel, M., & Hassinen, I. E. (2008). Leber hereditary optic neuropathy mutations in the ND6 subunit of mitochondrial complex I affect ubiquinone reduction kinetics in a bacterial model of the enzyme. *The Biochemical Journal,* 409(1),129–137. https://doi.org/10.1042/BJ20070866

Paumard, P., Vaillier, J., Coulary, B., Schaeffer, J., Soubannier, V., Mueller, D. M., Brèthes, D., di Rago, J. P., & Velours, J. (2002). The ATP synthase is involved in generating mitochondrial cristae morphology. *The EMBO journal,* 21(3), 221–230. https://doi.org/10.1093/emboj/21.3.221

Pavlidis, I. V., Patila, M., Bornscheuer, U. T., Gournis, D., & Stamatis, H. (2014). Graphene-based nanobiocatalytic systems: recent advances and future prospects. *Trends in biotechnologyy,* 32(6), 312–320. https://doi.org/10.1016/j.tibtech.2014.04.004

Pell, V. R., Spiroski, A. M., Mulvey, J., Burger, N., Costa, A., Logan, A., Gruszczyk, A. V., Rosa, T., James, A. M., Frezza, C., Murphy, M. P., & Krieg, T. (2018). Ischemic preconditioning protects against cardiac ischemia reperfusion injury without affecting succinate accumulation or oxidation. J*ournal of molecular and cellular cardiology*, 123, 88–91. https://doi.org/10.1016/j.yjmcc.2018.08.010

Peoples, J. N., Saraf, A., Ghazal, N., Pham, T. T., & Kwong, J. Q. (2019). Mitochondrial dysfunction and oxidative stress in heart disease. *Experimental & molecular medicine*, 51(12), 1–13. https://doi.org/10.1038/s12276-019-0355-7

Peralta, S., Torraco, A., Wenz, T., Garcia, S., Diaz, F., & Moraes, C. T. (2014). Partial complex I deficiency due to the CNS conditional ablation of *Ndufa5* results in a mild chronic encephalopathy but no increase in oxidative damage. *Human molecular genetics,* 23(6), 1399–1412. https://doi.org/10.1093/hmg/ddt526

Pettersen, E. F., Goddard, T. D., Huang, C. C., Couch, G. S., Greenblatt, D. M., Meng, E. C., & Ferrin, T. E. (2004). UCSF Chimera--a visualization system for exploratory research and analysis. *Journal of computational chemistry*, 25(13), 1605–1612. https://doi.org/10.1002/jcc.20084

Pfanner, N., Warscheid, B., & Wiedemann, N. (2019). Mitochondrial proteins: from biogenesis to functional networks. Nature reviews. *Molecular cell biology*, 20(5), 267–284.https://doi.org/10.1038/s41580-018-0092-0

Pfeffer, S., Woellhaf, M. W., Herrmann, J. M., & Förster, F. (2015). Organization of the mitochondrial translation machinery studied *in situ* by cryoelectron tomography. *Nature communications*, 6, 6019. https://doi.org/10.1038/ncomms7019

Picard, M., McManus, M. J., Gray, J. D., Nasca, C., Moffat, C., Kopinski, P. K., Seifert, E. L., McEwen, B. S., & Wallace, D. C. (2015). Mitochondrial functions modulate neuroendocrine, metabolic, inflammatory, and transcriptional responses to acute psychological stress. *Proceedings of the National Academy of Sciences of the United States of America,* 112(48), E6614–E6623. https://doi.org/10.1073/pnas.1515733112

Poepsel, S., Kasinath, V., & Nogales, E. (2018). Cryo-EM structures of PRC2 simultaneously engaged with two functionally distinct nucleosomes. *Nature structural & molecular biology*, 25(2), 154–162. https://doi.org/10.1038/s41594-018-0023-y

Poincenot, L., Pearson, A. L., & Karanjia, R. (2020). Demographics of a Large International Population of Patients Affected by Leber's Hereditary Optic Neuropathy. *Ophthalmology*, 127 (5), 679–688. https://doi.org/10.1016/j.ophtha.2019.11.014

Priyadarsini, S., Mohanty, S., Mukherjee, S., Basu, S., & Mishra, M. (2018). Graphene and graphene oxide as nanomaterials for medicine and biology application. *Journal Of Nanostructure In Chemistry,* 8(2), 123-137. https://doi.org/10.1007/s40097-018-0265-6

Pryde, K. R., & Hirst, J. (2011). Superoxide is produced by the reduced flavin in mitochondrial complex I: A single, unified mechanism that applies during both forward and reverse electron transfer. *Journal of Biological Chemistry*, 286(20), 18056–18065. https://doi.org/10.1074/jbc.M110.186841

Punjani, A., Rubinstein, J. L., Fleet, D. J., & Brubaker, M. A. (2017). cryoSPARC: algorithms for rapid unsupervised cryo-EM structure determination. *Nature methods*, 14(3),290–296. https://doi.org/10.1038/nmeth.4169

Qi, X., Sun, L., Lewin, A. S., Hauswirth, W. W., & Guy, J. (2007). The mutant human ND4 subunit of complex I induces optic neuropathy in the mouse. *Investigative ophthalmology & visual science,* 48(1), 1–10. https://doi.org/10.1167/iovs.06-0789

Quintana, A., Kruse, S. E., Kapur, R. P., Sanz, E., & Palmiter, R. D. (2010). Complex I deficiency due to loss of Ndufs4 in the brain results in progressive encephalopathy resembling Leigh syndrome. *Proceedings of the National Academy of Sciences of the United States of America,* 107(24), 10996–11001. https://doi.org/10.1073/pnas.1006214107

Quintana, A., Zanella, S., Koch, H., Kruse, S. E., Lee, D., Ramirez, J. M., & Palmiter, R. D. (2012). Fatal breathing dysfunction in a mouse model of Leigh syndrome. *The Journal of clinical investigation,* 122(7), 2359–2368. https://doi.org/10.1172/JCI62923

Reynaud-Dulaurier, R., Benegiamo, G., Marrocco, E., Al-Tannir, R., Surace, E. M., Auwerx, J., & Decressac, M. (2020). Gene replacement therapy provides benefit in an adult mouse model of Leigh syndrome. *Brain: a journal of neurology,* 143(6), 1686–1696. https://doi.org/10.1093/brain/awaa105

Rice, W. J., Cheng, A., Noble, A. J., Eng, E. T., Kim, L. Y., Carragher, B., & Potter, C. S. (2018). Routine determination of ice thickness for cryo-EM grids. *Journal of structural biology,* 204(1), 38–44. https://doi.org/10.1016/j.jsb.2018.06.007

Richardson, D. R., Lane, D. J., Becker, E. M., Huang, M. L., Whitnall, M., Suryo Rahmanto, Y., Sheftel, A. D., & Ponka, P. (2010). Mitochondrial iron trafficking and the integration of iron metabolism between the mitochondrion and cytosol. *Proceedings of the National Academy of Sciences of the United States of America,* 107(24), 10775–10782. https://doi.org/10.1073/pnas.0912925107

Robb, E. L., Hall, A. R., Prime, T. A., Eaton, S., Szibor, M., Viscomi, C., James, A.M., & Murphy, M. P. (2018). Control of mitochondrial superoxide production by reverse electron transport at complex I. *The Journal of biological chemistry,* 293(25), 9869–9879. https://doi.org/10.1074/jbc.RA118.003647

Rodenburg R. J. (2016). Mitochondrial complex I-linked disease. *Biochimica et biophysica acta,* 1857(7), 938–945. https://doi.org/10.1016/j.bbabio.2016.02.012

Roessler, M. M., King, M. S., Robinson, A. J., Armstrong, F. A., Harmer, J., & Hirst, J. (2010). Direct assignment of EPR spectra to structurally defined iron-sulfur clusters in complex I by double electron-electron resonance. *Proceedings of the National Academy of Sciences of the United States of America,* 107(5), 1930–1935. https://doi.org/10.1073/pnas.0908050107

Roestenberg, P., Manjeri, G. R., Valsecchi, F., Smeitink, J. A., Willems, P. H., & Koopman, W. J. (2012). Pharmacological targeting of mitochondrial complex I deficiency:the cellular level and beyond. *Mitochondrion,* 12(1), 57–65. https://doi.org/10.1016/j.mito.2011.06.011

Rongvaux, A. (2018). Innate immunity and tolerance toward mitochondria. *Mitochondrion*, 41(October 2017), 14–20. https://doi.org/10.1016/j.mito.2017.10.007

Ross, M. F., Da Ros, T., Blaikie, F. H., Prime, T. A., Porteous, C. M., Severina, I. I., Skulachev, V. P., Kjaergaard, H. G., Smith, R. A., & Murphy, M. P. (2006). Accumulation of lipophilic dications by mitochondria and cells. *The Biochemical journal,* 400(1), 199–208. https://doi.org/10.1042/BJ20060919

Ross, M. F., Prime, T. A., Abakumova, I., James, A. M., Porteous, C. M., Smith, R. A., & Murphy, M. P. (2008). Rapid and extensive uptake and activation of hydrophobic triphenylphosphonium cations within cells. *The Biochemical journal,* 411(3), 633–645. https://doi.org/10.1042/BJ20080063

Rostovtseva, T. K., & Bezrukov, S. M. (2008). VDAC regulation: role of cytosolic proteins and mitochondrial lipids. *Journal of bioenergetics and biomembranes*, 40(3), 163–170. https://doi.org/10.1007/s10863-008-9145-y

Rozbeský, D., Rosůlek, M., Kukačka, Z., Chmelík, J., Man, P., & Novák, P. (2018). Impact of Chemical Cross-Linking on Protein Structure and Function. *Analytical chemistry,* 90(2), 1104–1113. https://doi.org/10.1021/acs.analchem.7b02863

Rubinstein J. L. (2007). Structural analysis of membrane protein complexes by single particle electron microscopy. *Methods* (San Diego, Calif.), 41(4), 409–416. https://doi.org/10.1016/j.ymeth.2006.07.019

Runswick, M. J., Fearnley, I. M., Skehel, J. M., & Walker, J. E. (1991). Presence of an acyl carrier protein in NADH:ubiquinone oxidoreductase from bovine heart mitochondria. *FEBS letters,* 286(1-2), 121–124. https://doi.org/10.1016/0014-5793(91)80955-3

Russell, O. M., Gorman, G. S., Lightowlers, R. N., & Turnbull, D. M. (2020). Mitochondrial Diseases: Hope for the Future. *Cell,*181(1), 168–188. https://doi.org/10.1016/j.cell.2020.02.051

Russo, C. J., & Passmore, L. A. (2014a). Electron microscopy: Ultrastable gold substrates for electron cryomicroscopy. *Science*, 346(6215), 1377–1380. https://doi.org/10.1126/science.1259530

Russo, C. J., & Passmore, L. A. (2014b). Controlling protein adsorption on graphene for cryo-EM using low-energy hydrogen plasmas. *Nature methods*, 11(6), 649–652. https://doi.org/10.1038/nmeth.2931

Russo, C. J., & Passmore, L. A. (2016). Ultrastable gold substrates: Properties of a support for high-resolution electron cryomicroscopy of biological specimens. *Journal of structural biology,* 193(1), 33–44. https://doi.org/10.1016/j.jsb.2015.11.006

Sabatini, D. D., Bensch, K., & Barrnett, R. J. (1963). Cytochemistry and electron microscopy. The preservation of cellular ultrastructure and enzymatic activity by aldehyde fixation. *The Journal of cell biology*, 17(1), 19–58. https://doi.org/10.1083/jcb.17.1.19

Sabharwal, S. S., & Schumacker, P. T. (2014). Mitochondrial ROS in cancer: initiators, amplifiers or an Achilles' heel? Nature reviews. *Cancer,* 14(11), 709–721. https://doi.org/10.1038/nrc3803

Sagan, L. (1967). On the origin of mitosing cells. *Journal of Theoretical Biology,* 14(3), 225-IN6. https://doi.org/10.1016/0022-5193(67)90079-3

Sánchez-Caballero, L., Guerrero-Castillo, S., & Nijtmans, L. (2016). Unraveling the complexity of mitochondrial complex I assembly: A dynamic process. *Biochimica et biophysica acta,* 1857(7), 980–990. https://doi.org/10.1016/j.bbabio.2016.03.031

Sardanelli, A. M., Signorile, A., Nuzzi, R., Rasmo, D. D., Technikova-Dobrova, Z., Drahota, Z., Occhiello, A., Pica, A., & Papa, S. (2006). Occurrence of A-kinase anchor protein and associated cAMP-dependent protein kinase in the inner compartment of mammalian mitochondria. *FEBS letters,* 580(24), 5690–5696. https://doi.org/10.1016/j.febslet.2006.09.020

Sazanov L. A. (2015). A giant molecular proton pump: structure and mechanism of respiratory complex I. *Nature reviews.* Molecular cell biology, 16(6), 375–388. https://doi.org/10.1038/nrm3997

Sazanov, L. A., & Hinchliffe, P. (2006). Structure of the hydrophilic domain of respiratory complex I from Thermus thermophilus. *Science*, 311(5766), 1430–1436. https://doi.org/10.1126/science.1123809

Scacco, S., Petruzzella, V., Budde, S., Vergari, R., Tamborra, R., Panelli, D., van den Heuvel, L. P., Smeitink, J. A., & Papa, S. (2003). Pathological mutations of the human NDUFS4 gene of the 18-kDa (AQDQ) subunit of complex I affect the expression of the protein and the assembly and function of the complex. *The Journal of biological chemistry*, 278(45), 44161–44167. https://doi.org/10.1074/jbc.M307615200

Scacco, S., Vergari, R., Scarpulla, R. C., Technikova-Dobrova, Z., Sardanelli, A., Lambo, R., Lorusso, V., & Papa, S. (2000). cAMP-dependent phosphorylation of the nuclear encoded 18-kDa (IP) subunit of respiratory complex I and activation of the complex in serum-starved mouse fibroblast cultures. *The Journal of biological chemistry,* 275(23), 17578–17582. https://doi.org/10.1074/jbc.M001174200

Schägger, H., & Pfeiffer, K. (2000). Supercomplexes in the respiratory chains of yeast and mammalian mitochondria. The EMBO journal, 19(8), 1777–1783. https://doi.org/10.1093/emboj/19.8.1777

Scheres S. H. (2012). A Bayesian view on cryo-EM structure determination. *Journal ofmolecular biology*, 415(2), 406–418. https://doi.org/10.1016/j.jmb.2011.11.010

Scheres S. H. (2016). Processing of Structurally Heterogeneous Cryo-EM Data in RELION. *Methods in enzymology,* 579, 125–157. https://doi.org/10.1016/bs.mie.2016.04.012

Schmidt, C., & Robinson, C. V. (2014). A comparative cross-linking strategy to probe conformational changes in protein complexes. *Nature protocols,* 9(9), 2224–2236. https://doi.org/10.1038/nprot.2014.144

Schmidt, C., & Urlaub, H. (2017). Combining cryo-electron microscopy (cryo-EM) andcross-linking mass spectrometry (CX-MS) for structural elucidation of large protein assemblies. *Current opinion in structural biology*, 46, 157–168. https://doi.org/10.1016/j.sbi.2017.10.005

Schubert Baldo, M., & Vilarinho, L. (2020). Molecular basis of Leigh syndrome: a current look. *Orphanet journal of rare diseases,* 15(1), 31. https://doi.org/10.1186/s13023-020-1297-9

Sgro, G. G., & Costa, T. (2018). Cryo-EM Grid Preparation of Membrane Protein Samples for Single Particle Analysis. *Frontiers in molecular biosciences,* 5, 74. https://doi.org/10.3389/fmolb.2018.00074

Sharpley, M. S., Shannon, R. J., Draghi, F., & Hirst, J. (2006). Interactions between phospholipids and NADH:ubiquinone oxidoreductase (complex I) from bovine mitochondria. *Biochemistry,* 45(1), 241–248. https://doi.org/10.1021/bi051809x

Sheftel, A. D., Stehling, O., Pierik, A. J., Netz, D. J., Kerscher, S., Elsässer, H. P., Wittig, I., Balk, J., Brandt, U., & Lill, R. (2009). Human ind1, an iron-sulfur cluster assembly factor for respiratory complex I. *Molecular and cellular biology,* 29(22), 6059–6073. https://doi.org/10.1128/MCB.00817-09

Shemesh, A., Sood, G., & Margolin, E. (2020). Leber Hereditary Optic Neuropathy (LHON). *In StatPearls.* StatPearls Publishing.

Shi, J. M., Pei, J., Liu, E. Q., & Zhang, L. (2017). Bis(sulfosuccinimidyl) suberate (BS3) crosslinking analysis of the behavior of amyloid-β peptide in solution and in phospholipid membranes. *PloS one,* 12(3), e0173871. https://doi.org/10.1371/journal.pone.0173871

Shoshan-Barmatz, V., Krelin, Y., & Shteinfer-Kuzmine, A. (2018). VDAC1 functions in $Ca2^{+}$ homeostasis and cell life and death in health and disease. *Cell calcium,* 69, 81–100. https://doi.org/10.1016/j.ceca.2017.06.007

Sies, H., & Jones, D. P. (2020). Reactive oxygen species (ROS) as pleiotropic physiological signalling agents. *Nature reviews. Molecular cell biology,* 21(7), 363–383. https://doi.org/10.1038/s41580-020-0230-3

Signorile, A., Sardanelli, A. M., Nuzzi, R., & Papa, S. (2002). Serine (threonine) phosphatase(s) acting on cAMP-dependent phosphoproteins in mammalian mitochondria. *FEBS letters,* 512(1-3), 91–94. https://doi.org/10.1016/s0014-5793(02)02226-3

Silva-Pinheiro, P., Cerutti, R., Luna-Sanchez, M., Zeviani, M., & Viscomi, C. (2020). A Single Intravenous Injection of AAV-PHP.B-hNDUFS4 Ameliorates the Phenotype of $Ndufs4^{-/-}$ Mice. *Molecular Therapy - Methods and Clinical Development,* 17(June), 1071–1078. https://doi.org/10.1016/j.omtm.2020.04.026

Skladal, D., Halliday, J., & Thorburn, D. R. (2003). Minimum birth prevalence of mitochondrial respiratory chain disorders in children. *Brain: a journal of neurology*, 126(Pt 8), 1905–1912. https://doi.org/10.1093/brain/awg170

Slater, E. C., & Cleland, K. W. (1953). The calcium content of isolated heart-muscle sarcosomes. *The Biochemical journal*, 54(3), xxii.

Söding J. (2005). Protein homology detection by HMM-HMM comparison. *Bioinformatics (*Oxford, England), 21(7), 951–960. https://doi.org/10.1093/bioinformatics/bti125

Song, B., Lenhart, J., Flegler, V. J., Makbul, C., Rasmussen, T., & Böttcher, B. (2019). Capabilities of the Falcon III detector for single-particle structure determination. *Ultramicroscopy,* 203(January), 145–154. https://doi.org/10.1016/j.ultramic.2019.01.002

Starkov A. A. (2008). The role of mitochondria in reactive oxygen species metabolismand signaling. *Annals of the New York Academy of Sciences,* 1147, 37–52. https://doi.org/10.1196/annals.1427.015

Stehling, O., & Lill, R. (2013). The role of mitochondria in cellular iron-sulfur proteinbiogenesis: mechanisms, connected processes, and diseases. *Cold Spring Harbor perspectives in biology,* 5(8), a011312. https://doi.org/10.1101/cshperspect.a011312

Stein, L. R., & Imai, S. (2012). The dynamic regulation of NAD metabolism in mitochondria. T*rends in endocrinology and metabolism: TEM*, 23(9), 420–428. https://doi.org/10.1016/j.tem.2012.06.005

Sterky, F. H., Hoffman, A. F., Milenkovic, D., Bao, B., Paganelli, A., Edgar, D., Wibom, R., Lupica, C. R., Olson, L., & Larsson, N. G. (2012). Altered dopamine metabolism and increased vulnerability to MPTP in mice with partial deficiency of mitochondrial complex I in dopamine neurons. *Human molecular genetics,* 21(5), 1078–1089. https://doi.org/10.1093/hmg/ddr537

Stiller, S. B., Höpker, J., Oeljeklaus, S., Schütze, C., Schrempp, S. G., Vent-Schmidt, J., Horvath, S. E., Frazier, A. E., Gebert, N., van der Laan, M., Bohnert, M., Warscheid, B., Pfanner, N., & Wiedemann, N. (2016). Mitochondrial OXA Translocase Plays a Major

Role in Biogenesis of Inner-Membrane Proteins. *Cell metabolism,* 23(5), 901–908. https://doi.org/10.1016/j.cmet.2016.04.005

Strauss, K. A., DuBiner, L., Simon, M., Zaragoza, M., Sengupta, P. P., Li, P., Narula,N., Dreike, S., Platt, J., Procaccio, V., Ortiz-González, X. R., Puffenberger, E. G., Kelley, R. I., Morton, D. H., Narula, J., & Wallace, D. C. (2013). Severity of cardiomyopathy associated with adenine nucleotide translocator-1 deficiency correlates with mtDNA haplogroup. *Proceedings of the National Academy of Sciences of the United StatesofAmerica,* 110(9), 3453–3458. https://doi.org/10.1073/pnas.1300690110

Stroud, D. A., Formosa, L. E., Wijeyeratne, X. W., Nguyen, T. N., & Ryan, M. T. (2013). Gene knockout using transcription activator-like effector nucleases (TALENs) reveals that human NDUFA9 protein is essential for stabilizing the junction between membrane and matrix arms of complex I. *The Journal of biological chemistry,* 288(3), 1685–1690. https://doi.org/10.1074/jbc.C112.436766

Stroud, D. A., Surgenor, E. E., Formosa, L. E., Reljic, B., Frazier, A. E., Dibley, M. G., Osellame, L. D., Stait, T., Beilharz, T. H., Thorburn, D. R., Salim, A., & Ryan, M. T. (2016). Accessory subunits are integral for assembly and function of human mitochondrial complex I. *Nature*, 538(7623), 123–126. https://doi.org/10.1038/nature19754

Subramanian, K., Jochem, A., Le Vasseur, M., Lewis, S., Paulson, B. R., Reddy, T. R., Russell, J. D., Coon, J. J., Pagliarini, D. J., & Nunnari, J. (2019). Coenzyme Q biosynthetic proteins assemble in a substrate-dependent manner into domains at ER-mitochondria contacts. *The Journal of cell biology*, 218(4), 1353–1369. https://doi.org/10.1083/jcb.201808044

Sun, F., Huo, X., Zhai, Y., Wang, A., Xu, J., Su, D., Bartlam, M., & Rao, Z. (2005). Crystal structure of mitochondrial respiratory membrane protein complex II. *Cell*, 121(7), 1043–1057. https://doi.org/10.1016/j.cell.2005.05.025

Sun, F., Zhou, Q., Pang, X., Xu, Y., & Rao, Z. (2013). Revealing various coupling of electron transfer and proton pumping in mitochondrial respiratory chain. *Current opinion in structural biology,* 23(4), 526–538. https://doi.org/10.1016/j.sbi.2013.06.013

Tan, Y. Z., Baldwin, P. R., Davis, J. H., Williamson, J. R., Potter, C. S., Carragher, B., & Lyumkis, D. (2017). Addressing preferred specimen orientation in single-particle cryo-EM through tilting. *Nature methods*, 14(8), 793–796. https://doi.org/10.1038/nmeth.4347

Taylor, R. W., & Turnbull, D. M. (2005). Mitochondrial DNA mutations in human disease. Nature reviews. *Genetics,* 6(5), 389–402. https://doi.org/10.1038/nrg1606

Thompson, R. F., Walker, M., Siebert, C. A., Muench, S. P., & Ranson, N. A. (2016). An introduction to sample preparation and imaging by cryo-electron microscopy forstructural biology. *Methods*, 100, 3–15. https://doi.org/10.1016/j.ymeth.2016.02.017

Torraco, A., Peralta, S., Iommarini, L., & Diaz, F. (2015). Mitochondrial diseases part I: Mouse models of OXPHOS deficiencies caused by defects in respiratory complex subunits or assembly factors. *Mitochondrion,* 21, 76–91. https://doi.org/10.1016/j.mito.2015.01.009

Tucker, E. J., Compton, A. G., Calvo, S. E., & Thorburn, D. R. (2011). The molecular basis of human complex I deficiency. *IUBMB life*, 63(9), 669–677. https://doi.org/10.1002/iub.495

Twig, G., Elorza, A., Molina, A. J., Mohamed, H., Wikstrom, J. D., Walzer, G., Stiles, L., Haigh, S. E., Katz, S., Las, G., Alroy, J., Wu, M., Py, B. F., Yuan, J., Deeney,J. T., Corkey, B. E., & Shirihai, O. S. (2008). Fission and selective fusion govern mitochondrial segregation and elimination by autophagy. *The EMBO journal*, 27(2), 433–446. https://doi.org/10.1038/sj.emboj.7601963

Ugalde, C., Janssen, R. J., van den Heuvel, L. P., Smeitink, J. A., & Nijtmans, L. G.(2004). Differences in assembly or stability of complex I and other mitochondrial OXPHOS

complexes in inherited complex I deficiency. *Human molecular genetics*, 13(6), 659–667. https://doi.org/10.1093/hmg/ddh071

van den Heuvel, L., Ruitenbeek, W., Smeets, R., Gelman-Kohan, Z., Elpeleg, O., Loeffen, J., Trijbels, F., Mariman, E., de Bruijn, D., & Smeitink, J. (1998). Demonstration of a new pathogenic mutation in human complex I deficiency: a 5-bp duplication in the nuclear gene encoding the 18-kD (AQDQ) subunit. *American journal of human genetics*, 62(2), 262–268. https://doi.org/10.1086/301716

Vinothkumar, K. R., & Henderson, R. (2016). Single particle electron cryomicroscopy: trends, issues and future perspective. *Quarterly reviews of biophysics,* 49, e13. https://doi.org/10.1017/S0033583516000068

Vinothkumar, K. R., Zhu, J., & Hirst, J. (2014). Architecture of mammalian respiratory complex I. *Nature*, 515(7525), 80–84. https://doi.org/10.1038/nature13686

Vogel, R. O., Dieteren, C. E., van den Heuvel, L. P., Willems, P. H., Smeitink, J. A., Koopman, W. J., & Nijtmans, L. G. (2007). Identification of mitochondrial complex I assembly intermediates by tracing tagged NDUFS3 demonstrates the entry point of mitochondrial subunits. *The Journal of biological chemistry,* 282(10), 7582–7590. https://doi.org/10.1074/jbc.M609410200

Vogel, R. O., van den Brand, M. A., Rodenburg, R. J., van den Heuvel, L. P., Tsuneoka, M., Smeitink, J. A., & Nijtmans, L. G. (2007). Investigation of the complex I assembly chaperones B17.2L and NDUFAF1 in a cohort of CI deficient patients. *Molecular genetics and metabolism*, 91(2), 176–182. https://doi.org/10.1016/j.ymgme.2007.02.007

Vyas, S., Zaganjor, E., & Haigis, M. C. (2016). Mitochondria and Cancer. *Cell,* 166(3),555–566. https://doi.org/10.1016/j.cell.2016.07.002

Walker J. E. (2013). The ATP synthase: the understood, the uncertain and the unknown. *Biochemical Society transactions*, 41(1), 1–16. https://doi.org/10.1042/BST20110773

Wallace D. C. (2009). Mitochondria, bioenergetics, and the epigenome in eukaryotic and human evolution. *Cold Spring Harbor symposia on quantitative biology,* 74, 383–393. https://doi.org/10.1101/sqb.2009.74.031

Wallace, D. C., Singh, G., Lott, M. T., Hodge, J. A., Schurr, T. G., Lezza, A. M., Elsas, L. J., 2nd, & Nikoskelainen, E. K. (1988). Mitochondrial DNA mutation associated with Leber's hereditary optic neuropathy. *Science* (New York, N.Y.), 242(4884), 1427–1430. https://doi.org/10.1126/science.3201231

Wang, Y., & Hekimi, S. (2013). Mitochondrial respiration without ubiquinone biosynthesis. *Human Molecular Genetics,* 22(23),4768–4783. https://doi.org/https://doi.org/10.1002/biof.1160

Wang, Y., Oxer, D., & Hekimi, S. (2015). Mitochondrial function and lifespan of mice with controlled ubiquinone biosynthesis. *Nature Communications*, 6, 6393. https://doi.org/10.1038/ncomms7393

Watt, I. N., Montgomery, M. G., Runswick, M. J., Leslie, A. G., & Walker, J. E. (2010). Bioenergetic cost of making an adenosine triphosphate molecule in animal mitochondria. *Proceedings of the National Academy of Sciences of the United States of America,* 107(39), 16823–16827. https://doi.org/10.1073/pnas.1011099107

Wheeldon, I., Minteer, S. D., Banta, S., Barton, S. C., Atanassov, P., & Sigman, M. (2016). Substrate channelling as an approach to cascade reactions. *Nature chemistry*, 8(4), 299–309. https://doi.org/10.1038/nchem.2459

Wikström M. (1984). Two protons are pumped from the mitochondrial matrix per electron transferred between NADH and ubiquinone. *FEBS letters*, 169(2), 300–304. https://doi.org/10.1016/0014-5793(84)80338-5

Wikström, M., Sharma, V., Kaila, V. R. I., Hosler, J. P., & Hummer, G. (2015). NewPerspectives on Proton Pumping in Cellular Respiration. *Chemical Reviews*, 115(5), 2196–2221. https://doi.org/10.1021/cr500448t

Wilkinson, M. E., Kumar, A., & Casañal, A. (2019). Methods for merging data sets in electron cryo-microscopy. *Acta crystallographica. Section D, Structural biology*, 75(Pt 9), 782–791. https://doi.org/10.1107/S2059798319010519

Williams R. C. (1977). Use of polylysine for adsorption of nuclei acids and enzymes to electron microscope specimen films. *Proceedings of the National Academy of Sciences of the United States of America,* 74(6), 2311–2315. https://doi.org/10.1073/pnas.74.6.2311

Williams, R. C., & Glaeser, R. M. (1972). Ultrathin carbon support films for electron microscopy. *Science,*175(4025), 1000–1001. https://doi.org/10.1126/science.175.4025.1000

Wilson, N. R., Pandey, P. A., Beanland, R., Young, R. J., Kinloch, I. A., Gong, L., Liu, Z., Suenaga, K., Rourke, J. P., York, S. J., & Sloan, J. (2009). Graphene oxide: structural analysis and application as a highly transparent support for electron microscopy. *ACS nano*, 3(9), 2547–2556. https://doi.org/10.1021/nn900694t

Wirth, C., Brandt, U., Hunte, C., & Zickermann, V. (2016). Structure and function of mitochondrial complex I. *Biochimica et Biophysica Acta (BBA) - Bioenergetics,* 1857(7), 902–914. https://doi.org/10.1016/j.bbabio.2016.02.013

Wong, H. S., Dighe, P. A., Mezera, V., Monternier, P. A., & Brand, M. D. (2017). Production of superoxide and hydrogen peroxide from specific mitochondrial sites under different bioenergetic conditions. *The Journal of biological chemistry,* 292(41), 16804–16809. https://doi.org/10.1074/jbc.R117.789271

Wu, M., Gu, J., Guo, R., Huang, Y., & Yang, M. (2016). Structure of Mammalian Respiratory Supercomplex $I_1III_2IV_1$. *Cell*, 167(6), 1598-1609.e10. https://doi.org/10.1016/j.cell.2016.11.012

Xia, D., Esser, L., Tang, W. K., Zhou, F., Zhou, Y., Yu, L., & Yu, C. A. (2013). Structural analysis of cytochrome bc1 complexes: implications to the mechanism of function. *Biochimica et biophysica acta*, *1827*(11-12), 1278–1294. https://doi.org/10.1016/j.bbabio.2012.11.008

Xia, D., Yu, C. A., Kim, H., Xia, J. Z., Kachurin, A. M., Zhang, L., Yu, L., & Deisenhofer, J. (1997). Crystal structure of the cytochrome bc1 complex from bovine heartmitochondria. *Science*, 277(5322), 60–66. https://doi.org/10.1126/science.277.5322.60

Yakovlev, G., & Hirst, J. (2007). Transhydrogenation reactions catalyzed by mitochondrial NADH-ubiquinone oxidoreductase (complex I). *Biochemistry,* 46(49), 14250–14258. https://doi.org/10.1021/bi7017915

Yin, Z., Burger, N., Kula-Alwar, D., Aksentijević, D., Bridges, H. R., Prag, H. A., Grba, D. N., Viscomi, C., James, A. M, Mottahedin, A., Krieg, T., Murphy, M. P. & Hirst, J. (2021) Structural basis for a complex I mutation that blocks pathological ROS production. *Nature communications*, https://doi.org/10.1038/s41467-021-20942-w

Yip, C. Y., Harbour, M. E., Jayawardena, K., Fearnley, I. M., & Sazanov, L. A. (2011). Evolution of respiratory complex I: "supernumerary" subunits are present in the alpha-proteobacterial enzyme. The Journal of biological chemistry, 286(7), 5023–5033. *Journal of Biological Chemistry,* 286(7), 5023–5033. https://doi.org/10.1074/jbc.M110.194993

Yoshikawa, S., Muramoto, K., & Shinzawa-Itoh, K. (2011). Proton-pumping mechanism of cytochrome C oxidase. *Annual review of biophysics,* 40, 205–223. https://doi.org/10.1146/annurev-biophys-042910-155341

Yoshioka, C., Carragher, B., & Potter, C. S. (2010). Cryomesh: a new substrate for cryo-electron microscopy. *Microscopy and microanalysis: the official journal of Microscopy Society of America, Microbeam Analysis Society, Microscopical Society of Canada*, 16(1), 43–53. https://doi.org/10.1017/S1431927609991310

Youle, R. J., & Narendra, D. P. (2011). Mechanisms of mitophagy. *Nature reviews. Molecular cell biology,* 12(1), 9–14. https://doi.org/10.1038/nrm3028

Yu-Wai-Man, P., Griffiths, P. G., Hudson, G., & Chinnery, P. F. (2009). Inherited mitochondrial optic neuropathies. *Journal of medical genetics*, 46(3), 145–158. https://doi.org/10.1136/jmg.2007.054270

Zhang K. (2016). Gctf: Real-time CTF determination and correction. *Journal of structural biology,* 193(1), 1–12. https://doi.org/10.1016/j.jsb.2015.11.003

Zhang, L., Zhang, Z., Khan, A., Zheng, H., Yuan, C., & Jiang, H. (2020). Advances in drug therapy for mitochondrial diseases. *Annals of translational medicine*, 8(1), 17. https://doi.org/10.21037/atm.2019.10.113

Zhang, R., Hryc, C. F., Cong, Y., Liu, X., Jakana, J., Gorchakov, R., Baker, M. L., Weaver, S. C., & Chiu, W. (2011). 4.4 Å cryo-EM structure of an enveloped alphavirus Venezuelan equine encephalitis virus. *The EMBO journal,* 30(18), 3854–3863. https://doi.org/10.1038/emboj.2011.261

Zheng, S. Q., Palovcak, E., Armache, J. P., Verba, K. A., Cheng, Y., & Agard, D. A(2017). MotionCor2: anisotropic correction of beam-induced motion for improved cryo-electron microscopy. *Nature methods*, 14(4), 331–332. https://doi.org/10.1038/nmeth.4193

Zickermann, V., Wirth, C., Nasiri, H., Siegmund, K., Schwalbe, H., Hunte, C., & Brandt, U. (2015). Structural biology. Mechanistic insight from the crystal structure of mitochondrial complex I. *Science* (New York, N.Y.), 347(6217), 44–49. https://doi.org/10.1126/science.1259859

Zivanov, J., Nakane, T., Forsberg, B. O., Kimanius, D., Hagen, W. J., Lindahl, E., & Scheres, S. H. (2018). New tools for automated high-resolution cryo-EM structure determination in RELION-3. *eLife*, 7, e42166. https://doi.org/10.7554/eLife.42166

Zong, S., Wu, M., Gu, J., Liu, T., Guo, R., & Yang, M. (2018). Structure of the intact 14-subunit human cytochrome c oxidase. *Cell research*, 28(10), 1026–1034. https://doi.org/10.1038/s41422-018-0071-1

Zorov, D. B., Juhaszova, M., & Sollott, S. J. (2014). Mitochondrial reactive oxygen species (ROS) and ROS-induced ROS release. *Physiological reviews*, 94(3), 909–950. https://doi.org/10.1152/physrev.00026.2013